

Optical properties of organic semiconductor  
thin films: Static spectra and real-time  
growth studies

Dissertation

zur Erlangung des Grades eines Doktors

der Naturwissenschaften

der Fakultät für Mathematik und Physik

der Eberhard-Karls-Universität zu Tübingen

vorgelegt von

Ute Heinemeyer

aus: Bonn

2009



Tag der mündlichen Prüfung: 20.07.2009

Dekan: Prof. Dr. Wolfgang Knapp

1. Berichterstatter: Prof. Dr. Frank Schreiber
2. Berichterstatter: Prof. Dr. Alfred J. Meixner



# CONTENTS

<b>1</b>	<b>Deutsche Zusammenfassung</b>	<b>v</b>
1.1	Motivation . . . . .	v
1.2	Experimentelle Ergebnisse . . . . .	vi
1.2.1	Absorption von DIP in Lösung . . . . .	vii
1.2.2	Strukturelle und morphologische Eigenschaften von DIP Filmen . .	vii
1.2.3	Statische DIP Filmspektren . . . . .	vii
1.2.4	Echtzeit-Untersuchungen des Filmwachstums . . . . .	viii
1.2.5	Weiterführende optische Untersuchungen an DIP Filmen . . . . .	x
1.3	Schlussfolgerungen . . . . .	x
<b>2</b>	<b>Introduction</b>	<b>1</b>
<b>3</b>	<b>Fundamentals</b>	<b>5</b>
3.1	Organic semiconductors . . . . .	5
3.1.1	Monomers . . . . .	5
3.1.1.1	$\pi$ -electron system . . . . .	5
3.1.1.2	Molecular excitations . . . . .	6
3.1.1.3	Vibronic progression . . . . .	6
3.1.2	Molecular crystals . . . . .	7
3.1.2.1	Excitons and optical properties . . . . .	8
3.1.2.2	Exciton transfer . . . . .	10
3.1.3	Organic materials . . . . .	12
3.1.3.1	Diindenoperylene (DIP) . . . . .	12

3.1.3.2	Pentacene (PEN) . . . . .	17
3.1.4	Thin film growth . . . . .	18
3.2	Optics . . . . .	19
3.2.1	Dielectric function . . . . .	19
3.2.2	Fresnel equations . . . . .	21
3.2.3	Multilayers and matrix method . . . . .	22
<b>4</b>	<b>Experimental methods</b>	<b>25</b>
4.1	Sample preparation . . . . .	25
4.1.1	Preparation of the organic molecules . . . . .	25
4.1.2	Substrate preparation . . . . .	25
4.1.3	Vacuum system . . . . .	27
4.1.3.1	Evaporation cell . . . . .	27
4.1.3.2	Sample holder . . . . .	28
4.1.4	Organic molecular beam deposition . . . . .	28
4.2	Spectroscopic ellipsometry . . . . .	29
4.2.1	Principle . . . . .	29
4.2.2	Setup . . . . .	30
4.2.3	<i>Ex-situ</i> measurement . . . . .	31
4.2.4	<i>In-situ</i> measurement . . . . .	31
4.3	Differential reflectance spectroscopy . . . . .	32
4.3.1	Principle . . . . .	32
4.3.2	Setup . . . . .	32
4.3.3	Measurement . . . . .	33
4.4	Absorption spectroscopy . . . . .	33
4.4.1	Principle . . . . .	33
4.4.2	Setup and measurement . . . . .	34
4.5	Fluorescence spectroscopy . . . . .	34
4.5.1	Principle . . . . .	34
4.5.2	Setup and measurement . . . . .	35
4.6	Raman spectroscopy . . . . .	35
4.6.1	Principle . . . . .	35
4.6.2	Setup and measurement . . . . .	36

---

4.7	Tip-enhanced spectroscopic imaging . . . . .	36
4.7.1	Principle . . . . .	36
4.7.2	Setup and measurement . . . . .	37
4.8	X-ray reflectivity . . . . .	37
4.8.1	Principle . . . . .	37
4.8.2	Setup and measurement . . . . .	39
4.9	Atomic force microscopy . . . . .	39
4.9.1	Principle . . . . .	39
4.9.2	Setup and measurement . . . . .	40
<b>5</b>	<b>Results &amp; Discussion</b>	<b>41</b>
5.1	DIP absorption spectra in solution . . . . .	42
5.2	Substrate characterization . . . . .	44
5.2.1	Morphology . . . . .	44
5.2.2	Optical properties . . . . .	45
5.3	Structural and morphological film properties of DIP . . . . .	47
5.3.1	X-ray data . . . . .	47
5.3.1.1	DIP grown at $T = 130$ °C on Si substrates . . . . .	47
5.3.1.2	Comparison between DIP on glass and on $\text{Si}_{\text{ThO}_x}$ . . . . .	49
5.3.1.3	DIP films grown at $T = -105$ °C . . . . .	51
5.3.2	AFM data . . . . .	52
5.3.2.1	DIP films grown at $T = 130$ °C . . . . .	52
5.3.2.2	DIP films grown at $T = -105$ °C . . . . .	55
5.4	Static anisotropic dielectric function of DIP grown on $\text{SiO}_2$ . . . . .	55
5.4.1	Data analysis for uniaxial thin films . . . . .	56
5.4.1.1	Uniaxial anisotropy . . . . .	56
5.4.1.2	Thickness determination . . . . .	59
5.4.2	DIP data analysis and fit results . . . . .	59
5.4.2.1	Point-by-point fit . . . . .	60
5.4.2.2	Gaussian oscillator fit . . . . .	63
5.4.3	Discussion . . . . .	65
5.4.3.1	Molecular tilt angle . . . . .	65
5.4.3.2	Comparison to solution spectra . . . . .	65

---

5.4.3.3	Transition dipole . . . . .	66
5.4.3.4	Difference between in-plane and out-of-plane component . . . . .	67
5.4.3.5	Frenkel exciton transfer . . . . .	68
5.4.3.6	Mixing of Frenkel excitons and charge transfer states . . . . .	70
5.4.3.7	Concluding remarks . . . . .	71
5.5	Film growth followed by optical real-time measurements . . . . .	72
5.5.1	DIP film growth on Si <sub>Ntve</sub> . . . . .	73
5.5.1.1	Film growth at $T = 130$ °C followed by ellipsometry . . . . .	73
5.5.1.2	Film growth at $T = 130$ °C followed by DRS . . . . .	78
5.5.1.3	Film growth at $T = -100$ °C . . . . .	79
5.5.2	DIP film growth on glass . . . . .	79
5.5.2.1	Film growth at $T = 130$ °C . . . . .	80
5.5.2.2	Film growth at $T < -100$ °C . . . . .	84
5.5.3	PEN film growth . . . . .	86
5.5.3.1	Film morphology . . . . .	86
5.5.3.2	Static uniaxial dielectric function . . . . .	87
5.5.3.3	PEN film growth on Si <sub>Ntve</sub> . . . . .	88
5.5.3.4	PEN film growth on glass . . . . .	90
5.5.4	Discussion . . . . .	90
5.5.4.1	Transition arising during growth . . . . .	92
5.5.4.2	Energy shift during growth . . . . .	96
5.5.4.3	Concluding remarks . . . . .	100
5.6	Results of complementary optical methods . . . . .	101
5.6.1	Raman spectroscopy . . . . .	102
5.6.2	Fluorescence spectroscopy . . . . .	105
5.6.3	Tip-enhanced spectroscopic imaging . . . . .	107
<b>6</b>	<b>Outlook</b>	<b>113</b>
<b>7</b>	<b>Conclusion</b>	<b>115</b>
	<b>List of abbreviations</b>	<b>118</b>
	<b>Bibliography</b>	<b>119</b>



# CHAPTER 1

## DEUTSCHE ZUSAMMENFASSUNG

### 1.1 Motivation

Das Interesse an organischen Halbleitern hat in den letzten 20 Jahren stark zugenommen, da sie ein großes Potential für elektronische und opto-elektronische Anwendungen bieten, z. B. für Leuchtdioden, Feldeffekttransistoren und Solarzellen [1, 2, 3, 4, 5, 6]. Aus wissenschaftlicher sowie aus technologischer Sicht besteht ihr eigentlicher Reiz für die organische Elektronik in der großen Variabilität ihrer Eigenschaften. Die Moleküle oder Polymere sind wegen ihres konjugierten  $\pi$ -Elektronensystems ungesättigte Verbindungen des Kohlenstoffs, so dass sich elementare physikalische Eigenschaften, wie die elektronische Bandlücke oder die Beweglichkeit der Ladungsträger, mit Mitteln der präparativen organische Chemie variieren und optimieren lassen. Dies stellt einen fundamentalen Unterschied zur anorganischen Elektronik dar, die auf wenige Materialien wie Silizium oder Germanium zurückgreift. Dennoch werden die traditionellen Halbleiter nicht von organischen Materialien verdrängt werden, da letztere aufgrund ihrer vergleichsweise schwachen intermolekularen Wechselwirkung intrinsisch geringere Ladungsträgerbeweglichkeiten aufweisen [1, 2, 7]. Das Potential organischer Halbleiter liegt vielmehr in neuen innovativen Anwendungen wie großflächigen Displays, flexiblen Substraten oder Billig-Elektronik, von denen bereits einige, insbesondere OLED's, auf dem Markt zu finden sind.

Es gibt im wesentlichen zwei Materialklassen, die in der organischen Elektronik zur Anwendung kommen: Polymere und kleine Moleküle. In dieser Arbeit werden organische Moleküle untersucht, die hoch geordnete Strukturen in dünnen Filmen ausbilden können. Diese Filme werden durch organische Molekülstrahldeposition im Ultrahoch-Vakuum (UHV) hergestellt, wodurch ihre strukturellen, elektrischen und optischen Eigenschaften bestmöglich kontrollierbar sind. Das Filmwachstum hat einen bedeutenden Einfluss auf diese Eigenschaften, welche die Art der möglichen Anwendung in der Elektronik bestimmen. So kann durch die Substrat-Temperatur oder die Aufdampftrate die Filmstruktur verändert werden, was die Ladungsträgerbeweglichkeiten ebenso wie die optischen Eigen-

schaften beeinflusst.

Der Fokus dieser Arbeit liegt auf der Untersuchung der optischen Eigenschaften dünner Filme, welche eng mit den elektronischen und strukturellen Eigenschaften verknüpft sind. Sie stellen daher eine wichtige Grundlage zum Verständnis und zur Optimierung der Filme und ihrer Anwendungen dar. So können Absorptionsspektren über die Exziton-Phonon-Kopplung Auskunft geben, die beim Hüpftransport eine Rolle spielt [8]. Auch der durch die intermolekulare Wechselwirkung mögliche Exzitontransfer kann anhand optischer Dünnsfilmspektren untersucht werden [9,10], ebenso wie die Exzitudiffusionslänge, welche insbesondere für organische Solarzellen wichtig ist. Um diese Eigenschaften schon während des Filmwachstums beobachten und gegebenenfalls beeinflussen zu können, sind Echtzeit-Messungen notwendig. Optische Methoden, wie die in dieser Arbeit verwendete spektroskopische Ellipsometrie oder die differentielle Reflektionsspektroskopie (DRS), sind dafür besonders geeignet, weil sie nicht-invasiv und *in-situ*, also unter UHV Bedingungen, einsetzbar sind.

Konkret werden die optischen Eigenschaften von Diindenoperylen (DIP) auf oxidierten Silizium-Substraten ( $\text{Si}_{\text{Ntve}}$ ) untersucht. DIP ist in den letzten Jahren durch eine besonders gute kristalline Ordnung und hohe Leitfähigkeit in dünnen Filmen aufgefallen [11,12,13,14,15,16,17], worin ein großes Potential für elektronische Anwendungen gesehen wird. Zum Vergleich wird auch Pentacen (PEN) behandelt, eines der meist untersuchten organischen Moleküle, dessen optische Eigenschaften während des Filmwachstums jedoch noch weitgehend unbekannt sind. Da die statische dielektrische Funktion von PEN im Rahmen einer Diplomarbeit von A. Hinderhofer untersucht wurde [19,20], beschränkt sich diese Arbeit, neben einer ausführlichen Untersuchung von DIP Monomeren und Filmen, im wesentlichen auf die Echtzeit-Daten von PEN während des Filmwachstums.

## 1.2 Experimentelle Ergebnisse

Zum Verständnis der optischen Spektren dünner Filme ist es notwendig, die Eigenschaften eines freien Moleküls, d.h. eines Monomers, zu kennen, weshalb zu Beginn DIP Spektren in Lösung untersucht werden. Ebenso wichtig sind Kenntnisse zur strukturellen Anordnung der Moleküle im Film, die zum großen Teil, aber nicht in allen Fällen aus früheren Arbeiten bekannt sind, so dass strukturelle Voruntersuchungen notwendig sind. Im ersten Hauptteil dieser Arbeit werden die statischen Spektren von DIP Filmen nach dem Wachstum mit Hilfe von Ellipsometrie charakterisiert. Sie dienen als Grundlage für die nachfolgenden Echtzeit-Messungen während des Wachstums, die den zweiten Hauptteil dieser Arbeit bilden. Das Filmwachstum wird zusätzlich neben DIP auch für PEN untersucht, dessen statische Dünnsfilm-Spektren nur kurz zu Beginn des PEN-Filmwachstums erläutert werden. Zum Schluss werden weiterführende optische Untersuchungen an DIP Filmen vorgestellt, die neue Perspektiven eröffnen, wie die orts aufgelöste Spektroskopie jenseits der Beugungsgrenze, die in Kooperation mit D. Zhang *et al.* (AK Meixner, Physikalische und Theoretische Chemie Tübingen) durchgeführt wurde.

### 1.2.1 Absorption von DIP in Lösung

Die Absorptionsspektren von DIP Monomeren werden in Lösung mit zwei verschiedenen Lösungsmitteln im sichtbaren Bereich von 1.5-3 eV untersucht. Es werden keine spektralen Unterschiede zwischen DIP in Aceton und in 1,2-Dichlorobenzol festgestellt, mit Ausnahme einer relativen Energieverschiebung, die sich auf die bekannte 'Lösungsmittelverschiebung' zurückführen lässt. Aus der wohldefinierten vibronischen Progression des HOMO-LUMO-Übergangs kann die elektronisch-vibronische Kopplung mit Hilfe des Huang-Rhys Parameters  $S = 0.87$  bestimmt werden. Vergleiche mit Rechnungen zu Übergangsenergien und zur Deformation des Moleküls zeigen gute Übereinstimmung.

### 1.2.2 Strukturelle und morphologische Eigenschaften von DIP Filmen

Die Struktur von DIP Filmen auf oxidierten Si-Substraten ist weitgehend untersucht und kann durch eigene Röntgen-Messungen reproduziert werden [11, 12, 13, 14]. Bei Substrat-Temperaturen von  $T = 130$  °C wächst DIP in polykristalliner Form in der so genannten  $\sigma$ -Phase, d.h. die Moleküle stehen nahezu aufrecht auf dem Substrat und formen eine Fischgrätenstruktur mit zwei Molekülen pro Einheitszelle entsprechend der Hochtemperaturphase des Einkristalls [18]. Ähnliche Messungen von DIP auf Glas zeigen, dass die Filme deutlich rauer und weniger wohl geordnet sind, aber dennoch dieselbe kristalline Struktur aufweisen. Auch die Morphologie unterscheidet sich zwischen Filmen auf Glas und Si-Substraten, wie Höhenprofile von AFM-Messungen zeigen. Sie hängt zudem von der Schichtdicke ab. Während DIP auf Glas bereits bei geringen Schichtdicken raue Filme mit kleinen ( $\varnothing \approx 100$  nm) Inseln bildet, sind auf Si einzelne Monolagen sichtbar und das Inselwachstum ( $\varnothing \approx 300$  nm) setzt erst bei höheren Dicken ( $\sim 10$  nm) ein. Verringert man die Substrat-Temperatur beim Filmwachstum auf  $T = -105$  °C, so nimmt die kristalline Unordnung zu und die Rauigkeit ab, was mit der eingeschränkten Diffusion der Moleküle auf der Oberfläche zusammenhängt.

### 1.2.3 Statische DIP Filmspektren

Bevor mögliche Änderungen der optischen Eigenschaften während des Filmwachstums untersucht werden, wird zuerst das Spektrum bei statischen Bedingungen nach dem Filmwachstum bestimmt. Es dient als Referenz für die Volumeneigenschaften des Films und gibt Aufschluss über den Exzitontransfer im Material. Auch wenn sich dieser Teil der Arbeit auf DIP Filme beschränkt, ist die vorgestellte Datenanalyse allgemein für organische Dünne Filme auf Si<sub>Ntve</sub> gültig und wurde z. B. für PEN und Perfluoropentacen Filme zur Bestimmung der dielektrischen Funktion benutzt [19, 20].

Die dielektrische Funktion  $\varepsilon$  wird *ex-situ*, d.h. an Luft mit spektroskopischer Ellipsome-

trie bestimmt. Entsprechend der polykristallinen Ordnung, die keine Vorzugsrichtung in der Substratebene aufweist, kann experimentell gezeigt werden, dass der Film uniaxial anisotrop ist und die optische Achse senkrecht zur Substratoberfläche orientiert ist. Diese Geometrie erschwert die Datenanalyse, die zur Bestimmung von  $\varepsilon$  aus den Ellipsometriedaten eine wichtige Rolle spielt und daher detailliert diskutiert wird. Es zeigt sich, dass die Messung bei mehreren Einfallswinkeln (VASE) nicht ausreicht, um die Anisotropie des Films auf oxidiertem Silizium zu bestimmen. Stattdessen ist es nötig, zusätzlich Filme auf thermisch oxidiertem Silizium ( $d_{\text{ThOx}} \approx 150$  nm) oder auf Glas bei der Auswertung hinzuzunehmen. Aus der resultierenden Anisotropie ergibt sich, dass die Moleküle in einem Kippwinkel von  $\Theta \approx 17^\circ$  relativ zur Substratnormalen orientiert sind, was gut zu Ergebnissen aus AFM und Röntgenuntersuchungen passt [21, 11].

Der Vergleich mit den Lösungsmittelspektren zeigt deutliche Unterschiede zwischen einzelnen und kondensierten Molekülen. Zwar ist auch im Dünnsfilmspektrum die vibronische Progression erkennbar, aber neben einer Rotverschiebung des Übergangs sind insbesondere die relativen Intensitäten der vibronischen Subbänder verändert, was auf die Wechselwirkung zwischen den Molekülen hinweist. Die intermolekulare Kopplung ist außerdem richtungsabhängig, weshalb sich die beiden Komponenten des dielektrischen Tensors nicht nur in ihrer Intensität, sondern auch in ihrer spektralen Linienform unterscheiden. Mit Hilfe von Rechnungen, die im Rahmen der Exziton-Theorie von R. Scholz *et al.* durchgeführt wurden, kann der Transferparameter  $T = 0.09$  eV für Frenkel-Exzitonen und die Energiedifferenz  $\Delta_0 = E_{00}^{\text{CT}} - E_{00}^{\text{F}} = 0.26$  eV zwischen Frenkel und Ladungstransfer (CT) Exzitonen bestimmt werden. Während die 'in-plane' Komponente des dielektrischen Tensors durch höhere Übergänge beeinflusst wird und daher nicht allein durch das vorgestellte Modell beschrieben wird, kann die 'out-of-plane' Komponente gut modelliert werden. Es wird gezeigt, dass ein reines Frenkel-Exziton-Modell zur Beschreibung der Spektren nicht ausreicht und die Mischung zwischen Frenkel und CT-Exzitonen berücksichtigt werden muss, um die Linienform der 'out-of-plane' Komponente zu modellieren.

## 1.2.4 Echtzeit-Untersuchungen des Filmwachstums

Zur Verfolgung von optischen Änderungen während des Filmwachstums werden Ellipsometrie- und DRS-Messungen eingesetzt. Da *in-situ* Messungen nur bei einem Einfallswinkel durchgeführt werden, sind die Ellipsometriedaten für DIP auf  $\text{Si}_{\text{Ntve}}$  aufgrund der Anisotropie nicht eindeutig zu analysieren. Zwar kann gezeigt werden, dass es kleine Änderungen während des Wachstums gibt, diese lassen sich aber nicht sinnvoll quantifizieren. Bei DRS-Messungen spielt die uniaxiale Anisotropie dagegen keine Rolle, da nur die 'in-plane' Komponente des dielektrischen Tensors unter normalem Einfallswinkel bestimmt wird. Die Intensität der 'in-plane' Komponente ist jedoch im Vergleich zur 'out-of-plane' Komponente für die  $\sigma$ -Phase von DIP sehr klein und das DRS-Signal ist für dünne Filme ( $d < 10$  nm) auf  $\text{Si}_{\text{Ntve}}$  Substraten zu gering zur Datenanalyse. Im Gegensatz dazu wird die Reflektivität von Glas ohne Film deutlich stärker durch einen

dünnen absorbierenden Film verändert, was es ermöglicht das Absorptionsspektrum sogar im Submonolagenbereich zu messen.

Die 'in-plane' Komponente von PEN ist dagegen groß genug, um das DRS-Signal auch auf  $\text{Si}_{\text{Ntve}}$  auszuwerten, so dass das PEN-Filmwachstum auf  $\text{Si}_{\text{Ntve}}$ - und auf Glas-Substraten verglichen werden kann. Bevor jedoch die PEN Echtzeit-Spektren diskutiert werden, wird kurz die Morphologie der Filme vorgestellt. PEN-Filme werden bei Raumtemperatur gewachsen, um möglichst gut geordnete Strukturen zu erzielen. Die Morphologie unterscheidet sich im Vergleich zu DIP noch deutlicher zwischen Filmen auf Glas und auf  $\text{Si}_{\text{Ntve}}$ -Substraten, wo sich große Inseln bis zu  $\varnothing \approx 1 \mu\text{m}$  bilden können im Gegensatz zu Glas mit  $\varnothing \approx 200 \text{ nm}$ . Der Vergleich zwischen Absorptionsspektren, die bei  $\sim 20 \text{ nm}$  durch DRS und Ellipsometrie-Messungen bestimmt wurden, zeigt gute Übereinstimmung.

Es zeigt sich für DIP auf Glas, dass für  $d < 1.6 \text{ nm}$  keine spektralen Änderungen auftreten, oberhalb dieser Dicke jedoch eine vierte Mode bei  $E \approx 2.8 \text{ eV}$  erscheint. Der Anstieg ihrer Intensität kann durch ein  $1/d$ -Verhalten beschrieben werden und sättigt oberhalb von  $\sim 12 \text{ nm}$ , wo die Linienform dem statischen Ellipsometrie-Spektrum entspricht. Wächst man den Film dagegen bei tiefen Temperaturen ( $T = -105 \text{ }^\circ\text{C}$ ), ist keine bzw. nur eine sehr kleine vierte Mode zu beobachten, was zeigt, dass sie eng mit der strukturellen Ordnung zusammen hängt. Die spektrale Änderung während des Filmwachstums bei hohen Temperaturen kann daher so verstanden werden, dass sich aufgrund der rauen Glasoberfläche ein relativ ungeordneter Film in der Grenzschicht bildet, der oberhalb von  $\sim 1.6 \text{ nm}$  in der geordneten  $\sigma$ -Phase weiter wächst.

Während das Erscheinen der vierten Mode eine spezielle Eigenschaft von DIP Filmen bei hohen Temperaturen ist, lässt sich bei tiefen Temperaturen ein allgemeiner Effekt, nämlich eine Rotverschiebung des ersten Übergangs ( $\Delta E = 110 \text{ meV}$ ) mit einem  $1/d$ -Verhalten beobachten. Auch PEN auf Si und auf Glas zeigt eine Rotverschiebung ( $\Delta E = 40 \text{ meV}$ ), die im Fall von Si jedoch erst oberhalb von  $2 \text{ nm}$  auftritt, was der Dicke einer Monolage entspricht. Ein ähnliches Verhalten wurde auch bei PTCDA gefunden [22, 23]. Offensichtlich rührt die Energieverschiebung von der Wechselwirkung zwischen zwei Monolagen her. Der beobachtete Effekt lässt sich darauf zurückführen, dass Moleküle an der Oberfläche weniger stark dielektrisch abgeschirmt sind als im Volumen. Dadurch ist das Spektrum der Oberflächenmoleküle entsprechend der 'Lösungsmittelverschiebung' weniger stark rot verschoben, was sich bei einem steigenden Volumen-zu-Oberflächen-Verhältnis während des Filmwachstums als Rotverschiebung bemerkbar macht. Unterschiede zwischen PEN-Spektren auf Si und auf Glas können zudem auf die verschiedene Film-Morphologie zurückgeführt werden. Es bleibt jedoch offen, warum beim Filmwachstum von DIP bei tiefen Temperaturen eine sehr starke Rotverschiebung zu beobachten ist, während bei hohen Temperaturen eine Linienaufspaltung zu sehen ist. Dies kann erst eindeutig geklärt werden, wenn die Filmstruktur auf Glas bei tiefen Temperaturen eindeutig geklärt ist, auch wenn die optischen Echtzeit-Messungen bereits Hinweise auf mögliche strukturelle Änderungen während des Filmwachstums geben.

### 1.2.5 Weiterführende optische Untersuchungen an DIP Filmen

Zum Abschluss der Arbeit werden Ergebnisse an DIP Filmen vorgestellt, die mit ergänzenden optischen Methoden erzielt wurden. Die bisherigen Ergebnisse zu den Dünnsfilmspektren können dabei als Grundlage zur Interpretation von weitergehenden Untersuchungen dienen. Im Rahmen dieser Arbeit können zwar nicht alle Details erörtert werden, aber die Ergebnisse zeigen, was möglich ist und eröffnen Perspektiven für die Zukunft. Außerdem können Fragestellungen geklärt werden, die mit den bisherigen Methoden nicht zu untersuchen waren. So geben Raman-Messungen weitere Einblicke in die Exziton-Phonon Wechselwirkung. Während sich die vibronische Progression im Absorptionsspektrum durch eine effektive Mode beschreiben lässt, können mit Unterstützung von theoretischen Rechnungen durch R. Scholz *et al.* vier Atmungsmoden im Bereich von 1280-1650  $\text{cm}^{-1}$  in den Ramanspektren identifiziert werden. Außerdem zeigen die berechneten Huang-Rhys Faktoren, dass alle vier Moden an der Exziton-Phonon Kopplung beteiligt sind. Dies erklärt die mit der Energie zunehmende Verbreiterung der vibronischen Subbänder im Absorptionsspektrum.

Da die Fluoreszenz eine wichtige Grundlage für nachfolgende orts aufgelöste Messungen ist, wird sie für DIP Filme und Monomere bestimmt. Die Ergebnisse zeigen gute Übereinstimmung zu bereits veröffentlichten Spektren [24] und die vibronische Progression kann Aufschluss über die molekulare Deformation im Grundzustand geben. Außerdem zeigt sich, dass nur geringe Fluoreszenz bei  $\lambda = 633$  nm angeregt wird, was mit dem Absorptionsspektrum übereinstimmt. Im Gegensatz dazu wird bei orts aufgelösten Messungen, die in Kooperation mit D. Zhang *et al.* durchgeführt wurden, bei  $\lambda = 633$  nm ein starkes Photolumineszenzsignal beobachtet. Dabei kommt ein mit einem Parabolspiegel ausgestattetes konfokales Mikroskop zum Einsatz, das im Fokus 1-3 nm entfernt von der Probe eine Goldspitze mit etwa 10 nm Spitzenradius beleuchtet. Das Feld direkt unterhalb der Spitze ist um mehrere Größenordnungen verstärkt und führt zu einer Plasmon-Polariton-Kopplung zwischen Spitze und Film. Die resultierende Lumineszenz entspricht daher nicht der beobachteten Fluoreszenz aus den vorangegangenen Messungen, wohingegen die beobachteten TER (tip-enhanced Raman)-Banden den bereits identifizierten Schwingungsmoden von DIP zugeordnet werden können. Gleichzeitig aufgenommene Höhenprofile der Probe zeigen, dass die Inselränder im optischen Signal um ein Vierfaches verstärkt werden, was mit dem Trapping von Exzitonen an den Rändern gedeutet werden kann. Die maximale optische Auflösung von bis zu 17 nm liegt dabei weit unterhalb der Beugungsgrenze, was völlig neue Möglichkeiten zur Untersuchung von Korngrenzen auf der Nanometerskala eröffnet.

## 1.3 Schlussfolgerungen

In dieser Arbeit werden umfassende Untersuchungen zu den optischen Eigenschaften von homogenen DIP-Filmen angestellt, die eine wichtige Grundlage für die Unter-

suchung komplexer Systeme wie Mischkristallen oder nanostrukturierten Proben bilden. Der Vergleich zu Monomer-Spektren zeigt, dass intermolekulare Wechselwirkungen im Kristall die Spektren verändern, die auch stark von der Präparation der Filme abhängen. Neben einer ausgeprägten Anisotropie kann mit Unterstützung theoretischer Modelle der Exzitontransfer von Frenkel und CT Exzitonen untersucht werden. Die beobachtete Dickenabhängigkeit der Spektren während des Wachstums deckt Unterschiede zwischen Molekülen an Oberflächen bzw. Grenzflächen und im Volumen auf, was von großer Bedeutung für Bauelemente in elektronischen Anwendungen sein kann. Dies kann nicht nur für DIP-Filme sondern auch bei PEN-Filmen beobachtet werden. Ortsaufgelöste Messungen in Kooperation mit D. Zhang *et al.* zeigen zudem, dass es möglich ist die optischen Filmeigenschaften auf der Nanometer-Skala zu untersuchen. So können Domänenränder optisch sichtbar gemacht werden, die eine wichtige Rolle für mögliche Anwendungen spielen.





## CHAPTER 2

# INTRODUCTION

Semiconducting organic materials have been intensely studied in the last decades due to their interesting optoelectronic properties giving rise to a broad range of applications [1,2,3,4,5,6], such as organic field effect transistors (OFET) [25], organic light emitting diodes (OLED) or organic solar cells [26]. A considerable advantage, besides their potentially low production costs, is the large variety of compounds, which can be synthesized by organic chemistry allowing control of the optical and electronical properties. Although, organic semiconductors cannot compete in all areas in terms of performance with traditional inorganic semiconductors due to inherent (by several orders of magnitude) lower charge carrier mobilities [1,2,7], they are promising for innovative applications like large-area light emitting devices, flexible substrates or for low-cost electronics [4]. Several applications of organic semiconductors (in particular OLED's) have already been demonstrated and can be found on the market.

Since 1906, when Alfredo Pochettino discovered photo-conduction in anthracene crystals [27,28], organic semiconductors were known, but more than 60 years passed before the first OLED was built [29]. The strong interest in organic semiconductors started to evolve several years later, when the possibility arose to grow and to control thin films as well as to contact them reliably.

Organic materials can be divided into two main groups: polymers and low-weight molecules, both having their advantages and disadvantages. While the solubility of many polymers is an advantage making the low-cost ink-jet printing of electrical circuits and displays possible [30], low-weight organic molecules can form highly ordered crystalline structures with better electrical transport properties [7,1]. This thesis focuses on small organic molecules, which are evaporated in ultra-high vacuum (UHV), forming thin films when deposited on substrates. Obviously, the use of UHV is not compatible with the concept of true low-cost fabrication, but the preparation under well-defined conditions allows to better control and understand the structural, electrical and optical film properties, which is important to optimize the device performance.

Structural properties significantly influence the charge carrier mobility, which is the cru-

cial quantity that determines the frequency at which organic semiconductor devices can be operated. Structural order can also strongly affect the optical film properties due to different coupling of a given molecule with its environment, particularly for crystalline films. The electronic properties of organic thin films can differ significantly from the monomer or bulk-crystal properties. Moreover, they depend on the microscopic film morphology. Since the optical spectrum and the electronic properties are intimately related, efforts to improve the understanding of the material and the device performance have to include the optical properties, as the following points demonstrate:

1. The coupling between electronic excitations and internal vibrations can be directly determined from the visible spectrum [31]. The exciton-phonon coupling, frequently described by the Huang-Rhys parameter  $S$ , can be linked to the charge carrier mobility for hopping transport [8].
2. Exciton transfer, including neutral and charge transfer excitations, arises due to intermolecular coupling, which can modify the optical spectra significantly [9], allowing the determination of exciton transfer parameters. They give fundamental insight into the interaction within a molecular aggregate, which affects properties like charge transport and exciton diffusion.
3. Crystalline materials exhibit generally anisotropic properties, which are also found in the optical spectra. In the case of thin crystalline films, the relation between optical anisotropy and structural order makes it possible to determine the mean tilt angle of the molecules relative to the substrate normal. This also affects transport properties, which can be significantly anisotropic as it is e.g. reported for phonon-assisted charge-carrier transport [32].
4. The exciton diffusion length is particularly important for organic solar cells since exciton recombination limits the efficiency. The exciton diffusion length can be determined from absorption and photoluminescence spectra [33].
5. Resonant Raman spectroscopy allows studying of the deformation in the relaxed excited geometry of the molecule, which is directly linked to the exciton-phonon coupling. Furthermore, changes of the molecular conformation as well as of the crystalline order can be detected.

The optical film properties depend strongly on the film growth process. In case of organic molecular beam deposition (OMBD), where the molecules are evaporated in UHV (see Sec. 4.1.3), mainly the growth rate and the substrate temperature can be changed as well as the substrate itself. Distinct dielectric functions of differently grown films can be due to different structural order induced by the substrate or temperature effects but also the microscopic film morphology (e.g. grain boundaries, localized defects and roughness) [34], which influences the optical properties. Additionally, the substrate interacts with molecules at the interface, which can change their optical properties. The thin film

properties at the interface are particularly important because they determine the charge injection barrier.

Since the structure and morphology may change during film growth and also the impact of the substrate onto the optical properties decreases with thickness, the dielectric function of a film is generally expected to depend on the film thickness. Moreover, transitions from monomer-like molecules in the sub-monolayer range to bulk-like molecules at higher thicknesses can occur during growth due to changing intermolecular interactions [35]. In order to detect possible changes in the functional properties during growth, it is necessary to follow the optical properties in real-time during growth. Real-time measurements, i.e. time resolved measurements that are fast compared to the growth process under investigation, are crucial for studying the evolution of film growth, since otherwise transient changes and time-dependent effects cannot be observed. Furthermore, relative changes can be determined with significantly higher accuracy compared to absolute measurements of several individual films with different thicknesses. This allows the monitoring of the optical properties of films even in the sub-monolayer range. Optical methods, like ellipsometry and differential reflectance spectroscopy (DRS), as used in this work, are particularly well suited for following the film growth, since they are non-invasive, comparatively simple, and the acquisition time of 1-2 min is fast enough for real-time measurements.

This thesis focuses on the optical properties of diindenoperylene (DIP) thin films on  $\text{SiO}_2$  during and after growth. Recently, DIP has received increased attention due to its well-defined ordering [11, 12], interesting growth behavior [13, 14], promising electronic transport [15, 16], and exciton diffusion length [17, 33]. Since most of the structural information is known for DIP on  $\text{SiO}_2$ , while the dielectric function is less well understood, it is obvious to first study the optical film properties on the well-defined Si substrate covered with native oxide ( $\text{Si}_{\text{Ntve}}$ ). For comparison and for technical reasons DIP is also investigated on quartz glass. Since the films are crystalline, the dielectric function is expected to be anisotropic, which complicates the ellipsometry data analysis. Therefore, before possible optical changes during growth are investigated, the uniaxial dielectric function is established post-growth as a reference. In addition, the optical properties of pentacene (PEN) are determined during growth and compared to results obtained for DIP. PEN is one of the most intensely studied organic molecules forming also well-ordered films that show high mobility [36, 37]. Post-growth ellipsometry results reveal significant optical differences compared to DIP [20] and only little is known about PEN optical film properties during growth.

The thesis is organized as follows. In chap. 3 the properties of organic semiconductors, which are most important for this work, are briefly reviewed and DIP and PEN are introduced in more detail. Furthermore, a short introduction about optics for studying thin films is given. Chap. 4 presents the experimental methods used in this thesis including the OMBD technique for film growth. In addition to optical methods also complementary methods like X-ray reflectivity are employed to obtain information about the film structure and morphology, which can have a strong impact onto the optical properties. In chap. 5 the experimental results are presented and discussed. While DIP monomers and

films are investigated in detail, in case of PEN films mainly the optical properties during growth are analyzed, since the static spectrum was already determined by A. Hinderhofer within the scope of a diploma thesis [19,20]. First, DIP absorption spectra are determined in solution, which are taken as a reference for the monomer optical properties. After the characterization of the substrates, X-ray and AFM results for DIP films are presented serving as a basis for later discussions. In Sec. 5.4 the ellipsometry data analysis for uniaxial anisotropic DIP thin films is presented, followed by a detailed discussion of the resulting spectra. This includes a theoretical analysis concerning exciton transfer in DIP films that was performed by R. Scholz *et al.*. Sec. 5.5 presents real-time measurements determined for different film growths. First, real-time ellipsometry data are discussed for DIP on Si<sub>Ntve</sub> which do not give unambiguous results. Therefore, DRS is used to investigate DIP film growth on Si<sub>Ntve</sub> and on glass at low and high temperature. Furthermore, PEN film growth on Si<sub>Ntve</sub> and on glass is investigated, starting with a short introduction about the morphology of PEN films and their static absorption spectra. The film growth is compared between DRS and ellipsometry measurements followed by a general discussion concerning the effects found in the real-time measurements. In Sec. 5.6 complementary optical techniques are employed that give complementary information beyond the dielectric function while at the same time they benefit from the understanding of it. Raman spectroscopy on DIP films on Si<sub>Ntve</sub> gives additional insight into the exciton-phonon coupling and fluorescence allows to study the vibrational properties of the electronic ground state. Finally, tip-enhanced Raman (TER) and photoluminescence (PL) measurements, that were performed in collaboration with D. Zhang *et al.* (Meixner group, institute of physical and theoretical chemistry, Tübingen), are presented showing that grain boundaries can be optically detected with a lateral resolution (17 – 40 nm) significantly below the diffraction limit. The thesis closes with future perspectives (Chap. 6) and a summary (Chap. 7).

## CHAPTER 3

# FUNDAMENTALS

### 3.1 Organic semiconductors

Organic semiconductors can be divided into two main classes: polymers and small molecules. Both have in common that they contain a conjugated  $\pi$ -electron system leading to their characteristic optical properties. The most obvious difference between them is their size. While polymers consist of several repeating units that can extend several 100 nm, small molecules exhibit a length scale of typically a few nanometers. This thesis focuses on small organic molecules. The following sections will review their most relevant properties. Further details can be found in the literature [2, 1, 31].

#### 3.1.1 Monomers

##### 3.1.1.1 $\pi$ -electron system

Cyclic and conjugated molecules are most stable if they contain  $(4n + 2)\pi$ -electrons, i. e. if the ring consists of an uneven number of double bonds (Hückel rule<sup>1</sup>). The most prominent aromatic ring is benzene consisting of 6 C-atoms and 6 H-atoms. Many polycyclic aromatic hydrocarbons are composed of it. From quantum mechanics it is known that a double bond between C-atoms is realized by  $sp^2$  hybridization: one atomic  $s$ - and two atomic  $p$ -orbitals form three coplanar and degenerate molecular  $\sigma$ -orbitals. The third atomic  $p_z$ -orbital is unaltered and oriented perpendicular to the axis connecting the two C atoms. It constitutes the molecular  $\pi$ -orbital. Due to the alteration between single and double bonds, which is regarded as a resonance structure, the  $\pi$ -electrons are delocalized over the complete ring and possibly over further parts of the molecule giving rise to a high polarizability. Most of the characteristic physical properties of aromatic hydrocarbons trace back to the  $\pi$ -electrons.

---

<sup>1</sup>It is only strictly valid for single rings.

### 3.1.1.2 Molecular excitations

Three different types of excitations contribute to the energy state of a molecule: the electronic excitation  $E_{\text{el}}$ , the vibrational excitation  $E_{\text{vib}}$  and the rotational excitation  $E_{\text{rot}}$ . Since the mass of the nuclei exceeds the mass of the electron significantly, electrons can be considered to instantaneously follow the motion of the nuclei. This leads to the Born-Oppenheimer approximation stating that all three energy states can be separated according to [31]:

$$E = E_{\text{el}} + E_{\text{vib}} + E_{\text{rot}} \quad (3.1)$$

The excitation energies are usually very different. While the rotational energy is typically given by  $\sim 1/100$  eV, located in the microwave range, the vibrational energy corresponds to  $\sim 1/10$  eV in the IR range and the electronic energy is given by  $\sim 1 - 5$  eV close to the visible/UV.

All three energy contributions have to be considered for free molecules, e. g. molecules in the gas phase or in solution, although due to broadening mechanisms they cannot be resolved in solution. In case of aggregates, the degree of freedom is limited and no rotations take place<sup>2</sup>. The low energetic electronic transitions are dominated by  $\pi$ -electrons since they are more weakly bound than  $\sigma$ -electrons: Typically the highest occupied molecular orbital (HOMO) and the lowest unoccupied molecular orbital (LUMO) are  $\pi$ -states that are composed of lobes with alternating sign delocalized over two atomic sites, compare Fig. 3.1. The lowest electronic transitions, i. e. between the HOMO and the LUMO, is then a  $\pi - \pi^*$ -transition. Furthermore, electronic states are divided into singlet and triplet states distinguished by the total spin state of the molecule. Since the ground state is usually a singlet state and intersystem crossing is forbidden for optical transitions, if spin-orbit coupling is neglected, triplet states typically do not play a significant role for absorption spectra of low-weight organic molecules.

### 3.1.1.3 Vibronic progression

The geometry of a molecule differs generally for different electronic configurations, e. g. between the electronic ground state and the first optically excited state. The shape of this deformation can be understood from the node patterns of the two orbitals involved in the optical transition [38,39]. This is schematically shown in Fig. 3.1a), where the HOMO as well as the LUMO is representatively depicted for diindenoperylene (see Sec. 3.1.3.1): For bonds where a bonding region of the HOMO is replaced by an antibonding node of the LUMO, the bond length increases and vice versa, see Fig. 3.1b).

The molecular deformation upon electronic excitation leads to a coupling between the electronic excitations and internal vibrations. It is frequently described by the Huang-Rhys parameter  $S = m\omega\Delta Q^2/2\hbar$ , where  $\Delta Q$  quantifies the deformation, resulting in

---

<sup>2</sup>Exception: Some external phonons, namely librations correspond to partly molecular rotations.

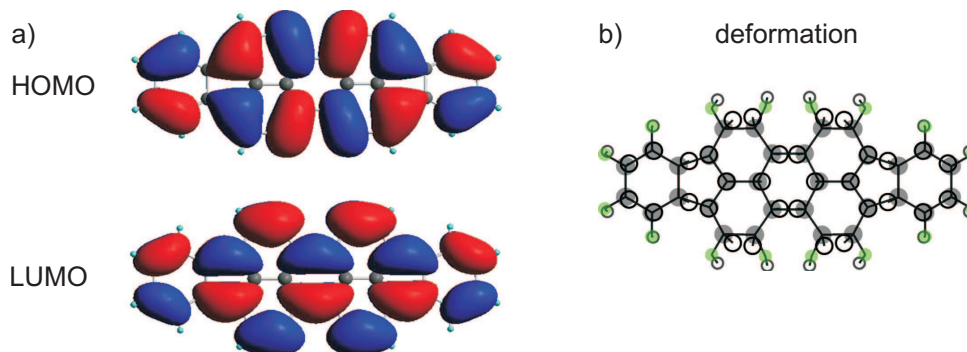


**Figure 3.1:** a) HOMO and LUMO of diindenoperylene (DIP). b) The deformation in the relaxed excited state (open circles), increased by a factor of 30, together with the relaxed ground state (solid circles). The small green circles correspond to hydrogen atoms and the big grey circles to carbon atoms. Taken from Ref. [40]

a reorganization energy  $\lambda = S\hbar\omega_{\text{vib}}$ . The coupling is also commonly described by the Franck-Condon principle: The nuclei do not move immediately to their positions of the conformationally relaxed excited molecular state when the electrons are excited as represented by the vertical arrows in Fig. 3.2. Therefore, additionally to an electronic excitation also vibrational states are excited. As illustrated in Fig. 3.2, this effect is visible in the absorption spectrum which exhibits a vibronic progression, i. e. it is splitted up in subbands originating from higher harmonics of a single molecular vibration. The coupling determines the intensity distribution of the vibronic excitations involved. In the simplest case of a displaced harmonic oscillator (assuming equal vibrational energies in  $S_0$  and  $S_1$ ), the intensities of the subbands  $n$  follow a Poisson distribution

$$I_n = e^{-S} S^n / n! \quad (3.2)$$

Generally, this simple harmonic approximation describes the intensity distribution well. For a more detailed analysis, where anharmonic potentials are applied to small molecules, the reader is referred to the literature [41]. Typically several vibrational modes are involved. They can be described by an effective vibrational mode if they are energetically similar. This leads to a broadening of the vibronic features with increasing energy.

### 3.1.2 Molecular crystals

Non-polar organic molecules mainly aggregate due to van-der-Waals interaction based on dispersion interactions. Since this interaction is weak compared to covalent or metallic bonding, many properties of single molecules remain in first approximation unchanged, such as the molecular length or vibrational energies. Therefore, a molecular crystal is sometimes described in the picture of an oriented gas, although there exist obviously

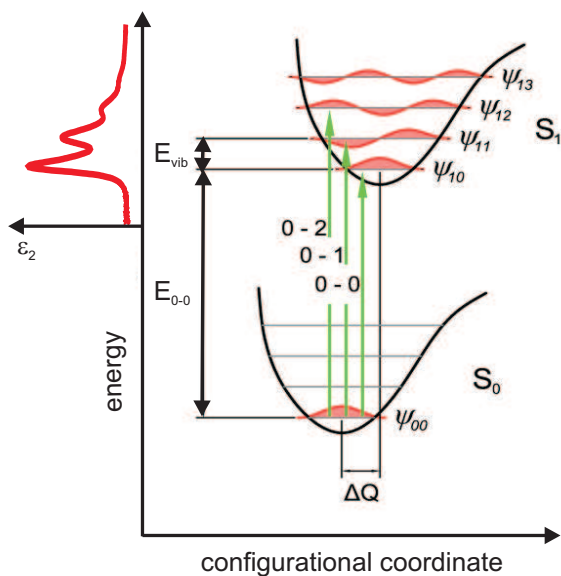


**Figure 3.2:** The internuclear potential and the corresponding vibrational energy states are plotted for the electronic ground and excited state  $S_0$  and  $S_1$  versus the configurational coordinate. The potentials are shifted by  $\Delta Q$  representing the deformation of the molecule upon electronic excitation. According to the Franck-Condon principle, optical transitions are represented by vertical arrows leading excitations of higher vibrational harmonics. This results in a vibronic progression that is visible in the absorption spectrum (on the left hand side).

differences. Properties like energy and charge transfer can only be explained by intermolecular interactions. Nevertheless, properties like binding energies, phonon energies or bandwidths are in molecular crystals significantly smaller compared to inorganic crystals due to smaller intermolecular interactions. Many aromatic molecules aggregate in structures with rather complex unit cells (e. g. monoclinic or triclinic) that can contain several molecules, compare Sec. 3.1.3.1 and 3.1.3.2. Usually several phases exist with similar crystal energies, which can be transformed by slight temperature or pressure changes. Some systems, in particular molecules with complex shapes, tend to form amorphous structures.

### 3.1.2.1 Excitons and optical properties

Two characteristic processes in molecular crystals are the generation and transfer of excitons, which are bound electron hole pairs. Generally, discrete molecular states split up into exciton bands due to their delocalization [42] similar to electronic bands in inorganic crystals. The optical properties of molecular crystals are determined by two different types of excitations: Bloch waves composed of neutral molecular excitations, called Frenkel excitons, and charge transfer states, see Fig. 3.3. A Frenkel exciton is essentially localized on a single molecule and can be regarded as an excited molecule in a crystal. In case of charge transfer excitons the electron-hole pair is distributed among two neighboring molecules corresponding to a pair of ions. Mott-Wannier excitons, electron hole pairs that are weakly bound and further away from each other, were not observed so far in molecular crystals. They are typically found in inorganic crystals. The exciton binding energy, which is given by the difference between the optical and the electronic band gap, can exceed several electron volts in case of molecular crystals. Therefore, excitons in organic systems are in contrast to those in inorganic systems quite stable making exciton transfer possible.



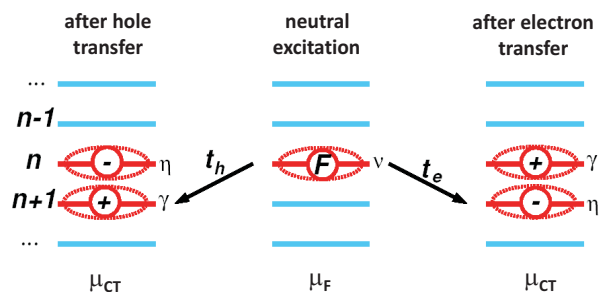


**Figure 3.3:** Visualization of three types of localized excited states in a stack of molecules. Center: neutral molecular excitation, left: CT state obtained from the neutral excitation after transferring a hole onto the neighboring site, right: CT state after transferring an electron. Taken from Ref [40].

Furthermore, due to the strong exciton binding energy, excitons essentially cannot be excited thermally into the conduction band.

The spectra of molecular crystals can resemble those of single molecules, but this changes completely if the transition dipole moment is strong and pronounced intermolecular coupling occurs. In the following the most important differences are listed which are due to interactions between the molecules:

1. *Energy shift*

Electronic transitions are usually red-shifted if molecules are embedded in a surrounding medium like a solvent or the molecules themselves. It is therefore often referred to the solvent shift, which can be explained in terms of quantum theory assuming the Franck-Condon principle and visualizing the absorption process as an electrical displacement within the absorbing molecule [43], i. e. the electrostatic work required to produce a dipole  $\mu$  in solution is decreased due to polarization effects, which can be expressed by the real part of the dielectric function  $\varepsilon_{1,\text{solv}}$  of the solvent.

2. *Davydov splitting*

The resonance interaction between  $n$  translationally inequivalent excited molecules per unit cell leads to a splitting into  $n$  states in analogy to  $n$  coupled harmonic oscillators. In case of two molecules per unit cell, as it is often the case for molecular crystals, this interaction results in an upper and a lower Davydov component [44]. They do not only differ in energy position but also in polarization.

3. *Additional transitions*

The degeneracy between excited molecular states can be lifted, and selection rules can be violated since not only the molecular symmetry has to be taken into account but also the symmetry of the crystal. Furthermore, also the conformational properties of the molecules, i. e. the molecular shape, may change upon aggregation giving rise to additional transitions.

4. *Anisotropy*

The optical properties of molecular crystals depend typically on the direction of the incident electric field, i.e they are anisotropic. This is, similar to atomic crystals, related to the crystalline structure that gives rise to angle dependent intermolecular

coupling. Furthermore, non-spherically shaped molecules exhibit orientational degrees of freedom contributing additionally to the anisotropy if preferred molecular orientations exist as it is the case in molecular crystals.

### 3.1.2.2 Exciton transfer

In this paragraph the theory of exciton transfer will be introduced based on an approach developed by R. Scholz *et al.* [10,40]. In cooperation with R. Scholz and L. Gisslén it will be applied to interpret experimental data.

While the molecular parameters  $S$  and  $\lambda$ , that are related to the internal deformation, can be regarded as unchanged in molecular crystals, the interaction between the transition dipoles on different molecules has to be taken into account. Therefore, so-called transfer matrix elements are added to the Hamiltonian to describe the transfer of excitations to different molecular sites. The Hamiltonian can be divided into a part  $H^F$  for the Frenkel exciton, a part  $H^{CT}$  for the CT states, and a mixing term  $H^{F-CT}$ :

$$H_{tot} = H^F + H^{CT} + H^{F-CT}, \quad (3.3)$$

The Hamiltonian for Frenkel excitons reads [44]:

$$\begin{aligned} H^F &= \sum_{\mathbf{n}\alpha\nu_e} E_{0g\nu_e} b_{\mathbf{n}\alpha\nu_e}^\dagger b_{\mathbf{n}\alpha\nu_e} \\ &+ \sum_{\mathbf{n}\alpha\nu_e} \sum_{\mathbf{m}\beta\mu_e} t_{\mathbf{n}\alpha\nu_e;\mathbf{m}\beta\mu_e} b_{\mathbf{n}\alpha\nu_e}^\dagger b_{\mathbf{m}\beta\mu_e} \end{aligned} \quad (3.4)$$

where  $\mathbf{n}$  and  $\mathbf{m}$  are indices for unit cells,  $\alpha, \beta \in \{A, B\}$  indicate the two basis molecules,  $\nu_e, \mu_e$  the indices of vibronic levels of the effective vibration, and  $E_{0g\nu_e}$  the transition energies of the different vibronic subbands of the molecule. The excitations are described by creation and annihilation operators for the vibronic level  $\nu_e$  of basis molecule  $\alpha$  in unit cell  $\mathbf{n}$ ,  $b_{\mathbf{n}\alpha\nu_e}^\dagger$  and  $b_{\mathbf{n}\alpha\nu_e}$ , respectively. The transfer matrix elements  $t_{\mathbf{n}\alpha\nu_e;\mathbf{m}\beta\mu_e}$  are composed of an electronic part  $T_{\mathbf{n}\alpha;\mathbf{m}\beta}$  weighted with vibronic Franck-Condon factors  $S_{0g\nu_e}$ :

$$t_{\mathbf{n}\alpha\nu_e;\mathbf{m}\beta\mu_e} = T_{\mathbf{n}\alpha;\mathbf{m}\beta} S_{0g\nu_e} S_{0g\mu_e} \quad (3.5)$$

This approach concentrates on the states where the deformation pattern is restricted to the excited site, ignoring possible vibrational excitations on neighboring molecules.

The second part of the Hamiltonian (3.3) represents the CT states involving two neighboring sites:

$$H^{CT} = E_{\gamma\eta}^{CT} \sum_{\mathbf{n}\alpha} \sum_{\gamma\eta} \left( c_{\mathbf{n}\alpha\gamma\eta,-1}^\dagger c_{\mathbf{n}\alpha\gamma\eta,-1} + c_{\mathbf{n}\alpha\gamma\eta,+1}^\dagger c_{\mathbf{n}\alpha\gamma\eta,+1} \right) \quad (3.6)$$

where  $E_{\gamma\eta}^{\text{CT}} = E_{00}^{\text{CT}} + (\gamma + \eta)\hbar\omega_{\text{eff}}$  is the on-site energy of a CT exciton with the two molecules involved in the vibronic states  $\gamma$  and  $\eta$  of the same effective mode used for a neutral excited molecule. The operators  $c_{\mathbf{n}\alpha\gamma\eta,f}^\dagger$  and  $c_{\mathbf{n}\alpha\gamma\eta,f}$  with  $f = \pm 1$  describe creation and annihilation of a CT state with an electron at lattice site  $\mathbf{n}$  and a hole at the neighboring lattice site  $\mathbf{n} + f\mathbf{a}$ , and  $\gamma$  and  $\eta$  are the vibronic levels of the cationic and anionic molecule, respectively.

Neutral excitations and CT states are mixed via

$$\begin{aligned} H^{\text{F-CT}} = & \sum_{\mathbf{n}\alpha\nu} \sum_{\mathbf{m}\gamma\eta} \left( c_{\mathbf{m}\alpha\gamma\eta,-1}^\dagger b_{\mathbf{n}\alpha\nu} (\delta_{\mathbf{m}\mathbf{n}} t'_h + \delta_{\mathbf{m},\mathbf{n}+1} t'_e) \right. \\ & \left. + c_{\mathbf{m}\alpha\gamma\eta,+1}^\dagger b_{\mathbf{n}\alpha\nu} (\delta_{\mathbf{m}\mathbf{n}} t'_h + \delta_{\mathbf{m},\mathbf{n}-1} t'_e) \right) \\ & + \text{h.c.} \end{aligned} \quad (3.7)$$

with electronic transfer matrix elements  $t'_e$  and  $t'_h$ . They account for the coupling between the neutral molecular excitations and the CT states for electrons and holes, respectively. They are modified by Franck-Condon factors

$$t'_e = t_e S_{\nu_e\gamma_+} S_{0_g\eta_-} \quad (3.8)$$

$$t'_h = t_h S_{0_g\gamma_+} S_{\nu_e\eta_-} \quad (3.9)$$

which involve the vibronic overlap between a charged state and a molecule in the lowest vibrational level (0) in the electronic ground state ( $g$ ) as well as the vibronic overlap between an oppositely charged state and a neutral excited molecule ( $e$ ) in the vibronic level  $\nu$ , i. e.  $S_{0_g\eta_-} = \langle 0_g | \eta_- \rangle$  and  $S_{\nu_e\gamma_+} = \langle \nu_e | \gamma_+ \rangle$ . In each case, the overlap factors account for smaller Huang-Rhys factors of  $S_{\text{eff}}^+$  and  $S_{\text{eff}}^-$  defined with respect to the neutral ground state, and the vibronic overlap between charged species and neutral excited molecule is defined from appropriate differences of the respective deformation patterns.

For a periodic crystal the Hamiltonian (3.3) can be block-diagonalized by a Fourier transformation into wave-vector representation. In case of a pure Frenkel exciton model it reads [44, 10]:

$$\begin{aligned} H^{\text{F}}(\mathbf{k}_e) = & E_{0_g\nu_e} \sum_{\alpha\nu_e} b_{\mathbf{k}_e\alpha\nu_e}^\dagger b_{\mathbf{k}_e\alpha\nu_e} \\ & + \sum_{\alpha\nu_e} \sum_{\beta\mu_e} T_{\alpha\beta}(\mathbf{k}_e) S_{0_g\nu_e} S_{0_g\mu_e} b_{\mathbf{k}_e\alpha\nu_e}^\dagger b_{\mathbf{k}_e\beta\mu_e} \end{aligned} \quad (3.10)$$

where  $T_{\alpha\beta}(\mathbf{k}_e)$  is the Fourier transform of  $T_{\alpha\beta}$  in real space. The optical excitation results in an exciton state with wave vector  $\mathbf{k}_e \approx 0$  in the vicinity of the  $\Gamma$  point of the Brillouin

zone. At  $\mathbf{k}_e = 0$ , the Fourier sums over the transfer matrix elements become

$$\begin{aligned} T_{AA} &= T_{AA}(\mathbf{0}) = \sum_{\mathbf{R}_{\mathbf{n}A;\mathbf{m}A}} T_{\mathbf{n}A;\mathbf{m}A} \\ T_{AB} &= T_{AB}(\mathbf{0}) = \sum_{\mathbf{R}_{\mathbf{n}A;\mathbf{m}B}} T_{\mathbf{n}A;\mathbf{m}B} \end{aligned} \quad (3.11)$$

The sum  $T_{AA}$  involves transfers towards the same basis molecule in different unit cells. Generally, it is dominated by the large transfer matrix elements towards the stack neighbors, whereas the sum  $T_{AB}$  includes transfer from a reference molecule of type  $A$  towards all molecules of type  $B$ . A further block diagonalization gives the transition dipoles along two orthogonal directions defined by the sum and difference of the transition dipole moments of the two basis molecules  $A$  and  $B$ , resulting in two diagonal elements of the dielectric tensor defined with respect to these Cartesian directions.

For calculating the exciton transfer, it is therefore crucial to know the crystalline structure and the molecular orientation in detail. In the following, this will be introduced inter alia for the systems under investigation.

### 3.1.3 Organic materials

One of the advantages of organic electronics is the nearly unlimited choice of materials. Which molecule to choose depends on the concrete application and other materials employed. Generally, the degree of purification is crucial for the electrical properties. Therefore, it is necessary to purify the material easily, which requires thermal and chemical stability. Furthermore, the molecular structure should favor self-organization within the organic film to obtain a highly ordered structure with large  $\pi$ -orbital overlap between adjacent molecules.

The organic molecules diindenoperylene (DIP) and pentacene (PEN) have shown promising thin film properties with high structural order and high mobilities. PEN is one of the most investigated organic molecules, but only little is known about its optical properties during growth. Although DIP has achieved increased attention in the last couple of years, it is still a less prominent molecule than PEN with mostly unknown optical properties. This thesis focuses mainly on the optical properties of DIP, but also results obtained for PEN will be discussed. Therefore, most of the relevant properties of DIP will be introduced in detail while PEN is only briefly presented.

#### 3.1.3.1 Diindenoperylene (DIP)

Diindenoperylene (DIP) is a polycyclic aromatic carbon hydrogen (PAH) with the chemical formula  $C_{32}H_{16}$ . As indicated by the name DIP is a perylene-derivate with two indeno units connected to the central perylene  $C_{20}H_{10}$  core (see Figs. 3.1, 3.4). DIP is also known

as periflanthene since it was first synthesized by the pyrolysis of fluoranthene  $C_{16}H_{10}$  [45]. DIP is a planar molecule with a molecular weight of 400.47 g/mol and belongs to the point group  $D_{2h}$ . Its spatial dimensions were estimated on the basis of the ‘Cambridge Crystallographic Database’ to  $\sim 18.4$  Å in length and  $\sim 7$  Å in width (with the H-atoms and their van-der-Waals radii taken into account) [46]. DIP has no polar groups and is only weakly soluble in most solvents. The shape of the conjugated  $\pi$ -system is expected to provide sufficient stability against oxidation [47]. Furthermore, it has a high decomposition temperature, i. e. it starts to carbonize below 540 °C [48], with a sublimation temperature below 350 °C<sup>3</sup>. This relative stability is one of the reasons for its suitability for OMBD (see Sec. 4.1.3).

In the following, first the crystal structures for DIP single crystals will be presented. One of them is correlated with the thin film structure and has a strong impact onto the optical spectra. Also theoretical calculations are based on it. Second, structural properties of DIP on  $SiO_2$  will be introduced that are relevant for investigations in this work. This will be followed by a general overview of DIP systems studied in combination with other materials. Finally the optical and electrical properties will be introduced.

**3.1.3.1.1 DIP single crystal phases** DIP crystallizes in a herringbone structure. Two different phases were recently determined for bulk crystals [16,18]: The low temperature  $\alpha$ -phase and the high temperature  $\beta$ -phase which are both shown in Fig. 3.4. The

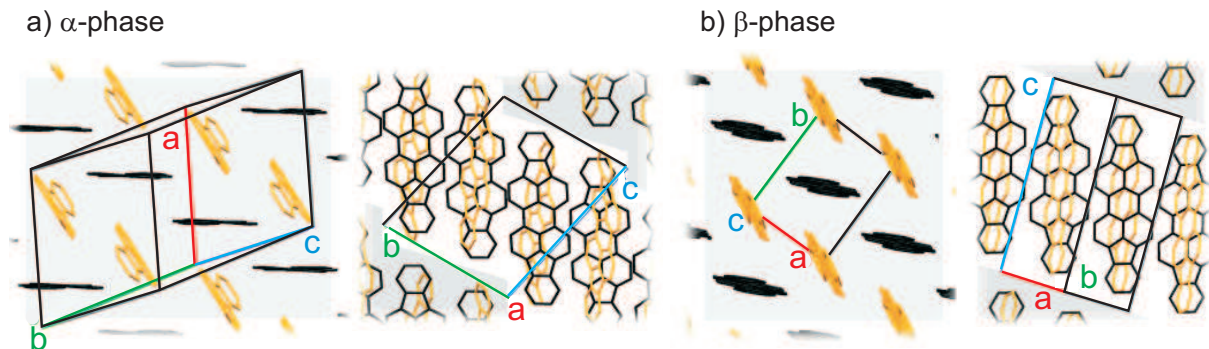


**Figure 3.4:** Herringbone layers of a) the  $\alpha$ -phase and b) the  $\beta$ -phase of DIP single crystals. While some DIP molecules in the  $\alpha$ -phase are twisted and bent, the  $\beta$ -phase exhibits mainly planar molecules. The pictures on the right hand sides in a) and b) show the herringbone layers from the side, illustrating the alignment of the rows. Pictures are taken from Ref. [18].

phase transition, which takes at  $\sim 403$  K place, involves a doubling of the unit cell volume and differentiates two symmetrically identical molecules into a bent and a twisted DIP conformational isomer. The triclinic low temperature  $\alpha$ -phase contains four molecules per unit cell with two conformationally different molecules, while the  $\beta$ -phase is monoclinic

<sup>3</sup>The exact sublimation temperature  $T_{\text{sub}}$  depends of course also on the pressure, in UHV  $T_{\text{sub}} < 300$  °C.

and it contains two planar molecules per unit cell. The lattice parameters of both single crystal phases are summarized in table 3.1.

phase	$T$ [K]	$a$ [Å]	$b$ [Å]	$c$ [Å]	$\alpha$ [°]	$\beta$ [°]	$\gamma$ [°]	$V_{\text{cell}}$ [Å <sup>3</sup> ]
$\alpha$	$\lesssim 403$	11.6592	13.0102	14.9663	98.440	98.0236	114.548	1991.3
$\beta$	$\gtrsim 403$	7.1709	8.5496	16.7981	90	92.416	90	1028.9

**Table 3.1:** Lattice parameters of the two phases of single DIP crystals according to Ref. [18]. The  $\beta$ -phase corresponds to the thin film phase under investigation.

**3.1.3.1.2 Structural properties of DIP films on SiO<sub>2</sub>** If grown under suitable conditions, i. e. using a substrate temperature of  $\sim 130$  °C and a deposition rate of  $\sim 10$  Å/min, DIP forms highly ordered polycrystalline thin films on SiO<sub>2</sub> substrates [11]. The single crystalline domains consists of a so-called  $\sigma$ -phase, which corresponds to the  $\beta$ -phase of the DIP single crystal [18]. The molecules are standing nearly upright giving rise to mono-molecular steps of 1.65 nm observed in AFM images [11, 21]. Taking the approximate length of the molecule into account, the tilt angle (relative to the surface normal, see Fig. 3.5) can be estimated to be  $\alpha \approx 20^\circ$ . NEXAFS-data (Near Edge X-ray absorption fine structure) gave a slightly smaller result:  $\alpha = (7 \pm 5)^\circ$  [49]. Since the substrate is isotropic, the crystalline domains are randomly oriented in the in-plane direction, whereas the molecules are highly ordered along the out-of-plane direction. This leads to a uniaxial symmetry of the organic film with the optical axis oriented parallel to the surface normal (see Fig. 3.5).

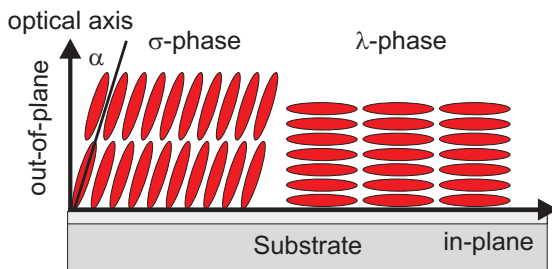


**Figure 3.5:**  $\sigma$ - and  $\lambda$ -phase of a DIP film on silicon oxide with nearly standing upright molecules ( $\alpha \approx 20^\circ$ ) or lying molecules, respectively. Since the film is polycrystalline with a random in-plane orientation it exhibits a uniaxial symmetry with the optical axis parallel to the surface normal.

Despite the good ordering of DIP films on SiO<sub>2</sub>, their roughness increases strongly with increasing film thickness, referred to as ‘rapid roughening’ phenomenon [13]. Real-time X-ray scattering during film growth showed that the film first grows in a layer-by-layer fashion and then starts to rapidly roughen above the 10th monolayer (ML) [14]. Post-growth studies gave qualitative similar results though quantitative slightly different values, i. e. the rapid roughening set in above 5 ML [21]. Therefore, the film growth corresponds to the Stranski-Krastanov growth, see Sec. 3.1.4.

Furthermore, it was possible to observe in-plane and out-of-plane real-time changes during growth [14, 50]: While the first few ML's grow strained with an out-of-plane lattice constant of 16.9 Å, it reduces to 16.6 Å for thick films. In-plane measurements revealed that the lattice parameter parallel to the surface expands by 2% upon adsorption of the second and third ML in a relatively collective fashion, e. g. changing also the underlying layer. These (partly transient) strain effects during growth are believed to be important for rationalizing the transition in the growth mode.

While at high substrate temperatures only the  $\sigma$ -phase is observed, an additional so called  $\lambda$ -phase occurs after a certain thickness if the substrate temperature is reduced [51, 14]. As illustrated in Fig. 3.5 the molecules are lying in the  $\lambda$ -phase in contrast to the  $\sigma$ -phase.

**3.1.3.1.3 DIP in combination with other substrates** This section summarized results that are obtained for DIP on different substrates to give a general overview, which is also important for future perspectives resulting from this work.

The structural properties of DIP films are strongly influenced by the choice of substrate material due to different van-der-Waals substrate-molecule interactions. DIP films on  $\text{Al}_2\text{O}_3$  were studied by Ossó *et al.* showing the same crystalline structure as on  $\text{SiO}_2$  but with a preferred in-plane orientation as well as larger grain size [52]. Also the growth on stepped sapphire follows a qualitatively similar scenario as on  $\text{SiO}_2$  with quantitative differences like the tendency on sapphire to grow lying down. On the other hand, for DIP growth on the relatively weakly interacting surface of rubrene, no  $\lambda$ -phase is found for temperatures down to 10 °C [14]. In contrast, DIP is found to grow on thick polycrystalline Au films preferentially in the lying  $\lambda$  phase, while a small fraction of the  $\sigma$ -phase is coexisting [12]. For DIP grown on Au(111) single crystals well ordered films with a clear epitaxial relation with the substrate and the lying phase could be obtained [53].

Also the thermal stability and morphology of Au metal contact on DIP films grown on  $\text{SiO}_2/\text{Au}$  was studied [12, 54]. It was shown that the interfacial properties depend strongly on the preparation condition. Under certain conditions well-defined interfaces with only slight interdiffusion could be obtained. Sellner *et al.* investigated sputtered  $\text{Al}_2\text{O}_3$  as encapsulating layers on top of DIP films grown on  $\text{SiO}_2$  showing that they enhance the thermal stability of the films significantly [55, 56]. The diffusion of Ag into crystalline films of DIP by means of radio-tracer measurements was investigated by Scharnberg *et al.* [57, 58].

Ossó *et al.* studied the organic-organic interface of  $\text{F}_{16}\text{CuPc}$  (perfluorinated copper-phthalocyanines) and DIP as a function of the deposition order (DIP on  $\text{F}_{16}\text{CuPc}$  vs.  $\text{F}_{16}\text{CuPc}$  on DIP). Barrena *et al.* found that for DIP on  $\text{F}_{16}\text{CuPc}$  self organization of DIP nanodots with high crystallinity occurred combined with a structural reconstruction of the underlying organic film [59].

**3.1.3.1.4 Electrical and optical properties of DIP thin films** DIP in combination with Au contacts shows p-conduction. Hole mobilities in thin film transistors

transition	energy (eV)	$f_{\text{osc}}$ (1)
$1B_{1u}(x)$	2.347	0.764
$1B_{2u}(y)$	2.970	0.001
$2B_{2u}(y)$	3.711	0.036
$2B_{1u}(x)$	3.944	0.051
$3B_{2u}(y)$	3.995	0.022
$3B_{1u}(x)$	4.220	0.587
$4B_{2u}(y)$	4.308	0.059
$4B_{1u}(x)$	4.514	0.640
$5B_{2u}(y)$	4.809	0.070
$5B_{1u}(x)$	4.908	0.321

**Table 3.2:** Lowest dipole-active transition energies for DIP in rectangular  $D_{2h}$  geometry.  $B_{1u}$   $\pi \rightarrow \pi^*$  transitions have their transition dipole along the long ( $x$ ) axis of the molecule, and  $B_{2u}$   $\pi \rightarrow \pi^*$  transitions along the short ( $y$ ) axis.  $B_{3u}$  transitions with transition dipole along the molecule normal ( $z$ ) do not occur in the energetic range below 5 eV. The lowest dipole-forbidden transition  $1B_{1g}$  at 2.333 eV is nearly degenerate with the  $1B_{1u}$  HOMO-LUMO transition. Taken from Ref. [40].

(TFT) in the range of  $10^{-2}$   $\text{cm}^2/\text{Vs}$  with maximal  $10^{-1}$   $\text{cm}^2/\text{Vs}$  were measured, decreasing strongly with the crystalline disorder [15]. In contrast, for DIP single crystals the mobility for electrons is found to be higher by one order of magnitude than for holes [16] indicating the potential of this material for applications where ambipolar transport is desired. Furthermore, it could be shown that the structural phase transition around 403 K affects the mobility behavior, although the exact microscopic mechanism for the observed temperature dependence is not yet understood [16]. An extraordinary large exciton diffusion length of  $\sim 100$  nm along the out-of-plane direction for DIP sandwiched between indium tin oxide (ITO) and Ag has been reported [17], although other results exist giving only 20 nm. Independently of the exact number, this makes DIP in combination with the balanced transport properties to be an interesting candidate for thin film photovoltaic device applications.

The optical properties of DIP thin films are less well investigated and are thus subject of this thesis. Heilig *et al.* studied the correlation between film morphology and time resolved confocal fluorescence spectroscopy [24]. Three characteristic fluorescence components with clearly different temperature and temporal behavior were observed (for DIP on quartz glass). Ossó *et al.* demonstrated the uniaxial anisotropy of DIP films on  $\text{SiO}_2$  substrates by spectroscopic ellipsometry [52] and Ramaniah *et al.* calculated the optical properties of single DIP molecules based on first-principle density-functional theory neglecting vibronic states [60].

R. Scholz calculated the vertical transition energies and the corresponding oscillator strength  $f_{\text{osc}}$  of DIP with time dependent (TD)-DFT [40], see table 3.2, optimizing the molecular geometry with the hybrid functional B3LYP [61,62]. In the visible, the optical properties are dominated by the HOMO-LUMO transition  $1B_{1u}(x)$  at 2.347 eV with an oscillator strength of  $f_{\text{osc}} = 0.764$ . Between the lowest transition and 4 eV, the calculation predicts some rather weak features, but above 4 eV, there are several strong transitions, all with transition dipoles along the long axis of DIP. These results serve as a basis for the discussion related to the monomer and thin film spectra.



### 3.1.3.2 Pentacene (PEN)

Pentacene (PEN,  $C_{22}H_{14}$ ) belongs to the planar polyacenes and consists of five linearly arranged benzene rings, see Fig. 3.6. The blue dye is one of the most popular compounds studied for applications in organic electronics [3, 39]. Despite the efforts in recent years, even for PEN several issues regarding the growth, structure, optical and phase behavior are still under investigation [36, 63, 64, 65, 66].

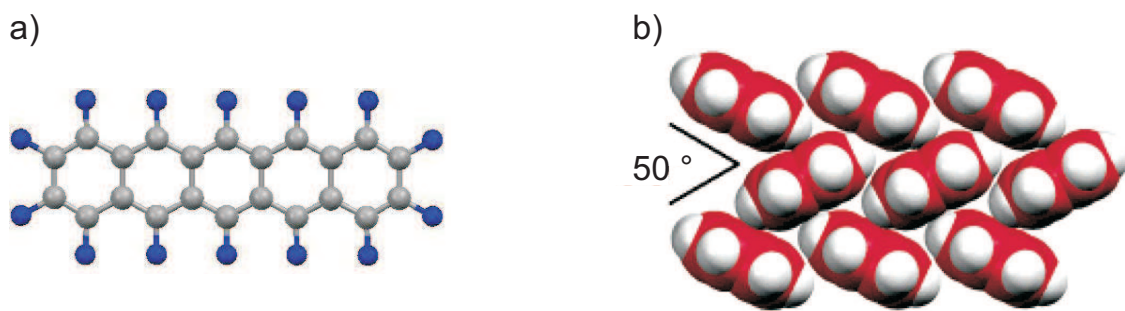


**Figure 3.6:** a) Molecular structure of Pentacene (PEN). Molecular length:  $\approx 16.5$  Å. b) Herringbone structure in the thin film phase, taken from Ref. [67].

Thin films of PEN condense at room temperature in a herringbone structure with triclinic unit cell and two molecules per unit cell (see Fig. 3.6b). Films on  $SiO_2$  [64, 65] and also on glass, exhibit a coexistence of the 'thin film phase' ( $d(001) = 15.4$  Å) and the 'bulk phase' ( $d(001) = 14.4$  Å) that differ in the lattice spacing (001). Data of both unit cells are reported in Tab. 3.3.

phase	a [Å]	b [Å]	c [Å]	$\alpha$ [°]	$\beta$ [°]	$\gamma$ [°]
'thin film' [68]	5.93	7.56	15.65	98.6	93.3	89.8
'bulk' [69]	6.49	7.41	14.75	77.3	85.7	80.9

**Table 3.3:** Lattice parameters of the 'thin film phase' and the 'bulk phase' for PEN grown on  $SiO_2$ .

It is not clarified yet if the 'bulk-phase' starts to grow from the beginning or if it evolves above a certain temperature dependent thickness [36, 65]. Nevertheless, it is significantly less pronounced for low thicknesses ( $d < 20$  nm) than for higher thicknesses.

Furthermore, the substrate and its surface treatment generally influences the grain size and morphology. This is shown for PEN on glass, where the grain size is reported to be smaller than on oxidized silicon [70, 71].

The optical properties of PEN films were investigated post-growth at thicknesses, where the 'bulk-phase' does not play a significant role. The first published data are based on an isotropic model for the film [72]. This approximation was extended by taking the uniaxial anisotropy into account [20]. It is similar to DIP due to the polycrystalline order

of the PEN films and will be discussed shortly in Sec. 5.5.3.2. In contrast to DIP the transition dipole of the HOMO-LUMO is polarized along the short axis of the planar PEN molecule. This has also a strong impact onto the anisotropy. Furthermore, it gives rise to a significant Davydov splitting.

### 3.1.4 Thin film growth

In organic electronics most devices are based on thin films. Due to the additional orientational and conformational degrees of freedom introduced by the extension of the molecules, the growth process becomes more complex compared to films composed of single atoms. Since the growth process is important to control and understand the thin film properties, it is subject of intensive research. In the following, the most important effects are introduced briefly.

The formation of a thin film involves the process of nucleation and growth [73]: Thermally evaporated molecules condense on a substrate and undergo several processes such as adsorption, surface diffusion, (re-)desorption and nucleation. The formation of clusters generally starts at energetically favorable sites such as steps, defects etc. Their stability depends on the number of incorporated molecules.

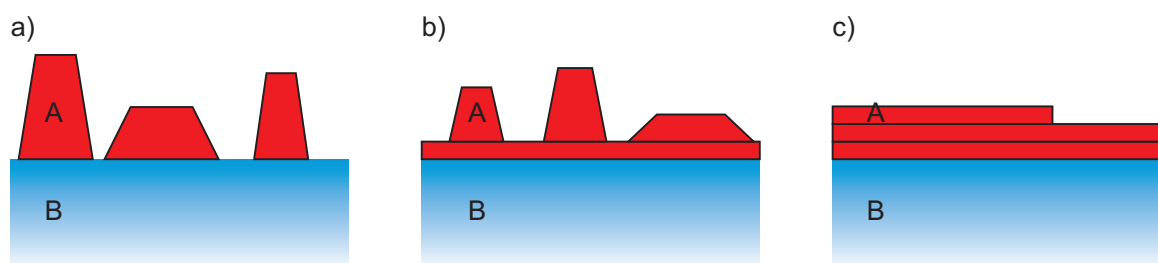


**Figure 3.7:** Three different growth modes: a) island (Volmer-Weber) growth, b) layer-plus-island (Stranski-Krastanov) growth, c) layer-by-layer (Frank-van-der-Merwe) growth.

Three basic growth modes can be distinguished for a heteroepitaxial system, as it is investigated in this thesis, where material *A* is deposited on material *B*, see Fig. 3.7. They are mainly determined by the surface energies  $\gamma_A$  and  $\gamma_B$  of the materials and the interface energy between both materials  $\gamma^*$ . Fig. 3.7a) represents island or Volmer-Weber growth where the intermolecular interactions are stronger than the bonding between the molecules to the substrate. In terms of surface energies this means:  $\gamma_B < \gamma_A + \gamma^*$ , leading to clusters growing in three dimensions. The opposite happens during layer-by-layer growth or Frank-van-der-Merwe growth (3.7c). The molecules are stronger bound to the substrate than to each other, ‘wetting’ the substrate,  $\gamma_A < \gamma_B + \gamma^*$ . The layer-plus-island, or Stranski-Krastanov growth (Fig. 3.7b) is an intermediate combination of the layer and island growth. It arises because  $\gamma^*$  increases as the layer thickness increases. Typically this layer is strained to (more or less) fit the substrate. After the formation of a

few layers the strain energy is large with respect to  $\gamma_A$ , subsequent layer growth becomes energetically unfavorable and islands form.

## 3.2 Optics

This section reviews physical concepts that are important to investigate optical properties of thin films. The Matlab programme written for the differential reflectance spectroscopy (DRS) data analysis is based on the equations presented in the following, which are therefore discussed in some detail. Also the commercial ellipsometry software makes use of it. Further details can be found in the literature [74, 75, 76, 77].

### 3.2.1 Dielectric function

The electromagnetic properties of a nonmagnetic medium are contained in the dielectric function  $\varepsilon = \varepsilon_1 + i\varepsilon_2$  which is directly related to the complex refractive index  $\tilde{n} = n + ik = \sqrt{\varepsilon}$ . While the real part describes the refraction of light, the imaginary part is related to its extinction and both components are connected via the Kramers-Kronig relations:

$$\varepsilon_1(\omega) - 1 = \frac{2}{P} \int_0^\infty \frac{\omega' \varepsilon_2(\omega')}{\omega'^2 - \omega^2} d\omega' \quad (3.12)$$

This means that  $\varepsilon_1$  can be calculated at any energy  $E = \hbar\omega$  from  $\varepsilon_2$ , if  $\varepsilon_2$  is known in the complete energy range. Since this is never the case it is practically sufficient to know  $\varepsilon_2$  in a finite range around  $\omega$  as long as it is small enough at the boundaries. The Kramers-Kronig relations between the real and imaginary parts of a response function are widely used in solid-state physics to evaluate the corresponding quantity if only one component is measured. They are among the most fundamental statements since only based on the analytical behavior and causal nature of the material response [78].

Generally, the dielectric function is a second rank ( $3 \times 3$ ) tensor reducing to a complex scalar for isotropic media. A biaxial system is characterized by the orientation of the principal axes and their corresponding three dielectric functions. In case of a uniaxial system, only the direction of the optical axis and two dielectric functions, i. e. four numbers, the real and imaginary part of the in-plane and of the out-of-plane axis, describe the optical properties of the medium (see Fig. 3.5).

The components of the dielectric tensor can be described by various analytical functions depending on the type of material and the energy range. The following models are used in this thesis [79]:

1. *Cauchy model*

The Cauchy function describes the dispersion for a material that is essentially non-absorbing over the analyzed energy range. It is given in terms of the real part of

the refractive index:

$$n = A + \frac{B}{\lambda^2} + \frac{C}{\lambda^4} \quad (3.13)$$

Additionally, an absorption tail can be included to account for transitions at higher energies:

$$k = \alpha e^{hc \cdot \beta (\frac{1}{\lambda} - \frac{1}{\gamma})} \quad (3.14)$$

$\alpha$  corresponds to the amplitude,  $\beta$  to an exponent and  $\gamma$  to the estimated energy position of the transition outside the energy range under investigation.

### 2. Oscillator model

Insulating or semiconducting media are usually best described by an oscillator model where each optical transition is given by one or several oscillators. The shape can vary, usually Lorentzian or Gaussian oscillators are used, depending on the broadening mechanisms involved. The natural line shape of a transition is given by a Lorentzian:

$$\varepsilon_n = \varepsilon_{1,n} + i\varepsilon_{2,n} = \frac{A_n B_n E_n}{E_n^2 - E^2 - iB_n E} \quad (3.15)$$

Line shapes that are broadened due to intermolecular interactions are typically described by Gaussian shapes:

$$\varepsilon_{2,n} = A_n e^{-\left(\frac{E-E_n}{B_n}\right)^2} \quad (3.16)$$

where  $A_n$  is the amplitude,  $E_n$  the energy position and  $B_n$  the width of the  $n$ th oscillator. The Lorentzian model is inherently Kramers-Kronig consistent while the Gaussian model describes only the imaginary part  $\varepsilon_2$  of the dielectric function and  $\varepsilon_1$  has to be calculated by eq. 3.12.

### 3. Effective medium approximation (EMA)

The EMA model describes a material which is composed of two or several components homogeneously. Several expressions exist that account for different mixtures under investigation. If two (or more) phases are mixed on an atomic scale the Lorentz-Lorentz expression is valid. The Maxwell-Garnett expression covers the case, where some guest material of bigger size is distributed homogeneously in a host medium. Here, the Bruggemann expression is used, where the fractions  $f_a$  and  $f_b$  of the host and guest material are similar or unknown [80]:

$$0 = f_a \frac{\varepsilon_a - \varepsilon}{\varepsilon_a + 2\varepsilon} + f_b \frac{\varepsilon_b - \varepsilon}{\varepsilon_b + 2\varepsilon} \quad (3.17)$$

$\varepsilon$  is the complex dielectric function of the composite and  $\varepsilon_a$  and  $\varepsilon_b$  are the dielectric functions of the single phases. The EMA model can describe rough surfaces if the inhomogeneities are significantly smaller than the wavelength of light, otherwise scattering effects have to be taken into account [34].

### 3.2.2 Fresnel equations

The transmission and reflection of a plane electromagnetic wave at a planar interface between two media is completely characterized when two mutually perpendicular polarizations are known. Conventionally the polarizations are chosen such that the electric vector is perpendicular (*s*-polarization) and parallel (*p*-polarization) to the plane of incidence which is defined by the wave vector  $\vec{k}$  and the surface normal  $\vec{n}$  (see Fig. 3.8a). The ratio of incident and reflected or transmitted electric field is called the Fresnel coefficient and is defined for both polarizations respectively:

$$r_{p/s} = \frac{E_{p/s}^r}{E_{p/s}^{\text{in}}} \quad \text{and} \quad t_{p/s} = \frac{E_{p/s}^t}{E_{p/s}^{\text{in}}} \quad (3.18)$$

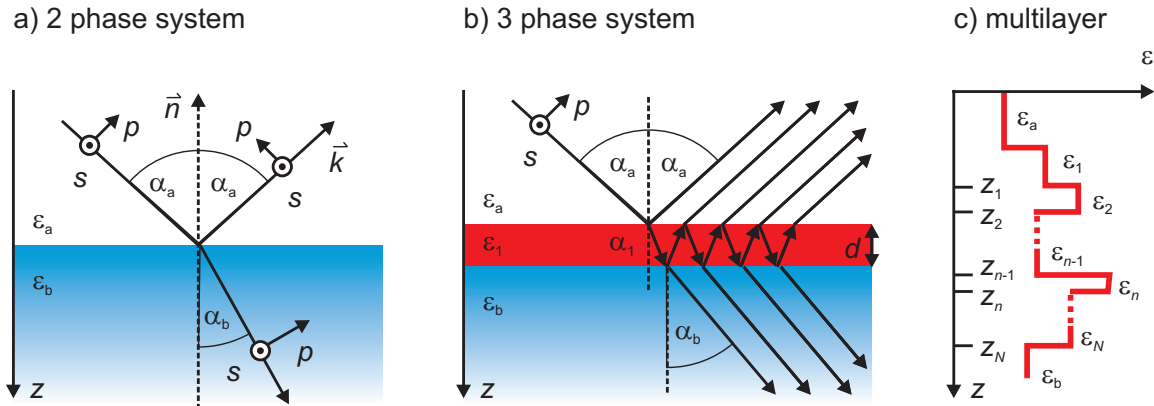


**Figure 3.8:** a) Reflection and transmission of a plane wave at an interface between 2 semi-infinite media with dielectric function  $\epsilon_a$  and  $\epsilon_b$ . b) Multiple reflection for the 3 phase system. c)  $\epsilon$ -profile for a multilayer system.

They depend on the dielectric functions of the involved media as well as on the angle of incidence, which is shown for reflection (for transmission see Ref. [75]):

$$r_p = \frac{\sqrt{\epsilon_b} \cos \alpha_a - \sqrt{\epsilon_a} \cos \alpha_b}{\sqrt{\epsilon_b} \cos \alpha_a + \sqrt{\epsilon_a} \cos \alpha_b} \quad \text{and} \quad r_s = \frac{\sqrt{\epsilon_a} \cos \alpha_a - \sqrt{\epsilon_b} \cos \alpha_b}{\sqrt{\epsilon_a} \cos \alpha_a + \sqrt{\epsilon_b} \cos \alpha_b} \quad (3.19)$$

The reflectivity  $R$ , which is important for DRS measurements, is defined as

$$R_{p/s} = \frac{I_{p/s}^r}{I_{p/s}^{\text{in}}} = |r_{p/s}|^2 \quad (3.20)$$

for *p*- and *s*-polarization, respectively.

Since the Fresnel coefficients differ for *p*- and *s*-polarization, the overall polarization state of light changes upon reflection (transmission). For isotropic media these polarization

states are eigenstates of reflection (transmission)-operations. This means that  $p$ -polarized light remains  $p$ -polarized and  $s$ -polarized light remains  $s$ -polarized, but their phase and amplitude changes differently. Therefore, the reflection (transmission) of light at an interface with two isotropic media is described in the Jones matrix formalism by a diagonal  $2 \times 2$  matrix [76, 77]:

$$\vec{E}^r = \begin{pmatrix} E_p^r \\ E_s^r \end{pmatrix} = \begin{pmatrix} r_p & 0 \\ 0 & r_s \end{pmatrix} \begin{pmatrix} E_p^{\text{in}} \\ E_s^{\text{in}} \end{pmatrix} \quad (3.21)$$

Generally, the off-diagonal elements do not vanish for anisotropic media. In case of uniaxial systems with the optical axis parallel to the plane of incidence the Jones matrix is also diagonal. This will be employed for the ellipsometry analysis.

### 3.2.3 Multilayers and matrix method

With the concept of the Fresnel coefficients the reflection of systems can be described that are more complex than the two phase system. The same holds for transmission but since it is not relevant for DRS and ellipsometry measurements, the reader is referred to the literature [75]. Fig. 3.8b) shows the three phase system with a single film of thickness  $d$  covering a substrate. All three phases are assumed to be homogeneous with sharp boundaries. The incident electromagnetic wave is reflected and transmitted multiple times between the interfaces of the film. All reflected rays have to be summed up to obtain the completely reflected wave. This has to be done for both polarizations separately, resulting in the so called 'Pseudo-Fresnel coefficients':

$$R_{p/s} = \frac{\sum_i (E_{i,p/s}^r)}{E_{p/s}^{\text{in}}} = \frac{r_{a1,p/s} + r_{1b,p/s} e^{i2\beta}}{1 + r_{a1,p/s} r_{1b,p/s} e^{i2\beta}} \quad \text{with} \quad \beta = 2\pi \frac{d}{\lambda} \sqrt{\varepsilon_1} \cos \alpha_1 \quad (3.22)$$

$\beta$  is called the phase thickness. For more complex systems the summation over all rays is not practicable anymore and the Pseudo-Fresnel coefficients are calculated via matrix methods. Each layer  $n$  is then described by a matrix  $M_n$  and the combination of all matrices represents the whole layer system, containing  $N$  layers:

$$M = \begin{pmatrix} m_{11} & m_{12} \\ m_{21} & m_{22} \end{pmatrix} = M_N M_{N-1} \dots M_n \dots M_2 M_1 \quad (3.23)$$

Matrices used in this thesis relate the field and its derivative between neighboring layers (see Chap. 12-2 in [75]) as is shown for  $s$ -polarization:

$$\begin{pmatrix} E_{n+1} \\ \frac{dE_{n+1}}{dz} \end{pmatrix} = M_n \begin{pmatrix} E_n \\ \frac{dE_n}{dz} \end{pmatrix} \quad \text{with} \quad M_n = \begin{pmatrix} \cos \delta_n & \sin \delta_n / q_n \\ q_n \sin \delta_n & \cos \delta_n \end{pmatrix} \quad (3.24)$$

The terms  $\delta_n = q_n(z_{n+1} - z_n)$  and  $q_n = \sqrt{\varepsilon_n \omega^2 - k^2 c^2}$  contain the layer thickness  $d = z_{n+1} - z_n$ , the complex dielectric function  $\varepsilon_n$  of the  $n^{\text{th}}$  layer, the frequency  $\omega$  and the wave

vector  $\vec{k}$  of the incident light as well as the speed of light  $c$  (see Fig.3.8c). Independent of the number of layers, assuming that they transmit the light sufficiently, the Fresnel coefficient can then be expressed in terms of the profile matrix  $M$  defined in eq. 3.23:

$$r_s = e^{2iq_a z_n} \frac{q_a q_b m_{12} + m_{12} - iq_b m_{11} + iq_a m_{22}}{q_a q_b m_{12} - m_{12} + iq_b m_{11} + iq_a m_{22}} \quad (3.25)$$

with

$$q_a = \frac{\omega}{c} \sqrt{\varepsilon_a - \varepsilon_a \sin^2 \alpha_a} \quad q_b = \frac{\omega}{c} \sqrt{\varepsilon_b - \varepsilon_b \sin^2 \alpha_b} \quad (3.26)$$

where  $\alpha_a$  is the angle of incidence and  $\varepsilon_a$  and  $\varepsilon_b$  are the dielectric functions of the ambient and the substrate, respectively.





## CHAPTER 4

# EXPERIMENTAL METHODS

### 4.1 Sample preparation

#### 4.1.1 Preparation of the organic molecules

The DIP molecules were bought from the PAH Research Institute in Greifenberg with 99.8% element purity, which means that the material consists of only 0.2% foreign atoms that are residua from the synthesis. 99.8% of the atoms are carbons and hydrogens but not all organic molecules are necessarily DIP. Therefore, the material was purified a second time by gradient sublimation by J. Pflaum to further increase the molecular purity. PEN molecules were bought from Aldrich (Fluka) with 99.9% element purity and were used without additionally purifying them.

The polycrystalline powder of the molecules is either evaporated onto different substrates and investigated as thin films or it is dissolved in spectroscopically clean acetone or 1,2-dichlorobenzene to study their monomeric properties.

#### 4.1.2 Substrate preparation

Three different kinds of substrates are used for the study of film growth:

1. Si(100) wafers with native oxide ( $\text{Si}_{\text{Ntve}}$ ) were bought from Si-Mat with some weak doping of boron (resistance: 17-23  $\Omega\text{cm}$ ).
2. Si(100) wafers with thermal oxide ( $\text{Si}_{\text{ThOx}}$ ) of two different thicknesses are used. They are made of  $\text{Si}_{\text{Ntve}}$  by thermal oxidation. The typical oxidation procedure is sketched in Fig. 4.1.

After the  $\text{Si}_{\text{Ntve}}$  wafer is transferred into the oven and flushed with nitrogen in order to avoid uncontrolled oxidation during the heat up, the temperature is raised at 8.3  $^{\circ}\text{C}/\text{min}$  from room temperature to 1050  $^{\circ}\text{C}$  and then kept constant. The  $\text{N}_2$

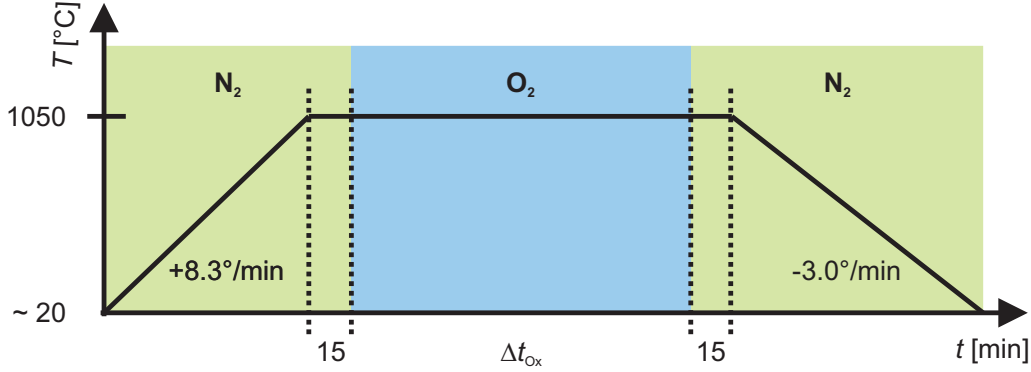


**Figure 4.1:** Thermal oxidation process: After the  $\text{Si}_{\text{Ntve}}$  wafer is heated up to  $1050\text{ }^\circ\text{C}$  under  $\text{N}_2$  atmosphere, the oxidation takes place under  $\text{O}_2$  atmosphere. Two different oxidation times  $\Delta t_{\text{Ox}} = 3\text{ h}, 16\text{ h}$  are used to obtain different thermal oxide thicknesses.

atmosphere is kept up for another 15 min to stabilize the temperature before the oxidation starts. After a given oxidation time  $\Delta t_{\text{Ox}}$ , which determines the thickness of the thermal oxide, the  $\text{N}_2$  flux is replaced by a dry  $\text{O}_2$  flux (2 l/min). After 15 min at  $\text{N}_2$  atmosphere the wafer is then cooled down at  $3\text{ }^\circ\text{C}/\text{min}$ . Two different oxidation times were used to achieve different thicknesses:  $\Delta t_{\text{Ox}} = 3\text{ h}, 16\text{ h}$ .

3. Quartz glass test wafers with 2 mm thickness from Schott are used that are roughened on the back side by either scratching with a diamond knife or grinding with wet metal grains to reduce back reflections. In order to avoid damage to the top surface during roughening of the back surface, the top surface is coated with the commercially available solution First Contact<sup>1</sup> beforehand, which can easily be removed afterwards. Additionally, it is tested how a translucent tape at the backside of the sample reduces the back reflections.

All substrates are cut in  $10 \times 5\text{ mm}^2$  samples either by a cutting machine or by hand with a diamond cutter. Shortly before transferring them into the vacuum system they are cleaned in an ultrasonic bath, first with spectroscopically clean acetone, and second with spectroscopically clean iso-propanol. Finally, they are rinsed with ultrapure water (conductivity  $\sigma = 18\text{ M}\Omega$ , Millipore). Usually two different substrates are fixed onto one sample holder using silver paste. In case of the glass substrate, independent of a rough or smooth back surface, only a small edge is covered with silver paste to make optical measurements possible. The samples are then heated shortly (10 min) *ex-situ* in order to fix and outgas the silver paste before transferring them into the vacuum system. At a pressure of  $\sim 10^{-7}$  mbar they are heated above  $\sim 400\text{ }^\circ\text{C}$  for typically 12 h to further outgas the silver paste and to remove water and other contaminants from the sample surface.

<sup>1</sup>It contains acetone, alcohol and inert polymers. See [www.photoniccleaning.com](http://www.photoniccleaning.com)

### 4.1.3 Vacuum system

The vacuum system consists of two chambers, i. e. a load lock, where the substrates are heated under HV condition, and a UHV chamber, where the films are grown by organic molecular beam deposition at a base pressure of  $\sim 10^{-10}$  mbar. A turbo molecular pump, an ion pump and a titanium sublimation pump evacuate the system. Windows (BOMCO) mounted to the UHV chamber allow to perform optical *in-situ* measurements at different angles of incidence during growth (see Fig. 4.2).

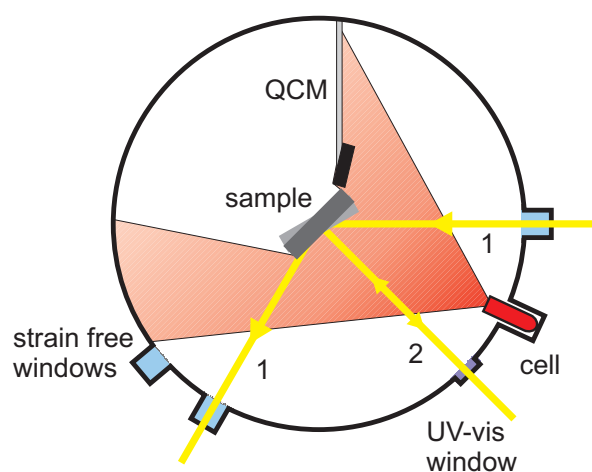


**Figure 4.2:** UHV chamber for organic molecular beam deposition: Three strain free windows allow *in-situ* ellipsometry measurements (beam 1). Additionally, a DRS setup can be mounted to a UV-vis window under normal incidence (beam 2). Note that beam 1 and 2 cannot be measured simultaneously for geometric reasons. With the quartz crystal microbalance (QCM) the film thickness is determined during growth.

#### 4.1.3.1 Evaporation cell

The molecules are evaporated from a self-built Knudsen cell (see Fig. 4.3), which can be heated up to  $\sim 500$  °C. It is  $\sim 20$  cm away from the sample holder. A ceramic crucible containing the molecules is surrounded by a ceramic cylinder, which is wrapped by a tungsten wire and shielded by two tantalum foils.

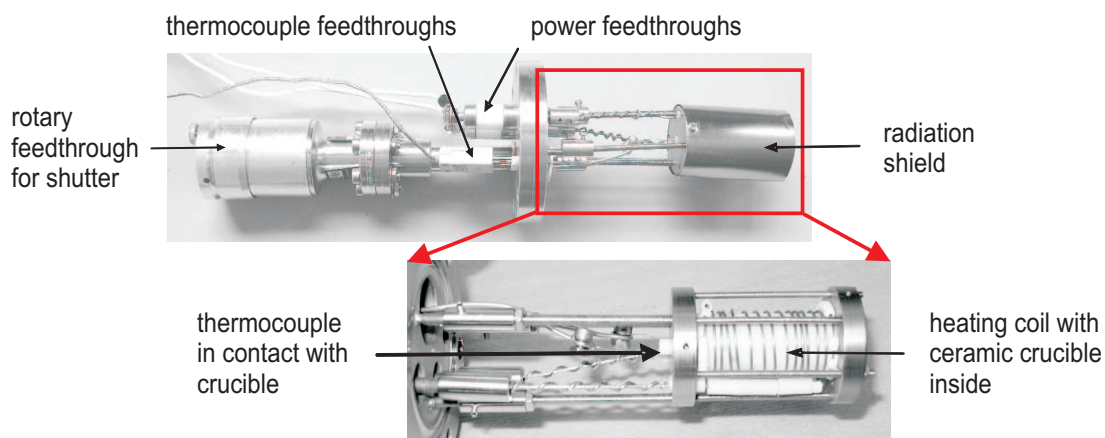


**Figure 4.3:** Home-built effusion cell to evaporate organic molecules.

A thermocouple, that consists of alumel and chromel, contacts the crucible and allows to measure its temperature. Depending on the position of the thermocouple deviations from the 'real' temperatures inside the crucible occur. The mouth of the crucible is covered by a tantalum shield with a  $\sim 2 \text{ mm}^2$  centered hole that determines the emission characteristic of the cell. An external shutter is used to start and stop the molecular flux.

#### 4.1.3.2 Sample holder

The sample holder is attached to a manipulator (Vacuum Generator), which allows for translations in the  $x$ -,  $y$ - and  $z$ -direction as well as for azimuthal and polar rotations, making a precise alignment of the sample possible. Furthermore, the substrate can be heated up to  $\sim 400 \text{ }^\circ\text{C}$  and cooled down to  $\sim -110 \text{ }^\circ\text{C}$  by liquid nitrogen. The cooling principle is shown in Fig. 4.4.

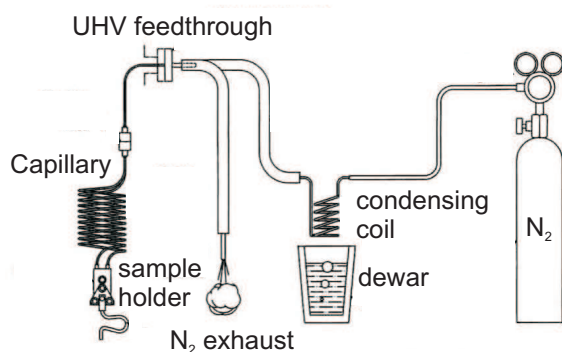


**Figure 4.4:** Sample cooling:  $\text{N}_2$  gas is pumped through a dewar filled with liquid nitrogen for liquidizing the gas. Via a feedthrough and a capillary the cooled  $\text{N}_2$  is transported to the sample holder, which can be cooled down to  $\sim -110 \text{ }^\circ\text{C}$ . Taken from Ref. [81].

$\text{N}_2$  gas at room temperature flows with a pressure of  $\sim 1.5 \text{ bar}$  through a copper coil, which is completely immersed in liquid nitrogen, cooling down the gas to  $77 \text{ K}$  ( $-196 \text{ }^\circ\text{C}$ ), i. e. liquidizing it. The coil is connected via a thermally isolated silicone tube to a liquid feedthrough. Inside the chamber the liquid nitrogen is guided by a stainless steel capillary, that surrounds the manipulator to a copper cooling reservoir, which is thermally connected to the sample holder. A sapphire plate ( $\text{Al}_2\text{O}_3$ ) between the cooling reservoir and the sample holder acts like a thermal switch: its thermal conductance is only high at low temperatures allowing also efficient heating of the sample.

#### 4.1.4 Organic molecular beam deposition

The evaporation cell is typically filled with  $\sim 300 \text{ mg}$  DIP, which is outgassed at  $\sim 200 \text{ }^\circ\text{C}$  for  $\sim 12 \text{ h}$  to reduce contaminations before the first film growth. The films are grown at a rate of  $0.5 - 4 \text{ \AA}/\text{min}$  corresponding to a cell temperature of  $250 \text{ }^\circ\text{C} - 270 \text{ }^\circ\text{C}$ , which is stabilized by a PID-control. In order to keep the rate constant, the temperature of the cell has to be increased slightly ( $1-2 \text{ }^\circ\text{C}$ ) after several film growths. The rate is monitored by a water cooled quartz crystal microbalance (QCM), which is located for each film growth at the same position close to the sample holder. The molecules are

usually evaporated onto two different substrates simultaneously, which are temperature stabilized. In the following the DIP film on native oxide will be referred to as DIP-Si<sub>Native</sub>, the films on thermal oxide as DIP-Si<sub>ThOx</sub> and on glass as DIP-Glass, respectively. Two different substrate temperatures are used:  $T = 130$  °C corresponding to the high temperature growth (HT growth) and  $T = -110$  °C corresponding to the low temperature growth (LT growth). In case of PEN the substrate temperature is kept at RT and either Si<sub>Native</sub> or glass is used.

## 4.2 Spectroscopic ellipsometry

### 4.2.1 Principle

Spectroscopic ellipsometry (SE) is a highly sensitive technique to study the optical properties of thin films [77]. It measures the change of polarization state of light reflected off the sample<sup>2</sup>. The quantity used to describe this changes is the complex ratio of the Fresnel coefficients:

$$\rho = \frac{r_p}{r_s} = \tan \Psi \exp(i\Delta) \quad (4.1)$$

The ellipsometric angles  $\Psi$  and  $\Delta$  describe the change in amplitude and phase of the polarization state, respectively. Since the ratio  $r_p/r_s$  is measured, ellipsometry does not depend on absolute intensities giving rise to high accuracy. Furthermore, the additional phase factor  $\Delta$  enhances the sensitivity compared to reflectivity measurements.  $\Psi$  and  $\Delta$  are obtained from the measured reflected intensity (see Ref. [79]) and are directly related to the optical properties of the sample by the Fresnel coefficients. In order to extract the dielectric function of a layer, eq. 4.1 has to be inverted, which is analytically possible only for the two phase system:

$$\varepsilon = \left( \frac{1 - \rho}{1 + \rho} \right)^2 \tan^2 \alpha \cdot \sin^2 \alpha + \sin^2 \alpha \quad (4.2)$$

Mainly two approaches exist to solve eq. 4.1 numerically, both having their advantages and disadvantages: First, a so called point-by-point fit can be performed where the dielectric function is optimized at each wavelength separately to fulfill eq. 4.1. Second, the dielectric function is described by some analytical function (see Sec. 3.2.1) whose parameters are optimized in a specific energy range. Since the analytical fit highly depends on the choice of initial parameters, it is usually necessary to perform a point-by-point fit beforehand. The advantage of the analytical fit is that the functions are typically Kramers-Kronig consistent and other physical constraints like the line shape etc. can be applied. On the other hand, the point-by-point fit does not depend on any constraints, which can be subject to errors. The ellipsometry data are analyzed with the commercially available

<sup>2</sup>Transmission ellipsometry does also exist but will not be discussed here.

WVASE32 software [79] and the fitting procedure is based on the Levenberg-Marquard-algorithm.

### 4.2.2 Setup

Spectroscopic ellipsometry data are acquired with a Woollam M-2000 Rotating Compensator ellipsometer. A CCD-array detector allows to detect the data in the energy range of 1.25 - 5 eV and a wavelength resolution of  $\Delta\lambda \sim 1.6$  nm within less than a second. Although the acquisition time is increased up to one minute by averaging the data over several hundred compensator revolutions to reduce the noise, this is still fast enough to follow the film growth in real-time. The spot size on the sample is  $\sim 4-20$  mm<sup>2</sup> depending on the angle of incidence.

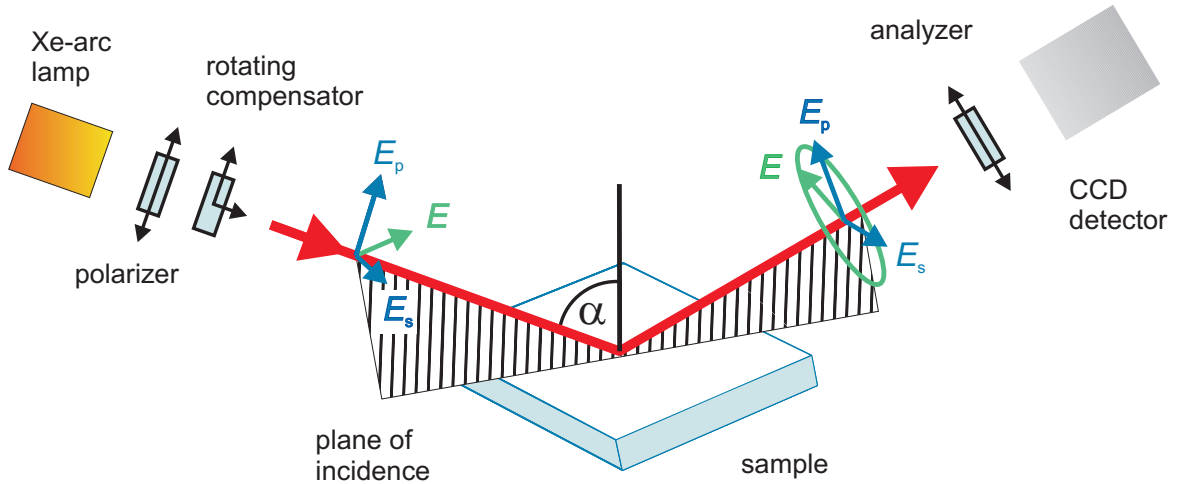


**Figure 4.5:** Setup of the Woollam M-2000 ellipsometer: A polarizer and a rotating compensator defines the polarization of the light emitted from a Xenon-arc lamp (1.23-5 eV). After it is reflected off the sample surface, a CCD camera combined with an analyzer detects the time-dependent intensity signal spectroscopically.

The schematic setup is shown in Fig. 4.5. The white light of a Xenon-arc lamp is polarized linearly by a fixed polarizer and passes a rotating compensator before it is reflected off the sample surface passing a fixed analyzer and hitting the CCD camera. The compensator is a birefringent crystal with its slow and fast axis perpendicular to the light beam. Depending on the relative angle  $\alpha_{PC}$  between the polarizer axis and the fast compensator axis it keeps the polarization linear ( $\alpha_{PC} = 0^\circ, 90^\circ, 180^\circ, 270^\circ$ ) or it transforms the linear polarization either in circular polarizations ( $\alpha_{PC} = 45^\circ, 135^\circ, 225^\circ, 315^\circ$ ) or in elliptic polarizations (any other  $\alpha_{PC}$ ). The rotation of the compensator causes, therefore, a periodically changing light polarization ( $T_{\text{period}} = T_{\text{rot-C}}/2$ ), which leads, due to the fixed analyzer in front of the detector, to a periodically changing intensity signal. The Fourier components of this signal are directly connected to the ellipsometry angles  $\Psi$  and  $\Delta$ , which are the experimental 'raw data' coming out of the ellipsometry measurement.

Before the first measurement, the angles of the polarizer and the analyzer relative to the plane of incidence (see Fig. 4.5) need to be set correctly. This is done by performing a calibration where the plane of incidence is determined. The calibration needs to be performed only after initializing the ellipsometer since an exchange of the sample does not change the plane of incidence if it is aligned correctly. The calibration is performed with a smooth and isotropic sample to avoid depolarization effects. Further details can be found in Ref. [82, 79].

### 4.2.3 *Ex-situ* measurement

The ellipsometer can be mounted onto the computer controlled Woollam goniometer to vary the angle of incidence (AOI) in the range of  $40^\circ - 90^\circ$  relative to the surface normal of the sample, which is mounted horizontally. The sample length of  $\sim 10$  mm limits the highest AOI up to  $\sim 80^\circ$  to avoid reflections from the edge or from beside the sample. The variable angle spectroscopic ellipsometry (VASE) data are typically measured from  $40^\circ - 80^\circ$  in steps of  $5^\circ$ . More angles of incidence would not increase the experimental information [77].

The calibration for the *ex-situ* setup is usually performed with a Si(100) reference wafer from Woollam that has a thermal oxide thickness of 20 nm. The revolutions of the compensator per measurement are typically 200 for a Si-substrate and 400 for a glass substrate. The *ex-situ* ellipsometry measurements are always performed as soon as the films are taken out of the chamber, although serious degradation has not been observed for DIP and PEN films so far.

### 4.2.4 *In-situ* measurement

For *in-situ* measurements the ellipsometer can be mounted onto the UHV chamber that is equipped with three strain free quartz windows to avoid strain induced birefringence, see beam 1 in Fig.4.2. Each *in-situ* measurement takes place at a fixed angle of incidence which can be chosen to be  $\sim 60^\circ$  or  $\sim 70^\circ$ . Due to the mounting tolerance of the ellipsometer the exact angle of incidence can differ by  $\pm 0.5^\circ$  from the dial value and it needs to be determined from the ellipsometry data after the measurement.

The calibration for the *in-situ* setup is performed on the same substrate, which is selected to be measured during film growth. Since the alignment does not work as well as for the *ex-situ* setup, the intensity signal can be slightly lower and the revolutions per measurement are typically chosen to be 400 for Si-substrates and 800 for glass substrates, corresponding to an acquisition time of 1 min and 2 min, respectively. Since the constant growth rate is  $\sim 1 \text{ \AA}/\text{min}$ , the thickness increases by 1-2  $\text{ \AA}$  per measurement, which is still small compared to the thickness of one DIP monolayer ( $\sim 16 \text{ \AA}$ ).

## 4.3 Differential reflectance spectroscopy

### 4.3.1 Principle

Differential reflection spectroscopy (DRS) is a second very sensitive method employed to study the optical properties of thin films. The DRS signal is defined by

$$DRS = \frac{R(d) - R_0}{R_0} \quad (4.3)$$

where  $R_0$  corresponds to the reflectivity of the bare substrate and  $R(d)$  to the reflectivity of the substrate covered by the film with thickness  $d$ . Since the ratio between reflectivities is taken, errors concerning the absolute intensity cancel and only intensity fluctuations influence the signal. At normal incidence and in case of very thin films on a transparent substrate (i. e. for  $d/\lambda \ll 1$ ) the DRS signal can be related directly to the imaginary part  $\varepsilon_2$  of the dielectric function according to Ref. [83]:

$$DRS = \frac{8\pi d}{\lambda(1 - n_{\text{sub}}^2)} \varepsilon_2 \quad (4.4)$$

This simplifies the analysis greatly, although it is impossible to determine  $\varepsilon_1$ . In case of thicker films the dielectric function is determined by an analytical fit with e. g. Gaussian oscillators using a Matlab code that is based on the matrix method (see 3.2.3). A point-by-point fit cannot be applied since only one experimental parameter per energy exists, but two parameters (the real and the imaginary part of the dielectric function) have to be determined. A further simplification is that the measurements are performed at normal incidence. Therefore, the uniaxial anisotropy of the films does not have to be taken into account since only the in-plane component is probed.

### 4.3.2 Setup

DRS data are acquired with a DH-2000 deuterium tungsten halogen light source and an USB2000 spectrometer from Ocean Optics. A CCD-array detector allows to measure the spectrum in the energy range of 1.43 – 6.89 eV and a wavelength resolution of  $\Delta\lambda \approx 0.3 - 0.4$  nm within 3 ms. The setup corresponds to a common reflectivity assembly at normal incidence, which is shown in Fig. 4.6.

A 600  $\mu\text{m}$  bifurcated optical fiber is mounted  $\sim 15$  cm in front of the UV-vis-window of the UHV chamber (see also Fig. 4.2). One fiber arm is connected to the light source while the other is connected to the detector, allowing to emit and detect the light nearly at the same position. An achromatic collecting lens with a focal length of  $f = 8$  cm is mounted  $g \approx 14$  cm in front of the fiber to focus the light onto the sample giving a spot size of  $\sim 2.5$  mm<sup>2</sup>. The distance between the lens and the sample is  $b \approx 19$  cm.



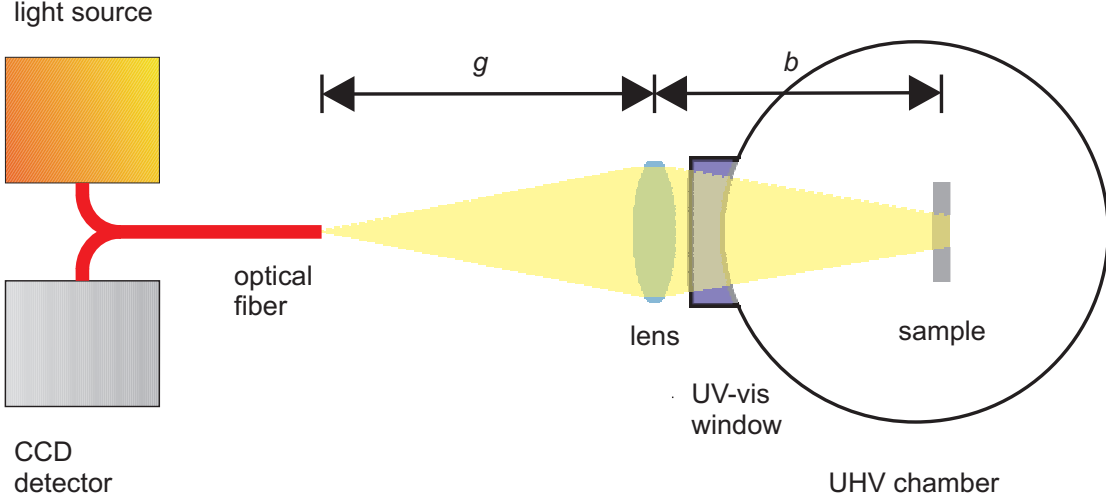


**Figure 4.6:** DRS setup for *in-situ* measurements at normal incidence with  $g \approx 14$  cm and  $b \approx 19$  cm for following the film growth in real-time.

### 4.3.3 Measurement

The reflected intensity is measured *in-situ* at normal incidence before and during the film growth. The integration time depends on the substrate under investigation, a typical value for a Si substrate is  $t_{\text{int}} \sim 10$  ms and for a glass substrate  $t_{\text{int}} \sim 60$  ms. Therefore, the acquisition time of one spectrum is chosen to be  $\sim 1$  min, in case of a Si substrate, or  $\sim 2$  min, in case of a glass substrate, such that the time resolution is sufficient to follow the film growth in real-time and the noise is reduced significantly by averaging over several thousands of spectra. This means that the averaging number of spectra for a Si substrate is typically  $n = 6000$  and for a glass substrate  $n = 2000$ . After the measurement the intensity data are processed to DRS data defined by equation 4.3.

## 4.4 Absorption spectroscopy

### 4.4.1 Principle

If a light beam passes a sample its intensity will be reduced, i. e. the transmission  $T = I/I_0$  is typically smaller than one. The main reason is absorption of the sample, if it is not transparent, but also reflection at the interface as well as scattering from inhomogeneities will diminish the intensity. If the sample is very smooth and homogeneous, and if the refractive index of the sample does not differ strongly from the environment, it is a good approximation to neglect the last two effects and to determine the absorption coefficient  $\alpha$  with Beers-Lambert law:

$$I(d) = I_0 e^{-\alpha d} \quad (4.5)$$

$I_0$  is the incident light intensity and  $I(d)$  the intensity after passing the sample with thickness  $d$ . The optical density  $OD$  or absorbance  $A$  is defined by  $OD = -\log(T) = \alpha d \log(e)$ . Since the electronic transitions of the solvent, in this case acetone and 1,2-dichlorobenzene, are at much higher energies compared to the transition of the solute, their influence on the transition energies of the solute can be estimated with simple methods based on the refractive index in the transparent region of the solvent [84]. For solutions with low concentration the imaginary part of the dielectric function can be calculated according to Ref. [85]:

$$\varepsilon_2 = 2k_{\text{molecule}}n_{\text{solvent}} \quad (4.6)$$

with the extinction coefficient  $k = \alpha c/2\omega$ .

#### 4.4.2 Setup and measurement

Optical transmission spectra are measured with a Cary50 UV-vis spectrometer in the energy range of 1.4–4 eV and with a wavelength resolution of 0.5–1 nm for DIP dissolved in solution.  $1.6 \pm 0.2$  mg of DIP is either dissolved in 25 ml acetone (refractive index  $n \approx 1.36$ ) or in 25 ml 1,2-Dichlorobenzene ( $n \approx 1.55$ ), corresponding to a concentration of  $c = m_{\text{DIP}}/(M_{\text{DIP}}V_{\text{solvent}}) = (1.6 \pm 0.2) \cdot 10^{-4}$  mol/l. In case of acetone the real concentration is rather smaller since not the whole amount of DIP could be dissolved. In order to exclude non-linear optical effects and dimerization the concentration is diluted by a factor of 4, 8 and 20 consecutively for both solvents.

### 4.5 Fluorescence spectroscopy

#### 4.5.1 Principle

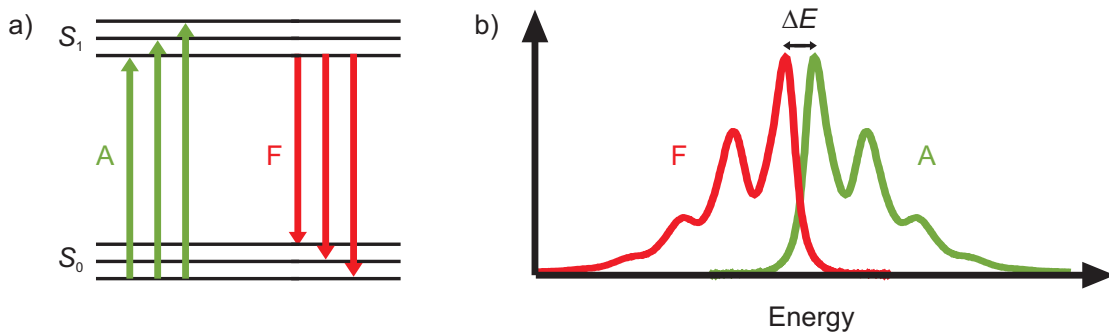


**Figure 4.7:** a) Jablonski diagram: Absorption (A) and fluorescence (F) between the singlet states  $S_0$  and  $S_1$  including their vibrational states. b) Illustration of the possible mirror symmetry between absorption and fluorescence spectra together with the Stokes shift  $\Delta E$ .

Fluorescence is essentially the inverse process of absorption [31]. It corresponds to the case, where photons are emitted from an optically excited singlet state, as Fig. 4.7 illustrates. Since the lifetime of the excited electronic state  $S_1$  is usually sufficient long for the excited molecule to attain thermal equilibrium in the excited electronic state, the fluorescence emission occurs primarily from the zero-point vibrational level of  $S_1$ . In the ideal case the fluorescence spectrum corresponds to the absorption spectrum that is mirrored at the  $0 - 0$  transition, if the same vibrational levels for the electronic ground state  $S_0$  and for the electronic excited state  $S_1$  are assumed. Typically, additional broadening and a red-shift called the Stokes shift is introduced due to interactions with the environment.

### 4.5.2 Setup and measurement

The fluorescence of DIP films on  $\text{SiO}_2$  as well as DIP dissolved in acetone is investigated. The spectra are measured with a Cary Eclipse Fluorescence spectrometer in the energy range of 1.5 – 2.5 eV. The excitation wavelength  $\lambda_{\text{ex}}$  is chosen according to the prior experimentally determined absorption spectra of the film and of the monomers, such that the absorption and hence the fluorescence intensity is maximized. In case of thin films the sample surface is oriented such that the reflected light does not hit the detector. The angle of incidence could not be varied precisely and it was typically in the range of 25-55 °.

## 4.6 Raman spectroscopy

### 4.6.1 Principle

Raman scattering, which was first described by C. V. Raman in 1928 [86], is based on inelastic photon scattering that allows to spectrally resolve the excitation of vibrational modes<sup>3</sup>. In this thesis Raman spectroscopy is used as a complementary method to gain further insight into the exciton-phonon coupling process. Details concerning this method can be found in the literature [87, 88, 89, 90].

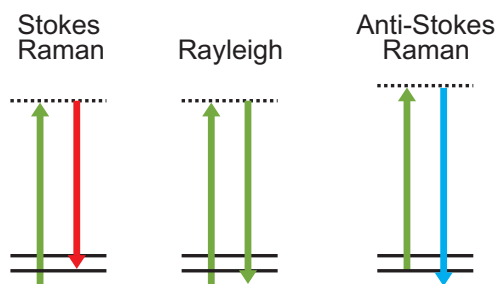


**Figure 4.8:** Elastic (Rayleigh) and inelastic (Stokes and Anti-Stokes) scattering processes. Dotted line: Virtual state. Solid lines: Vibrational states of the electronic ground state.

<sup>3</sup>Also rotational modes can be excited but they do not play a role for the samples under investigation.

An overview gives Fig. 4.8 representing the optical excitation process for the elastic and the inelastic scattering. Since at room temperature most of the molecules populate the vibrational ground state, only the Stokes process contributes significantly. Resonant Raman scattering occurs, if the virtual excited state coincides with a real electronic state, which increases the scattering cross section significantly. It probes the deformation of the molecule in the electronic excited state that is involved in the scattering process.

## 4.6.2 Setup and measurement

Raman spectra are measured with a Horiba Jobin Yvon Labram HR spectrometer equipped with a liquid nitrogen cooled CCD detector and a confocal microscope. Either a frequency doubled 50 mW Nd:YAG laser with  $\lambda_{\text{ex}} = 532 \text{ nm}$  ( $E = 2.33 \text{ eV}$ ) or a 17 mW HeNe-laser with  $\lambda_{\text{ex}} = 633 \text{ nm}$  ( $E = 1.96 \text{ eV}$ ) is used for excitation in a back scattering geometry with both the incident and the scattered beam passing the objective of the microscope. In order to achieve a spectral resolution of  $0.3 - 0.4 \text{ cm}^{-1}$  ( $0.04 - 0.05 \text{ meV}$ ), a grating with  $g = 1800 \text{ mm}^{-1}$  is employed. The incident laser power  $P_0$ , measured for each wavelength with the  $10\times$  objective, is  $P_0(532\text{nm}) = 7 \text{ mW}$  and  $P_0(633\text{nm}) = 10 \text{ mW}$ . It can further be reduced by filters ranging from  $OD0.3$  to  $OD4$ , which corresponds to  $P = P_0/10^{0.3}$  and  $P = P_0/10^4$ , respectively. Three objectives, a  $10\times$ , a  $50\times$  and a  $100\times$ , allow varying the size and intensity of the laser focus. All spectra are measured *ex-situ* at room temperature. Since the degradation of the molecules is a serious issue giving rise to vanishing Raman peaks, the measurements are performed always at a fresh spot that was not illuminated by the laser before. Furthermore, the integration time as well as the laser intensity is kept as small as possible.

## 4.7 Tip-enhanced spectroscopic imaging

### 4.7.1 Principle

The resolution of a confocal microscope, as it is employed for standard Raman spectroscopy, is limited by diffraction, i. e. no distance smaller than

$$\Delta x = \frac{1.22\lambda}{2 \cdot NA} \quad (4.7)$$

can be detected ( $NA = n \sin \alpha$  is the numerical aperture with the refractive index  $n$  and half the opening angle  $\alpha$  of the focusing element) [91]. For studying optical properties on the nanometer scale beyond the diffraction limit new techniques have been developed that are subject of intensive research [92]. One possibility is to illuminate a metal tip and to excite plasmons, i. e. collective conducting electron vibrations in the metal [93]. This results in a high evanescent electric field underneath the tip with a very short decay range of only some nanometers. Therefore, the enhanced field can be used as a nanometer sized light source making optical investigations beyond the diffraction limit possible.

## 4.7.2 Setup and measurement

In collaboration with D. Zhang *et al.* (Meixner group, institute of physical and theoretical chemistry, Tübingen) tip-enhanced spectroscopic measurements on DIP films are performed employing a home-built parabolic mirror assisted near-field optical microscope [94]. The basic principle of this technique is to approach an electrochemically etched sharp gold tip closely to the sample surface controlling the distance by shear-forces [95]. The tip is radially illuminated by He-Ne laser light ( $\lambda = 633$  nm) that is polarized along the tip shaft (see Fig. 4.9), and acts like an optical antenna. The excitation field is confined to a very small sub-diffraction volume at the tip apex, retrieving emitted or scattered photons to the far field for detection. Compared to the conventional near-field optical microscopes, a parabolic mirror is used for tip illumination and signal collection, which are performed from the top of the sample under perfect diffraction and polarization conditions. Therefore, no restrictions apply with respect to the conductivity or transparency of the sample substrates. Further details can be found in the literature [94, 96, 93].

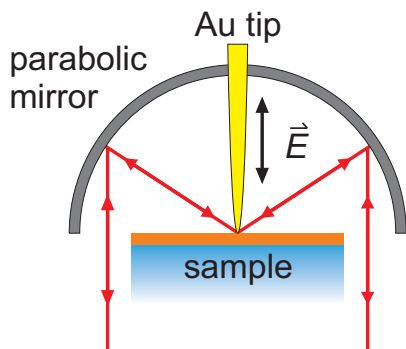


**Figure 4.9:** Sample stage of the parabolic mirror assisted near-field optical microscope, showing the beam path with the corresponding electric field  $\vec{E}$  at the Au tip and the sample in the focus of the parabolic mirror.

The setup allows to record simultaneously the topography and correlated chemical information via Raman and PL spectroscopy. The topographic resolution of this technique can reach a few nanometers, whereas the optical resolution is essentially determined by the apex size of the antenna tip, which is about 10 nm.

## 4.8 X-ray reflectivity

### 4.8.1 Principle

X-ray reflectivity is a sensitive method for thin films to determine their thickness, roughness and structural properties. For details of this technique the reader is referred to the literature [97]. Here only basic concepts are introduced that are important for the data analysis.

The formalism for describing X-ray reflectivity resembles that of optical reflectivity, since it is based on the Fresnel formalism for electromagnetic waves (see Sec. 3.2.2). The interaction of X-rays with matter can also be described by a complex index of refraction

if the electron density  $\rho$  can be considered as continuous. This is the case for small angles of incidence<sup>4</sup>:

$$n = 1 - \delta + i\beta \quad \text{with} \quad \delta = \frac{\lambda^2 r_e \rho}{2\pi} \quad \text{and} \quad \beta = \frac{\lambda \mu}{4\pi} \quad (4.8)$$

where  $\lambda$  is the wavelength,  $r_e = 2.82 \cdot 10^{-5} \text{ \AA}$  the classical electron radius and  $\mu$  the absorption coefficient. One main difference compared to visible light is that the real part of the refractive index is slightly *smaller* than one, e. g.  $\delta > 0$ , giving rise to total reflection *below* the critical angle  $\Theta_c$ .

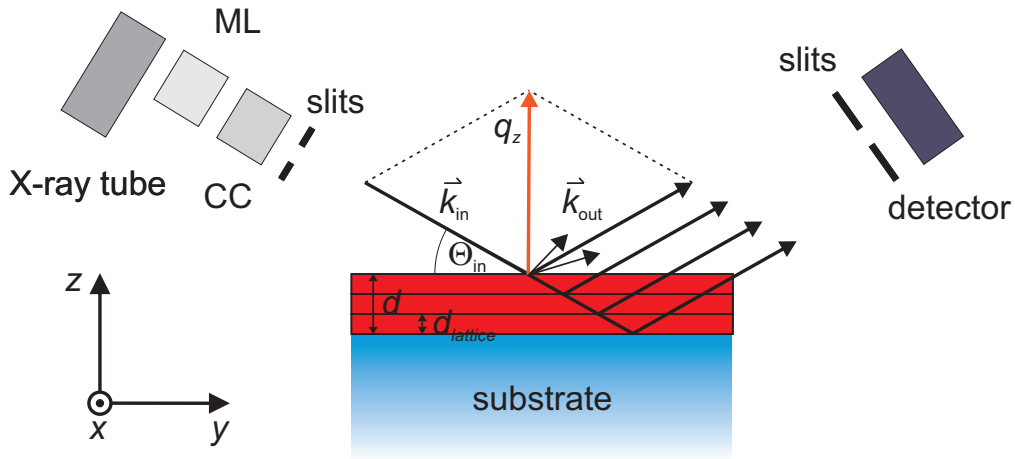


**Figure 4.10:** Geometry for X-ray reflectivity and general setup with multilayer (ML) and channel cut (CC).

Fig. 4.10a) shows the scattering geometry with the incident and reflected wave vector  $\vec{k}_{\text{in}}$ ,  $\vec{k}_{\text{out}}$  and the corresponding angle of incidence  $\Theta_{\text{in}}$ . The scattering vector  $\vec{q} = \vec{k}_{\text{out}} - \vec{k}_{\text{in}}$  is oriented along the surface normal since  $|\vec{k}_{\text{in}}| = |\vec{k}_{\text{out}}|$  applies for elastic scattering. The  $z$  component can then be obtained from the angle of incidence and the wavelength:

$$q_z = \frac{4\pi}{\lambda} \sin \Theta_{\text{in}} \quad (4.9)$$

The Fresnel coefficients  $r_{i,i+1}$  for each interface of a layer system can be calculated by a recursive formalism developed by Parratt [98]. It allows to model the  $q_z$  dependency of the normalized reflected X-ray intensity to determine the layer thickness similar to optical reflectivity. If the surface roughness  $\sigma$  of a film is smaller than its thickness the Fresnel coefficient can be modified by

$$r_{\text{rough}} = r_{\text{ideal}} \cdot e^{-2k_{(\text{in},z)} \cdot k_{(\text{out},z)} \cdot \sigma^2} \quad (4.10)$$

<sup>4</sup>Note that the angle of incidence for X-ray reflection is defined relative to the surface (see Fig. 4.10), whereas for optical reflection it is defined relative to the surface normal.

to account for roughness. In this thesis all reflectivity data are modeled by a software from the Hahn-Meitner-Institute in Berlin [99], which is based on the Parratt formalism. Furthermore, Bragg reflections occur according to the Bragg condition if a film has a periodic structure in the out-of-plane direction:

$$n\lambda = 2d_{\text{lattice}} \sin \Theta_{\text{Bragg}} \quad (4.11)$$

This allows to determine the out-of-plane lattice spacing  $d_{\text{lattice}}$ . It is also possible to determine the mosaicity, i. e. the out-of-plane orientational order of the crystallites, from a so-called rocking scan at the Bragg condition. For a rocking scan the angle of incidence is kept fixed at  $\Theta_{\text{Bragg}}$  while the sample is slightly rotated around the  $x$ -axis (see Fig. 4.10).

## 4.8.2 Setup and measurement

X-ray reflectometry data are measured with a GE/Seifert X-ray reflectometer and Cu  $K_{\alpha 1}$  radiation ( $\lambda = 1.541 \text{ \AA}$ ) *ex-situ* in air. A multilayer mirror and a double bounce compressor monochromator (channel cut) reduce the beam divergence. Both, the scintillation point detector and the X-ray tube including the optics are mounted to a goniometer that allows to vary the angle of incidence between  $0 - 40^\circ$  with an accuracy of less than  $0.002^\circ$ . The sample stage can be moved in the  $z$ -direction and rotated around the  $x$ - and  $y$ - axes. Horizontal slits behind the channel cut and in front of the detector determine the beam width and the angular resolution. A vertical slit close to the sample limits the beam width in  $x$ -direction such that it corresponds to the sample width to suppress noise.

The reflected intensity is measured for different  $\Theta_{\text{in}}$  fulfilling the specular condition ( $\Theta_{\text{in}} = \Theta_{\text{out}}$ ), whereas the detector angle is typically off by  $0.1^\circ$  ( $\Theta_{\text{out}} = \Theta_{\text{in}} \pm 0.1^\circ$ ) when diffuse scattering is measured. A rocking scan is obtained by moving the source and detector arm at the Bragg condition such that the relative angle between them stays constant. This corresponds effectively to a rocking of the sample.

## 4.9 Atomic force microscopy

### 4.9.1 Principle

Atomic force microscopy (AFM) is used to obtain complementary information about the film morphology giving insight into the surface roughness and the island size, also molecular tilt angles can be estimated [21]. The basic idea of an AFM is that the local attractive or repulsive force between a tip and the sample is converted into a bending or deflection of the cantilever, where the tip is attached. The deflection is measured by a laser beam directed at the back of the cantilever as it is shown in Fig. 4.11.

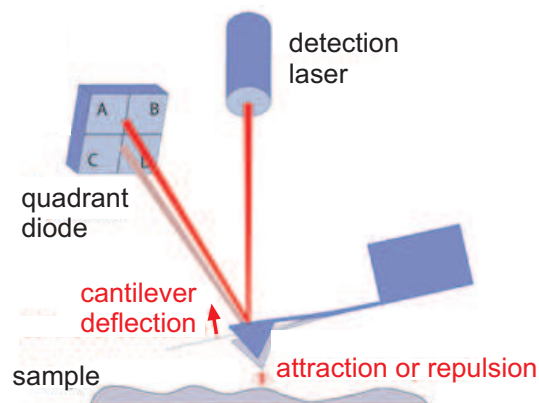


**Figure 4.11:** Basic principle and setup of an AFM: The distance dependent interactions between sample and tip can be optically detected by the deflection of the cantilever. This allows to measure e. g. the height profile of the surface. Taken from Ref. [100].

## 4.9.2 Setup and measurement

AFM data are acquired *ex-situ* with a Digital Instruments Multimode AFM and with a JPK NanoWizard II AFM in tapping mode. In this operation mode the distance of the oscillating cantilever is controlled by the oscillation amplitude, which decreases with decreasing distance. This allows to scan the surface without contacting and scratching the surface, which could cause damages to the organic films. Different sharp and variably coated Si cantilevers are employed giving similar results. Typical operation parameters are: setpoint  $s = 1.3 - 1.8$  V with a scanning speed of  $v = 4 - 5$   $\mu\text{m/s}$ . In order to avoid degradation of the samples they are usually measured within a few weeks after film growth. The data are processed and analyzed with the freely available software WSxM [101].



## CHAPTER 5

# RESULTS & DISCUSSION

In this chapter the experimental results are presented and discussed. The work focuses mainly on the optical properties of DIP thin films, but also PEN film growth is investigated by real-time measurements. Since the monomer optical properties are essential for the interpretation of the film spectra, they are presented first for DIP, followed by the characterization of the substrates. Then the structural and morphological film properties, which can have a strong impact onto the optical properties, are investigated by X-ray and AFM measurements in Sec. 5.3. After this general introduction, the first main part of this thesis (Sec. 5.4) deals with *ex-situ* ellipsometry results for DIP thin films that serve as a reference for real-time measurements. First, the ellipsometry data analysis is presented for uniaxial anisotropic thin films followed by a detailed discussion of the resulting spectra for DIP films on  $\text{Si}_{\text{Ntve}}$  substrates. This includes a theoretical analysis concerning exciton transfer that was performed by R. Scholz *et al.*. In the second main part of the thesis the real-time measurements determined for different film growths are presented, including PEN thin films, whose morphological and static optical properties are briefly introduced. First, real-time ellipsometry data are discussed for DIP on  $\text{Si}_{\text{Ntve}}$ , which do not give unambiguous results. Therefore, DRS is used to investigate DIP film growth on  $\text{Si}_{\text{Ntve}}$  and on glass at low and at high temperature. Furthermore, PEN film growth on  $\text{Si}_{\text{Ntve}}$  and on glass is investigated with DRS and compared to ellipsometry results followed by a general discussion concerning the observed effects during growth. In Sec. 5.6 complementary optical techniques are employed to address issues that are beyond the dielectric function and that are strongly related to the film properties under investigation. Raman spectroscopy on DIP films on  $\text{Si}_{\text{Ntve}}$  gives additional insight into the exciton-phonon coupling and fluorescence allows to study the vibrational properties of the electronic ground state. Finally, tip-enhanced Raman (TER) and photoluminescence (PL) measurements that were performed in collaboration with D. Zhang *et al.* (Meixner group, institute of physical and theoretical chemistry, Tübingen) are presented showing that grain boundaries in DIP films can be optically detected with a lateral resolution (17 – 40 nm) significantly below the diffraction limit.

## 5.1 DIP absorption spectra in solution

The normalized imaginary part  $\varepsilon_2$  of the dielectric function of DIP dissolved in acetone and in 1,2-dichlorobenzene is shown in Fig. 5.1.  $\varepsilon_2$  is determined from the measured optical density  $OD$  (see eq. 4.6 in Sec. 4.4) using the refractive index  $n_{\text{acetone}} = 1.36$  and  $n_{\text{dichlorobenzene}} = 1.55$ , respectively.

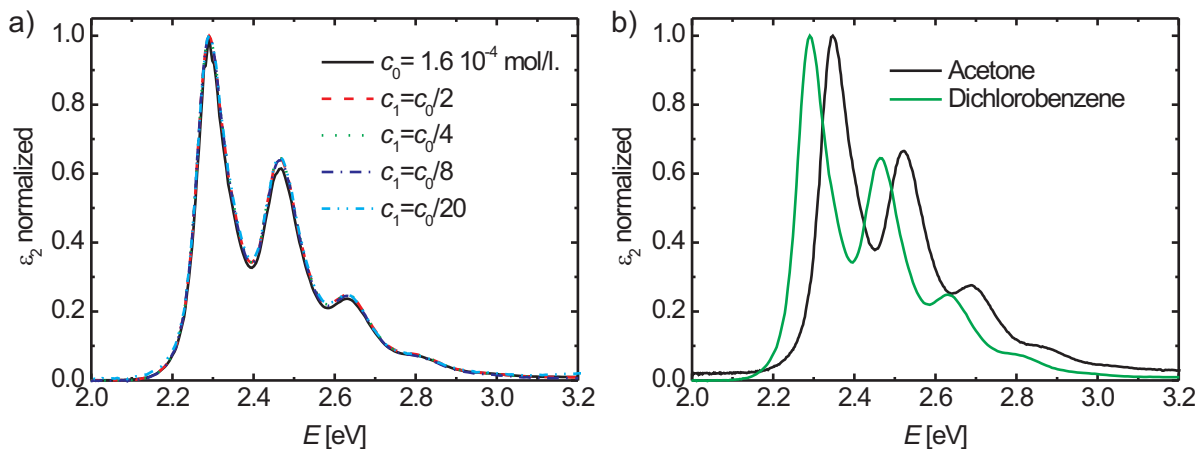


**Figure 5.1:** Normalized imaginary part of the dielectric function determined from transmission measurements on DIP in solution showing clearly a vibronic progression. a) DIP dissolved in 1,2-dichlorobenzene for various concentrations. b) Comparison: DIP dissolved in 1,2-dichlorobenzene (green) and dissolved in acetone (black).

Fig. 5.1a) shows the normalized spectra for DIP dissolved in 1,2-dichlorobenzene for various concentrations. It clearly demonstrates that the spectral shape does not depend on the concentration and non-linear effects do not play a role in this regime. The same result is obtained for DIP dissolved in acetone, which is not shown here. Therefore, the concentration, which is difficult to determine accurately, is not important to be known exactly for investigating the spectral shape and energy positions. The normalized spectra obtained for both solvents are plotted in one graph for comparison in Fig. 5.1b). In both cases the HOMO-LUMO transition can be observed, which is clearly associated with a vibronic progression (see Sec. 3.1.1.3). While the spectral shape agrees very well, a significant energy shift can be observed: The 0-0 transition is red-shifted by  $\Delta E = 57$  meV in case for 1,2-dichlorobenzene compared to acetone meaning that the solvent shift is bigger for 1,2-dichlorobenzene:  $\Delta E_D > \Delta E_A$ . This can be qualitatively understood in terms of the refractive index, which is related to the polarizability of the solvent giving rise to the solvent shift. It is smaller for acetone than for 1,2-dichlorobenzene.

Fig. 5.2 shows the experimentally determined and normalized  $\varepsilon_2$  for DIP dissolved a) in acetone and b) in 1,2-dichlorobenzene together with a Gaussian fit. The energy spacing and the intensities of the subbands can be fitted to a Poisson progression (see eq. 3.2)

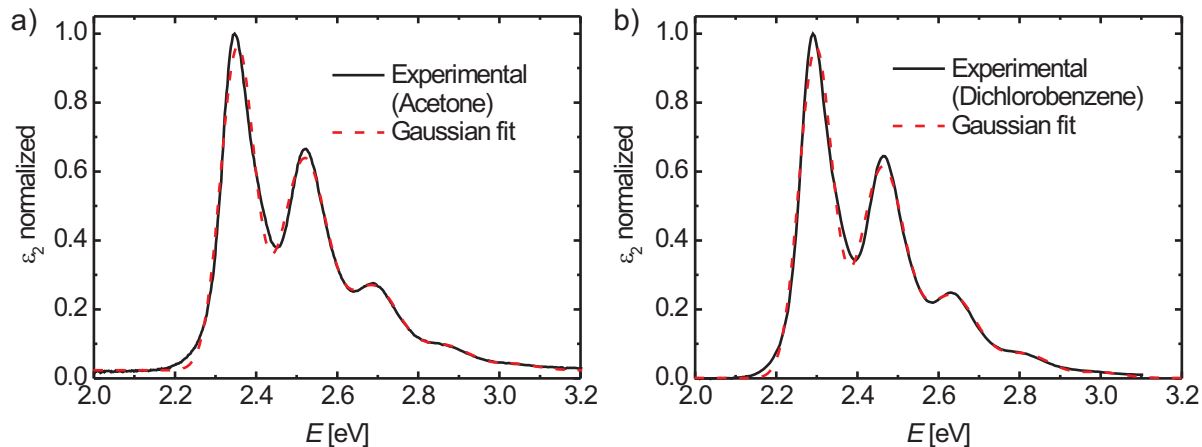


**Figure 5.2:** Fit to experimental data for a) acetone and b) 1,2-dichlorobenzene. The fit results agree well between both solvents. In both cases the fit function is a Poisson progression with a Huang-Rhys factor of  $S = 0.87$  for an effective mode at  $\hbar\omega_{\text{eff}} = 0.17$  eV with variable Gaussian broadenings.

with variable Gaussian broadening:

$$\varepsilon_2 = y_0 + A_0 B_0 \sum_{i=0}^{i=4} \frac{S^i}{i! B_i} e^{-\left(\frac{E-E_i}{B_i}\right)^2} \quad (5.1)$$

where  $y_0$  is some offset,  $A_i$  is the amplitude,  $B_i$  the width and  $E_i$  the energy position of the  $i$ th Gaussian oscillator, corresponding to the  $0-i$  transition, respectively. Due to the similar spectral shape of both spectra, the fit results agree very well between both solvents: The energy spacing is in both cases  $\hbar\omega_{\text{eff}} \approx 0.17$  eV and the effective Huang-Rhys factor is  $S_{\text{eff}} = 0.87$  ( $S_{\text{eff}} = 0.88$  for acetone), resulting in a reorganization energy of  $\lambda = S_{\text{eff}} \hbar\omega_{\text{eff}} = 0.15$  eV. Furthermore, the peak width broadens slightly from  $\sim 0.06$  eV for the  $0-0$  transition to  $\sim 0.08$  eV for the  $0-3$  transition.

The DIP solution spectrum resembles a nearly ideal example for a vibronic progression, which is typical for organic molecules. The Gaussian model is based on the following assumptions: First, the internuclear potential is in good approximation given by a Gaussian potential, where the higher harmonics have equal energy spacing. Second, only one vibrational mode contributes to the electronic vibrational coupling. Obviously, both assumptions are sufficiently fulfilled in case of DIP, although it is far from clear why only one vibrational mode should contribute. The increased broadening of the peaks at higher energy indicates that several modes are involved, which cannot be resolved spectroscopically. In the region of interest, resonant Raman spectra reveal four strongly elongated modes in the range between  $1285$  and  $1610$   $\text{cm}^{-1}$ , see Sec. 5.6.1. Due to their small energy spacing they result in an effective vibrational mode  $\omega_{\text{eff}}$  that is observed in the vibronic progression.

The energy position of the  $0-0$  transition is for acetone  $E_{00}^A = 2.35$  eV and for 1,2-

dichlorobenzene  $E_{00}^D = 2.297$  eV. It corresponds to a vertical transition energy of  $\langle E^A \rangle = E_{00}^A + \lambda = 2.50$  eV and  $\langle E^D \rangle = 2.297$  eV in the ground state geometry, respectively. The comparison theoretical calculations shows good agreement. According to table 3.2 the lowest calculated dipole-active  $1B_{1u}$  transition is  $\langle E \rangle = 2.347$  eV. Allowing for a typical solvent shift of  $-0.25$  eV this transition would be red-shifted to a vertical transition energy of about 2.1 eV in solution, which is  $\sim 0.2 - 0.4$  eV below the experimentally observed vertical transition energy, depending on the solvent. This is a rather good agreement compared to other theoretical calculations [60].

## 5.2 Substrate characterization

In order to investigate thin film properties, the substrate has to be characterized beforehand. It is known that the substrate morphology influences the film structure and morphology, thus also its optical properties. Furthermore, the ellipsometry and DRS data analysis is only possible, if the optical properties of the underlying substrates are known. Therefore, the most important substrate properties will be investigated in the following sections.

### 5.2.1 Morphology

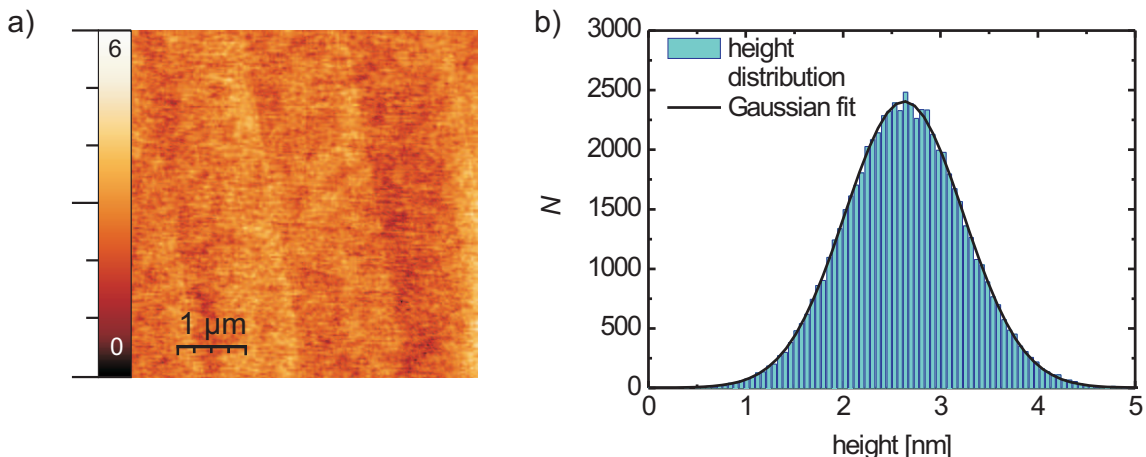


**Figure 5.3:** a)  $5 \times 5 \mu\text{m}^2$  AFM height scan of a SiNtve substrate showing a flat surface. The color scale on the left hand side correlates the color with the relative height measured in nanometer. b) Height distribution with Gaussian fit. The Gaussian width  $\sigma = 0.6$  nm defines the surface roughness, which is very small.

Fig. 5.3 a) shows a  $5 \times 5 \mu\text{m}^2$  AFM height scan of a SiNtve. The slant stripes from top to bottom are rather artefacts than real surface structures. Since the surface is very smooth, the inclination of the substrate as well as experimental error bars influence the picture,

which depends also on the flattening procedure that is used. Nevertheless, the local height variation is always  $\sim 0.3$  nm, which corresponds to the experimental noise limit of the AFM indicating that the surface is really smooth. Fig. 5.3b) shows the corresponding height distribution plotted for the  $5 \times 5 \mu\text{m}^2$  scan. The surface roughness is defined by the root mean square error of this distribution given by the Gaussian fit:  $\sigma = 0.6$  nm. This value can be regarded as the upper limit of the local surface roughness. The surface of thermal oxidized Si wafers is slightly rougher but very similar to the native oxide and is therefore not shown here.

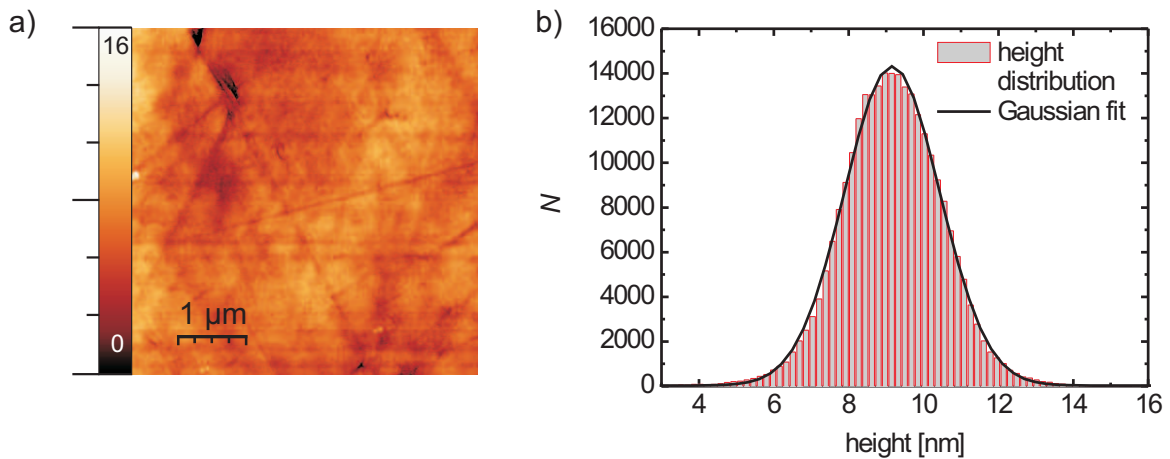


**Figure 5.4:** a)  $5 \times 5 \mu\text{m}^2$  AFM height scan of a quartz glass substrate revealing small scratches on the surface. The relative height is given by the color scale on the left hand side in nanometer. b) Height distribution with Gaussian fit giving  $\sigma = 1.3$  nm.

In contrast, the glass surface is less well-defined compared to the native oxide surface of a crystalline Si wafer (see Fig. 5.4a), where a  $5 \times 5 \mu\text{m}^2$  height scan is depicted. Scratches are visible that are typically 3 – 5 nm deep and some overall unevenness can be observed. Furthermore, in the middle of the picture on the left hand side a  $\sim 10$  nm high bump is visible, which is very likely not a dust particle, since one can find it on several positions of the cleaned sample. The height distribution plotted in Fig. 5.4b) shows a corresponding higher surface roughness:  $\sigma = 1.3$  nm.

## 5.2.2 Optical properties

The optical substrate properties are investigated by *ex-situ* spectroscopic ellipsometry measurements. Fig. 5.5 shows the ellipsometry angles  $\Psi$  and  $\Delta$  for three Si substrates. Two of them were oxidized for different periods of time  $\Delta t_{\text{Ox}}$ . For the shortest oxidation time ( $\Delta t_{\text{Ox}} \approx 1$  h) the well known band edge of Si is visible around 3.3 eV, compare data for the native oxide. With increasing oxidation time and thus with increasing thickness additional peaks arise, which are due to interference effects in the oxide layer giving access

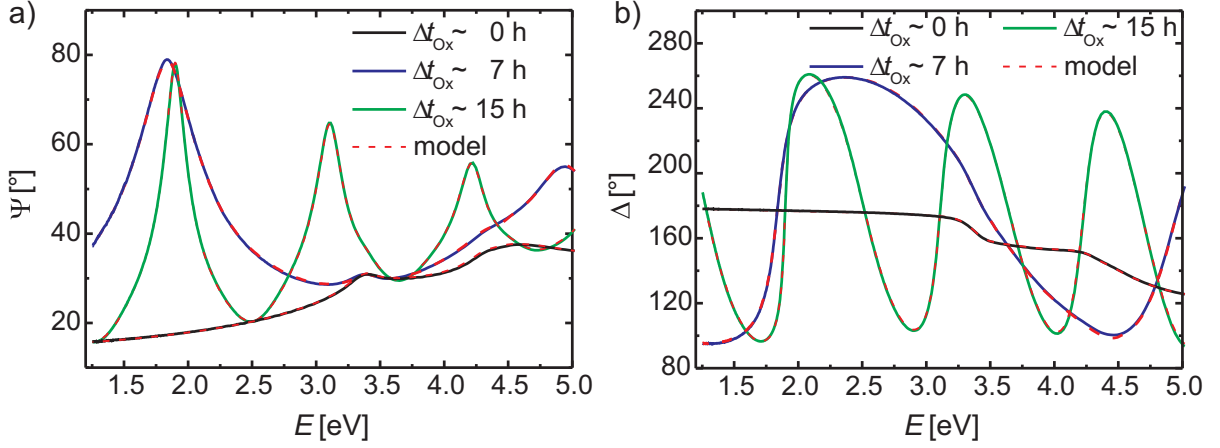


**Figure 5.5:** Ellipsometry angles a)  $\Psi$  and b)  $\Delta$  versus energy for three Si substrates with different oxide thicknesses at  $\alpha = 65^\circ$ . The layer model describes the data well and allows to determine the oxide thicknesses (see Tab. 5.1).

to the oxide thickness.

The result of the multiple sample analysis (performed at various angles of incidence) is plotted as dashed red curves, which describe the data very well. In addition to the different oxide thicknesses also the refractive index of the thermal oxide is determined using the Cauchy equation, see 3.13. The fit results are:  $A = 1.43$ ,  $B = -1.4510^{-3}$  and  $C = 1.9210^{-4}$ . The refractive index is modeled equally for all thermal oxides independently of the oxide thickness. The dielectric function of the native oxide, of the Si substrate and of an additional interfacial layer are also taken from the database [102]. The interfacial layer thickness is determined to be  $d_{\text{in}} = 1.47$  nm for both thermal oxides, whereas it is not used for native oxide. The fit results for all oxide thicknesses are summarized in Tab. 5.1. In case of the thermal oxides the thickness can vary over the whole Si-wafer by a few nanometers.

$\Delta t_{\text{Ox}}$ [h]	0	3	16
$d_{\text{ThOx}}$ [nm]	$1.91 \pm 0.02$	$146.7 \pm 0.2$	$428.7 \pm 0.5$

**Table 5.1:** Fit results for native and thermal oxide thickness obtained by different oxidation times.

The spectroscopic  $\Psi$ -data for different glass substrates measured at  $\alpha = 65^\circ$  are shown in Fig. 5.6. The back surface of the glass is treated in three different ways: first it is as smooth as the front surface (black curve), second it is roughened by scratching or grinding (blue line) and third it is covered with a translucent tape (green line).

While the blue and green curves are nearly identical, the black line deviates significantly below 4.5 eV where the quartz glass is transparent. This shows how the ellipsometry

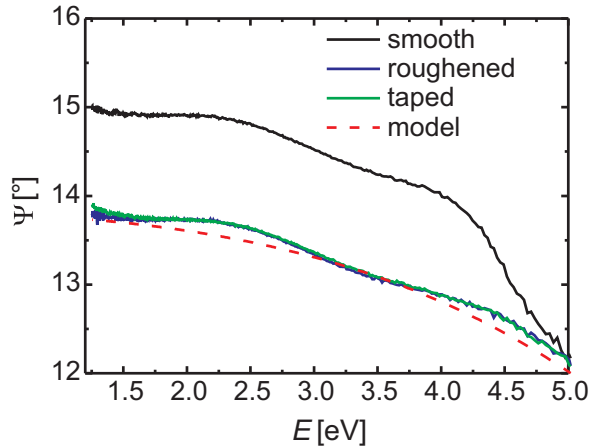


**Figure 5.6:** Spectroscopic  $\Psi$  data at  $\alpha = 65^\circ$  for glass substrates with differently treated back surfaces. Different methods are equally well suited for suppressing back reflections, whereas differences occur for a smooth back surface. The Cauchy model describes the data with suppressed back reflection well.

data are influenced by the back surface reflections, which can be suppressed equally well by roughening or taping, using the effect of index matching between the tape and the glass [103]. The model (dashed red curve) describes the data with suppressed back reflections well giving the following fit results for the Cauchy model:  $A = 1.49$ ,  $B = 2.4910^{-3}$ ,  $C = -9.7210^{-5}$  (see eq. 3.13). Additionally, an absorption tail is used with  $\alpha = 0.0075$ ,  $\beta = 0.0075$  and  $\gamma = 4$  eV (see eq. 3.14). In conclusion it is shown that different methods are equally well suited to suppress back reflections, which is necessary to model the data correctly. Roughening of the back surface has the advantage that also *in-situ* measurements can be performed whereas taping allows to measure also transmission measurements before ellipsometry measurements.

## 5.3 Structural and morphological film properties of DIP

### 5.3.1 X-ray data

#### 5.3.1.1 DIP grown at $T = 130^\circ\text{C}$ on Si substrates

Fig. 5.7a) shows a typical reflectivity (black line) and diffuse scan (green line) measured on DIP deposited at  $T = 130^\circ\text{C}$  on Si covered with native oxide. Three regions are labeled that show distinct features:

1. Total internal reflection edge below the critical angle  $\Theta_{\text{crit}}$
2. Kiessig oscillations
3. Bragg peak with Laue oscillations

While the total reflectivity edge is determined by the electron density of the materials (here: DIP,  $\text{SiO}_2$  and Si), the Kiessig oscillations are the result of constructive and de-

structive interferences between the reflected waves at the interfaces. The Bragg peak with its Laue oscillations is due to interference at the crystal lattice planes.

For further analysis the reflectivity scan has to be corrected by subtracting the diffuse scan to obtain the purely specularly reflected intensity. Furthermore, a so-called footprint correction has to be performed to take the limited size of the sample (typical length of 5-10 mm) for small angles of incidence into account. The effect is most pronounced in region 1 where the signal increases below  $\Theta_{\text{crit}}$  instead of staying constant.

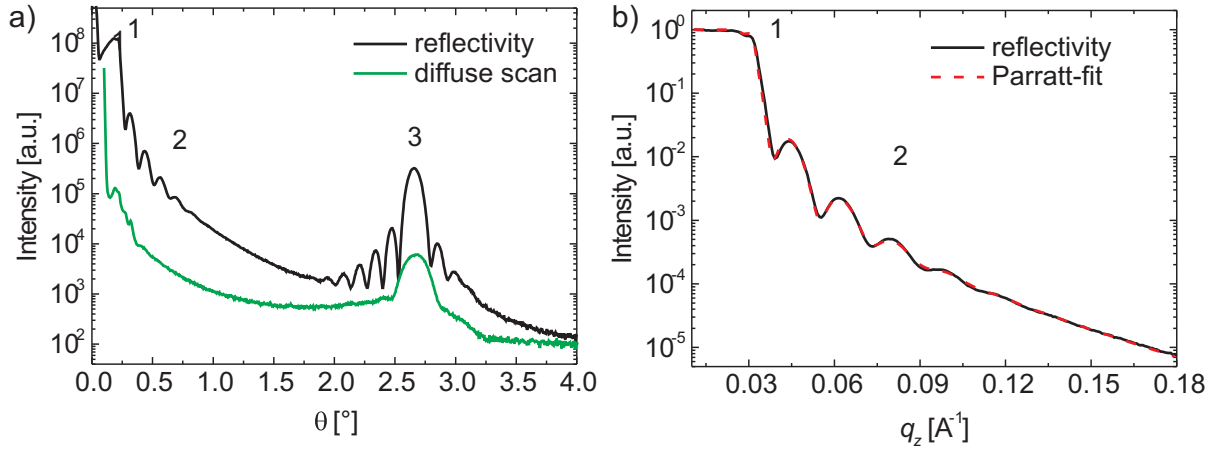


**Figure 5.7:** a) Reflectivity and diffuse scan versus angle of incidence  $\Theta$  for a DIP film grown at  $T = 130$  °C on  $\text{Si}_{\text{Ntve}}$ . Label 1 indicates the internal reflection edge, label 2 the Kiessig oscillations and label 3 the Bragg peak with Laue oscillations. b) Normalized and corrected reflectivity data versus scattering vector with Parratt-fit for the  $q$ -range smaller than the Bragg condition. The fit is based on  $\rho_{\text{Si}} = 0.71$   $e/\text{\AA}^3$ ,  $\rho_{\text{SiO}_2} = 0.70$   $e/\text{\AA}^3$  giving  $\rho_{\text{DIP}} = 0.4$   $e/\text{\AA}^3$ ,  $d_{\text{SiO}_2} = 1.8$  nm and  $d_{\text{DIP}} = 32$  nm.

The corrected normalized reflectivity data are plotted in Fig. 5.7b) versus the scattering vector  $q_z$  obtained from  $\Theta$  by eq. 4.9 corresponding to the angular range labeled with 1 and 2 in Fig. 5.7a). The intensity below  $\Theta_{\text{crit}}$  is now constant. Furthermore, the film thickness can be determined from the Kiessig oscillations. Neglecting refraction effects for small  $\Theta$ , the periodicity  $\Delta q_z$  in reciprocal space is directly related to  $d_{\text{film}}$ :

$$\Delta q_z = \frac{2\pi}{d_{\text{film}}} \quad (5.2)$$

For a more detailed analysis, including refraction effects, a Parratt-fit is performed (see Sec. 4.8) describing the reflectivity data in the plotted  $q_z$ -range very well (see red curve in Fig. 5.7b). The resulting film thickness is  $d_{\text{film}} = 32 \pm 0.2$  nm. Furthermore, the surface roughness can be obtained from the damping of the Kiessig oscillations (see eq. 4.10) to be  $\sigma = 2.3$  nm, showing that the film is very smooth. The electron density of the DIP film is determined to be  $\rho_{\text{DIP}} = 0.4$   $e/\text{\AA}^3$ .



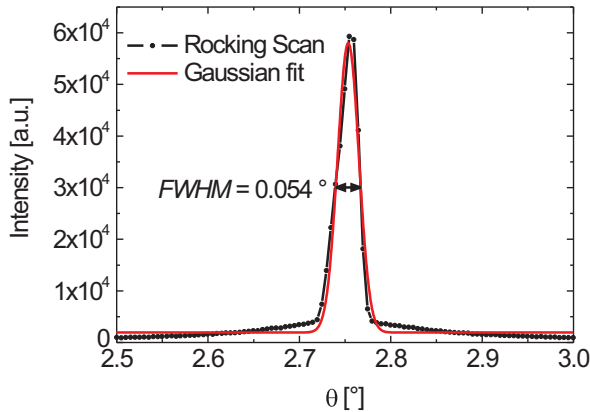


**Figure 5.8:** Rocking scan of the 32 nm thick DIP film grown on  $\text{Si}_{\text{Ntve}}$ . The  $FWHM = 0.054^\circ$  is determined from the Gaussian fit plotted as a red curve.

While the Kiessig oscillations are observable for any smooth thin film covering a substrate, the Bragg peak, labeled with 3 in Fig. 5.7a), occurs only for crystalline films allowing to determine their out-of-plane lattice spacing. According to eq. 4.11 the lattice spacing for the DIP film can be estimated from Fig. 5.7a) with  $\Theta_{\text{Bragg}} = 2.65^\circ$  to be  $d_z = 1.66$  nm, which agrees well with the literature [11]. For a more detailed analysis a fit has to be performed modeling the periodic electron density, which is beyond the scope of the present work. Here it is sufficient to conclude that the lattice spacing corresponds to the  $\sigma$ -phase with nearly upright standing molecules. Furthermore, the almost undamped oscillations around the Bragg reflections, called Laue oscillations, are evidence for a laterally homogeneous coherent thickness, i. e. a well-defined number of ordered ML's.

The high crystalline order is also documented by the rocking scan obtained for the same sample, which is plotted in Fig. 5.8. The Gaussian fit reveals a rocking width of  $FWHM = 0.054^\circ$  showing that orientational distribution along the surface normal is small.

### 5.3.1.2 Comparison between DIP on glass and on $\text{Si}_{\text{ThOx}}$

Fig. 5.9a) shows the reflectivity scan for a 22.3 nm thick DIP film grown on quartz glass at  $T = 130^\circ\text{C}$  (integration time  $t_{\text{int}} = 30$  s). For comparison the reflectivity scan of a simultaneously grown DIP film covering a Si substrate with 147 nm thick thermal oxide is shown in Fig. 5.9c), which gives similar results compared to DIP films on  $\text{Si}_{\text{Ntve}}$  (see Fig. 5.7). The main difference compared to native oxide are the additional Kiessig oscillations resulting from the thermal oxide layer. They are much smaller than those responsible for the DIP film due to the higher thickness of the thermal oxide.

The comparison between the films on glass and on thermal oxide reveals some differences: While the Bragg peak position is nearly identical for both films leading to a lattice spacing of  $d_z = 1.66$  nm, the Bragg intensity is smaller and the Laue oscillations are not visible for DIP on glass. This indicates that the coherent thickness for DIP on glass is small and no well ordered monolayers are formed. This lower order can also be observed by comparing the diffuse scan with the specular scan. For larger  $\Theta$  both intensities are equally high

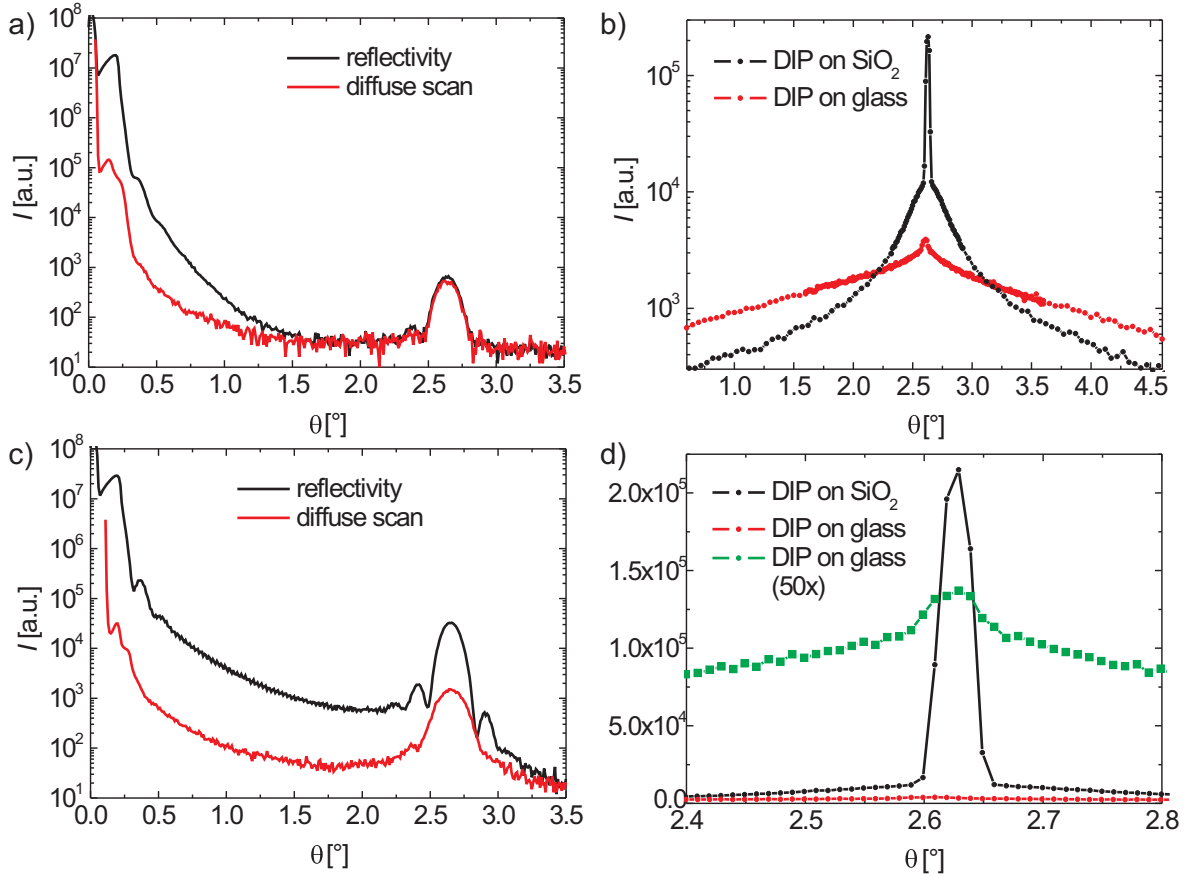


**Figure 5.9:** a) Reflectivity and diffuse scan for DIP grown at  $T = 130^\circ\text{C}$  on glass ( $t_{\text{int}} = 30\text{ s}$ ). c) Reflectivity and diffuse scan for DIP ( $t_{\text{int}} = 30\text{ s}$ ) grown simultaneously on  $\text{Si-ThO}_x$ . b) Rocking scan for both samples ( $t_{\text{int}} = 200\text{ s}$ ) plotted with a logarithmic scale allowing to see the big ‘foot’ under the rocking peak. d) Linearly plotted rocking scan. For better comparison the rocking scan for glass is additionally plotted 50 times enlarged. From a Gaussian fit the rocking width for DIP on Si with  $\text{FWHM} = 0.056^\circ$  and for DIP on glass with  $\text{FWHM} = 0.10^\circ$  is obtained.

showing that mainly scattered intensity is detected. Also the Kiessig oscillations are damped much stronger on glass than on thermal oxide revealing that the DIP film on glass is rougher. Therefore, the thickness can only be determined reliably on thermal oxide.

The rocking scans of both samples are plotted together in Fig. 5.9b) on a logarithmic scale and in Fig. 5.9d) on a linear scale. The integration time was for both samples  $t_{\text{int}} = 200\text{ s}$ . In accordance to the reflectivity scans the intensity of the rocking scan is more than one order of magnitude smaller for the glass sample compared to the thermal oxide sample. As can be seen on the logarithmic scale, both scans show on top of a broad ‘foot’ a small peak in the center. The width of this peak determines the mosaicity of the film, whereas the broad ‘background’ contains information about the height-height correlation. On the

linear scale this 'background' is in case of the thermal oxide sample very small while for the glass sample it is broader and of the same order of magnitude as the peak. For extracting more quantitative information about the height-height correlation a detailed analysis is necessary, which is beyond the scope of this work. Here it can be concluded that it differs significantly between DIP on Si and on glass, which is strongly related to the different roughness of both films.

Nevertheless, Gaussian fits of both central peaks reveal that the Bragg peak of the glass sample is less than twice as broad as the peak of the thermal oxide sample:  $FWHM_{\text{glass}} = 0.10^\circ$  and  $FWHM_{\text{Si}} = 0.056^\circ$ , thus the alignment of the molecules is comparable. Although, large mosaicity leads to a small Bragg peak, which is observed for the glass sample, a small Bragg peak does not necessarily mean large mosaicity. It mainly means that the molecules do not scatter coherently, which could also be due to roughness (e. g. linear displacement between molecules/crystals), which seems to be the case for the glass sample. Beside of roughness also an overall curvature of the glass surface could lead to a broad rocking scan, which cannot be excluded.

### 5.3.1.3 DIP films grown at $T = -105^\circ\text{C}$

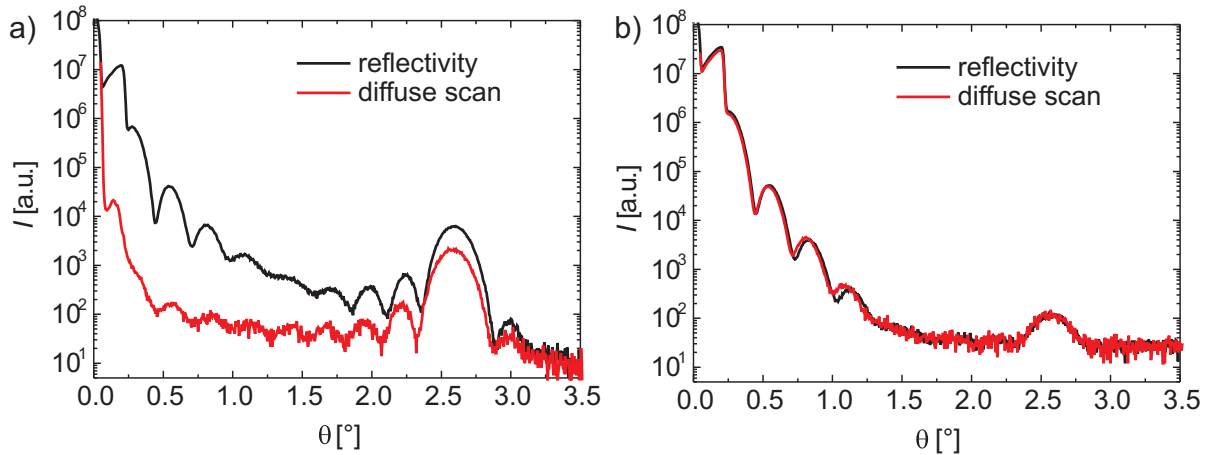


**Figure 5.10:** Reflectivity and diffuse scans of 16 nm thick DIP films grown simultaneously at  $T = -105^\circ\text{C}$  a) on  $\text{Si}_{\text{Ntve}}$  ( $t_{\text{int}} = 15\text{ s}$ ) and b) on glass ( $t_{\text{int}} = 20\text{ s}$ ). Note that the measurement is performed at room temperature.

Fig. 5.10a) shows the reflectivity and diffuse scan for a 16 nm thick DIP film grown at  $T = -105^\circ\text{C}$  (LT) on  $\text{Si}_{\text{Ntve}}$  and measured at RT. The pronounced Kiessig oscillations reveal that the film is very smooth. Furthermore, the  $\sigma$ -phase exists since the Bragg peak at  $\Theta = 2.61^\circ$  is visible, although it is by a factor of  $\sim 2.5$  smaller compared to a similar thick film grown at  $T = 130^\circ\text{C}$  (HT). This indicates less well ordering as it is expected for films grown at low temperature, since the smaller kinetic energy of the molecules limits their diffusion. Nevertheless, the structural order is still high and the rocking scan is only

slightly broadened ( $FWHM = 0.058^\circ$ ).

In case of DIP on glass the smoothening effect is even more pronounced (see Fig. 5.10b). While the Kiessig oscillations are nearly damped out for films grown at HT, they are clearly visible for films grown at LT. This allows to determine the film thickness to be  $d = 15.6$  nm, which agrees well to the thickness determined on Si ( $d = 16.1$  nm). Also for DIP on glass a small Bragg peak is visible but the intensity of the diffuse scan is nearly as large as the reflectivity scan. This indicates strong scattering due to structural disorder, which is supported by the smeared out rocking scan. Note that the X-ray measurements take place at RT. Real-time X-ray measurements during LT growth reveal that crystallization occurs upon heating post-growth [104]. Therefore, the crystalline structure is probably even less well-defined than expected from the presented *ex-situ* measurements.

## 5.3.2 AFM data

### 5.3.2.1 DIP films grown at $T = 130^\circ\text{C}$

Fig. 5.11 shows AFM height pictures for a 34 nm thick DIP film grown at  $130^\circ\text{C}$  simultaneously on  $\text{Si}_{\text{Ntve}}$  (a) and on quartz glass (b). In both cases molecular islands of the polycrystalline film with different sizes are visible: While on  $\text{Si}_{\text{Ntve}}$  the islands have a diameter of 200 – 400 nm, the island size on glass is with  $\sim 150$  nm significantly smaller. Also the island shapes differ. The color scale on the left hand side of both pictures correlates the plotted color with the corresponding height measured in nanometer, indicating slightly higher structures for DIP on glass compared to DIP on  $\text{Si}_{\text{Ntve}}$ .

For a more quantitative comparison, the height profile determined for the lines shown as black bars in the AFM pictures are plotted below. In case of DIP on  $\text{Si}_{\text{Ntve}}$  the smallest visible step height is 1.5 – 1.7 nm, corresponding to the height  $d_{\text{ML}}$  of one ML with essentially upright standing molecules [11,21]. The islands are shaped like terraces exhibiting step sizes that are multiples of  $d_{\text{ML}}$ . In contrast, those mono-molecular steps are not visible for DIP on glass, revealing rather round shaped islands. Furthermore, the height profiles indicate that the film on glass is rougher than on  $\text{Si}_{\text{Ntve}}$  since the maximal height difference is  $\sim 34$  nm on glass compared to  $\sim 21$  nm on  $\text{Si}_{\text{Ntve}}$ .

In order to obtain a statistically more significant statement, the roughness is analyzed for a  $10 \times 10 \mu\text{m}^2$  AFM scan of the same sample, which is not depicted here. Fig. 5.12 shows the corresponding height distribution for DIP a) on  $\text{Si}_{\text{Ntve}}$  and b) on quartz glass. The Gaussian fits (see black lines in Fig. 5.12) reveal that the DIP film on glass ( $\sigma = 5.5$  nm) is only slightly rougher than on  $\text{Si}_{\text{Ntve}}$  ( $\sigma = 4.8$  nm). Both films differ at  $d = 34$  nm rather in island size and shape than in roughness. This is also indicated by the fact that the height distribution for glass is well described by a Gaussian distribution, whereas for  $\text{Si}_{\text{Ntve}}$  deviations are observed. These deviations show that the relative height values are not only statistically distributed but some values are preferred. For smaller film thicknesses

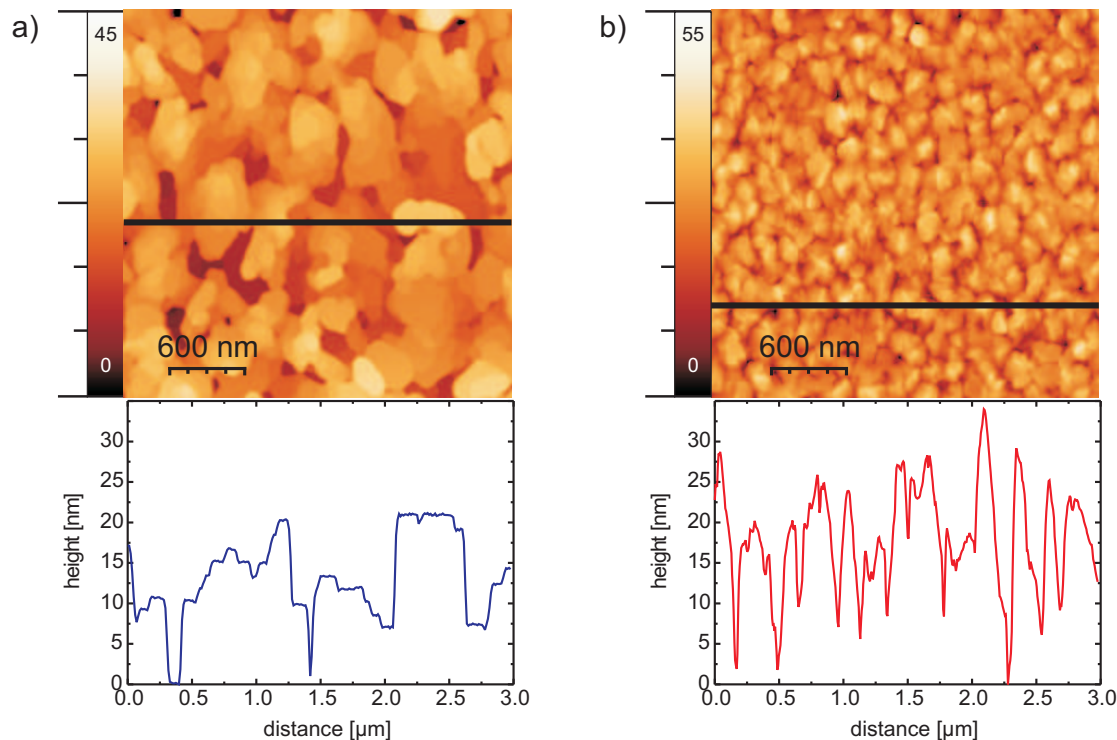


**Figure 5.11:**  $3 \times 3 \mu\text{m}^2$  AFM height pictures for a 34 nm thick DIP film grown at  $130^\circ\text{C}$  simultaneously on a) a  $\text{Si}_{\text{Ntve}}$  substrate and b) a quartz glass substrate. The color scale on the left hand side of both pictures correlates the plotted color with the corresponding height measured in nanometer. The lower part depicts the height profile corresponding to the line shown in the AFM picture above.

the deviations become more pronounced and the height distribution shows 2 – 3 peaks with a spacing of  $d_{\text{ML}}$ , revealing layer-by-layer growth. This is not observed for DIP films on glass, where the islands are roundly shaped without pronounced monolayer steps.

In Fig. 5.13  $5 \times 5 \mu\text{m}^2$  AFM height scans are plotted for DIP films with different thicknesses grown simultaneously on  $\text{Si}_{\text{Ntve}}$  (upper pictures: a-d) and on quartz glass (lower pictures: e-h). As discussed already for the thickest films at  $d = 34$  nm, the island size and shape differs significantly for all thicknesses between films grown on  $\text{Si}_{\text{Ntve}}$  and films grown on glass. For thinner films the differences become even more pronounced.

For DIP on  $\text{Si}_{\text{Ntve}}$  layer-by-layer growth can be observed below  $\sim 12$  nm: Picture a) and b) show large islands that differ in height by  $d_{\text{ML}} - 3d_{\text{ML}}$ . They correspond to ML's that are not yet completely filled with molecules. In picture c) at  $d = 12$  nm first smaller islands can be observed and the film starts to roughen. In contrast, DIP on glass forms already at  $d = 2$  nm small islands, see picture e), giving rise to significant roughness. The high bumps in the upper part of the picture are probably no molecules but rather glass 'bumps' observed also for bare glass substrates. Even at  $d = 12$  nm (g), the substrate is still visible and no closed ML has formed, which changes for thick films, see h).

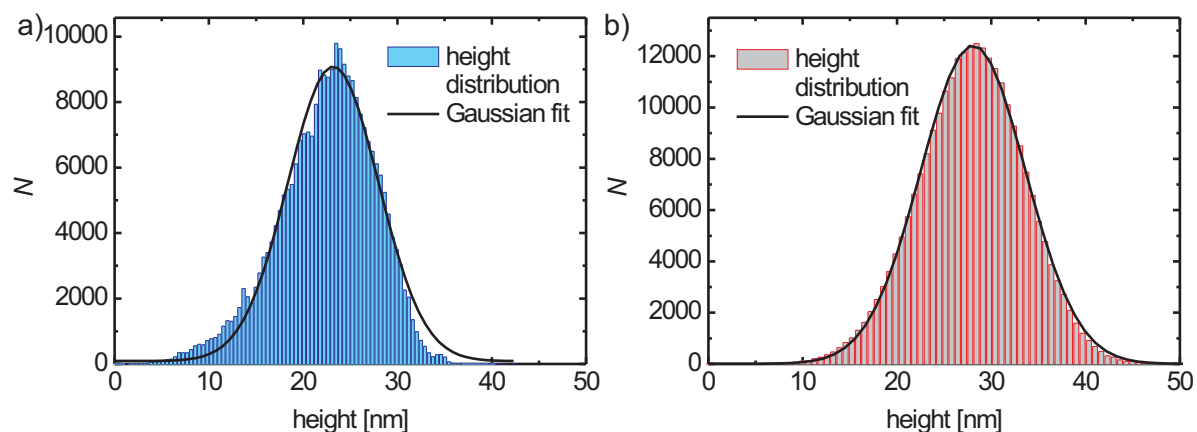


**Figure 5.12:** Height distribution determined from a  $10 \times 10 \mu\text{m}^2$  AFM scan for a 34 nm thick DIP film grown at  $130^\circ\text{C}$  simultaneously a) on  $\text{Si}_{\text{Ntve}}$  and b) on quartz glass. The black curves represent Gaussian fits for determining the roughness, which is given by the root mean square error of the height distribution: a)  $\sigma_{\text{DIP-Si}} = 4.8 \text{ nm}$ , b)  $\sigma_{\text{DIP-gl}} = 5.5 \text{ nm}$ .

While the roughness of DIP films on  $\text{Si}_{\text{Ntve}}$  increases with thickness, it does not change as significantly for glass, since it is very rough from the beginning. Instead, the 'relative roughness' compared to the film thickness, rather decreases with thickness for DIP on

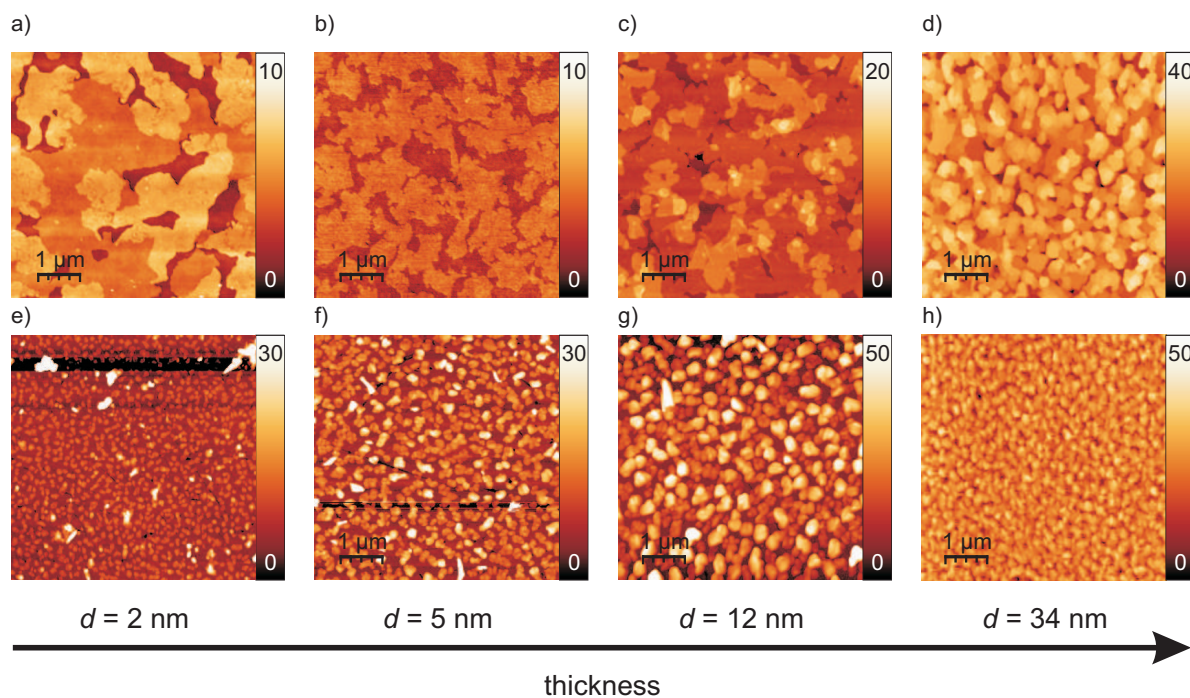


**Figure 5.13:** Thickness dependent  $5 \times 5 \mu\text{m}^2$  AFM height scans for DIP grown simultaneously on  $\text{Si}_{\text{Ntve}}$  (upper part) and on glass (lower part) at  $T = 130^\circ\text{C}$ .

glass. It is important to note that the AFM measurements are performed *ex-situ* and the influence of air and water may affect the morphology. Nevertheless, the results obtained for DIP on  $\text{Si}_{\text{Ntve}}$  agree well with *in-situ* measurements [21] and, therefore, strong differences are also not expected for DIP on glass.

### 5.3.2.2 DIP films grown at $T = -105\text{ }^\circ\text{C}$

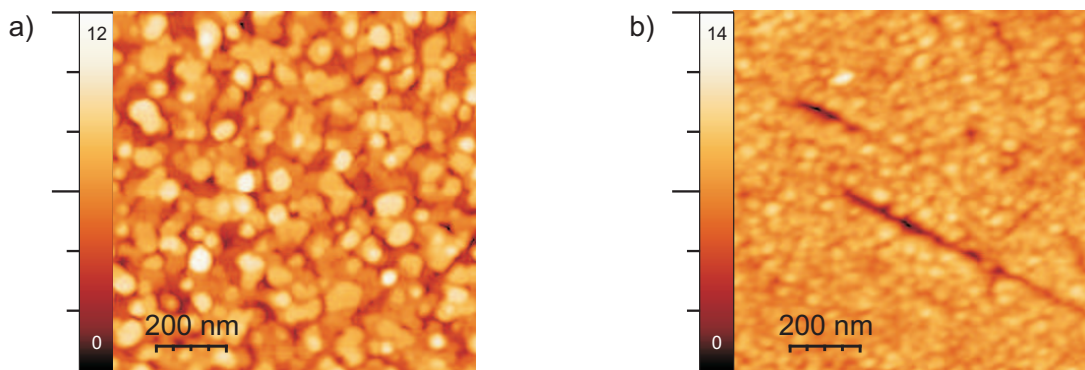


**Figure 5.14:**  $1 \times 1\ \mu\text{m}^2$  AFM height scans for 20 nm thick DIP films grown simultaneously at  $T = -105\text{ }^\circ\text{C}$  a) on a Si-substrate, b) on a glass substrate. The roughness is significantly decreased compared to HT growth: a)  $\sigma_{\text{DIP-Si}} = 1.4\text{ nm}$ , b)  $\sigma_{\text{DIP-gl}} = 0.86\text{ nm}$ .

DIP films grown on both substrates at low temperature (LT,  $T = -105\text{ }^\circ\text{C}$ ) are shown in Fig. 5.14. They are clearly smoother compared to films grown at high temperature (HT,  $T = 130\text{ }^\circ\text{C}$ ), which is in accordance to the X-ray results. With  $\sigma_{\text{DIP-gl}} = 0.86\text{ nm}$ , which is lower than the roughness of the bare glass substrate, the film on glass is even smoother than the film on  $\text{Si}_{\text{Ntve}}$ ,  $\sigma_{\text{DIP-Si}} = 1.4\text{ nm}$ . Nevertheless, two scratches are visible for DIP on glass, which stem most likely from the glass substrate itself. Furthermore, the islands are considerably smaller ( $\varnothing \approx 150\text{ nm}$ ) and do not show ML steps on  $\text{Si}_{\text{Ntve}}$ , indicating low order. The islands on glass have a diameter of  $\varnothing \approx 50\text{ nm}$ . Since the measurements are performed *ex-situ* at RT, differences between the film morphology at RT after growth and at LT during growth cannot be excluded. Nevertheless, if there are differences it is expected that the films are even smoother at LT during growth since the heating up to RT rather leads to crystallization of the film giving rise to higher roughness.

## 5.4 Static anisotropic dielectric function of DIP grown on $\text{SiO}_2$

This section presents the analysis of spectroscopic ellipsometry data that are measured *ex-situ* after film growth. Furthermore, the results of the obtained dielectric function will be discussed, which serve as a reference for real-time studies, where the change of the

optical properties during film growth is investigated (see Sec. 5.5). This section is limited to DIP thin films, but a similar analysis was done for PEN on SiO<sub>2</sub> by A. Hinderhofer in the framework of his diploma thesis [19]. The results for PEN are shortly introduced in Sec. 5.5.3 where the PEN real-time measurements are shown.

Since only a fixed film thickness per sample can be analyzed *ex-situ*, it is chosen to be  $d \approx 30$  nm for achieving the highest possible sensitivity for anisotropy while keeping roughness effects small. Both effects increase with film thickness. The main analysis focuses on the energy range  $E = 1.4 - 3$  eV where the HOMO-LUMO transition of DIP takes place. Since also data up to 5 eV are available and the data analysis is very similar compared to the lower energy region, they are presented as well giving insight into higher transitions.

### 5.4.1 Data analysis for uniaxial thin films

Since the approach for the data analysis is crucial and a substantial part in ellipsometry studies, the procedures and concepts will be described in some detail. The data analysis presented here is based on data obtained for DIP grown at  $T = 130$  °C on Si substrates covered with oxide. Nevertheless, it applies in general to uniaxial anisotropic organic thin films on SiO<sub>2</sub> and it is not limited to DIP. It was e. g. applied to PEN and perfluoropentacene (PFP) films on SiO<sub>2</sub> [20].

#### 5.4.1.1 Uniaxial anisotropy

Employing uniaxial symmetry obviously follows directly from the structural properties presented in Sec. 5.3.1 for DIP grown on SiO<sub>2</sub> at  $T = 130$  °C as long as the light spot is much larger than the island size, which is safely fulfilled. Spectroscopic ellipsometry data support the assumption that the film is uniaxial anisotropic with the optical axis oriented parallel to the surface normal (see Fig. 3.5):

1. The measured off-diagonal elements of the matrix describing the sample (see Sec. 3.2.2), are essentially zero, indicating that one of the optical axes has to be parallel to the surface normal.
2. The azimuthal orientation of the sample does not influence the ellipsometry data, indicating an in-plane isotropy.
3. An isotropic fit does not describe the ellipsometry data correctly.

The last point is illustrated in Fig. 5.15, where the experimental  $\Psi$ -data of DIP on thermal oxide for three different angles of incidence are plotted. The dashed black curves represent an isotropic fit, which was performed at  $\alpha = 65$  °. While this isotropic fit describes the data well at  $\alpha = 65$  °, coinciding nearly with them, differences are visible above 2.5 eV



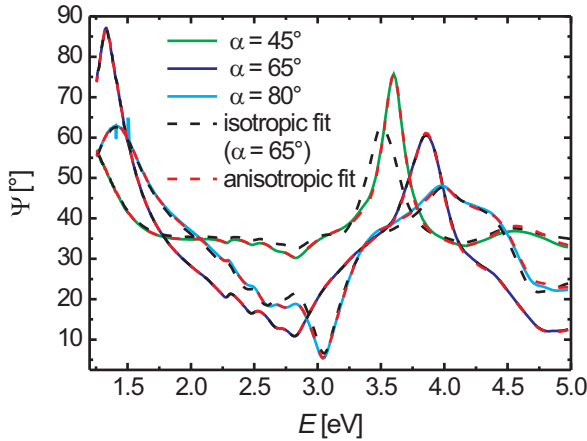


**Figure 5.15:** Ellipsometry angle  $\Psi$  measured for DIP on thermal oxide for different angles of incidence (AOI). The isotropic fit (dashed black lines), obtained for  $\alpha = 65^\circ$ , differs in some energy regions from the data at other AOI, whereas the anisotropic multiple sample fit (dashed red lines) agrees for all AOI very well.

at  $\alpha = 45^\circ$ ,  $80^\circ$ . The fact that the isotropic model describes the experimental data perfectly at  $\alpha = 65^\circ$  shows that ellipsometry data measured at one angle of incidence and on one substrate are not sufficient to determine the uniaxial anisotropy. Additional information such as several angles of incidence or different substrates are necessary. On the contrary, the data are described well for all angles of incidence by the dashed red curves in Fig. 5.15 b) representing a uniaxial model, which will be discussed in the next paragraph.

There exist several possibilities to determine uniaxial anisotropy. Obviously, the set of four parameters (real and imaginary part for the in-plane and the out-of-plane component of the dielectric function) cannot be determined by two measured parameters  $\Psi$  and  $\Delta$  per wavelength/energy. Measuring at several AOI's does not necessarily solve this problem: From the literature it is known that variable angle spectroscopic ellipsometry (VASE) is not very sensitive to uniaxial anisotropy [105, 106, 107]. This is mainly due to the fact that the incident beam of light is refracted at the ambient-film interface leading to a much smaller angle of incidence  $\alpha_{\text{in}}$  inside the film compared to  $\alpha_{\text{out}}$  outside the film (see Fig. 5.16). Therefore,  $\alpha_{\text{in}}$  does not vary significantly when changing  $\alpha_{\text{out}}$  and mainly the in-plane component of the uniaxial film is probed for different  $\alpha_{\text{out}}$ .

Following possibilities for determining the uniaxial anisotropy were proposed in the literature:

1. One possibility to decorrelate the components of the anisotropic dielectric function is to fit the dielectric function of several films with different thicknesses simultaneously assuming the same dielectric function as well as the same morphology for different thicknesses [108, 109].
2. In order to avoid strong refraction at the ambient-film interface, immersion ellipsometry can be applied using an appropriate ambient medium [110]. The disadvantage of this technique is that the film needs to be in close contact to the ambient medium by using e. g. optical gels that may change or even destroy the film and additional

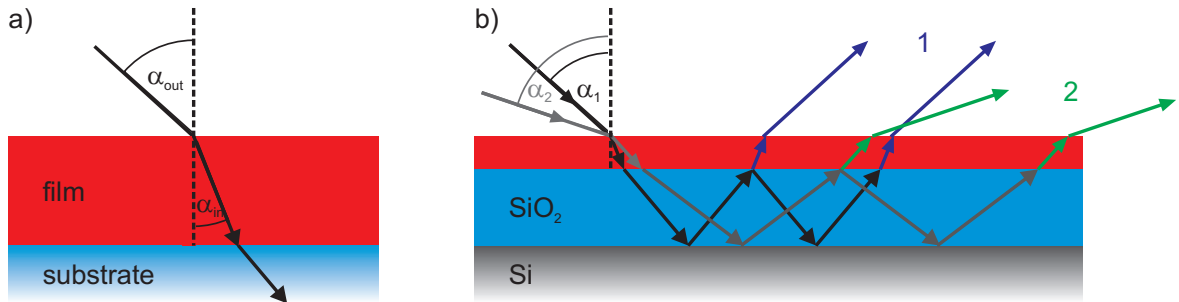


**Figure 5.16:** a) Refraction at the ambient-film interface with corresponding angle of incidence  $\alpha_{in}$  inside the film. b) Principle of interference enhancement with thermal oxide: Inter alia the light is reflected at the SiO<sub>2</sub> interfaces. Depending on the AOI different wavelengths interfere constructively, e. g. blue light for  $\alpha_1$  or green light for  $\alpha_2$ , giving rise to different optical properties of the substrate.

unknown parameters are introduced.

3. Instead of changing the ambient also the optical properties of the substrate can be varied to determine the uniaxial anisotropy. Since the dielectric function for films on different substrates has to be assumed to be equal, the chemical and morphological properties of the substrates need to be similar. Otherwise, it is well known that different substrates lead to different film properties.
4. The combination of transmission and reflection ellipsometry allows also to extract the real and imaginary parts of the in-plane and out-of-plane dielectric function [111]. The advantage is that this can be done on the same substrate. The disadvantage is that the substrate has to be obviously transparent, which is not the case for Si covered with native oxide.
5. In order to avoid assumptions concerning the optical properties of films on different substrates, it is proposed to use a single thick thermal oxide substrate [106]. Interference effects in the thick oxide layer lead to optical substrate properties depending on the angle of incidence as Fig. 5.16 b) illustrates. Since the optical path of the light reflected at the oxide interfaces changes with the angle of incidence, constructive interference occurs at different wavelengths for different AOI's, thus leading to changed optical properties of the substrate. The major drawback of this method is the potentially strong influence of uncertainties in the optical functions of the thermal oxide, possibly given by inhomogeneities of the oxide properties.

Method 1 is not considered in this thesis, since the assumption of thickness independent optical properties is typically not fulfilled and instead optical changes during film growth are subject of investigation. Also method 2 is not tested because of the possibly strong influence of the ambient medium. Since method 4 is based on a transparent substrate it is also not suitable to study DIP on Si covered with SiO<sub>2</sub>, although thin films on glass

could be investigated with it. Instead, method 3 and 5 will be applied to extract the uniaxial anisotropy. In case of  $\text{Si}_{\text{Ntve}}$ , quartz glass is chosen as an equivalent substrate with different optical properties for fitting DIP on two substrates simultaneously. Still, due to impurities the chemical properties of quartz glass may differ slightly compared to those of the  $\text{Si}_{\text{Ntve}}$  or  $\text{Si}_{\text{ThOx}}$  surface. AFM-measurements show that the glass surface is rougher resulting in rougher organic films (see Sec. 5.3.2). This is also confirmed by X-ray data, which, nevertheless, also show that the film crystal structure can be considered as similar. Therefore, it is a good approximation to assume the optical properties of both films on glass and on  $\text{Si}_{\text{Ntve}}$  ( $\text{Si}_{\text{ThOx}}$ ) as identical. Possible influences of roughness will be discussed in Sec. 5.5.2. The interference enhancement (method 5) seems to be even better suited since DIP on thermal oxide does not differ significantly compared to DIP on  $\text{Si}_{\text{Ntve}}$ . It is therefore also tested and compared to results obtained with method 3.

#### 5.4.1.2 Thickness determination

The separation of the film thickness and the dielectric function of the film is a classical ellipsometry problem [112]. On a wavelength-by-wavelength basis this separation is in principle impossible on opaque films since there are two measured quantities ( $\Psi$  and  $\Delta$ ) but three unknown parameters: the film thickness  $d$  and the real and imaginary part of the dielectric function ( $\varepsilon_1$  and  $\varepsilon_2$  respectively). This problem can be solved by using an analytical function, namely the Cauchy equation in a transparent range (see eq. 3.13 in Sec. 3.2.1) for describing the dielectric function and thus for reducing the number of fit parameters. If the films are very thin ( $\lesssim 10$  nm) this separation is virtually impossible because of the high correlation between  $\varepsilon_1$  and  $d$ , which can be shown mathematically in thin film linear expansions of the ellipsometric equations [113]. Also anisotropy is correlated with the film thickness and the analysis of the ellipsometry data alone does not give unambiguous results.

Therefore, the DIP film thickness on  $\text{SiO}_2$  (native or thermal oxide) is determined by X-ray reflectometry (see Sec. 5.3.1). In case of thermal oxide an anisotropic Cauchy model could be applied but already small deviations of the thermal oxide's dielectric function and thickness lead to strong deviations in the DIP film thickness, which therefore cannot be determined accurately. Moreover, it is essentially impossible to determine the film thickness by ellipsometry on top of a glass substrate due to similar refractive indices [114]. Therefore, the DIP thickness on glass is assumed to be the same as on  $\text{Si}_{\text{Ntve}}$  ( $\text{Si}_{\text{ThOx}}$ ). Once the dielectric function with its anisotropy is properly determined for a specific e. g. DIP film, it is of course possible to use it for determining the thickness of other DIP films with ellipsometry.

#### 5.4.2 DIP data analysis and fit results

In this section single sample analysis is compared to multiple sample analysis where two films on different substrates are fitted simultaneously assuming the same dielectric func-

tion of the films. In order to make sure that this assumption is best possible fulfilled only those films are analyzed together, which were grown simultaneously on both substrates. Four different fits are performed in order to extract the uniaxial optical constants of the DIP film on SiO<sub>2</sub>. Two single sample fits, referred to as ‘Si<sub>Ntve</sub> fit’ or ‘Si<sub>ThOx</sub> fit’, are performed using the ellipsometry data of either a DIP-Si<sub>Ntve</sub> or a DIP-Si<sub>ThOx</sub> film, respectively. Fitting the DIP-Si<sub>Ntve</sub> and the DIP-Si<sub>ThOx</sub> film simultaneously is referred to as ‘Si<sub>Ntve</sub> + Si<sub>ThOx</sub> fit’, while fitting the DIP-Si<sub>Ntve</sub> film and the DIP-Glass film together is referred to as ‘Si<sub>Ntve</sub> + Glass fit’. If nothing else is stated the thermal oxide is 146 nm thick. First, point-by-points fits are performed, for further analysis a Gaussian oscillator model is fitted to the data.

#### 5.4.2.1 Point-by-point fit

The dielectric functions obtained from the ‘Si<sub>ThOx</sub> fit’ and from both multiple sample fits are plotted in Fig. 5.17 in the complete available energy range  $E = 1.25 - 5$  eV. Although the ‘Si<sub>Ntve</sub> fit’ describes the ellipsometry data as well, it is not plotted here since it does not give reasonable results, e. g. the Kramers Kronig relation is violated and unphysical jumps occur in the dielectric function. This indicates that on native oxide the uniaxial anisotropy cannot be determined by VASE. The real part  $\varepsilon_1$  is shown in Fig. 5.17 a) and c) and the imaginary part  $\varepsilon_2$  is plotted in Fig. 5.17 b) and d). Due to the pronounced anisotropy, the in-plane component is nearly one order of magnitude smaller than the out-of-plane component. For a better comparison of the lineshapes it is plotted in the lower panels c) and d) separately.

All three fits lead to a similar anisotropy and dielectric function, although there appear some differences. The biggest deviation is visible above 3.5 eV in the out-of-plane component, where higher transitions take place. Their energy positions and amplitudes vary significantly between all three fits. Interestingly the results for the in-plane component agree very well in this energy range whereas mainly differences in absolute values appear below 3 eV. The overall spectral shape agrees in both components for all fit results below 3 eV well.

In order to distinguish the best fit for describing the DIP film usually the mean square error (MSE) is compared, which is defined as follows:

$$\text{MSE} = \sqrt{\frac{1}{2N - M} \chi^2} \quad (5.3)$$

with

$$\chi^2 = \sum_{i=1}^N \left[ \left( \frac{\Psi_i^{\text{model}} - \Psi_i^{\text{exp}}}{\sigma_{\Psi,i}^{\text{exp}}} \right)^2 + \left( \frac{\Delta_i^{\text{model}} - \Delta_i^{\text{exp}}}{\sigma_{\Delta,i}^{\text{exp}}} \right)^2 \right] \quad (5.4)$$

$N$  is the number of measured  $(\Psi, \Delta)$ -pairs,  $M$  is the number of fit parameters and  $\sigma$  corresponds to the standard deviation of  $\Psi$  or  $\Delta$ . If a model describes the data perfectly

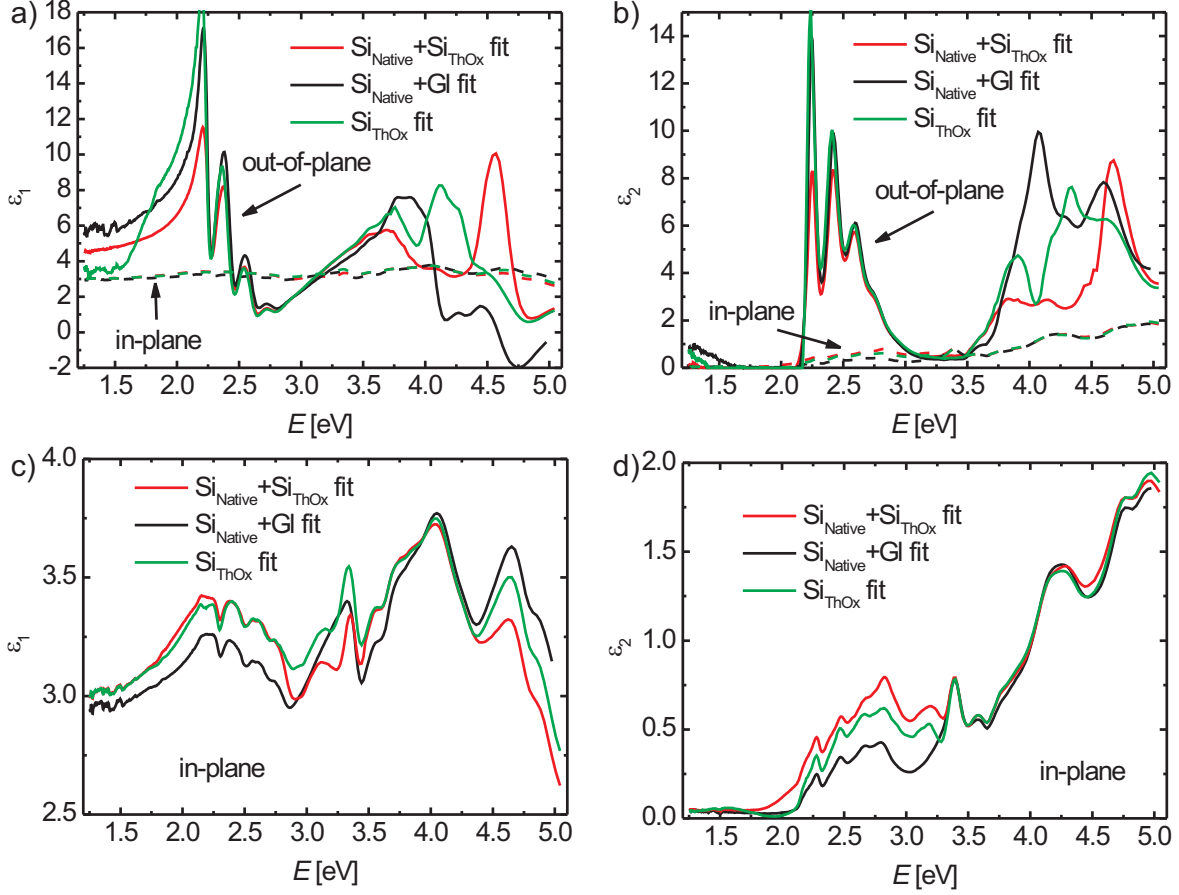


**Figure 5.17:** Fit results plotted for different point-by-point fit procedures (see text): a) real-part of the dielectric function, b) imaginary-part of the dielectric function. The solid curves represent the out-of-plane component and the dashed curves the in-plane component. To better compare the line shape, the in-plane component is additionally plotted in the lower panels separately for c) the real and d) the imaginary part.

$MSE = 0$ . In case of a point-by-point fit the MSE is calculated for each energy with  $N = 2 \cdot n_0$ , where  $n_0$  is the number of measured angles of incidence, and  $M = 4$ . The energy dependent MSE for all four fits is presented in Fig. 5.18.

From these plots, mainly the fit quality of a single fit between different energy regions can be compared, showing e. g. that the ‘ $\text{Si}_{\text{Native}} + \text{Si}_{\text{ThOx}}$  fit’ describes the data at low energies better than at high energies. Nevertheless, it is problematic to compare absolute MSE-values between different measurements due to systematic errors [115]. Strictly, it makes only sense to compare MSE-values of different models applied to the same data set, which is not given for the cases shown here, e. g. the ‘ $\text{Si}_{\text{Native}}$  fit’ is performed on native  $\text{SiO}_2$  whereas the data set used for the ‘ $\text{Si}_{\text{Native}} + \text{Si}_{\text{ThOx}}$  fit’ additionally includes thermal  $\text{SiO}_2$ . Therefore, it cannot be concluded from Fig. 5.18 that the ‘ $\text{Si}_{\text{Native}}$  fit’ works best although

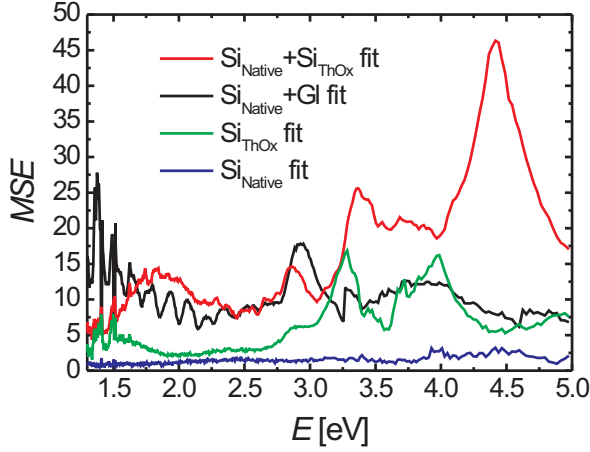


**Figure 5.18:** Energy dependent mean square error (MSE) obtained for different point-by-point fits showing the fit quality at different energies. Note that the fits are performed on different data sets and the absolute MSE values are not directly comparable.

its MSE values are smallest. It rather indicates limited sensitivity of the native oxide data to uniaxial anisotropy. The fit parameters are correlated, giving not unambiguous results. In contrast, the multiple sample analysis, using either an additional thermal oxide or a glass substrate decorrelate the fit parameters, which can be demonstrated by comparing the correlation matrix for the different fits. The correlation coefficient  $S_{ij}$  is calculated from the elements of the covariance matrix  $C$  [115, 79]:

$$S_{ij} = \frac{C_{ji}}{\sqrt{C_{jj}C_{ii}}} \quad (5.5)$$

where  $i$  and  $j$  label different fit parameters. For  $|S_{ij}| = 1$  the fit parameters are highly correlated and cannot be determined separately whereas for  $|S_{ij}| = 0$  they are completely independent.

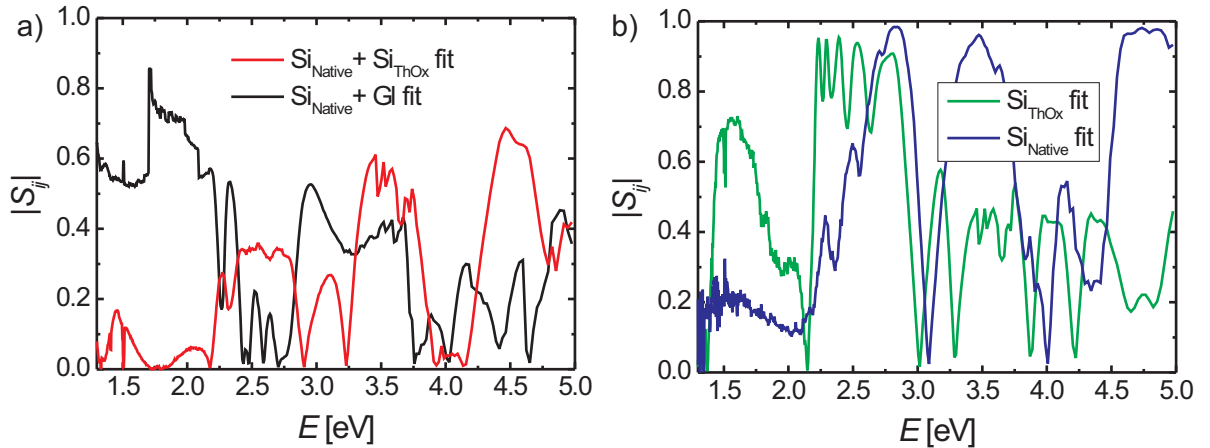


**Figure 5.19:** Energy dependent correlation coefficient  $|S_{i,j}|$  between the in-plane and the out-of-plane component of  $\epsilon_2$  for (a) multiple sample analysis, b) single sample analysis.

Fig. 5.19 a) and b) show the correlation between the in-plane and the out-of-plane component of  $\varepsilon_2$  for all four fit procedures. The other correlation coefficients are not depicted since they show similar behavior. It is clearly visible that the fit parameters are less correlated in nearly the whole energy range for the multiple sample fits (a) compared to the single sample fits (b). Only the 'Si<sub>Ntve</sub> + Gl fit' shows higher correlations below 2 eV, where the DIP film is transparent. Interestingly, in the range of  $E = 2 - 3$  eV the correlations for the 'Si<sub>ThOx</sub> fit' are bigger than those for the 'Si<sub>Ntve</sub> fit' indicating that for smaller energies the interference enhancement does not work as well when using a 146 nm thick thermal oxide. If Si<sub>ThOx</sub> with 426 nm thickness is employed the correlations vanish also in the low energy region. Nevertheless, the 146 nm thick Si<sub>ThOx</sub> seems to be better suited for the data analysis because the fit results are influenced by inhomogeneities in Si<sub>ThOx</sub> like index grading or surface roughness, which are less pronounced in the thinner thermal oxide.

Since both multiple sample fits show low fit parameter correlations and similar fit results, they are best suited to determine the dielectric function of uniaxial organic thin films. Differences between them are likely due to systematic errors such as different film morphologies between DIP on glass and on Si<sub>Ntve</sub>, which are observed by AFM measurements (see Sec. 5.3.2). Additional EMA layers and fitting at slightly different thicknesses does not change the 'Si<sub>Ntve</sub> + Gl fit' results qualitatively. Still, scattering effects are not included in the model, which are expected to be most pronounced above 3 eV, where the wavelength ( $\lambda < 400$  nm) resembles the length scale of the islands. Therefore, the significant differences between the fit results above 3 eV in the out-of-plane component can probably be ascribed to scattering or uncertainties of the film thickness. In conclusion, the error bar of the out-of-plane dielectric function, i. e. its line shape, its absolute intensity and the energy position of the higher transitions has to be regarded as significantly larger compared to the results obtained below 3 eV. In contrast, the in-plane component seems to be much less uncertain, which agrees to the fact that ellipsometry is more sensitive to this component.

Since the film morphology between DIP on Si<sub>Ntve</sub> and DIP on Si<sub>ThOx</sub> agrees very well, the 'Si<sub>Ntve</sub> + Si<sub>ThOx</sub> fit' gives the most reliable result for the dielectric function of DIP thin films on SiO<sub>2</sub>. Therefore, the following analysis will be based on the 'Si<sub>Ntve</sub> + Si<sub>ThOx</sub> fit' results, which will be limited to the low energy range ( $E < 3$  eV), where the HOMO-LUMO transition takes place.

#### 5.4.2.2 Gaussian oscillator fit

To further investigate the DIP dielectric function in the low energy range ( $E < 3$  eV), where the HOMO-LUMO transition takes place, the Si<sub>Ntve</sub> and Si<sub>ThOx</sub> ellipsometry data are fitted by a Gaussian oscillator model based on the point-by-point 'Si<sub>Ntve</sub> + Si<sub>ThOx</sub> fit' results. The corresponding dielectric functions for both, the point-by-point fit and the Gaussian oscillator fit are presented in Fig. 5.20 showing good agreement for the real and imaginary part. Since the Gaussian oscillator model is Kramers Kronig consistent

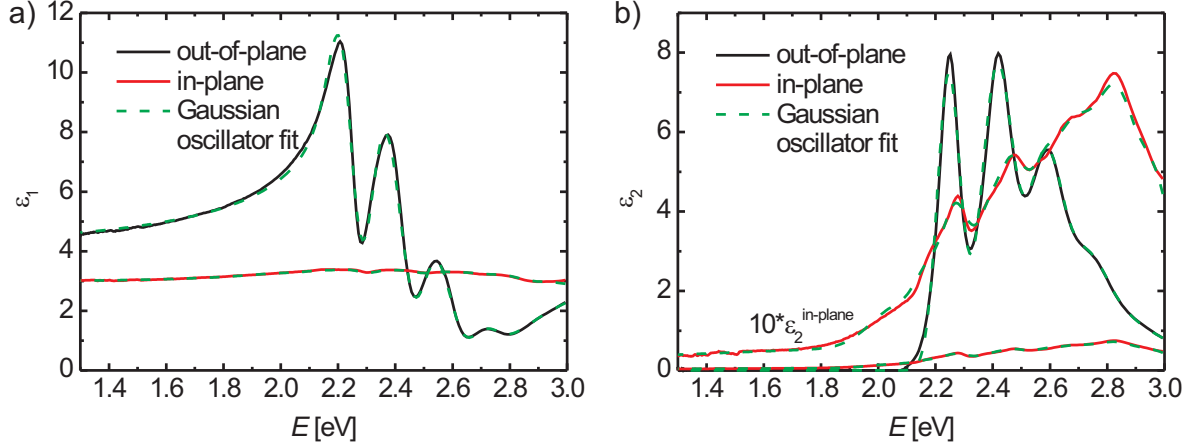


**Figure 5.20:** a) Real part  $\epsilon_1$  and b) imaginary part  $\epsilon_2$  for the in-plane and the out-of-plane component versus energy obtained by a multiple sample analysis with a point-by-point fit (solid curves) and a Gaussian oscillator fit (green dashed curves). The in-plane component of  $\epsilon_2$  is additionally magnified by a factor of 10 to better show its lineshape.

this proves that the point-by-point fit results are also Kramers Kronig consistent. The in-plane component of  $\epsilon_2$  is additionally plotted ten times magnified to better show its line shape, which has a more complicated substructure compared to that of the out-of-plane component. Therefore, ten oscillators are used to describe the in-plane component instead of five oscillators for the out-of-plane component. Note that also a Gaussian oscillator model leads to significantly different results if only the single DIP-Si<sub>Ntve</sub> data are fitted. The correlation between the in-plane and the out-of-plane component for DIP-Si<sub>Ntve</sub> cannot be reduced by using, e. g. Gaussian oscillators for describing the dielectric function. This correlation does not depend on the model but solely on the experimental data that are used and a multiple sample analysis has to be performed.

Both, the in-plane and the out-of-plane component of  $\epsilon_2$  (see Fig. 5.20b) exhibit at least four distinguishable transitions, which can be assigned to a modified vibronic progression of the HOMO-LUMO transition (see Sec. 3.1.1.3) differing significantly between both components. While the relative intensities of the out-of-plane component rather decrease with increasing energy the in-plane component shows the opposite behavior. Also the spacing between the vibronic subbands differs for both directions: The effective vibronic energy of the out-of-plane component is  $E_{01} - E_{00} = 0.165 \pm 0.005$  eV and  $E_{02} - E_{01} = 0.162 \pm 0.005$  eV, whereas the energy spacing in the in-plane component is higher ( $E_{01} - E_{00} = 0.202 \pm 0.005$  eV and  $E_{02} - E_{01} = 0.194 \pm 0.005$  eV). The in-plane component shows additionally a different line shape: The first two peaks are splitted up in two components ( $\Delta E \approx 92$  meV), which can therefore not be described by a single Gaussian oscillator.



### 5.4.3 Discussion

#### 5.4.3.1 Molecular tilt angle

The difference between the intensities of the in-plane and of the out-of-plane component reveals the strong uniaxial anisotropy. Assuming that the observed dielectric tensor arises entirely from neutral excitations of DIP molecules with transition dipole moments along their long axes, the area under the observed components of  $\varepsilon_2$  can be used to determine the average orientation of the molecules. The tilt angle  $\theta$  of the molecule relative to the surface normal can be deduced from

$$\tan^2 \theta = \frac{2I_{\text{in-plane}}}{I_{\text{out-of-plane}}} \quad (5.6)$$

where  $I$  is the transition intensity given by the area under the  $\varepsilon_2$  curves. The number 2 accounts for the in-plane isotropy, i. e. that two components of the dielectric tensor are averaged. The estimate for the tilt angle based on the lowest peak at  $E_{00} = 2.252$  eV gives  $\theta = 17^\circ$  in excellent agreement with the published crystal structure of the thin film phase [18]. On the other hand, due to the different line shapes between both components reported in Fig. 5.20 b), an estimate for the tilt angle based on the entire area under the curves would result in a larger tilt angle  $\theta = 26^\circ$ . This discrepancy indicates that a precise determination of the molecular orientation based on the imaginary part of the dielectric tensor would require an exciton model taking the intermolecular coupling into account and quantifying both the in-plane and the out-of-plane components.

#### 5.4.3.2 Comparison to solution spectra

The normalized thin film spectra for both directions and the normalized monomer spectrum obtained from DIP dissolved in 1,2-dichlorobenzene are plotted in Fig. 5.21 for comparison. The spectrum measured for DIP dissolved in acetone is not shown here since it agrees except for some energy shift very well with the result obtained for 1,2-dichlorobenzene (see Fig. 5.1). Obvious differences are visible, such as a red-shift  $E_{00}^{\text{film}} - E_{00}^{\text{mono}} = -0.04$  eV for the lowest vibronic subband, which is in case of acetone  $\Delta E = -0.1$  eV. This finding agrees with calculations for similar compounds like PTCDA, where this difference is even larger ( $-0.16$  eV) [116]. Usually, the gas-to-solvent shift is smaller than the gas-to-crystal shift, which is also confirmed in case of DIP.

Furthermore, the effective vibronic energy of the out-of-plane component, i. e. the energy spacing between the subbands, agrees well with the result obtained for the monomer, whereas the effective vibronic energy of the in-plane component, mainly induced by the line splitting, is higher. The relative intensities of the vibronic subbands differ for both thin film components with respect to the monomer spectrum. Although the similarity between the out-of-plane component and the monomer spectrum is higher than for the in-plane component, there are still significant differences, revealing a strong influence of the

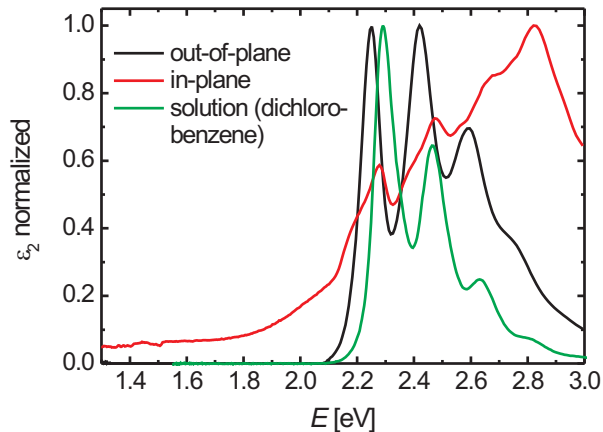


**Figure 5.21:** Normalized imaginary part of the dielectric function for the out-of-plane (black) and for the in-plane (red) component of 33 nm thick DIP films on SiO<sub>2</sub> obtained by a point-by-point fit using multiple sample analysis. For comparison the normalized spectrum of DIP dissolved in 1,2-dichlorobenzene is shown as a green line.

exciton transfer between different molecular sites. This will be discussed in the following paragraphs.

#### 5.4.3.3 Transition dipole

If the entire absorption band arises from Frenkel excitons, its overall strength can be expressed according to Ref. [10] as

$$\int dE \operatorname{tr}[\varepsilon_2(E)] = \frac{2\pi Z\mu^2}{\varepsilon_0 V_0} \quad (5.7)$$

where  $Z = 2$  is the number of basis molecules,  $V_0 = 1029 \text{ \AA}^3$  the volume of the crystal unit cell obtained from the DIP thin film structure (see Sec. 3.1.3.1), and  $\mu$  the transition dipole involved in the optical excitation. The Gaussian oscillator fit of the observed dielectric function in Fig. 5.20 b) yields an area of 4.2 eV, so that the experimental data results in a transition dipole of  $\mu = 6.6 \text{ Debye} = 1.4 e\text{\AA}$ . TD-DFT calculations of the lowest transition at the B3LYP/TZVP level yield a transition dipole of  $\mu = 9.42 \text{ Debye} = 1.96 e\text{\AA}$ , resulting in an expected area of 8.5 eV, which is larger than the experimental result [40]. For similar perylene compounds like PTCDA, a TD-DFT transition dipole of 8.25 Debye at the B3LYP/TZVP level was calculated, exceeding also the value of 6.45 Debye derived from the experimental data [117].

Therefore, from a comparison with PTCDA, the calculated transition dipole can be considered to be an upper bound, whereas the experimentally determined transition dipole rather defines a lower bound because roughness of the film reduces the filling factor below 100%. Since AFM- and X-ray data show that the roughness is  $\sigma \approx 4.8 \text{ nm}$ , which is still small compared to the mean film thickness of 33 nm, the experimental value of the transition dipole is expected to be closer to the realistic value than the calculated value. Generally, absolute transition dipoles are actually both difficult to calculate and to measure, and the still good agreement between experiment and calculations should be seen as a major success.

#### 5.4.3.4 Difference between in-plane and out-of-plane component

The fact that the shapes of the in-plane and out-of-plane components of  $\varepsilon_2$  do not coincide (see Fig. 5.21) indicates that the optical response cannot arise exclusively from the single molecular HOMO-LUMO transition. Despite the obvious differences for the lowest two vibronic bands, the strength of the in-plane component corresponds to about 5% of the out-of-plane component, in good agreement with the geometric considerations in eq. (5.6) related to the orientation of the molecular transition dipole and the resulting in-plane contribution.

The origin of the high energy part of the in-plane dielectric function could be due to contributions of the second Davydov component arising from Frenkel excitons. The intensity of both Davydov components is given by the vectorial superposition of the transition dipoles  $\vec{\mu}_A$  and  $\vec{\mu}_B$  related to the two basis molecules:

$$|\vec{\mu}_1| = \frac{|\vec{\mu}_A + \vec{\mu}_B|}{\sqrt{2}} \quad |\vec{\mu}_2| = \frac{|\vec{\mu}_A - \vec{\mu}_B|}{\sqrt{2}} \quad (5.8)$$

Due to the small angle between the long axes of the basis molecules of only  $1.4^\circ$  determined by Heinrich *et al.* [18], these transition dipoles are superimposed as  $|\vec{\mu}_1| = \sqrt{2} \cos 0.7^\circ \mu$  and  $|\vec{\mu}_2| = \sqrt{2} \sin 0.7^\circ \mu$  with  $\mu = |\vec{\mu}_A| = |\vec{\mu}_B|$ . Therefore, the small Davydov component  $\mu_2$  carries only a fraction of  $1.5 \times 10^{-4}$  of the total strength of the first absorption band. Such a tiny optical response is clearly far below the sensitivity of the ellipsometry setup, especially since it probes mainly the projection of both Davydov components onto the in-plane and the out-of-plane component. Therefore, the difference between the line shapes of the in-plane and the out-of-plane cannot arise from different Davydov components of the HOMO-LUMO transition. For this reason, the relative size and signs of the transfer matrix elements  $T_{AA}$  and  $T_{AB}$  (see eq. 3.12) defining both Davydov components cannot be determined.

Instead, the origin of the high energy part of the in-plane dielectric function has to be assigned to different types of transitions like CT excitons. TD-DFT calculation of the lowest 16 transitions in a cluster containing two *A* and two *B* basis molecules, performed by R. Scholz *et al.*, reveal very small transition dipoles arising from CT transitions relying on the molecular HOMO and LUMO orbitals. Therefore, from the weakness of the small Davydov component arising from Frenkel excitons and the absence of substantial CT dipoles involving the same orbitals, the HOMO-LUMO transitions can be ruled out as a possible assignment for the upper part of the in-plane component of the dielectric tensor.

However, keeping in mind that the lowest dipole-forbidden molecular transition based on HOMO-1 and LUMO is nearly degenerate with the HOMO-LUMO transition (see Tab. 3.2) and that the second dipole-allowed (HOMO-2)-LUMO transition is not so far higher in energy, it is clear that each of these molecular excitations generates a corresponding set of CT transitions between neighboring sites. In a cluster of four DIP molecules the assessment of all these transitions would require a TD-DFT calculation of the lowest 48 transitions. From simple energetic considerations, an assignment of the upper part of

the in-plane dielectric function to the orbital pairings (HOMO-2)-LUMO and (HOMO-1)-LUMO and their respective CT states seems to be the only possibility, but at the present stage, any more quantitative statements about the strength of these CT transitions would remain purely speculative.

Therefore, the exciton model (see Sec. 3.1.2) will be applied to the out-of-plane component of the dielectric tensor only, which is dominated by the large molecular transition dipoles of the lowest dipole-allowed excitation, compare Table 3.2. Even though the CT transition dipoles are very small, it will be demonstrated that the shape of the dielectric function is strongly influenced by the interference between Frenkel excitons and charge transfer transitions.

#### 5.4.3.5 Frenkel exciton transfer

The theoretical analysis concerning the exciton transfer was performed by R. Scholz *et al.*, which was introduced in Sec. 3.1.2. It is based on the experimentally determined out-of-plane component of the dielectric function presented in Fig. 5.20 as well as on the molecular parameters  $S$  and  $\lambda$  obtained from the monomer spectra (see Sec. 5.1). Since  $S$  and  $\lambda$  are related to the internal molecular deformation, they can be regarded as unchanged in a molecular aggregate. Furthermore, the calculations are based on the DIP thin film structure determined by Heinrich *et al.* (see Sec. 3.1.3.1 and Ref. [18]). First, the model concerning Frenkel exciton transfer is applied, which is then extended to the mixing between Frenkel excitons and CT states.

In the following, the transfer matrix  $T_{AA} + T_{AB}$  (see eq. 3.12) that influences the dielectric function of the dominant Davydov component will be abbreviated as  $T$ . In case of Frenkel excitons the average transition energy  $\langle E \rangle$  can be related to a sum of molecular parameters and the exciton transfer  $T$ :

$$\langle E \rangle = E_{00} + S\hbar\omega + T, \quad (5.9)$$

where  $E_{00}$  is the transition between the lowest vibronic levels of the molecule, and  $\langle E \rangle$  is the center of mass of the imaginary part of the dielectric function  $\varepsilon_2$  in the crystalline phase [118, 119].

For simplicity, the unknown gas-to-crystal shift is assumed to be contained in the molecular parameter  $E_{00}$  used for the crystalline phase. It has to be distinguished from the lowest vibronic feature in the observed spectra because the latter relates to the lowest branch of the exciton dispersion near the  $\Gamma$  point of the Brillouin zone,  $\mathbf{k} \approx 0$ . In first order perturbation theory, the lowest subband at  $\Gamma$  is expected to occur at about

$$E_{00}(\Gamma) \approx E_{00} + e^{-S}T + O(T^2), \quad (5.10)$$

A more precise value can be obtained from a diagonalization of the Hamiltonian for Frenkel excitons [117, 10]. Therefore, under the simplifying assumption that the absorption line

shape can be related entirely to the molecular HOMO-LUMO transition, realistic values for  $E_{00}$  and  $T$  can be read off from the energetic position of the experimentally observed peak  $E_{00}(\Gamma)$  and the center of mass of  $\varepsilon_2$ . From the Gaussian oscillator fit performed on the experimental data the center of mass is obtained by

$$\langle E \rangle = \frac{\sum_{i=1}^{1=5} (I_i \cdot E_i)}{I_{\text{tot}}} \quad (5.11)$$

where  $I_i$  is the intensity and  $E_i$  the energy position of the  $i$ th oscillator and  $I_{\text{tot}}$  the total intensity for all oscillators below 3 eV, giving  $\langle E \rangle = (2.50 \pm 0.02)$  eV. Together with the experimentally determined value  $E_{00}(\Gamma) = (2.252 \pm 0.005)$  eV, the center of mass  $\langle E \rangle$  can be reproduced with a transfer parameter  $T = 0.142$  eV and  $E_{00} = 2.21$  eV, so that at  $\Gamma$ , the excitonic dispersion shifts upwards by 0.042 eV.

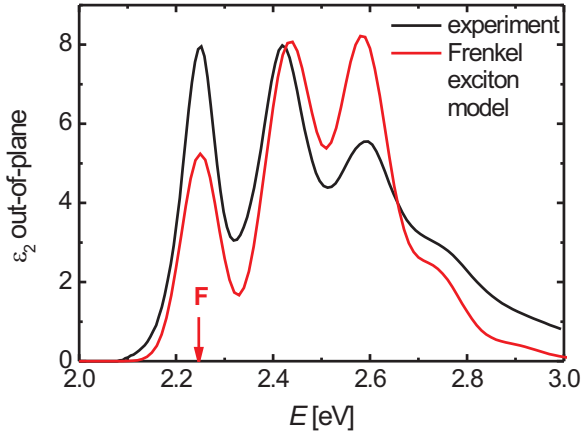


**Figure 5.22:** Experimental out-of plane component  $\varepsilon_2$  (black) and the result of the Frenkel exciton model (red). The energy  $E_{00}$  of the Frenkel exciton is marked by an arrow.  $E_{00} = 2.25$  eV and  $T = 0.142$  eV are determined by using the experimental results  $\langle E \rangle = (2.50 \pm 0.02)$  eV,  $E_{00}(\Gamma) = (2.252 \pm 0.005)$  eV,  $\hbar\omega_{\text{eff}} = 0.17$  eV, and  $S = 0.87$ .

The line shape arising from the Frenkel exciton model with the above parameters is shown in Fig. 5.22, where the broadenings of the vibronic subbands are taken from the fit to the experimental data. The general features are qualitatively reproduced, and the calculated positions of the subbands agree with the observation within absolute deviations below 0.02 eV. However, the relative intensities of the subbands disagree with the measured data: The central subband fits quite well, whereas the first subband at lower energies is underestimated and the third subband at higher energies is overestimated. Furthermore, the distribution width of all subbands given by  $\Delta E = \sqrt{\langle (E - \langle E \rangle)^2 \rangle} = \sqrt{S} \hbar\omega$  (see [120]), is underestimated, which is mainly visible at higher energies. This difference indicates additional broadening mechanisms, which cannot be accounted for in this simple Frenkel exciton model.

Moreover, the relatively large transfer parameter reduces the intensity of the  $E_{00}$  subband, so that its area remains far below the observed spectra. Therefore, in the mixed Frenkel-CT model introduced in Sec. 3.1.2, a smaller transfer parameter will be used, recovering a reasonable intensity of the  $E_{00}$  band.

### 5.4.3.6 Mixing of Frenkel excitons and charge transfer states

In order to improve the exciton model additional CT states are taken into account (see Sec. 3.1.2). In case of the Frenkel exciton the Huang-Rhys factor for the effective mode of  $\hbar\omega_{\text{eff}} = 0.17$  eV is again given by the experimentally determined value  $S = 0.87$ , whereas it is calculated in B3LYP/TZVP geometry for the positively and negatively charged molecule to be  $S^+ = 0.28$  and  $S^- = 0.61$ , respectively. From a B3LYP/TZVP calculation of a stacked dimer based on the DIP thin film geometry the hole and electron transfer parameters can be related to the splittings of the frontier orbitals  $\Delta E_{\text{HOMO}} = 2|t_h|$  and  $\Delta E_{\text{LUMO}} = 2|t_e|$  [121]. The patterns of the resulting orbitals give  $t_h = 0.066$  eV and  $t_e = -0.032$  eV. Additional TD-DFT calculations of the dipole-allowed transitions in such a stacked dimer provide furthermore the information that the transition dipole of the CT state is only about 1% of the transition dipole of a neutral molecular excitation, so that it is irrelevant for the line shape of the optical response. Instead, the large component of the observed dielectric tensor reported in Fig. 5.20 b) reveals directly the Frenkel exciton parentage of the mixed Frenkel-CT states.

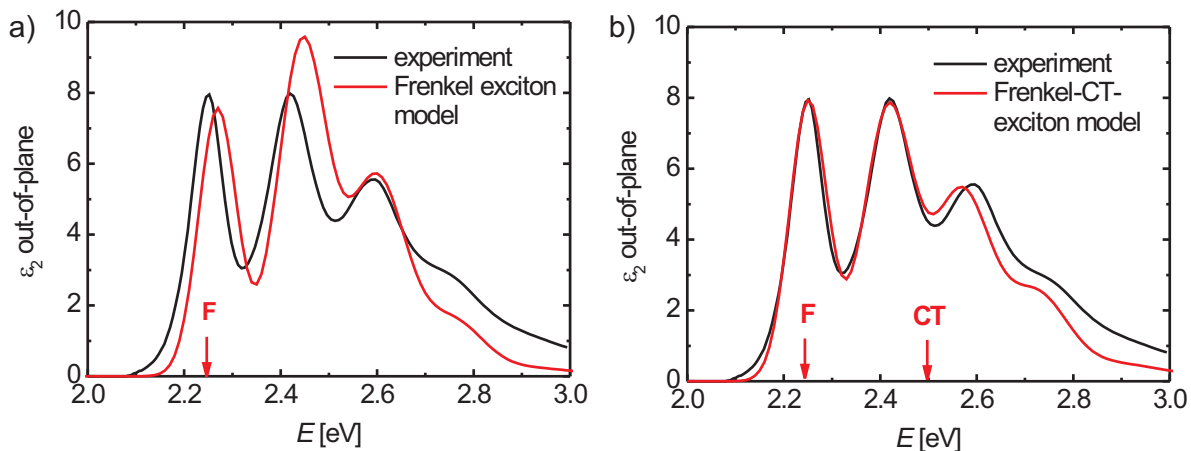


**Figure 5.23:** a) Frenkel exciton model with the parameters  $E_{00}^{\text{F}} = 2.24$  eV and  $T = 0.09$  eV, which differ from those in Fig. 5.22. They are used for the Frenkel-CT model, shown in b), including the interference between Frenkel and CT excitons ( $E_{00}^{\text{CT}} = 2.50$  eV). The energies of the Frenkel and the CT exciton are marked by arrows.

The energy  $E_{00}^{\text{F}}$  can easily be adjusted to the measured position of the lowest structure in  $\epsilon$ , but the transfer parameters  $T_{AA}$  and  $T_{AB}$  and the lowest level of the CT state,  $E_{00}^{\text{CT}}$ , are not yet determined. For the transfer of neutral excitations, a sum of  $T_{AA} + T_{AB} = 0.09$  eV is found to be reasonable, irrespective of the assignment to the amount of exciton transfer  $T_{AA}$  between the same basis molecules and the transfer  $T_{AB}$  between different basis molecules, which is difficult to determine (see Sec. 5.4.3.4). The transfer parameter remains smaller than the value derived from the sum rule in Sec. 5.4.3.5 because this is the only possibility to increase the relative area of the  $E_{00}(\Gamma)$  subband, compare Fig. 5.23 a).

It shows the experimental data together with the pure Frenkel model using  $T = 0.09$  eV. In the mixed Frenkel-CT model, the line shape at higher energies depends sensitively on the difference between Frenkel and CT energies, and the best agreement is found for  $E_{00}^{\text{CT}} - E_{00}^{\text{F}} = 0.26$  eV or  $E^{\text{CT}} = 2.50$  eV, compare Fig. 5.23 b). When performing a variation of this energy difference by  $\pm 0.05$  eV, the agreement between the model calculation and the observed line shape deteriorates significantly. From this finding it can be concluded that the difference between the two types of crystal excitations is  $\Delta_0 = E_{00}^{\text{CT}} - E_{00}^{\text{F}} = 0.26 \pm 0.05$  eV, with a rather small uncertainty. This value is a crucial parameter for device applications like the modulation of the optical response by applied electric fields, photocurrents, or solar cells.

When comparing the line shape of the calculation involving only Frenkel excitons with the mixed Frenkel-CT model, the most striking difference concerns the intensity of the  $E_{01}$  subband. In the used parameter set, this Frenkel subband is nearly resonant with the  $E_{00}^{\text{CT}}$  transition of the CT manifold, so that the interaction between these two excitonic features via electron and hole transfer is rather efficient. As a result, parts of the intensity of the  $E_{01}$  subband are fed into an increase of all other subbands, so that the relative height of the four largest peaks is substantially improved. A minor shortcoming of the model calculation consists in the fact that the energetic distance between the peaks  $E_{01}(\Gamma)$  and  $E_{02}(\Gamma)$  is underestimated by about 0.02 eV. This indicates that the Frenkel-CT model is still lacking some interaction within the exciton manifold, presumably a CT state involving the orbitals HOMO-1 or HOMO-2, or vibronic excitations on molecules surrounding the optically excited sites, as discussed previously for a purely one-dimensional system [122].

#### 5.4.3.7 Concluding remarks

In conclusion, it was demonstrated that crystalline DIP thin films exhibit a pronounced uniaxial anisotropy, which can be determined by multiple sample analysis of VASE data. The thin film spectrum shows a pronounced vibronic progression in both components, which differ clearly in line shape. Although the out-of-plane component agrees better with the monomer spectrum than the in-plane component, in both cases significant differences compared to the monomer spectrum can be observed, which are due to the coupling of the aggregated molecules. While the out-of-plane component can be described by an exciton model, taking Frenkel and CT excitons into account, the in-plane component is most likely affected by additional higher transitions, which would require a more complex model. For the out-of-plane component it was shown that the experimental dielectric function is strongly influenced by the interference between Frenkel excitons and charge transfer excitons. Based on electron and hole transfer parameters of  $t_e = -0.032$  eV and  $t_h = 0.066$  eV determined from DFT calculations for pairs of molecules, the difference between the excitation energy of CT and Frenkel states can be extracted as  $E_{00}^{\text{CT}} - E_{00}^{\text{F}} = 0.26$  eV.

## 5.5 Film growth followed by optical real-time measurements

The anisotropic dielectric function of DIP on SiO<sub>2</sub> at  $d \approx 30$  nm discussed in the previous section serves as a 'bulk-like' (static) reference for real-time measurements during film growth. The corresponding spectra for PEN will be briefly presented in Sec. 5.5.3. One advantage of real-time measurements is that *relative* changes can be observed during growth. This gives rise to smaller experimental errors compared to *ex-situ* and static measurements of several samples that differ in thickness. Therefore, it is possible to study also very thin films in the sub-monolayer regime. Furthermore, potential transient changes during growth can be observed, which is not possible for static post-growth measurements.

The dielectric function of a film is generally expected to depend on the film thickness since transitions from monomer-like molecules in the sub-monolayer range to bulk-like molecules at higher thicknesses occur, which may be optically visible due to changing intermolecular interactions [35]. Furthermore, the influence of the substrate reduces with increasing thickness that can change the optical properties of the molecules. Also structural and morphological film properties can vary during growth having a strong impact onto the optical film properties [121, 80]. Possible spectral changes during film growth may be categorized as follows:

1. Energy shift (like solvent shift).
2. Transitions appearing or disappearing.
3. Redistribution of oscillator strength.
4. Changing optical anisotropy.

Nevertheless, even if the intermolecular coupling is strong and the 'bulk-like' thin film spectrum deviates from the monomer spectrum, optical changes do not have to be observed during growth, since completely isolated molecules are generally not detected. Instead nucleating and growing molecular islands are investigated and it is not clear whether their optical properties change during growth. Since a variety of aspects like molecular deformations, vibrational degrees of freedom, intermolecular coupling, and the film structure influence the optical spectra, it is rather difficult to predict the spectrum of a film based on the knowledge of the individual molecules. Therefore, experimental investigations are necessary that are presented in the following sections, first for DIP and subsequent for PEN thin films.



### 5.5.1 DIP film growth on Si<sub>Ntve</sub>

#### 5.5.1.1 Film growth at $T = 130$ °C followed by ellipsometry

In this section spectroscopic ellipsometry data are presented, which are measured *in-situ* to optically follow the film growth. Before the time-dependent data are analyzed, the *ex-situ* results are compared to *in-situ* results measured at the same final film thickness  $d = 33$  nm. Since the *in-situ* measurements are performed at one fixed angle of incidence ( $\alpha = 59.5$  °), it is impossible to determine the uniaxial dielectric function solely from these data. Also using a thermal oxide as a substrate does not help since the interference enhancement relies on the measurement at different AOI's (see Sec. 5.4.1.1). Therefore, the *ex-situ* model discussed in the previous section (Sec. 5.4.2) is taken as a reference, which needs to be only slightly modified.

**5.5.1.1.1 Differences between static *ex-situ* and *in-situ* spectra** As Fig. 5.24a) illustrates, the *ex-situ* model describes the *in-situ* ellipsometry data at  $d = 33$  nm reasonably well, although small differences occur due to altered experimental conditions:

1. The *in-situ* data are taken at  $T = 130$  °C for which the best possible structural order is obtained, whereas the *ex-situ* data are always measured at room temperature ( $T = 23$  °C). This temperature difference does not only change the dielectric function of the DIP film but also that of the Si substrate causing differences between *in-situ* and *ex-situ* measurements. For reducing the systematic differences the dielectric function of Si is determined prior to the film growth at  $T = 130$  °C. The results agree well with the published dielectric function of Si at elevated temperatures [123].
2. Possible influences of the ambient, like oxidation [124] or water penetrating into the film, as it is reported for PEN [125], are not present under UHV conditions causing differences between *in-situ* and *ex-situ* measurements. Since DIP is very stable against oxidation, possible differences could only be due to water covering the organic film.

Already slight modifications of the out-of-plane dielectric function (see Fig. 5.24b) suffice to describe the *in-situ* data very well (see red curve in Fig. 5.24a), keeping the in-plane component constant. Of course the temperature and the ambient condition will not only influence the out-of-plane component but also the in-plane component. Nevertheless, both components cannot be determined together unambiguously from *in-situ* measurements and simplifying assumptions have to be made. Modifying only the in-plane component does also lead to an improved model for the *in-situ* data. Therefore, not too much significance should be attached to the differences obtained between *in-situ* and *ex-situ* models of the dielectric function. They are very small and indicate systematic experimental differences, as discussed above, without having a strong impact onto possible real-time changes, where mainly relative changes of the dielectric function are observed and small errors of the reference spectrum do not play a role.

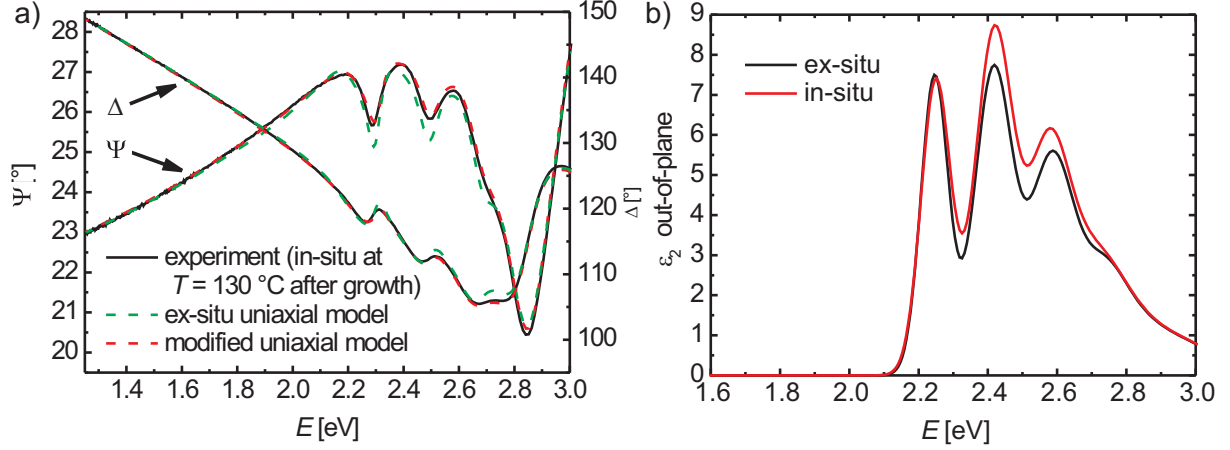


**Figure 5.24:** a) Ellipsometry angles  $\Psi$  and  $\Delta$  measured *in-situ* at  $\alpha = 59.5^\circ$  and at  $T = 130^\circ\text{C}$  after film growth at  $d = 33\text{ nm}$ . The model determined *ex-situ* (green) needs to be slightly modified (red) to describe the data well. b) Comparison between modified *in-situ* result and *ex-situ* result for the out-of-plane dielectric function. For simplicity the in-plane component is kept fixed and agrees to the *ex-situ* result.

In the following real-time data during growth will be analyzed. First a model is tested, which is based on the uniaxial dielectric function determined *ex-situ* and modified *in-situ*, assuming that it does not change with film thickness. Therefore, this model will be called uniaxial-constant model. Second, a model will be discussed where the thickness dependence of the dielectric function is taken into account.

**5.5.1.1.2 Uniaxial constant model** Fig. 5.25a) shows the increasing film thickness versus time measured with the QCM with a linear fit giving a growth rate of  $2.88\text{ \AA}/\text{min}$ . The QCM thickness is calibrated by *ex-situ* X-ray and *in-situ* ellipsometry measurements at the final film thickness which agree very well. The thickness is fitted to each time slice of the ellipsometry data using the uniaxial-constant model for describing the film dielectric function. The fit results (see green dashed curve) deviate slightly from the QCM thickness. This is most pronounced for smaller thicknesses with a maximal deviation of  $\Delta d = 0.8\text{ nm}$ . The deviation is probably due to roughness, which reduces with decreasing film thickness [13]. Roughness is neither taken into account for calibrating the QCM thickness nor for the real-time ellipsometry fit since it introduces additional parameters that are difficult to determine independently.

The real-time ellipsometry data are plotted in Fig. 5.25b) versus time for five specific energies showing the thickness dependence of  $\Psi$ . The black curves represent the uniaxial-constant model taking the linearly increasing film thickness with a growth rate of  $2.88\text{ \AA}/\text{min}$  into account. It can be seen that the constant dielectric function describes the data for all plotted energies below  $2.65\text{ eV}$  very well. This indicates that the time-dependent change of  $\Psi$  during film growth is mainly due to thickness oscillations and the

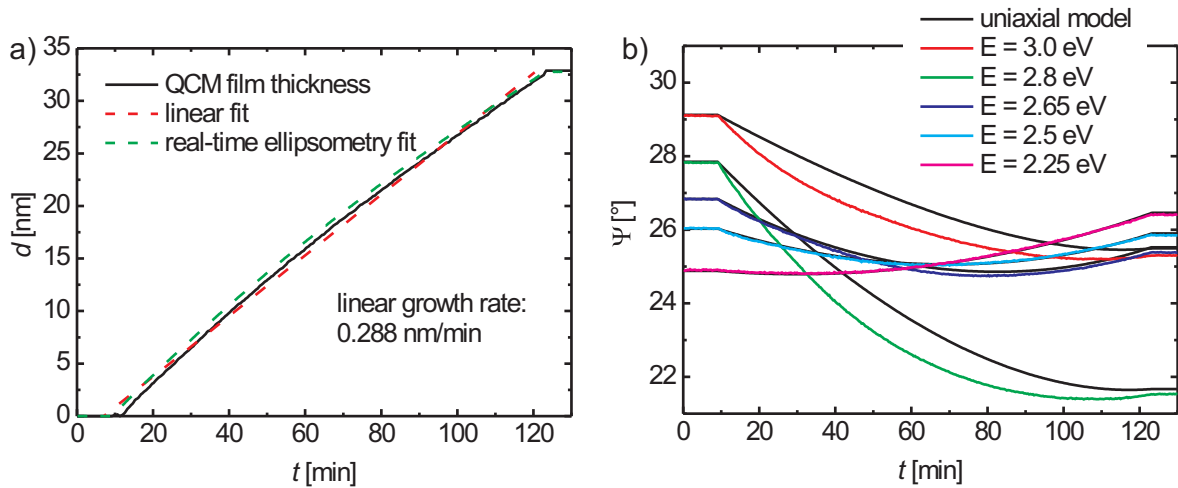


**Figure 5.25:** a) Film thickness measured with the QCM during growth (black curve) plotted together with a linear fit (red dashed curve) to determine the nearly constant growth rate. A real-time ellipsometry fit (green dashed curve) gives very similar but slightly higher thicknesses. b)  $\Psi(t)$  for selected energies during film growth. The black lines correspond to a model based on the growth rate of  $2.88 \text{ \AA}/\text{min}$  and the thickness independent uniaxial dielectric function, showing mainly deviations for high energies.

dielectric function can be regarded as constant. In contrast, deviations from the model are visible for higher energies indicating optical changes during growth in this regime.

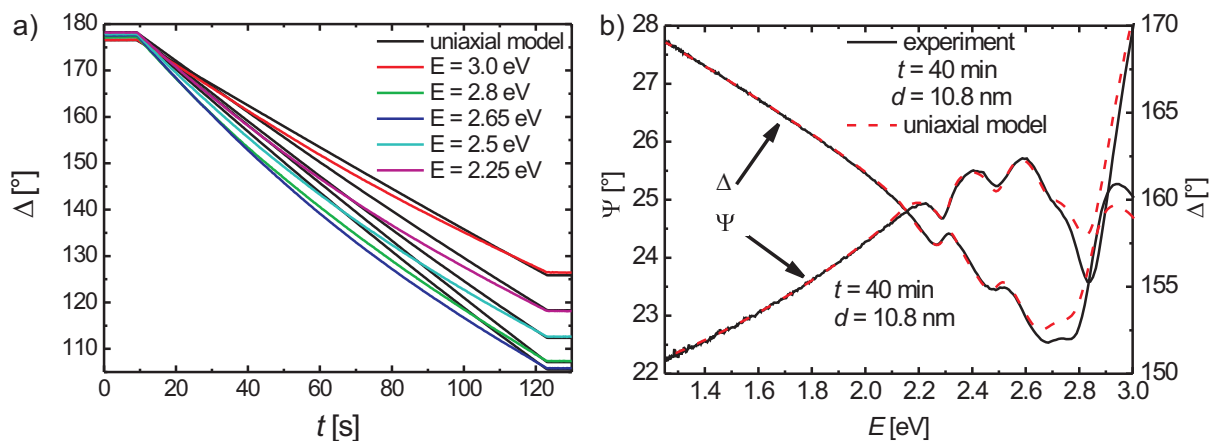


**Figure 5.26:** a)  $\Delta(t)$  for selected energies during film growth. The model is based on the constant growth rate of  $2.88 \text{ \AA}/\text{min}$  and the thickness independent uniaxial dielectric function. b)  $\Psi$  and  $\Delta$  spectra during growth for  $t = 40 \text{ min}$  corresponding to a film thickness of  $d = 10.8 \text{ nm}$ . The uniaxial model describes the data below  $2.6 \text{ eV}$  well, whereas deviations occur for higher energies. This indicates that the dielectric function changes with thickness mainly above  $2.6 \text{ eV}$ .

Time-dependent  $\Delta$ -data are depicted in Fig. 5.26a). Since  $\Delta$  is more sensitive to  $d$ , small deviations from the linear thickness behavior (see Fig. 5.25a) result in differences between experimental data and the model. If the film thickness is not approximated by a linear growth, but the fit result from the ellipsometry data is used, both  $\Psi$ - and  $\Delta$ -data agree well to the uniaxial-constant model in the low energy range, as Fig. 5.26b) shows. The spectrum of  $\Psi$  and  $\Delta$  is plotted for  $t = 40$  min corresponding to a film thickness of  $d = 10.8$  nm. The constant dielectric function describes the film at this thickness below 2.6 eV quite well whereas deviations are observable for higher energies as already expected from Fig. 5.25b). The uniaxial-constant model is, therefore, not sufficient to describe the real-time data during growth, but changes have to be taken into account. They can be due to a thickness dependence of the dielectric function, but also roughness effects can play a role. They affect the optical properties [80] and DIP films are known to roughen rapidly above  $\sim 10$  ML [13].

**5.5.1.1.3 Thickness dependent model** For modeling optical changes during growth either the in-plane component or the out-of-plane component can be fitted using Gaussian oscillators. Fig. 5.27a) shows the spectroscopic fit results for various film thicknesses obtained for the in-plane component while the out-of-plane component is fixed. Significant changes are visible not only for the energy range above 2.6 eV. The dark blue curve corresponds to the reference spectrum at  $d = 33$  nm. The 'fourth mode', positioned at  $\sim 2.8$  eV (see Sec. 5.4.3), shifts to higher energies with decreasing film thickness such that below  $\sim 13$  nm only three modes are visible that belong to the  $\pi - \pi^*$  transition.

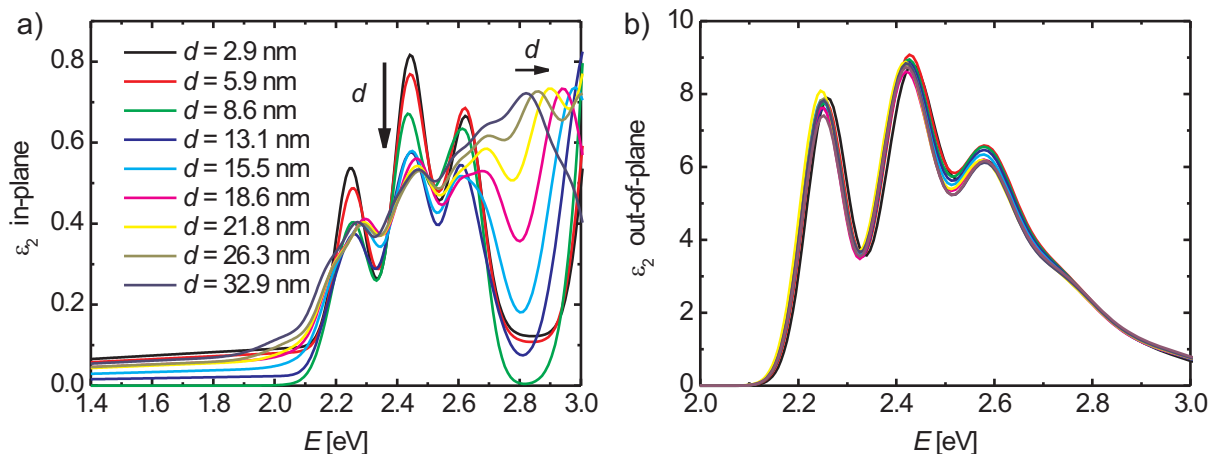


**Figure 5.27:** a) Fit results for the in-plane dielectric function at different thicknesses, keeping the out-of-plane component fixed. Significant changes can be observed. b) Fit results for the out-of-plane dielectric function at different thicknesses, keeping the in-plane component fixed. Only small changes are visible. Both models, presented in a) and b) describe the experimental ellipsometry data well indicating that the fit results are not unique.

Furthermore, for thin films the line shape of the first three modes resembles the shape of the out-of-plane component. In contrast, nearly no spectral changes are present when the out-of-plane component is fitted instead of the in-plane component as can be seen from Fig. 5.27b). Although the uniaxial-constant model does not describe the experimental data sufficiently, only small modifications of the out-of-plane component are necessary to reproduce the data well. Both models, fitting either the in-plane or the out-of-plane component, describe the ellipsometry real-time data well although the resulting dielectric function differs significantly. Thus, it is not possible to distinguish the best model solely from these data and additional measurements have to be performed.

**5.5.1.1.4 Different approaches** One possibility is to investigate DIP films with different thicknesses *ex-situ* at variable angles of incidence, comparing the results with models obtained for *in-situ* and real-time measurements. This means that the advantages of real-time measurements are lost, e. g. being able to investigate transient changes during growth and reducing the error bars by comparing relative changes of the same film. Although the dielectric function of different  $\sim 30$  nm thick films is well reproduced for *ex-situ* measurements, the possible optical changes during growth are quite small making it necessary to perform highly accurate measurements. Since already differences between *in-situ* and *ex-situ* measurements of the very same film are observed (see Fig. 5.24b), which could be bigger than possible changes during growth, investigating the thickness dependence *ex-situ* does not seem to be the method of choice.

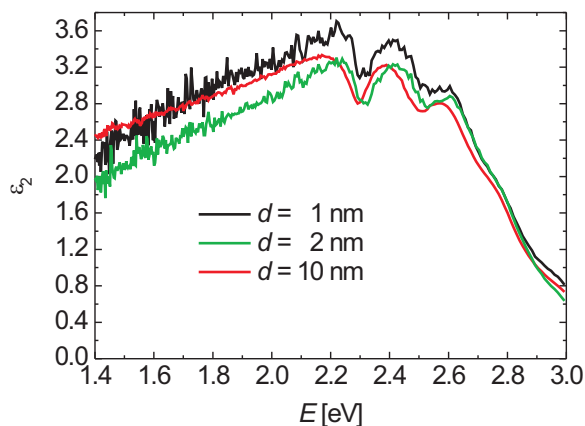


**Figure 5.28:** Isotropic dielectric function determined by real-time ellipsometry measurements during DIP growth on  $\text{Si}_{\text{Ntve}}$  for different thicknesses. The absorption in the low energy range is a fitting artefact. Nevertheless, the point-by-point fit results show that no significant optical changes occur for low thicknesses during growth.

Furthermore, the sensitivity to uniaxial anisotropy decreases with film thickness also for VASE-measurements and despite of systematic experimental errors also the data analysis becomes difficult. As investigations of films in the ML range (1-3 nm) show, the uniaxial anisotropy cannot be determined and an anisotropic fit leads to an isotropic dielectric function where the in-plane and the out-of-plane component coincide. This simplifies the real-time analysis for very thin films and an isotropic fit can be performed, which does not show relative changes (see Fig. 5.28). The absorption in the low energy range is a

fitting artefact resulting from the simplified model, which nevertheless shows, that in the low thickness range no optical changes occur for DIP on  $\text{Si}_{\text{Ntve}}$ .

In conclusion, ellipsometry data do not show optical changes for low thicknesses during growth, whereas at high thicknesses small optical changes are visible. They may affect only slightly the out-of-plane component or more strongly the high energy range of the in-plane component. Since those changes are difficult to quantify due to the uniaxial anisotropy, differential reflectance spectroscopy (DRS) is performed to gain additional insight into the spectral changes during growth, which is discussed in the following section.

### 5.5.1.2 Film growth at $T = 130\text{ }^\circ\text{C}$ followed by DRS

Differential reflectance spectroscopy (DRS) probes only the in-plane component of the film, since measurements are performed at normal incidence. On the one hand, this simplifies the data analysis significantly compared to ellipsometry (see Sec. 5.5.1.1), on the other hand it is not possible to determine the out-of-plane component during growth. Fig. 5.29a) shows the measured intensity signal for a  $\text{Si}_{\text{Ntve}}$  sample before (black line) and after deposition (red line) with DIP molecules. The signal depends on the sample under investigation but it is mainly influenced by the characteristics of the halogen light source determining the overall shape. Since the intensity is small above 2.6 eV and below 1.6 eV compared to the maximum around 2 eV, the signal to noise ratio is expected to be bigger at high and low energies. Furthermore, it is visible that a 20 nm thick DIP film rather decreases the reflected light giving rise to a negative DRS signal.

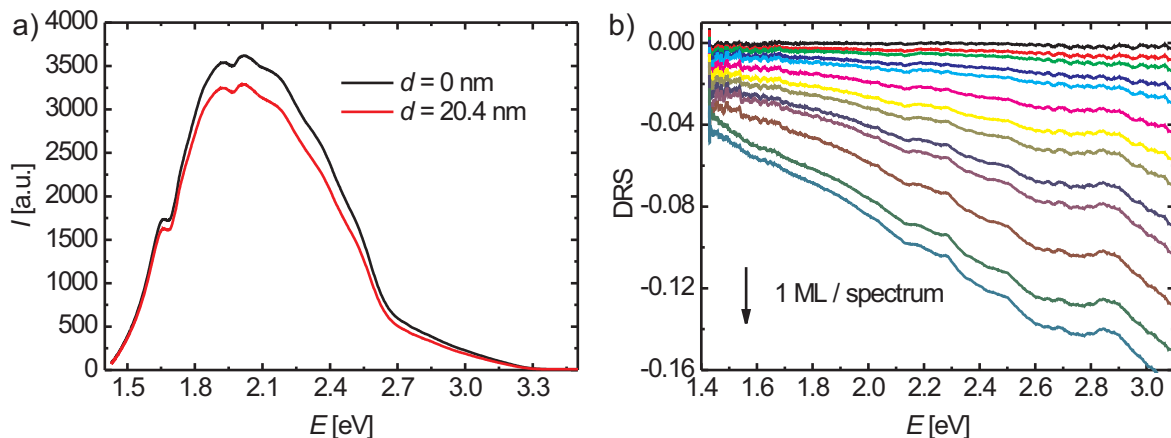


**Figure 5.29:** a) Reflected intensity signal measured at normal incidence for a  $\text{Si}_{\text{Ntve}}$  substrate before (black curve) and after deposition (red curve) with DIP. b) Thickness dependent DRS-signal obtained from the measured reflected intensity during film growth.

From the measured reflected intensity the DRS signal is calculated (see Sec. 4.3), which is shown in Fig. 5.29b) for several thicknesses during film growth. The thickness is given by experimental QCM data, which are calibrated with the final film thickness determined

*ex-situ* by ellipsometry. Below 10 nm nearly no spectral features are visible and the signal is very small. With increasing thickness some DIP specific fingerprints appear in the spectrum. Simulations show that the DRS signal for DIP on a Si<sub>Ntve</sub> is indeed as small as experimentally determined, which is not the case for every organic film on Si as will be shown later in Sec. 5.5.3. Due to the well ordered DIP film and the nearly upright standing molecules, the intensity of  $\varepsilon_2$  for the in-plane component is very small (compare Fig. 5.20) leading to a small DRS-signal. Therefore, it is difficult to perform a unique fit for extracting the in-plane dielectric function of the DIP film. To follow the film growth of DIP on Si<sub>Ntve</sub> with DRS measurements, the quartz glass substrate seems to be better suited than the Si substrate as will be presented in Sec. 5.5.2.

### 5.5.1.3 Film growth at $T = -100$ °C

Remarkably, the DRS signal measured during DIP growth at  $T = -100$  °C on Si<sub>Ntve</sub> does not differ from the signal measured during growth at high temperature. It is mainly influenced by noise. Therefore, it is not possible to extract the dielectric function reliably. Since X-ray and AFM measurements indicate that the crystalline order is reduced for films grown at low temperature (see Sec. 5.3.1,5.3.2), this should have an impact on the optical properties of the film, which cannot be observed due to the low signal. Nevertheless, it can be concluded that at least the immediate environment of a given molecule responsible for the coupling does not change. Furthermore, no significant reorientation of the molecules takes place since an increasing molecular tilt angle ( $\Theta > 17$  °) would enhance the signal remarkably due to the larger projection of the dipole transition onto the in-plane component. The growth temperature of  $T = -100$  °C is obviously too high to trigger such an effect. Probably, mainly the crystalline quality changes, such as the domain size, as AFM pictures have shown (see Sec. 5.3.2).

## 5.5.2 DIP film growth on glass

Using a transparent glass substrate for DRS measurements has several advantages. First, the small reflectivity of glass is changed more significantly by a thin absorbing film than the large reflectivity of Si covered by native oxide, leading therefore to a bigger DRS signal for DIP on glass. Second, the DRS signal is directly proportional to the imaginary part of the dielectric function  $\varepsilon_2$  if a very thin film covers a transparent substrate (see Sec. 4.3). This thin film approximation simplifies the analysis for DIP films with thicknesses lower than  $\sim 2$  nm by using equation 4.4 to calculate  $\varepsilon_2$  from the DRS spectra. The drawback of using a glass substrate instead of a Si substrate is its less well-defined surface, as AFM picture show (see Sec. 5.2.1), which also influences the film morphology (see Sec. 5.3.2). Due to the pronounced roughness, it is difficult to determine the film thickness on glass with a homogeneous layer model. Therefore, the thickness for calibrating the QCM data is determined on a film, which is simultaneously grown on a Si<sub>Ntve</sub> substrate. The QCM film thickness can be regarded rather as a measure of the number of molecules adsorbed

on the glass substrate than the 'real' film thickness, assuming that the probability for adsorption on glass is similar to that on  $\text{Si}_{\text{Ntve}}$ .

### 5.5.2.1 Film growth at $T = 130\text{ }^\circ\text{C}$

**5.5.2.1.1 Sub-ML range** The ultra-thin film spectra for DIP growing on glass are shown in Fig. 5.30, making use of the thin film approximation. They correspond to thicknesses ranging from 0.2 nm to 1.6 nm, indicating high sensitivity of DRS to very thin films.

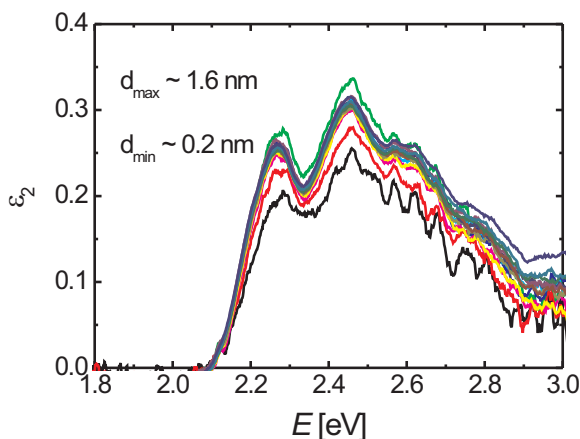


**Figure 5.30:** Imaginary part of the dielectric function  $\varepsilon_2$  for different film thicknesses below  $d = 1.6\text{ nm}$ , obtained by the thin film approximation, which agrees well with Gaussian oscillator fits in this thickness range. Within the error bars no spectral changes are visible, only the spectrum at 1.6 nm (dark blue curve) shows a small intensity increase in the high energy range.

The noise of the intensity is clearly larger above 2.5 eV, which is due to the low intensity for higher energies (compare Fig. 5.29). For all thicknesses the vibronic progression of the  $\pi - \pi^*$ -transition is clearly visible. Within the error bars, which are mainly given by the noise, no spectral changes upon molecular deposition observable. Only at high energies in the dark blue spectrum, which corresponds to the thickest film at  $d = 1.6\text{ nm}$ , a slight but significant intensity increase can be observed.

**5.5.2.1.2 Spectra above 1.6 nm** DRS spectra above 1.6 nm are shown in Fig. 5.31a) for DIP on glass at different thicknesses. The vibronic progression is directly observable and the intensity increases with thickness. In order to extract the dielectric function of the film for higher thicknesses, the thin film approximation is no longer valid and a Kramers-Kronig consistent fit based on the matrix formalism (see Sec. 3.2.3) has to be performed. This can be and was done, of course, also in the thin film regime giving the similar results as determined by the thin film approximation shown in Fig. 5.30. The thickness dependent fit (dashed grey curve) describes the experimental data very well. The DIP film is described by a homogeneous layer modeling  $\varepsilon_2$  with 8 Gaussian oscillators as depicted in Fig. 5.31b) for  $d = 3.2\text{ nm}$ . The first three visible transitions are described by two Gaussians while the fourth modes can be modeled by a single Gaussian. The remaining Gaussian accounts for transitions at higher energies. Although the number of Gaussians



in the low energy range seems to be reducible for  $d = 3.2$  nm, it becomes necessary for higher thicknesses to correctly model the line shape. In comparison, the in-plane component measured *ex-situ* by ellipsometry was described by ten Gaussian oscillators. The additional oscillators mainly accounted for some background, which is not present in the DRS spectra.

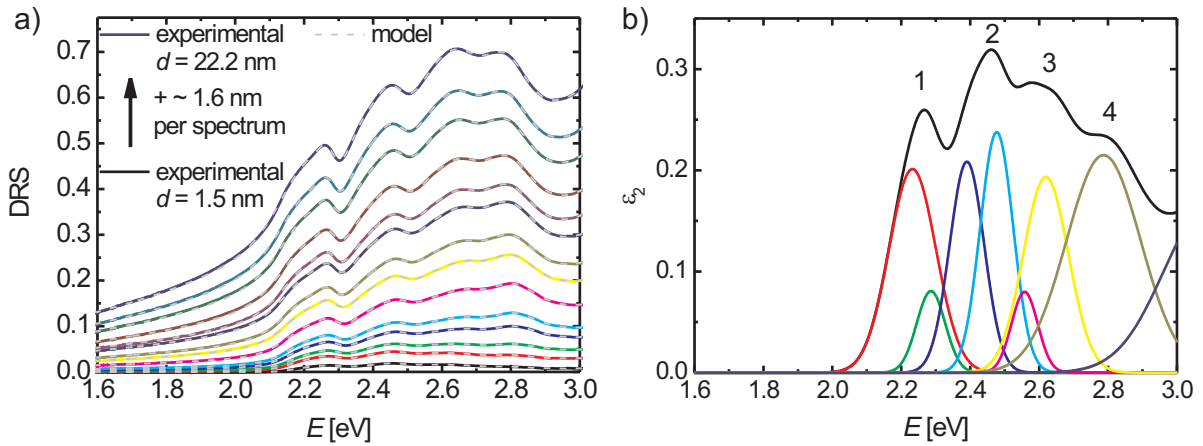


**Figure 5.31:** a) Experimental DRS spectra at different DIP film thicknesses varying from 1.5 nm to 22.2 nm in steps of  $\sim 1.6$  nm per spectrum. The film is grown at  $T = 130$  °C. The fit using eight Gaussians for describing the dielectric function  $\epsilon_2$  of the DIP film is plotted for each thickness as dashed grey lines. It describes the data very well. b) Corresponding fit result  $\epsilon_2$  at  $d = 3.2$  nm obtained with eight Gaussian oscillators. Four distinct modes are visible that are labeled by numbers.

The resulting spectra for other thicknesses are plotted in Fig. 5.32 where  $d$  varies from 1.5 nm to 22.2 nm in steps of  $\sim 1.6$  nm. The real part of the dielectric function plotted in a) increases constantly with thickness, showing the biggest change between  $d = 1.5$  nm (black curve) and  $d = 3.2$  nm (red curve). This step like behavior cannot be considered significant, since in the thin film limit DRS data are not sensitive to  $\epsilon_1$  (see eq. 4.4), which therefore cannot be determined correctly. For higher thicknesses the results are more reliable and the increasing offset of  $\epsilon_1$  might be due to increasing transitions at higher energies.

In Fig. 5.32b) the imaginary part  $\epsilon_2$  is plotted showing also significant changes during growth. The most dramatic change appears between 2.7-2.9 eV in the spectra, where the fourth mode increases strongly. Already at  $d = 3.2$  nm an increased intensity of the fourth mode is visible, which grows further with increasing thickness. It mainly affects the third mode while the intensity of the first two transitions in the lower energy range remain nearly unaltered during growth. In order to quantify the thickness dependence, the relative intensity between the fourth mode and the first mode is plotted in Fig. 5.33a) versus thickness. A strong increase of the fourth mode until  $\sim 12$  nm is visible, where saturation sets in. The thin film range, where no changes occur, can be better observed

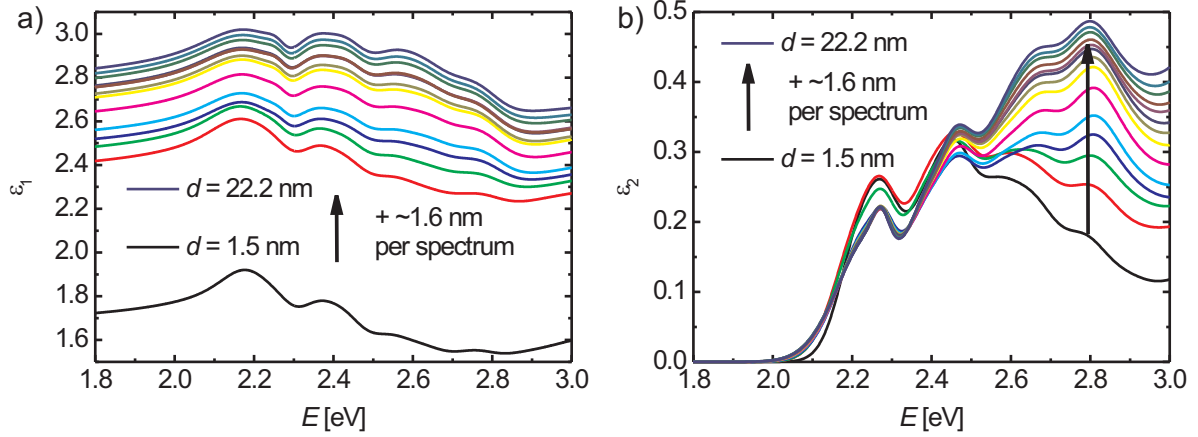


**Figure 5.32:** Dielectric function for different thicknesses obtained during DIP film growth on glass at  $T = 130^\circ\text{C}$ . The film thickness  $d$  varies from 1.5 nm to 22.2 nm in steps of  $\sim 1.6$  nm per spectrum. a) The real part  $\epsilon_1$  shows mainly an increasing offset during growth. b) The imaginary part  $\epsilon_2$  shows, that a fourth mode appears during growth, which is indicated by an arrow.

in the  $1/d$  plot, which is therefore shown in the inset (black curve).

Additionally, the line shape of the first two modes changes with thickness but no energy shift is visible. Since the effect is quite small, the normalized  $\epsilon_2$  is plotted in Fig. 5.33b) for three different thicknesses showing only the energy range of the first transition.

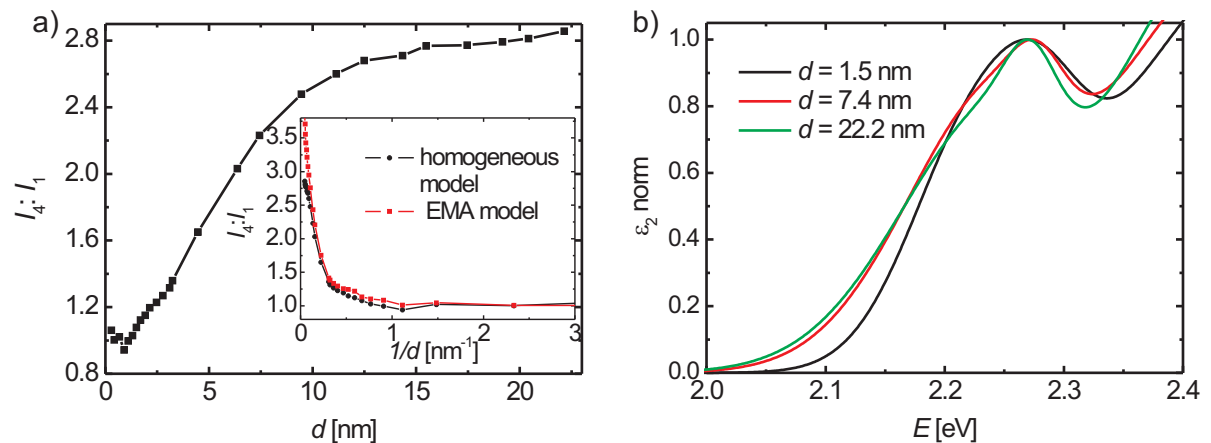


**Figure 5.33:** a) Thickness dependence of the relative intensity between first and fourth mode: It increases up to  $\sim 12$  nm where saturation sets in. The inset shows the  $1/d$  dependence allowing to better investigate the lower thickness range, where no changes are visible. The additional red curve is obtained by taking roughness into account (see text) and agrees well. b) The normalized imaginary part of the dielectric function for three different thicknesses showing the changes of the spectral line shape during growth.

While for thicknesses smaller than  $d = 1.5$  nm the first mode can be described by a single Gaussian, a low energy shoulder appears during growth, which is getting more pronounced with increasing thickness. Although this spectral change is small, it is not a fitting artefact, because the line shape can be read off the DRS raw data directly. For thin films  $\varepsilon_2$  can be calculated directly from the DRS-data using eq. 4.4 and at higher thicknesses the observed line splitting agrees to *ex-situ* ellipsometry results.

**5.5.2.1.3 Effect of roughness** So far, the film was assumed to be perfectly homogeneous and flat, but AFM measurements show that DIP films on glass exhibit significant roughness (see Sec. 5.3.2). Roughness can be included to the layer model by using an additional EMA layer, which increases the number of fit parameters significantly. The thickness and the underlying homogeneous film thickness are correlated and difficult to determine separately. Furthermore, the evolution of roughness during growth is not well known for DIP on glass, although *ex-situ* measured AFM pictures give some insight. For simplicity roughness is kept constant during film growth and the complete DIP film is described by an EMA layer. To further reduce the number of fit parameters, the material density of void and DIP is set to 50%. For keeping the molecular density constant the thickness is increased by a factor of two compared to the homogeneous DIP layer. These model parameters might not account for the real roughness perfectly, but they can be regarded as the limiting case in contrast to the homogeneous layer model. The real film morphology will lie between both limiting models. The influence of roughness onto the relative intensity  $I_4 : I_1$  is shown in the inset of Fig. 5.33a), where  $I_4 : I_1$  versus the inverse thickness is plotted for both kind of data analyses, i. e. assuming the DIP film to be homogeneous and flat (black curve) and modeling the film by an EMA layer (red curve). It is clearly visible that the thickness dependence is not affected by using an EMA layer, which agrees especially well for low thicknesses. For higher thicknesses the absolute value of  $I_4 : I_1$  is bigger for the EMA model but the shape of the curves are still very similar. Quantitatively, the EMA fit leads to higher absolute values of  $\varepsilon_2$ , which are by a factor of  $\sim 1.7$  increased compared to the homogeneous fit result. Nevertheless, the thickness dependent behavior of the fourth mode shows good agreement between both data analyses. The effect of roughness rather influences the absolute  $\varepsilon_2$  values than the relative changes during growth.

**5.5.2.1.4 Comparison to ellipsometry and solution spectra** The normalized  $\varepsilon_2$  is plotted in Fig. 5.33 for ellipsometry and DRS fit results to compare their line shapes. The red curve corresponds to the in-plane component and the green curve to the out-of-plane component of the ellipsometry result determined *ex-situ* at  $d = 33$  nm. In addition to DRS results at low ( $d = 1.5$  nm) and at high ( $d = 22.2$  nm) thicknesses are shown. As can be seen the DRS result at  $d = 22.2$  nm reproduces the ellipsometry in-plane component quite well, while the DRS line shape at  $d = 1.5$  nm resembles more that of the ellipsometry out-of-plane component. Still, differences are visible: The transitions are broader in the DRS spectrum at  $d = 1.5$  nm compared to the out-of-plane spectrum

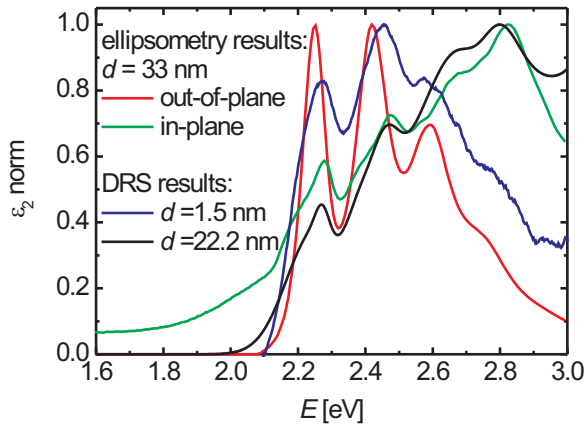


**Figure 5.34:** Normalized imaginary part  $\varepsilon_2$  of the dielectric function to compare line shapes of ellipsometry and DRS results: For  $d = 1.5$  nm the DRS result resembles rather the out-of-plane component while for  $d = 22.2$  nm it approaches the shape of the in-plane component.

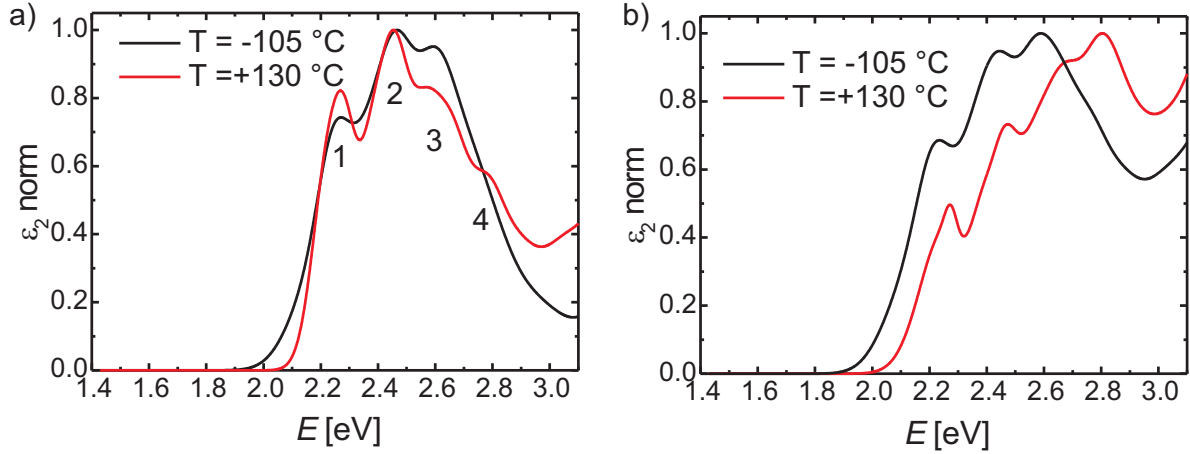
and also the relative intensities differ. The offset visible in the ellipsometry in-plane component, which is probably a fitting artefact, does not appear in the DRS spectra.

Comparing the absolute values between ellipsometry and DRS results shows that the DRS result is by a factor of  $\sim 1.6$  smaller than the in-plane component of the ellipsometry result. As can be shown by measurements at a different system (see Sec. 5.5.3), this difference is not caused by systematic errors between both methods. It most likely rather arises due to different morphologies between films on different substrates: While the ellipsometry result is obtained by a multiple sample analysis, using Si substrates covered with native and thermal oxide, the DRS results are based on DIP films grown on glass substrates, which are significantly rougher (see Sec. 5.3.2). Fits based on the EMA-model show that if roughness is included into the data analysis, the absolute number of  $\varepsilon_2$  increases, reducing the difference in absolute values between ellipsometry and DRS results.

### 5.5.2.2 Film growth at $T < -100$ °C

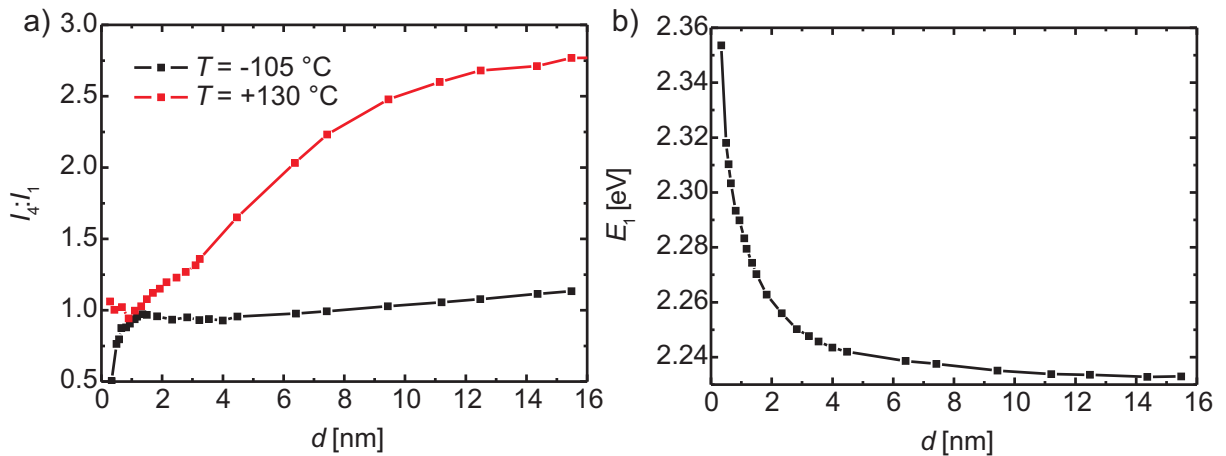
The low temperature (LT) growth of DIP on glass differs from the high temperature (HT) growth, as it is expected from X-ray and AFM measurements (see Sec. 5.3.1 and 5.3.2). Although the absolute values of the spectra as well as their shape could not be reproduced exactly between different films grown at  $T < -100$  °C, which might be due to uncertainties of the substrate temperature, the overall qualitative differences between LT and HT growth are significant and always the same.

Fig. 5.35 shows representatively the normalized dielectric function of a film grown at low (black curve) and at high (red curve) temperature for a)  $d = 1.5$  nm and b)  $d = 14.4$  nm. Although the line shape of the HT and LT spectra differs less at  $d = 1.5$  nm than at  $d = 14$  nm, also at low thicknesses significant differences can be observed, which are very well reproducible for different film growths. First, the relative intensity between the first and the third mode differs. Second, the lines are broadened in case of LT growth, which might, third, lead to the effect that no separate fourth mode is visible for LT growth in



**Figure 5.35:** Normalized imaginary part  $\varepsilon_2$  of the dielectric function for two films grown at  $T = -105\text{ }^\circ\text{C}$  (black curve) and at  $T = 130\text{ }^\circ\text{C}$  (red curve) plotted for different thicknesses: a)  $d = 1.5\text{ nm}$ , b)  $d = 14\text{ nm}$ .

contrast to HT growth. At  $d = 14\text{ nm}$  even bigger differences occur and the increased fourth mode visible in the HT spectrum cannot be observed in the LT spectrum. The almost complete absence of the fourth mode is not for all LT films observable but in every case the fourth mode is less pronounced compared to the HT film. Fig. 5.36a) shows the thickness dependence of  $I_4 : I_1$  for a film grown at LT revealing significant differences compared to the additionally plotted HT result, although the fourth mode increases slightly with thickness.



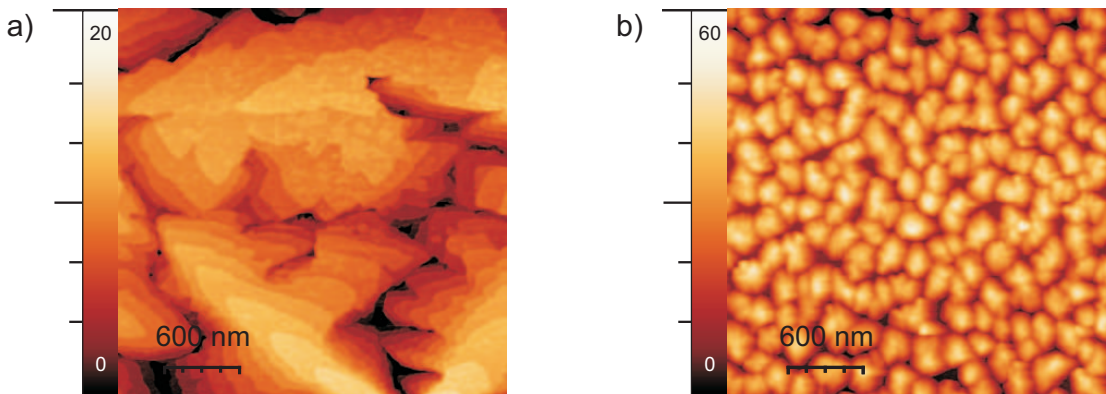
**Figure 5.36:** a) Relative intensity between fourth mode and first transition for HT ( $T = 130\text{ }^\circ\text{C}$ ) and LT ( $T = -105\text{ }^\circ\text{C}$ ) growth versus film thickness, revealing strong differences. b) Energy position of the first transition  $E_1$  during LT growth versus thickness. In case of HT growth no energy shift is visible, rather a line splitting.

Furthermore, at  $d \approx 14$  nm the LT spectrum is red-shifted by more than 110 meV compared to the HT spectrum, whereas at  $d \approx 1.5$  nm the energy positions between LT and HT spectra agree well. No energy shift occurs for HT films during growth. The energy position of the first peak  $E_1$  is plotted for LT growth versus film thickness in Fig. 5.36b). A similar shift can be observed for transition 2 and 3, whereas transition 4 does not show such a pronounced red-shift. Since the line shape does not split in case of LT growth, the transitions can be described by single Gaussians, simplifying the analysis of the energy position. It can be seen that the peak shifts already in the sub-monolayer range strongly, whereas above  $\sim 5$  nm saturation takes place. This will be further discussed in Sec. 5.5.4.

### 5.5.3 PEN film growth

Additionally to DIP films, also the optical properties of PEN films are studied after and during growth. One reason for studying PEN film growth is that both methods, ellipsometry and DRS, can be better compared for PEN films than for DIP films as will be shown and discussed in the following. Another reason is that PEN is a widely studied molecule [36] but only little is known about its optical properties during growth. Since the morphology plays a significant role for interpreting the real-time spectra, first AFM measurements of PEN on Si and on glass will be briefly presented. This is followed by an introduction of the static spectra, which were determined by A. Hinderhofer in the framework of his diploma thesis [19,20]. Similar to DIP they serve as a bulk-like reference for the real-time measurements that are presented finally.

#### 5.5.3.1 Film morphology



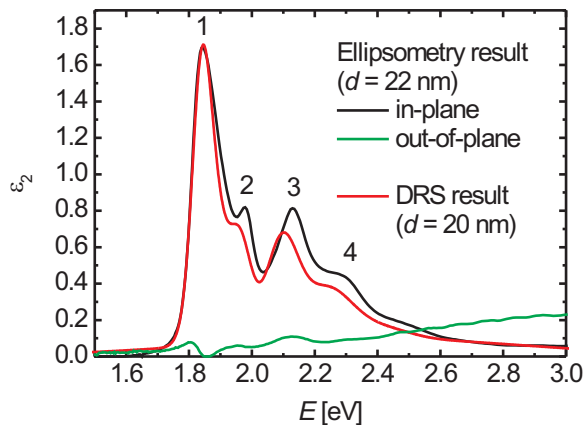
**Figure 5.37:**  $3 \times 3 \mu\text{m}^2$  AFM height scans for PEN grown simultaneously a) on  $\text{Si}_{\text{Ntve}}$  and b) on glass at  $T = 26^\circ\text{C}$ . The film thickness is  $d = 22.5$  nm.

Fig. 5.37 shows  $3 \times 3 \mu\text{m}^2$  AFM height scans obtained for PEN films grown simultaneously a) on  $\text{Si}_{\text{Ntve}}$  and b) on glass at RT. Similar to DIP the film on  $\text{Si}_{\text{Ntve}}$  exhibits monomolecular steps of  $1.7 - 2$  nm, which agrees to the (001) lattice spacing and the molecules

are standing nearly upright. The islands of PEN films on  $\text{Si}_{\text{Ntve}}$  extend more than  $1 \mu\text{m}$ . In contrast, they have a diameter of only  $\sim 200 \text{ nm}$  for PEN on glass, which resembles the finding for DIP: No mono-molecular steps are visible on glass and the molecular domains are significantly smaller. In contrast to DIP, the PEN film on glass is with  $\sigma = 9.1 \text{ nm}$  significantly rougher than on  $\text{Si}_{\text{Ntve}}$ , where  $\sigma = 3 \text{ nm}$  can be observed, which agrees to results published in the literature [126].

### 5.5.3.2 Static uniaxial dielectric function

The *ex-situ* spectra for  $\sim 20 \text{ nm}$  thick PEN films grown at RT on  $\text{Si}_{\text{Ntve}}$  were determined using the same multiple sample analysis as for DIP thin films (see Sec. 5.4.1). Similar to DIP films on  $\text{Si}_{\text{Ntve}}$  also PEN films are polycrystalline exhibiting a pronounced uniaxial anisotropy, which is shown in Fig. 5.38. The  $a$  and  $b$  axes of the crystallites coincide with the experimentally determined in-plane component (black curve), while the out-of-plane component (green curve) corresponds nearly to the crystallographic  $c$  axis. In contrast to DIP films, the in-plane component is by a factor of  $\sim 5$  bigger than the out-of-plane component that is difficult to determine reliably.



**Figure 5.38:**  $\varepsilon_2$  determined for PEN films on  $\text{Si}_{\text{Ntve}}$  *ex-situ* from ellipsometry, showing a pronounced uniaxial anisotropy, where the out-of-plane component is significantly smaller than the in-plane component. The *in-situ* DRS results agree well with the in-plane component determined by ellipsometry.

The measured anisotropy is in good agreement with the tilt angle  $\alpha = (10 \pm 5)^\circ$  of the PEN molecules on  $\text{Si}_{\text{Ntve}}$  [127] taking into account that the transition dipole is essentially oriented along the short axis of the molecule. The pronounced first peak of the in-plane component is positioned at  $E_1 = 1.85 \text{ eV}$  indicating the optical band gap, which is in agreement with absorption measurements on glass and previous ellipsometry measurements [72, 128]. The spectral feature at  $1.97 \text{ eV}$ , labeled with 2, has been assigned to Davydov splitting [128, 129] but is currently still debated [130]. The subsequent peaks above  $2 \text{ eV}$  (3 and 4) exhibit an equal energy spacing of  $170 \pm 10 \text{ meV}$  and are, therefore, likely to be associated with a vibronic progression.

Similar to DIP, the *in-situ* and *ex-situ* ellipsometry results agree well, despite of some small differences and strong oxidation effects can be excluded as they occur, for instance,

in rubrene [124]. In Fig. 5.38 additionally the dielectric function for a similarly thick PEN film is shown, which is determined by *in-situ* DRS measurements. As can be seen, the absolute values agree perfectly between the DRS-result and the in-plane component of the ellipsometry measurement. Also the line shape can be reproduced well although some differences for higher energies are observable. The fact that the DRS measurement on Si-substrates works significantly better for PEN than for DIP is due to the following reasons: First, the in-plane component of PEN films is about 3 – 4 times bigger than the in-plane component of DIP films leading to a stronger signal. Second, the band gap of PEN films is red-shifted compared to DIP films and the observed transitions occur in the energy range, where the measured reflected intensity signal is higher (compare Fig. 5.29), which reduces the noise.

### 5.5.3.3 PEN film growth on $\text{Si}_{\text{Ntve}}$

Fig. 5.39a) shows the thickness dependent DRS signal during PEN film growth on  $\text{Si}_{\text{Ntve}}$  at RT. For the curves shown, the thickness varies from 1.5 nm to 20 nm in steps of about one ML. The spectral features of the PEN in-plane component are clearly visible in the experimental DRS data. While the overall DRS signal decreases, the signal of the first transition increases and shows a pronounced energy shift to lower energies with increasing thickness. Since additionally the real part of the dielectric function influences the DRS signal for higher thicknesses, which can cause also some energy shift in the raw data, a fit based on the matrix formalism and seven Gaussian oscillators is performed, which describes the experimental data well.

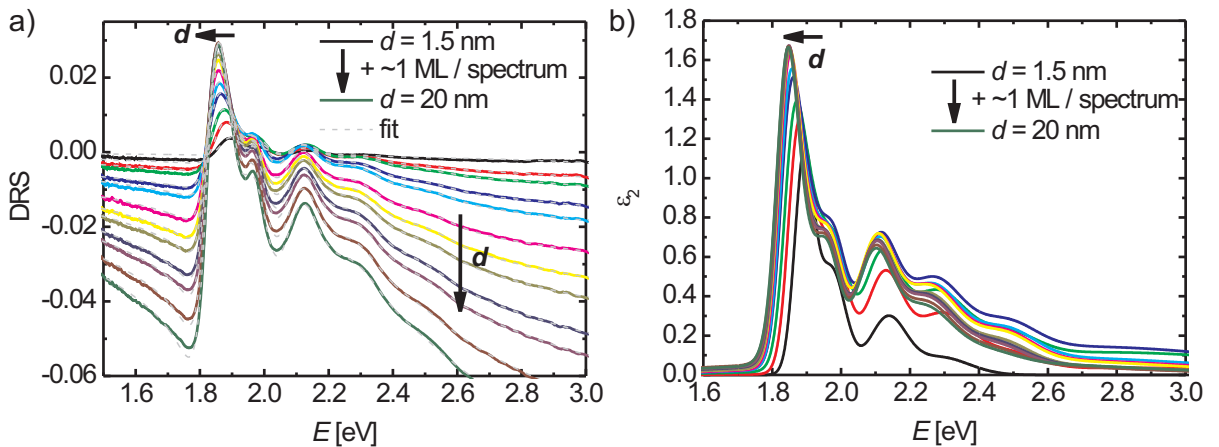


**Figure 5.39:** a) Real-time DRS data with Gaussian fit during PEN film growth on  $\text{Si}_{\text{Ntve}}$  at room temperature. b) Resulting imaginary part of the dielectric function at different thicknesses, which varies from 1.5 nm to 20 nm in steps of about 1 ML.

The resulting dielectric function  $\epsilon_2$  is shown in Fig. 5.39b). The shift to smaller energies during growth is clearly visible for the first and the following transitions. The relative



intensities do not change and the thickness dependence of the absolute intensity is most likely due to uncertainties of the film thickness that may be related to the changing roughness during growth.

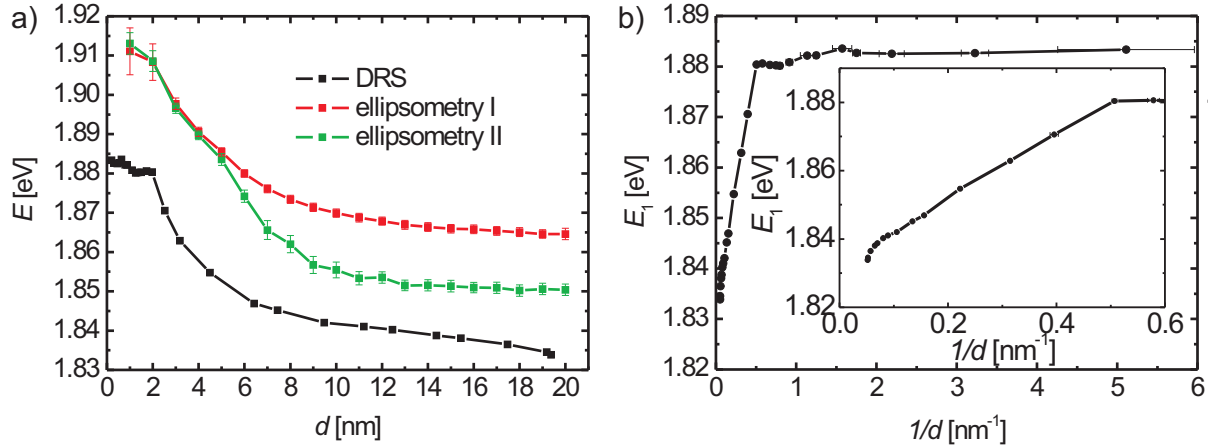


**Figure 5.40:** a) Thickness dependent energy position of the first peak for PEN on SiN<sub>tve</sub> determined by ellipsometry and DRS measurements agreeing qualitatively. The difference between Fit I and II stem from different fitting procedures (see text). b)  $E_1$  determined by DRS is plotted versus the inverse thickness to better compare the small thickness range (i. e. high  $1/d$ ), where no changes are visible above  $1/d \approx 0.6$  nm<sup>-1</sup> ( $d \approx 2$  nm, see a), see also inset.

The energy position of the first peak is plotted in Fig. 5.40a) versus film thickness, showing an overall energy shift of more than  $\sim 40$  meV. While the energy position stays nearly constant within the first ML, a significant decrease is visible above  $\sim 2$  nm, which starts to saturate above  $\sim 7$  nm. Additional real-time ellipsometry measurements reveal a similar result (see black and green curve) although some offset of  $\sim 15$  meV is observable, which is likely due to systematic experimental differences. The ellipsometry fits I and II differ in the fitting procedure, indicating that the Gaussian oscillators of the other transitions influence each other leading to additional error bars of the fit. This is also observed for the DRS measurements. Nevertheless, the overall thickness dependence is unaffected by these issues. The inverse thickness dependence of the DRS result is plotted in Fig. 5.40b), which allows to observe the small thickness (i. e. high inverse thickness) range in more detail. It shows clearly that the energy position is constant above  $0.6$  nm<sup>-1</sup> ( $d \approx 2$  nm), whereas a linear behavior is observable below, which is plotted additionally and enlarged in the inset.

The DRS analysis reveals that also peaks at higher energies are red-shifted during growth (see Fig. 5.39b). The maximal energy shift varies between 30 meV and 50 meV, but the thickness dependent behavior agrees for all peaks: In the sub-monolayer range only a small shift is observed, while the strong red-shift sets in above  $\sim 2$  nm, which starts to saturate above  $\sim 7$  nm.

### 5.5.3.4 PEN film growth on glass

Differences are observed between PEN film growth on glass and on  $\text{Si}_{\text{Ntve}}$ , as Fig. 5.41a) and b) illustrate, where the energy position  $E_1$  of the first peak is plotted versus thickness and versus the inversed thickness, respectively, for both sample growths measured by DRS. While the overall red-shift of  $\sim 40$  meV can be observed also for PEN on glass, and at  $d \approx 0.3$  nm ( $1/d \approx 3$  nm $^{-1}$ ) the energy position agrees for both films, significant differences are observable during growth. In case of PEN on glass the shift starts already in the sub-monolayer range following a different thickness behavior. In contrast to PEN on  $\text{Si}_{\text{Ntve}}$ , the strong energy shift reduces above  $\sim 2$  nm, compare Fig. 5.41a). Furthermore, the inverse thickness plot does not show a linear behavior for PEN on glass in the lower inverse thickness range (see inset of Fig. 5.41b).

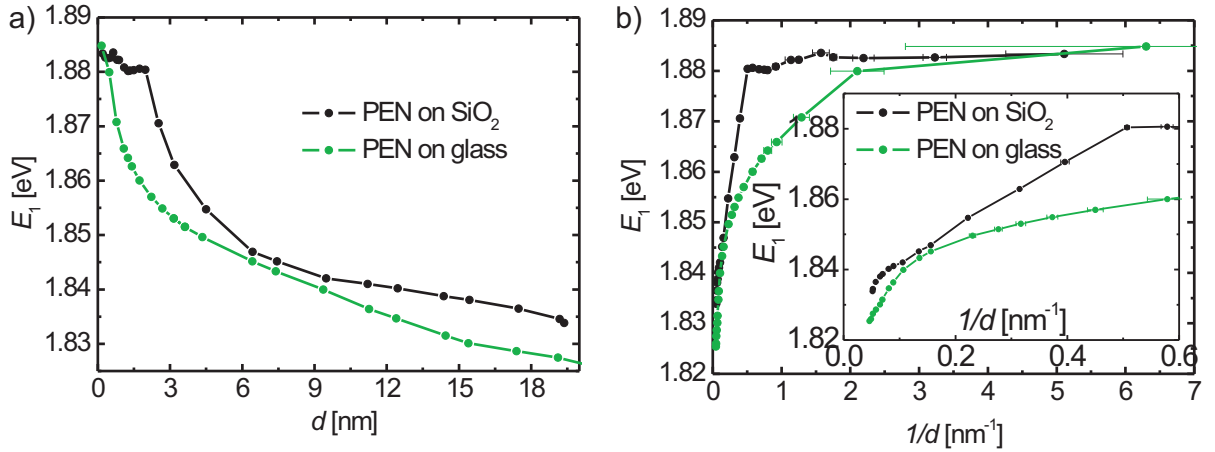


**Figure 5.41:** Comparison between PEN film growth on  $\text{Si}_{\text{Ntve}}$  (black curve) and on glass (green curve): a) Thickness dependence, b) inverse thickness dependence of  $E_1$ , both showing significant differences. The inset of b) plots the low inverse thickness range.

Apart from the thickness dependence of the energy positions, also the absolute values of  $\varepsilon_2$  differ between PEN on glass and on  $\text{Si}_{\text{Ntve}}$ . In accordance with the analysis of DIP films, where the limiting case of a complete rough and smooth film was investigated (see Sec. 5.5.2),  $\varepsilon_2$  of PEN films on glass is by a factor of  $\sim 2$  smaller compared to PEN on  $\text{Si}_{\text{Ntve}}$  when modeling the film without EMA layer. The thickness dependence of the energy position is not affected by the data analysis, whether an EMA layer is included or not, it rather affects the absolute values of  $\varepsilon_2$ .

## 5.5.4 Discussion

In all real-time measurements spectral changes are observed during film growth that depend on the growth condition as well as on the thickness range and on the sample

under investigation. The different optical changes can mainly be categorized as follows: First, a transition arising during growth and, second, an energy red-shift with increasing film thickness. The arising transition is only observed for HT growth of DIP on glass, indicating that this effect is intimately related to the specific properties of DIP thin films. In contrast, the energy shift is a more general observation that appears for any sample under investigation except for DIP HT film growth. The energy shift differs mainly quantitatively between different samples. Furthermore, it is important to note that in some cases also thickness ranges exist, where no spectral changes occur.

Different types of interactions play a key role for optical thin film spectra that are illustrated in Fig. 5.42a):

1. Coupling between molecules within one molecular layer (in-plane), which is believed to be strongest for upright standing molecules due to the strong  $\pi - \pi$  interaction.
2. Coupling between molecules in adjacent layers (out-of-plane).
3. Coupling between molecules and the substrate.

Obviously the ratio between all three effects changes during film growth, which can give rise to the observed optical changes.

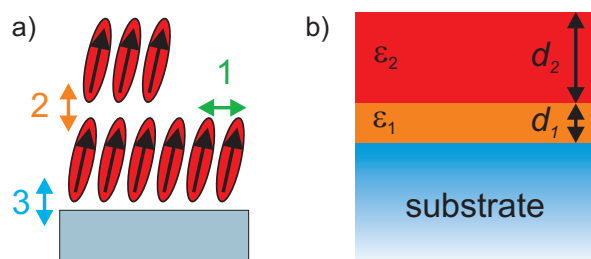


**Figure 5.42:** a) Different molecular interactions: 1) within one ML, 2) between different ML's, 3) with the substrate. b) Layer model to account for different optical properties within the film due to interactions with the substrate.

The most simple models that may be considered for describing the observed optical behavior during growth, are:

1. No spectral changes occur during growth and the optical spectra do not depend on the film thickness.
2. The film can be modeled as a composition of two different layers having different optical properties, which do not change during growth. One layer represents the optical bulk properties, whereas the other layer can be either an interfacial layer close to the substrate, as it is illustrated in Fig. 5.42b), or a surface layer on top of the film. In both cases, the surface to volume ratio changes during growth and the bulk properties get more pronounced.

Of course, also more complex models are possible, where the film is described by additional layers, including e. g. a roughness layer. Nevertheless, the simple models are a good

starting point to analyze the observed changes, and they can be extended if necessary. Furthermore, it should be mentioned that these models are independent of the exact nature of the optical properties under investigation, i. e. whether a mode arises or an energy position shifts. They describe solely the thickness dependence of the spectral feature.

In the following, the experimentally observed spectral behavior is discussed on the basis of both models starting with the arising transition of DIP during growth.

#### 5.5.4.1 Transition arising during growth

**5.5.4.1.1 Thickness dependence** In case of DIP grown at  $T = 130$  °C on glass (HT films) a fourth mode appears during growth in the high energy range. Before the underlying mechanism will be discussed in some detail, first the thickness dependence is characterized. The most simple model, where no optical changes take place, obviously does not describe the DIP HT film growth on glass. In contrast, the model cannot be excluded for DIP film growth on Si, since X-ray data do not show strong evidence for structural changes that affect the optical properties during growth. Furthermore, the optical real-time data do not give unambiguous results that can clarify this issue. Therefore, the following discussion will be restricted to DIP film growth on glass.

While for thicknesses below 1.6 nm no spectral changes are visible, above 1.6 nm a strong increase of the fourth mode appears and in the simplest case the thickness dependence of model 2 has to be taken into account: The DIP film is composed of two different layers with thicknesses  $d_1$ ,  $d_2$  and complex dielectric functions  $\varepsilon_1$ ,  $\varepsilon_2$  (see Fig. 5.42b). The average dielectric function observed in the experiments is then given by:

$$\varepsilon_{\text{average}} = \begin{cases} \varepsilon_1 & \text{for } d < d_1 \\ \varepsilon_2 + \frac{d_1}{d}(\varepsilon_1 - \varepsilon_2) & \text{for } d > d_1 \end{cases} \quad (5.12)$$

using  $d = d_1 + d_2$  to describe the complete film thickness. Fig. 5.43 shows the experimental data plotted in a) versus  $d$  and in b) versus  $1/d$  together with two fits. Fit 1 (red curve) is based on the equation

$$I_4 : I_1 = a + b/d \quad (5.13)$$

where  $a$  and  $b$  are fit parameters. It describes the experimental data for thicknesses above 3 nm ( $1/d < 0.3$  nm) well. For this thickness range a linear dependence versus  $1/d$  can be observed, see also the inset of Fig. 5.43b).  $d_1 = 3.1$  nm can be determined from the slope  $b$ , if the experimentally determined dielectric function at 22 nm is used as the 'bulk' reference  $\varepsilon_2$  and the dielectric function below 1.6 nm is used for  $\varepsilon_1$ . Furthermore, Fig. 5.43b) shows that for high  $1/d$  values, e. g. for small thicknesses, the relative intensity  $I_4 : I_1$  stays constant, which corresponds to  $d < d_1$  in the model.

Although this simple model describes the data for low and high thicknesses well, the thickness range between 3 and 1.5 nm is not perfectly described indicating that the film

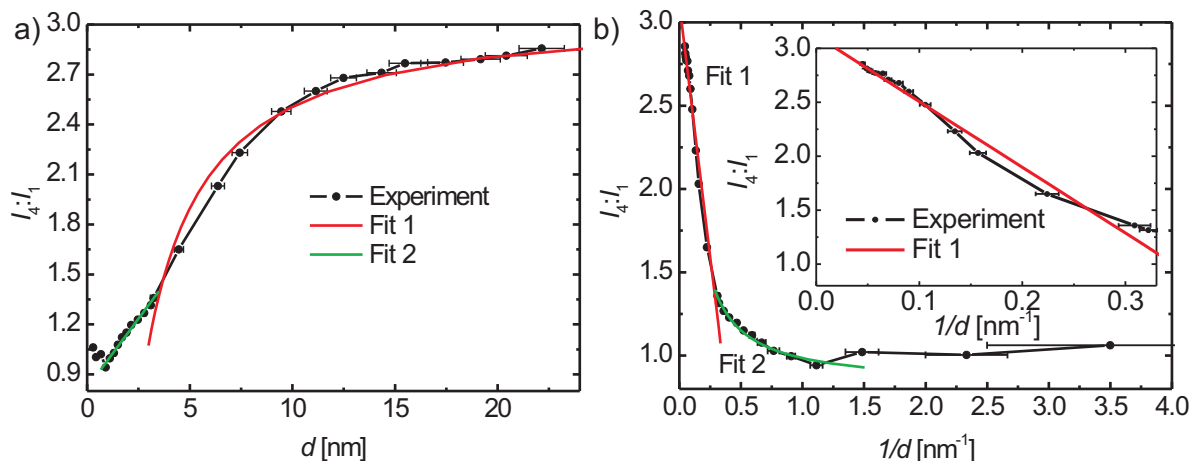


**Figure 5.43:** Thickness dependence of the fourth mode versus a) thickness and b) inversed thickness. Fit 1 based on equation  $I_4 : I_1 = a_1 + b_1/d$  describes the linear behavior below  $0.3 \text{ nm}^{-1}$  (see also inset of b), giving the following results:  $a_1 = 2.8$ ,  $b_1 = -3.6 \text{ nm}$ . Fit 2 based on  $I_4 : I_1 = a_2 + b_2 \cdot d$  describes the data well for  $d = 1 - 3 \text{ nm}$  with  $a_1 = 0.82$ ,  $b_1 = 0.17 \text{ nm}^{-1}$ .

growth is more complex than captured by the model. Including additional layers for describing the DIP film does not seem to be appropriate since the experimental  $1/d$  data do not show a linear behavior with different slopes.  $I_4 : I_1$  is rather proportional to  $d$  as can be seen in Fig. 5.43a), where Fit 2 (green curve) corresponds to a linear fit  $I_4 : I_1 = a_2 + b_2 \cdot d$  describing the data for  $d = 1 - 3 \text{ nm}$  very well. These deviations from model 2 show that the film cannot be described by two (or three) distinct layers. Instead a continuous transition from 'state 1' (i. e. surface/interfacial layer properties) to 'state 2' (i. e. bulk-like properties) has to be considered without sharp interfaces.

In conclusion, the thickness dependence of the fourth mode indicates that a surface or interfacial layer exists, which differs optically from the bulk properties. In the following, possible reasons are discussed that could explain the observed thickness dependence.

**5.5.4.1.2 Nature of the fourth mode** Although the exact nature of the fourth mode is not yet fully understood, it may be interpreted as contributions from Frenkel and (CT) excitations of higher transitions (see Sec. 5.4.3.4). It is clear that the fourth mode is definitely a signature of the intermolecular coupling, which is specific for DIP HT films, since it does not occur in the monomer spectrum. Furthermore, it is significantly less pronounced for LT films where the fourth mode does nearly not appear during growth. LT films exhibit less structural order than HT films as X-ray and AFM measurements show. This can be understood in terms of the kinetic energy of the adsorbing molecules, which is decreased by the lower substrate temperature. The reduced molecular diffusion on the surface does not allow to form as highly oriented structures for  $T = -105 \text{ }^\circ\text{C}$  as for  $T = 130 \text{ }^\circ\text{C}$  film growth. Since the fourth mode is less pronounced at LT film growth,

it therefore can be regarded as a measure of the crystalline order.

X-ray real-time measurements during HT growth of DIP on  $\text{Si}_{\text{Ntve}}$  do not indicate significant changes of the structural order during growth except for some transient changes in the in-plane structure within the first few ML's [50]. Therefore, and since the fourth mode is believed to be related to the structural order, it is not immediately obvious that the fourth mode changes during growth, especially at higher thicknesses. Nevertheless, the DRS results are obtained for DIP on glass, where the structural order of the films differs in some aspects compared to films grown on  $\text{Si}_{\text{Ntve}}$ . While the overall crystalline structure agrees between DIP films on glass and on  $\text{Si}_{\text{Ntve}}$ , as the same Bragg peak in X-ray measurements shows (see Sec. 5.3.1), DIP films on glass exhibit higher roughness, which is most pronounced for lower film thicknesses. Therefore, the growth behavior of DIP on glass and thus the optical properties during growth cannot be regarded as identical compared to DIP on Si, although the optical spectra agree for high thicknesses ( $d > 20$  nm) quite well. Thus, possible structural changes, that could occur during DIP growth on glass, will be discussed in the following.

**5.5.4.1.3 Molecular reorientation during growth** One possible structural change during growth is molecular reorientation, which would give rise to a different dielectric function in the first ML compared to the bulk. Since  $\varepsilon_2$  differs significantly between the in-plane and the out-of-plane component, molecular reorientation would strongly influence the spectra. It could be induced by surface roughness and/or by coupling to the substrate. The latter is not very likely since  $\text{Si}_{\text{Ntve}}$  is an inert substrate and the intermolecular coupling is typically stronger than the coupling to the substrate, leading to standing upright molecules. Furthermore, for DIP on Si substrates covered by native oxide, no reorientation effects in the first few ML's are observed during growth by X-ray reflectivity [14]. Also AFM pictures for DIP on  $\text{Si}_{\text{Ntve}}$  support that the molecules are standing upright in the first ML [21]. Nevertheless, chemical differences between quartz glass and native oxide covering Si could lead to a different coupling between the molecules and the substrate inducing molecular reorientation. However, it is more likely that the surface roughness of glass could induce some disorder in the first few ML's, giving rise to nearly lying down molecules. Above a certain thickness, where the molecules have filled the unevenness, the well ordered thin film structure could start to grow.

For higher molecular tilt angles  $\Theta > 17^\circ$ , the observed  $\varepsilon_2$  should be significantly bigger compared to the highly ordered  $\sigma$ -phase with  $\Theta \approx 17^\circ$  because the in-plane projection of the dipole transition increases. In good approximation this can be modeled by mixing the spectra of the in-plane ( $\varepsilon_{\text{in}}$ ) and the out-of-plane component ( $\varepsilon_{\text{out}}$ ), determined by ellipsometry (on glass), with different fractions  $P$  between  $\varepsilon_{\text{in}}$  and  $\varepsilon_{\text{out}}$ : If all molecules are lying, the DRS result should resemble  $\varepsilon_{\text{out}}$ . If the molecules are standing (with  $\Theta = 17^\circ$ ), the DRS result should correspond to  $\varepsilon_{\text{in}}$ , which is experimentally observed for high film thicknesses. Although the DRS spectra in the sub-monolayer range resemble the line shape of  $\varepsilon_{\text{out}}$  (see Fig. 5.34), the absolute value of  $\varepsilon_2$  is by one order of magnitude smaller. This means that only a small fraction of molecules could lie down in the low thickness

range, which would be equivalent to the case that many molecules have only a slightly bigger tilt angle than  $\Theta = 17^\circ$ .

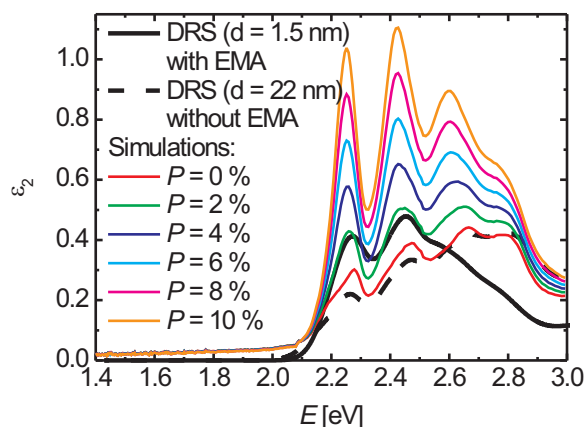


**Figure 5.44:** Simulated  $\varepsilon_2 = P \cdot \varepsilon_{\text{out}} + (1 - P) \cdot \varepsilon_{\text{in}}$  with different fractions  $P$ , modeling different molecular tilt angles  $\Theta$ .  $\varepsilon_{\text{out}}$  is the out-of-plane and  $\varepsilon_{\text{in}}$  the in-plane component determined by ellipsometry. The experimental DRS result at  $d = 22$  nm agrees well with the spectrum  $P = 0\%$ , whereas the spectrum at  $d = 1.5$  nm cannot be modelled correctly.

Fig. 5.44 shows the simulated spectra given by  $\varepsilon_2 = P \cdot \varepsilon_{\text{out}} + (1 - P) \cdot \varepsilon_{\text{in}}$  for different fractions  $P$ . It is clearly visible that the spectrum with  $P = 0\%$  corresponds to the DRS spectrum obtained at  $d = 22$  nm. If some additional broadening would be included, the spectral line shape with  $P = 10\%$  could resemble the DRS spectrum at  $d = 1.5$  nm, but the absolute intensities differ strongly. These differences have to be considered seriously, since real-time data detect relative changes during growth, which are quite accurately to determine. Nevertheless some uncertainties of the absolute values of  $\varepsilon_2$  may exist, which will be discussed in the following.

Uncertainties of the film thickness  $d$  have the strongest impact onto the absolute  $\varepsilon_2$ -values, especially for very thin films. Although  $d$  is determined by simultaneous QCM measurements, the QCM data are calibrated by ellipsometry or X-ray measurements post-growth at high thicknesses. Therefore, the following possibilities have to be taken into account, that introduce errors to  $d$ :

1. The roughness might change during growth affecting the film thickness.
2. The adsorption rate of the molecules might differ for molecules attaching to the substrate or attaching to the film. The QCM measurement cannot determine those differences affecting mainly the measurement at low thickness.

The second point, i. e. a variable adsorption rate, is difficult to quantify since the absolute number of adsorbed molecules needs to be determined for low thicknesses. Although differences between the adsorption rate at low and at high thickness might exist, they were not reported so far. Therefore, no strong impact onto the film thickness is expected, but it cannot be excluded completely. The first point, i. e. the effect of roughness, is more easily to quantify. The upper limit of the  $\varepsilon_2$  error bar can be estimated by assuming the film at low thicknesses to be completely rough (with EMA) and at high thicknesses

to be completely flat (without EMA). This leads to a maximal uncertainty of  $\varepsilon_2$  by a factor of  $\sim 2$ . Even if this error bar is taken into account, the DRS result at  $d = 1.5$  nm cannot be reproduced by any fraction  $P$ . It is clearly visible that, in case of molecular reorientation, the first two modes should rather decrease in contrast to the experimentally observed increase of the fourth mode. Therefore, deviations from the tilt angle  $\Theta = 17^\circ$  may occur, but they cannot solely explain the observed optical changes.

**5.5.4.1.4 Structural changes beyond molecular reorientation** Although molecular reorientation can be excluded as the only explanation for the arising fourth transition, general crystalline disorder at low thicknesses could still lead to the observed effect. Since the glass surface is quite rough, it is very likely that for films at small thicknesses the crystalline order is lower than at higher thicknesses, where the well known thin film phase evolves. The disorder does not have to affect the tilt angle, but it can be given by changed intermolecular distances (in-plane as well as out-of plane) or a changed herringbone angle between the molecules in the unit cell. If the fourth mode is due to a specific intermolecular coupling, those effects will have a strong impact onto the optical properties [121, 131]. LT film growths, where additional molecular disorder is created resulting in a significantly less pronounced fourth mode, support this idea.

The finding that no changes are visible for  $d < 1.6$  nm can also be understood, since the well ordered phase does not start to grow from the beginning. Scratches or bumps on the glass surface could serve as nucleation seeds, giving rise to low ordered molecular aggregates and only above a certain thickness the  $\sigma$ -phase starts to grow. Why this is the case at  $d = 1.6$  nm is not clear, but that this thickness corresponds to the thickness  $d_{\text{ML}}$  of 1 ML is probably a fortunate coincidence since the film does not grow in a layer-by-layer fashion. Additional structural investigations would be necessary to clarify the thin film structure on glass below  $d = 1.6$  nm.

**5.5.4.1.5 Concluding remarks** It can be concluded that the thickness dependence of the fourth mode indicates that a surface or interfacial layer for DIP grown at HT on glass exists, which differs optically from the bulk properties. Most likely some interfacial layer close to the glass substrate forms, which exhibits significantly less order compared to the thin film 'bulk' structure. This is supported by LT measurements, where the fourth mode is generally less pronounced due to lower ordering. Since the explanation is based on the fact that the substrate surface is rough, this effect is not expected to occur on the smooth  $\text{Si}_{\text{Ntve}}$  surface, where no changes are observed by ellipsometry in the low energy range.

#### 5.5.4.2 Energy shift during growth

**5.5.4.2.1 General origin and thickness dependence** A strong red-shift of the transitions by more than 110 meV is observed for DIP LT growth on glass for thicknesses



between  $d \approx 0.2$  nm and  $d \approx 15$  nm. Also PEN films exhibit a thickness dependent energy shift between thin and thick films ( $\Delta E_{\max} \approx 40$  meV) on Si<sub>Ntve</sub> as well as on glass, whereas for DIP on glass grown at  $T = 130$  °C rather a line splitting of the first two transitions appears than an energy shift.

Generally, a red-shift of transitions during growth is expected due to an increased intermolecular interaction, as reported e. g. for Alq<sub>3</sub> on Si(111) [132]. It arises mainly due to dielectric screening, considering the 'solvent' or environment shift, i. e. the shift of transition energies in the molecular crystal with respect to the free molecule. A similar peak shift was observed for PTCDA on mica [35, 23]. Only a small energy shift is reported in the sub-monolayer range, while a strong red-shift of 65 meV is observed between 2-4 ML, which becomes less pronounced for higher thicknesses. This thickness dependence was interpreted in terms of a changed surface to volume ratio and could be described by a  $1/d$  thickness dependence for  $d > 2$  ML. As proposed by Agranovich *et al.* [22] the outermost molecular layers are blue-shifted due to on-site effects, which can be understood by a decreased solid state shift caused by the reduced number of nearest neighbors, or in the continuum approach by a decreased dielectric screening for molecules sitting in the surface layers. Note, that this approach does not take any coupling to the substrate into account, which is believed to have only a minor impact onto the optical properties in case of Si<sub>Ntve</sub>.

This effect can be modeled by composing the film of two layers where one spectrum is shifted by  $\Delta E_{\text{surf}}$  relative to the other. In case of a single Gaussian the observed average dielectric function is then given according to Ref. [22] by:

$$\varepsilon_2 \propto (N - n) \cdot e^{-x^2} + n \cdot e^{-(x-\delta)^2} \quad (5.14)$$

with  $x = (E - E_0)/\sigma$  and  $\delta = \Delta E_{\text{surf}}/\sigma$ . The total number of ML's is given by  $N = d/d_{\text{ML}}$  and  $n$  is the number of ML's with a blue-shifted spectrum. Furthermore,  $\delta \ll 1$  since only one peak is experimentally observed and no peak splitting is visible. From the first derivative of eq. 5.14 the thickness dependent energy position  $E$  can be determined:

$$E \approx E_0 + n\Delta E_{\text{surf}}/N \quad (5.15)$$

where  $\Delta E_{\text{surf}}$  represents the energy shift of the transition in the outermost molecular layer with respect to the bulk transition energy  $E_0$ .

According to eq. 5.15 a linear behavior is observed for DIP films grown at LT on glass as well as for PEN on Si<sub>Ntve</sub> if the peak position is plotted versus  $1/d$ , see insets of Fig. 5.36 a) and b) respectively. In case of DIP, the energy shift starts to set in directly with the beginning of film growth. The fit  $E_1 = A + B/d$  with  $A = 2.23$  eV and  $B = 0.044$  eV/nm describes the data for all thicknesses well although of course small deviations occur. If the inverse thickness range is restricted below  $1 \text{ nm}^{-1}$  (i. e.  $d > 1$  nm), the fit works still better giving  $A = 2.23$  eV and  $B = 0.061$  eV/nm. The bulk transition energy  $E_0 = A$  does not depend on the thickness range. It agrees well with the peak position  $E_1$  observed at high thicknesses.

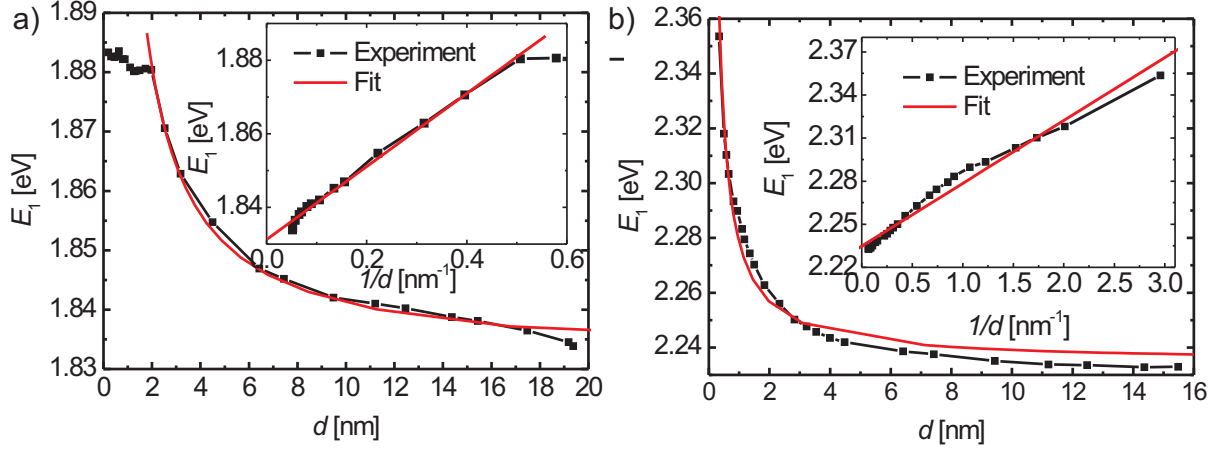


**Figure 5.45:** a) Energy position of the first peak for PEN on  $\text{Si}_{\text{Ntve}}$  versus film thickness and versus inversed thickness, see inset. A fit (red) based on  $E_1 = A + B/d$  with  $A = 1.83$  eV and  $B = 0.099$  eV/nm describes the data very well above 2 nm (below  $0.5$   $\text{nm}^{-1}$ ). b) Thickness dependence of  $E_1$  for DIP grown at  $T = -105$  °C on glass, showing a similar behavior as PEN. The shift is already observable for low thicknesses as can be also seen in the inset, where  $E_1$  is plotted versus  $1/d$ . The fit gives  $A = 2.23$  eV and  $B = 0.044$  eV/nm.

In contrast to DIP, the linear fit describes the PEN data only for inverse thicknesses below  $0.5$   $\text{nm}^{-1}$  (thicknesses above 2 nm), which corresponds roughly to 1 ML. Above  $0.5$   $\text{nm}^{-1}$  no energy shift is visible. The linear fit gives  $A = 1.83$  eV and  $B = 0.099$  eV/nm. Also for PEN the fitted bulk transition energy  $A = E_0 = 1.83$  eV agrees well with the energy position observed at high thicknesses. Deviations from the linear fit for PEN at small inverse thicknesses (high thicknesses) might be due to the fact that the 'bulk phase' starts to evolve. The dielectric function of this phase is not known, although the optical properties of single crystals are investigated in detail [133], but it is not clear whether they coincide with those of the bulk phase. Therefore, it is difficult to separate it from the 'thin film phase' in the optical spectra.

From the slope  $B = n \cdot d_{\text{ML}} \cdot \Delta E_{\text{surf}}$  the energy shift  $\Delta E_{\text{surf}}$  can be determined if  $n$  is known. In case of PTCDA  $n = 2$  was used to determine  $\Delta E_{\text{surf}} = 110$  meV [22, 23]. For PEN and DIP  $n = 1$  seems to be a more suitable choice since significant structural differences exist compared to PTCDA thin films. PTCDA molecules grow typically lying down forming  $\pi$ -stacked dimers with short intermolecular distances. They interact strongly along the out-of-plane direction, which can be observed optically by transitions from monomer (i. e. 1 ML) via dimer (i. e. 2 ML's) to oligomer (i. e.  $d \gtrsim 3$  ML's) spectra during film growth [23]. In contrast, DIP and PEN molecules are standing upright on  $\text{Si}_{\text{Ntve}}$ , even in the first ML as it is reported for PEN [134] as well as for DIP grown at HT [21]. Therefore, the intermolecular coupling for DIP and PEN is expected to be stronger along the in-plane direction where the  $\pi$ -overlap is larger. The coupling between different layers, probed by the optical real-time measurements, is expected to be less pronounced and only directly

neighboring layers influence each other. Therefore,  $n = 1$  seems to be better suited for DIP and PEN to determine  $\Delta E_{\text{surf}}$ . This is also valid for DIP grown on glass at LT, even if the structural order differs compared to films grown on  $\text{Si}_{\text{Ntve}}$  at HT, as optical real-time and X-ray measurements indicate. Even if the molecules grew lying down, which is not evidenced by X-ray measurements, the molecular interaction would be still expected to be smaller compared to PTCDA, since the  $\pi$ -stacking for DIP is less dense.

The blue-shift for the outermost layer is determined accordingly for DIP to be  $\Delta E_{\text{surf}} = 27 - 37$  meV (depending on the fitting range used) taking  $d_{\text{ML}} = 1.65$  nm into account. This appears not to be sensible, since an energy shift of 27 meV in the DIP surface layer cannot cause an overall shift of 110 meV. In this context it is important to note that eq. 5.15 assumes layer-by-layer growth, which is not the case for DIP grown on glass. Thus, the energy shift in the surface layer rather has to be estimated from the overall shift than from eq. 5.15, which is with  $\Delta E_{\text{surf}} \approx 110$  meV surprisingly high. It corresponds to the observed value for PTCDA [23] indicating a similar strong coupling between different ML's. In contrast, PEN films grow for small thicknesses in a layer-by-layer fashion and  $\Delta E_{\text{surf}} = 55$  meV can be determined based on  $d_{\text{ML}} = 1.8$  nm and eq. 5.15. This on-site shift is by a factor of two smaller compared to PTCDA, which is in qualitative agreement to the expected lower intermolecular coupling. Whether the quantitative difference is realistic cannot be decided easily, but the qualitative behavior can be nicely rationalised.

The thickness dependence of  $E_1$  can be modeled for DIP LT growth on glass as well as for PEN growth on  $\text{Si}_{\text{Ntve}}$  taking on-site effects for the outermost layer into account. PEN growth as well as DIP HT growth on glass shows a different thickness dependence. For further analysis, the structural and morphological film properties have to be considered. Therefore, first PEN film growth will be discussed and compared for glass and  $\text{Si}_{\text{Ntve}}$  substrates, followed by a comparison between DIP film growth on glass at low and at high temperatures.

**5.5.4.2.2 Comparison between PEN film growth on  $\text{Si}_{\text{Ntve}}$  and on glass** Although the overall energy shift  $\Delta E \approx 40$  meV agrees between PEN film growth on glass and on  $\text{Si}_{\text{Ntve}}$ , significant differences are detectable:

1. The energy shift of  $E_1$  sets in for PEN on glass from the beginning of film growth, whereas for PEN on  $\text{Si}_{\text{Ntve}}$  nearly no energy shift is visible for sub-monolayer thicknesses.
2. On glass no clear  $1/d$  dependency can be observed (see Fig. 5.40b), as it is the case for PEN on  $\text{Si}_{\text{Ntve}}$  (see Fig. 5.45a).

The first point can be understood as follows: The completion of the first ML does not affect the energy position  $E_1$  significantly since the observed islands do not change their optical properties during 2D growth. Although significant optical differences are expected between monomers and clusters, this kind of transition cannot be observed since nucleating islands are formed quickly in the beginning of film growth [66]. Instead, only the

deposition of molecules on top of each other, i. e. the coupling between different ML's gives rise to the observed energy shift. Since PEN on Si<sub>Ntve</sub> grows in the beginning in a layer-by-layer fashion [66, 50], the energy shift is only observable for  $d > d_{\text{ML}}$ . In contrast the film morphology of PEN on glass differs significantly, and 3D islands start to grow before the first ML is completed [71]. Therefore, the induced red-shift, which sets in when the second and third ML start to grow, is already observed for thinner films compared to PEN on Si<sub>Ntve</sub>. The thickness dependence of  $E_1$  for PEN on glass resembles qualitatively the observation made for PTCDA in air, where clustering was observed for the first two ML's due to the ambient conditions supporting this idea [23].

Nevertheless, according to the second point in the above listing, deviations from the  $1/d$  behavior occur for PEN on glass. This might be due to a changing morphology during growth giving rise to a different change of the surface to volume ratio compared to layer-by-layer growth. Furthermore, also the 'bulk phase' might be more pronounced compared to PEN on Si<sub>Ntve</sub> changing the optical properties slightly.

**5.5.4.2.3 Comparison between DIP film growth at low and at high temperatures** The difference between HT and LT growth of DIP on glass is even larger. While LT growth shows a pronounced energy shift already at low thicknesses, which can be modeled by a  $1/d$  dependency, no energy shift but rather a mode splitting is visible in HT growth. Apart from morphological differences both films differ also in structure as can be evidenced e. g. by the absence of the fourth mode in case of LT growth. The line splitting is observed in combination with the appearance of the fourth mode indicating some correlation. Therefore, the line splitting is also due to intermolecular coupling, which could be attributed to Davydov splitting. Nevertheless, the small Davydov component influencing mainly the in-plane component of the film is much smaller than the large Davydov component, see Sec. 5.4.3.4. Therefore, it is unlikely to be responsible for such a pronounced effect. The main difference between HT and LT growth seems to be the film structure, having a strong impact onto the optical properties. One could speculate that the tilt angle of the molecules in the LT film is larger leading to an increased in-plane transition dipole. This would affect the coupling between different ML's, since generally the coupling between dipoles differs between a 'parallel configuration' and a 'head to tail configuration' known as hypochromism and hyperchromism, respectively [135, 136]. Nevertheless, calculations are necessary to quantify these differences. Also the film structure on glass needs to be investigated in more detail by e. g. real-time X-ray measurements to gain insight into the molecular orientation.

### 5.5.4.3 Concluding remarks

In conclusion, the optical real-time observations of organic films during growth reveal, how the dielectric function depends on the film thickness. Additionally they allow to detect spectra already in the sub-monolayer range. While the ellipsometry data are difficult to analyse due to the uniaxial anisotropy of the films, DRS seems to be a better suited

method, since only the in-plane component is probed. Nevertheless, depending on the effect and on the sample under investigation, ellipsometry is also capable to detect real-time changes as is demonstrated for PEN film growth. In case of DIP, ellipsometry shows that no spectral changes occur in the low thickness range during growth, whereas the possible changes for higher thicknesses are difficult to quantify. Combining both techniques would help to gain additional insight into the out-of-plane component of the dielectric tensor.

Two main effects are observed during growth of different samples for the in-plane component of their spectra: In case of DIP grown at HT on glass an arising transition (the fourth mode at high energies) and a line splitting is observed, whereas no energy shift is visible. In contrast, for DIP grown at LT on glass an overall energy red-shift of 110 meV is detected during growth, similar to PEN grown at RT on  $\text{Si}_{\text{Ntve}}$  and on glass, where the energy shift ( $\Delta = 40$  meV) is smaller. While the arising transition is a specific property of DIP related to the structural order of the film, the energy shift is a more general effect. The  $1/d$  thickness dependence above a certain film thickness allows to gain insight into the origin of both effects. The arising transition indicates that an interfacial layer with lower structural order forms for DIP on glass, whereas the red-shift during growth can be identified as a blue-shift of the outermost molecular layer due to lower dielectric screening compared to molecules in the 'bulk'. In addition to the thickness also morphology affects the optical properties during growth as the comparison between PEN growth on  $\text{Si}_{\text{Ntve}}$  and on glass demonstrates. The optical differences between HT and LT growth of DIP on glass are considered to be mainly related to structural differences. Thus, real-time measurements can detect also structural and morphological changes during growth, which are in addition to the optical properties important for device applications.

## 5.6 Results of complementary optical methods

So far, the optical properties of thin films were studied by investigating their dielectric function in correlation with structural and morphological film properties, giving insight into exciton-phonon coupling, exciton transfer or growth related phenomena. The fundamental understanding of the optical properties of DIP thin films gained in the preceding sections can be used to explore further optical properties. Naturally details remain beyond the scope of this thesis, but the following results indicate, what is possible, and open future perspectives. Furthermore, additional optical techniques give complementary information beyond the dielectric function while at the same time they benefit from the understanding of it. For example, the vibrational modes responsible for the observed vibronic progression cannot be spectrally resolved in the absorption spectra, and Raman spectroscopy is a suitable method to gain insight into the vibrational degrees of freedom. Resonant Raman spectra probe the deformation of the molecule in the relaxed excited geometry that was calculated to interpret the monomer spectra. Furthermore, spatially resolved film properties are difficult to study by ellipsometry or DRS, since generally the

measurements average over a large ( $1-4 \text{ mm}^2$ ) sample area. Although imaging techniques exist for ellipsometry [137, 138], the broad distribution of angles of incidence complicates the data analysis and the spatial resolution is limited by diffraction. For studying the optical properties on the nanometer scale, tip-enhanced optical measurements were developed in recent years [93]. They are applied to DIP thin films on  $\text{Si}_{\text{Ntve}}$  in cooperation with D. Zhang *et al.* (Meixner group, institute of physical and theoretical chemistry, Tübingen). Since tip-enhanced Raman as well as PL spectra are measured, it is important to study first Raman and PL properties of the DIP film without tip-enhancement for comparison.

### 5.6.1 Raman spectroscopy

Overall, DIP has  $3N - 6 = 3(32 + 16) - 6 = 138$  modes and 72 of them are Raman active. This section focuses on the 'central' region of the Raman spectrum, which is relevant for the exciton-phonon coupling ( $1000 - 2000 \text{ cm}^{-1}$ ). At higher wavenumbers ( $\sim 3000 \text{ cm}^{-1}$ ) mainly C-H stretching vibrations can be observed, whereas at very low wavenumbers intermolecular vibrations (phonons) are found, which are beyond the scope of this thesis.

Raman spectra of a 20 nm thick DIP film grown at  $T = 130 \text{ }^\circ\text{C}$  on  $\text{Si}_{\text{Ntve}}$  are shown in Fig. 5.46 for two different excitation wavelengths, corresponding to a) pre-resonant Raman with  $\lambda_{\text{ex}} = 633 \text{ nm}$  (1.96 eV) and b) resonant Raman with  $\lambda_{\text{ex}} = 532 \text{ nm}$  (2.33 eV), which is seen from the absorption spectrum in Fig. 5.20b) with the first transition located at 2.25 eV.

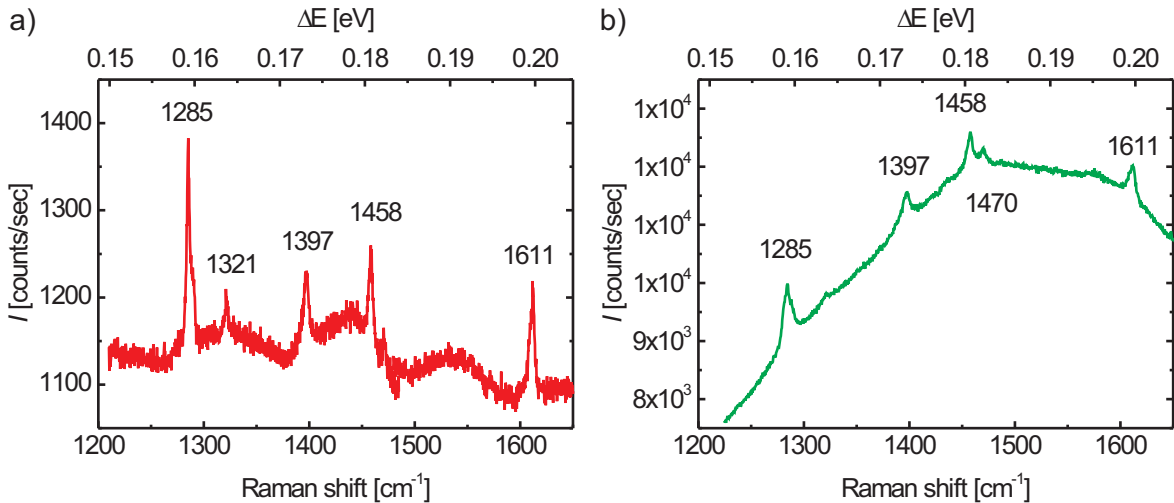


**Figure 5.46:** Raman bands of a 20 nm thick DIP film on  $\text{Si}_{\text{Ntve}}$  grown at  $T = 130 \text{ }^\circ\text{C}$  measured with two different excitations wavelength: a)  $\lambda_{\text{ex}} = 633 \text{ nm}$  (1.96 eV), b)  $\lambda_{\text{ex}} = 532 \text{ nm}$  (2.33 eV). Apart from the different PL background both spectra show similar Raman peaks, which contribute to the observed vibronic progression. In addition to the measured Raman shift also the corresponding phonon energy  $\Delta E$  is shown for comparison.

The most significant difference between both excitation wavelengths is the photoluminescence (PL) background, which is very pronounced for the resonant case. Also strong 'degradation effects', e. g. vanishing Raman peaks and decreasing PL background, could be observed during the measurements with both excitation wavelengths showing differences in the time scale. While for  $\lambda_{\text{ex}} = 532$  nm the 'degradation' is visible on a time scale of  $\sim 25$  s, it takes  $\sim 20$  min for  $\lambda_{\text{ex}} = 633$  nm. Whether the 'degradation' is due to the ambient, leading to e. g. photo-oxidation, or due to optical bleaching needs to be investigated in more detail. Nevertheless, generally the data measured at  $\lambda_{\text{ex}} = 633$  nm are less affected by these issues since the integration time is shorter than the degradation time in contrast to measurements with  $\lambda_{\text{ex}} = 532$  nm. Therefore, the pre-resonant Raman spectra are in case of DIP better suited to study the deformation of the molecule upon optical excitation.

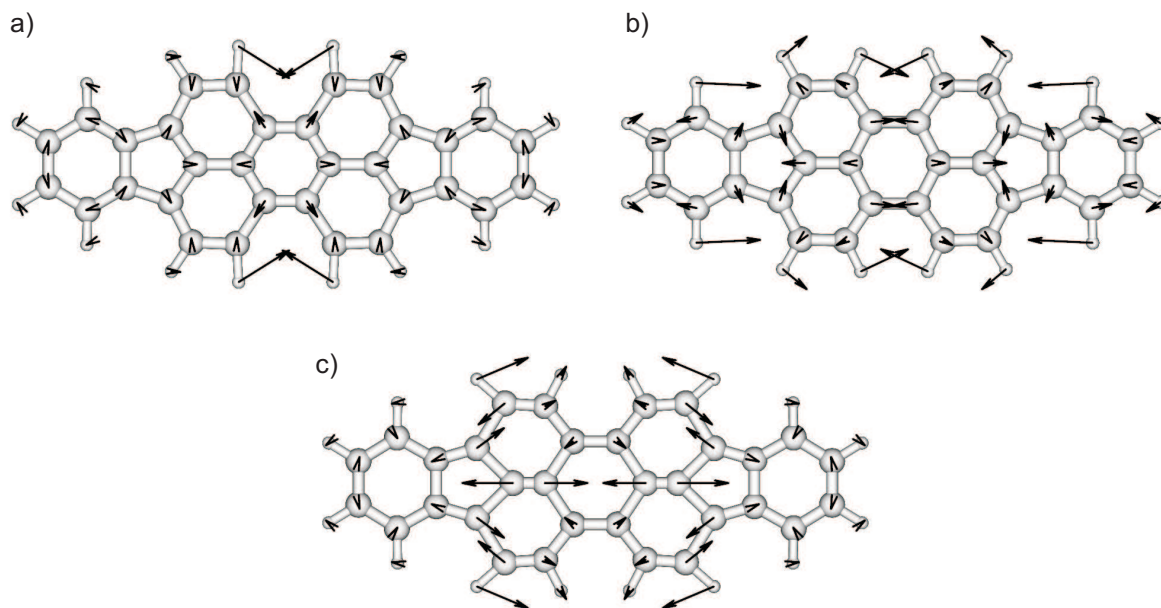


**Figure 5.47:** The three most strongly elongated breathing modes of DIP in the energy range of interest at: a)  $1277\text{ cm}^{-1}$ , b)  $1447\text{ cm}^{-1}$  and c)  $1592\text{ cm}^{-1}$ . The arrows indicate the direction and the relative size of the vibration. The modes are calculated by R. Scholz *et al.*

For both excitation wavelengths several Raman modes are visible between  $1200$  and  $1650\text{ cm}^{-1}$ . Recent Hartree-Fock calculations based on the B3LYP geometry have shown that they can be assigned to breathing modes, which are due to elongations of the bond length in the perylene core including especially the compression of the central hexagon [120]. A refined analysis employing constrained TD-DFT calculations allows to predict the energy positions of the modes more accurately [139]. It is based on the same calculation related to the deformation of the excited molecule as it was applied to the optical spectra [40], see Sec. 5.1. The three most elongated breathing modes in the respective energy range are depicted in Fig. 5.47. The mode calculated at  $1277\text{ cm}^{-1}$

corresponds to the measured mode at  $1284\text{ cm}^{-1}$ . It is mainly a breathing mode of the central ring superimposed with an in-plane C-H bending motion, compare Fig. 5.47a). The mode calculated at  $1447\text{ cm}^{-1}$  (see Fig. 5.47b) agrees also well with the measured value of  $1458\text{ cm}^{-1}$  and is dominated by C-C stretching motions. The same holds for the two modes measured at  $1321$  and  $1397\text{ cm}^{-1}$ , which are not depicted. The highest mode calculated at  $1593\text{ cm}^{-1}$  and measured at  $1611\text{ cm}^{-1}$  has patterns resembling optical phonons in graphite. Since these modes affect mainly the perylene core, those measured for DIP are very similar compared to e. g. PTCDA [38].

Furthermore, exciton-phonon coupling constants  $g$ , that are related to the Huang-Rhys factor via  $S = g^2$ , were calculated for these modes indicating strong coupling [120]. The energy range plotted on top of the Raman plot show in Fig. 5.46 and determined from the difference between the scattered photon energy and the excitation energy ( $\Delta E = E_{\text{sc}} - E_{\text{ex}}$ ) corresponds to the vibrational energy. It agrees well with the optically observed effective mode energy  $\Delta E = 0.17\text{ eV}$  in the vibronic progression, see Sec. 5.1. Therefore, the observed Raman modes can be identified to contribute to the vibronic progression. Due to the small energy difference between the modes, it is possible to describe them in the optical spectra by a single effective mode.

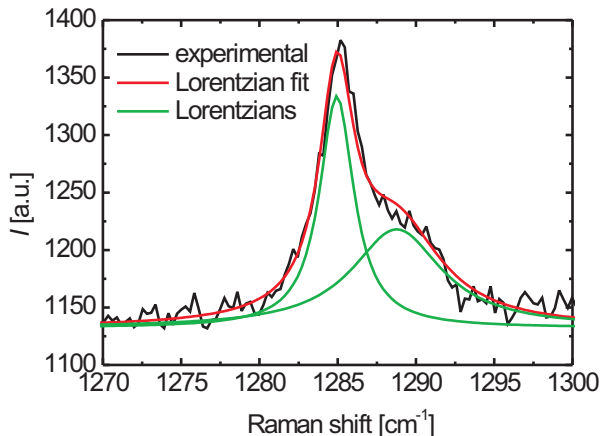


**Figure 5.48:** Breathing mode at  $1285\text{ cm}^{-1}$  with high wavenumber shoulder. The fit (red curve) consists of two Lorentzians (green curves) with a wavenumber spacing of  $4\text{ cm}^{-1}$ .

All peaks in Fig. 5.47 can be fitted well by single Lorentzians, except for the lowest energy mode at  $1285\text{ cm}^{-1}$ , which exhibits a high wavenumber shoulder (see Fig. 5.48). The plotted fit (red curve) consists of two Lorentzians (green curves) with a wavenumber spacing of  $\sim 4\text{ cm}^{-1}$ , which could be assigned to Davydov splitting. In case of PTCDA crystals it is reported that several modes in the higher wavenumber region ( $1200\text{--}1600\text{ cm}^{-1}$ ) exhibit a Davydov splitting ranging from  $0.7$  to  $2.4\text{ cm}^{-1}$  [140]. The observed mode splitting for DIP is significantly higher. In case of DIP on  $\text{TiO}_2$ , a similar mode splitting was observed, and it was speculated that it arises due to different coexisting phases [141]. Since X-ray results show that DIP on  $\text{Si}_{\text{Ntve}}$  grows at  $T = 130\text{ }^\circ\text{C}$  highly ordered and solely in the  $\sigma$ -phase, this explanation does not seem to be likely for DIP on  $\text{Si}_{\text{Ntve}}$ . Furthermore, calculations show that only one mode exists around  $1280\text{ cm}^{-1}$  [139] and an overlap between two distinct modes can be excluded. Therefore, Davydov splitting seems to be most likely,



but further investigations are necessary to clarify this issue.

In conclusion, pre-resonant and resonant Raman spectra show similar spectra except for a significantly different PL background and of course resonant enhancement. The observed peaks can be identified as breathing modes that contribute to the exciton-phonon coupling observed in the optical spectra.

### 5.6.2 Fluorescence spectroscopy

*Cw*-Fluorescence spectra measured at RT are presented in this section for DIP dissolved in acetone as well as for a  $\sim 20$  nm thick DIP film grown on Si<sub>Ntve</sub>. While the solution spectrum determines the properties of the monomers in analogy to the absorption spectrum, the fluorescence spectrum of the thin film serves as a reference for the tip-enhanced spectra that are discussed in the following section.

Different excitation wavelengths  $\lambda_{\text{ex}}$  are tested giving similar spectra that mainly differ in intensity. If  $\lambda_{\text{ex}} = 633$  nm ( $E = 1.96$  eV) is used, as it is done for tip-enhanced measurements, nearly no fluorescence signal is detected. This agrees with the experimentally determined absorption spectra for dissolved DIP and thin films, since at this energy no significant molecular excitation takes place. The fluorescence spectra measured with  $\lambda_{\text{ex}} = 442$  nm ( $E = 2.8$  eV) show a stronger signal, which is shown normalized for better comparison in Fig. 5.49a) for DIP in solution (green curve) and DIP thin films (green curve). In both cases the vibronic progression is clearly visible and the distinct transitions are labeled by numbers from 1 to 4. In addition to the red-shift of the thin film spectrum, the most pronounced difference between both spectra is the increased broadening in case of the solution spectrum, as well as different energy spacings. This is most clearly visible in case of peak 1, which in the solution spectrum is rather a high energy shoulder. Furthermore, the intensity increase at high energies in case of DIP films is not a spectral feature, but it is due to reflections of the incident light beam at the sample surface.

Fits based on four independent Gaussians (dashed red curves) describe the data well and allow to quantify the observed differences. The energy spacing between Peak 2 and 3 is for both spectra similar ( $\Delta E_{\text{film}} = 0.143$  eV and  $\Delta E_{\text{solution}} = 0.154$  eV), whereas in case of Peak 1 and 2 significant differences are visible ( $\Delta E_{\text{film}} = 0.156$  eV and  $\Delta E_{\text{solution}} = 0.121$  eV). Recently temperature dependent and time resolved fluorescence spectra of DIP thin films on quartz glass were investigated [24]. Three spectral series with different nature could be distinguished that are positioned around 2.1 eV, corresponding to the first peak of the thin film spectrum. They were related to an excitonic level and trap-states of different site energies. The other peaks correspond to the 0-1 and 0-2 transition of the vibronic progression, probing the geometric deformation in the electronic ground state.

Comparing the normalized dielectric function with the fluorescence spectra (see Fig. 5.49b), allows to determine the Stokes shift for DIP films and DIP in solution to be  $\Delta E_{\text{film}} = 112$  meV and  $\Delta E_{\text{solution}} = 59$  meV, based on peak 1 in the fluorescence

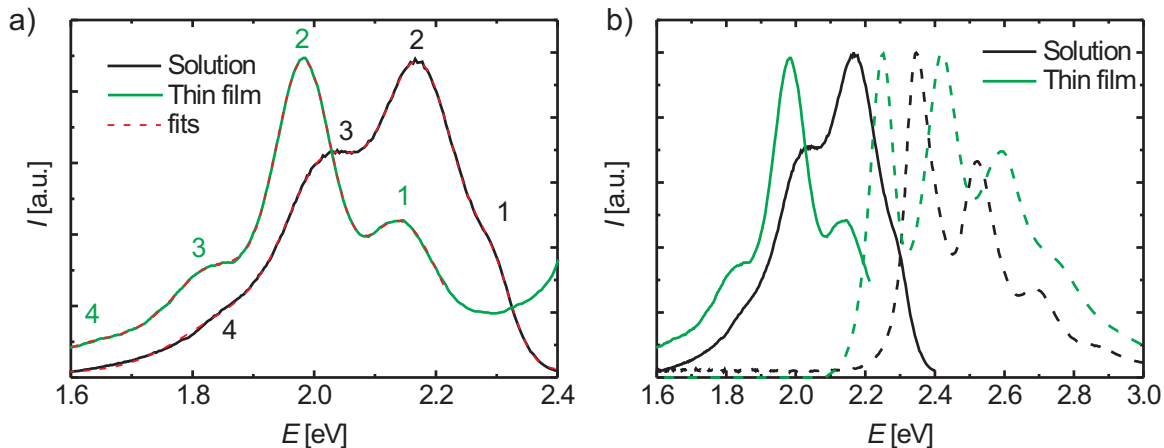


**Figure 5.49:** a) Normalized fluorescence spectra of DIP dissolved in acetone (black curve) and of a 20 nm thick DIP film on  $\text{Si}_{\text{Ntve}}$  (green curve) measured with an excitation wavelength of  $\lambda_{\text{ex}} = 442$  nm ( $E = 2.8$  eV). The fits (dashed red curve) are based on four independent Gaussian oscillators. b) Normalized fluorescence spectra (solid curves) and absorption spectra (dashed curves) for DIP dissolved in acetone (black curves) and DIP thin films on  $\text{Si}_{\text{Ntve}}$  (green curves). For simplicity only the out-of-plane component is shown for the thin film spectrum.

spectra. For simplicity only the out-plane component of the thin film spectrum is shown in Fig. 5.49b) since no difference with respect to the energy position  $E_1$  exists compared to the in-plane component. The Stokes shift for DIP in solution is comparable to that of PTCDA ( $\Delta E = 30 - 40$  meV) [10], where it is assigned to deformations of the low-frequency internal breathing modes in the relaxed excited state of the molecule. In contrast, the Stokes shift is twice as large for DIP films, which is not observed for PTCDA.

The absorption and the fluorescence spectra do not show a mirror symmetry, which indicates that the nuclear configuration of the ground and excited electronic state differ, leading to different vibrational wave functions [31]. This is also supported by the significantly smaller energy spacing for the fluorescence spectra ( $\Delta E_{\text{fl}} \approx 0.14 - 0.15$  eV) compared to the absorption spectra ( $\Delta E_{\text{e}_2} = 0.17$  eV). Furthermore, it is known that certain interactions due to dispersion forces broaden the vibrational spectra. The loss of vibrational structure is due to certain solvent-solute interactions, while the change of the relative intensities, e. g. the Franck Condon envelope is due to the environmental modification of the molecular potential energy surface [31].

In conclusion, the fluorescence spectra of DIP show a pronounced vibronic progression, which probes the deformation of the electronic ground state. Differences between the solution and the thin film spectrum are due to molecular interactions. The results obtained for the thin film spectrum agree with spectra published in the literature. Furthermore, according to the absorption spectra, only little fluorescence is visible for  $\lambda_{\text{ex}} = 633$  nm, which is of relevance for the tip-enhanced spectra discussed in the following section.

### 5.6.3 Tip-enhanced spectroscopic imaging

As was demonstrated by the optical real-time measurements in Sec. 5.5, the optical properties of molecules depend on their surrounding environment due to intermolecular interactions. So far, the spectral properties were investigated as a function of thickness, averaging them laterally. However, even apparently homogeneous films, as they are studied in this thesis, exhibit spatial inhomogeneities due to their polycrystalline structure. AFM pictures show island growth from the beginning or above certain thicknesses giving rise to domain boundaries. Also for layer-by-layer growth domain boundaries exist that might not be visible in the height profile, but that can have an impact onto the optical or electrical film properties [142]. For studying these effects it is necessary to perform spatially resolved optical measurements on the nanometer scale that are near or beyond the diffraction limit of light.

Nano-optics is an emerging field motivated by the rapid advance of nanoscience and nanotechnology and new techniques have been developed that are subject of intensive research [143, 92]. Employing tip-enhanced spectroscopic measurements allows not only for the determination of the correlated topographic and optical information with high resolution [93] but also for an ultrahigh sensitivity, e. g. making it possible to optically detect single molecules [144]. In the following, results of tip-enhanced measurements including Raman (TER) and PL spectra are shown for DIP thin films that are achieved in cooperation with D. Zhang *et al.* (Meixner group, institute of physical and theoretical chemistry, Tübingen) [145].

In Fig. 5.50a) the well known topographic image of a 30 nm thick DIP film grown at  $T = 130$  °C on  $\text{Si}_{\text{Ntve}}$  is shown for a scan area of  $1.5 \times 0.7 \mu\text{m}^2$ . It reveals the film morphology with stepped terraces in accordance to AFM images measured at similar DIP films (see Sec. 5.3.2). The simultaneously recorded near-field optical image of the same area is shown in Fig. 5.50b). The data are obtained with an excitation wavelength of  $\lambda_{\text{ex}} = 633$  nm, a laser power of  $\sim 170 \mu\text{W}$  at the focus, radially polarized light and a tip-sample distance of  $\sim 3$  nm. The signal is measured with an avalanche photo diode (APD) detecting the scattered and emitted intensity without spectral information.

The near-field optical image shows bright lines, bright spots and dark regions appearing at first glance like random features. However, a thorough comparison with the topography reveals that the bright regions correlate with most of the DIP domain boundaries. Clear correlations are observed at many places including the regions labeled as 1, 2, and 3 in the blue circles, both in the topographic and in the near-field optical images. A line profile through the topographic image with its corresponding optical intensity (which is FT flattened including 5 neighboring data points) supports this (see Fig. 5.50c), demonstrating also sharp optical resolution of 20 – 40 nm at single molecular boundaries. The highest spatial resolution observed with the tip-enhanced measurements on DIP films is  $\sim 17$  nm [145]. Moreover, enhanced optical contrast is also observed in several regions where no molecular steps are observable, indicating domain boundaries that cannot be accessed by AFM measurements. Furthermore, the average intensity of the optical signal

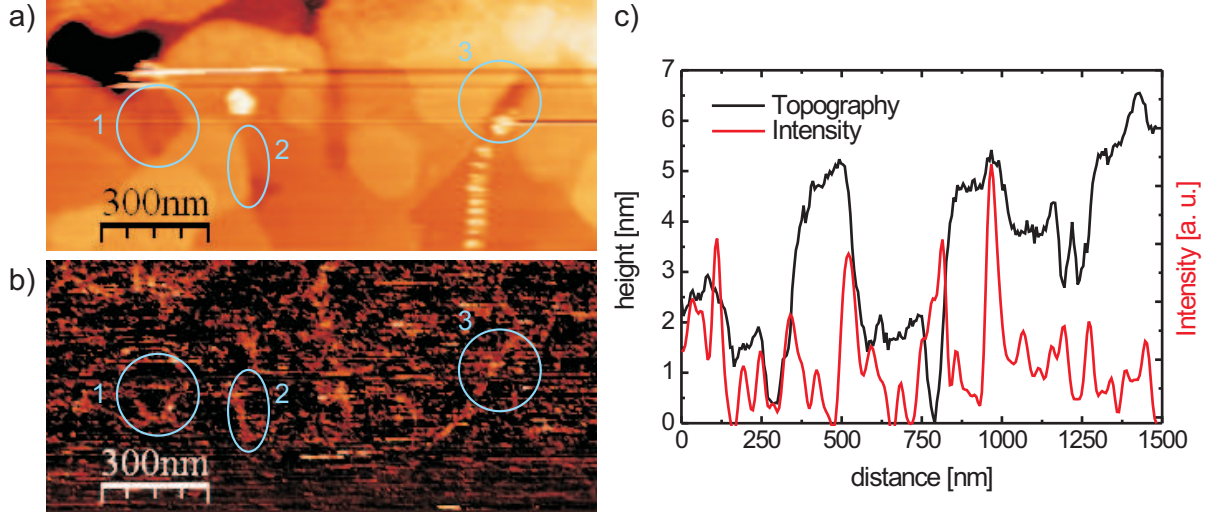


**Figure 5.50:** Simultaneously recorded a) topographic and b) near-field optical images of DIP on  $\text{SiN}_{\text{tve}}$ . The blue circles labeled with numbers mark regions, where correlations between both images are visible, which are mainly domain boundaries. c) A line profile through the topographic image and its corresponding optical intensity demonstrates the correlation showing an optical spatial resolution of 20 – 40 nm.

from the bright region is about four times higher than that of the dark region and does not depend significantly on the step height.

In addition to the optical and topographic images also Raman (and PL) spectra are obtained. Before TER spectra are shown, the confocal Raman spectra are compared to those presented in Sec. 5.6.1, where a Horiba Jobin Yvon spectrometer was employed. Fig. 5.51a) shows the good agreement between both spectra, where the DIP breathing modes are visible as discussed in Sec. 5.6.1. The significant broader peak width of spectrum (1) is due to a lower spectral resolution since different gratings are used: Spectrum (1) is measured with  $g = 600 \text{ mm}^{-1}$  and spectrum (2) with  $g = 1800 \text{ mm}^{-1}$ .

Fig. 5.51b) shows the tip-enhanced spectrum (red curve) measured at a domain boundary together with the confocal measurement (black curve). Both results are obtained with a  $g = 600 \text{ mm}^{-1}$  grating using the radially polarized laser mode employing different integration times (20 s with tip and 240 s without tip). The tip-enhanced spectrum shows a pronounced PL background and enhanced Raman bands. The modes at  $520 \text{ cm}^{-1}$  and at  $940 \text{ cm}^{-1}$  belong to the Si substrate. They are significantly reduced in the tip-enhanced spectrum compared to the observed Raman bands between  $1200$  and  $1650 \text{ cm}^{-1}$ , which belong to DIP breathing modes and agree well to the confocal measurements (see Fig. 5.51a).

Furthermore, no spectral differences can be observed between spectra on domain boundaries and inside a domain, except for an overall red-shift of the PL background at the domain boundaries as is shown in Ref. [145]. The dispersive PL background is generally

of minor interest in most tip-enhanced Raman spectra (TERS). It can be considered to arise from the coupling between tip and sample and differs fundamentally from the fluorescence spectra reported in Sec. 5.6.2. However, it dominates the optical intensity and it seems to be the key for a deeper understanding of the observed enhancement at the domain boundaries. If both spectra are normalized to the Raman bands of the substrate at  $520\text{ cm}^{-1}$ , a tip induced enhancement of the broad PL emission by a factor of  $\sim 2600$  can be found, which is by a factor of 4 smaller inside a domain.

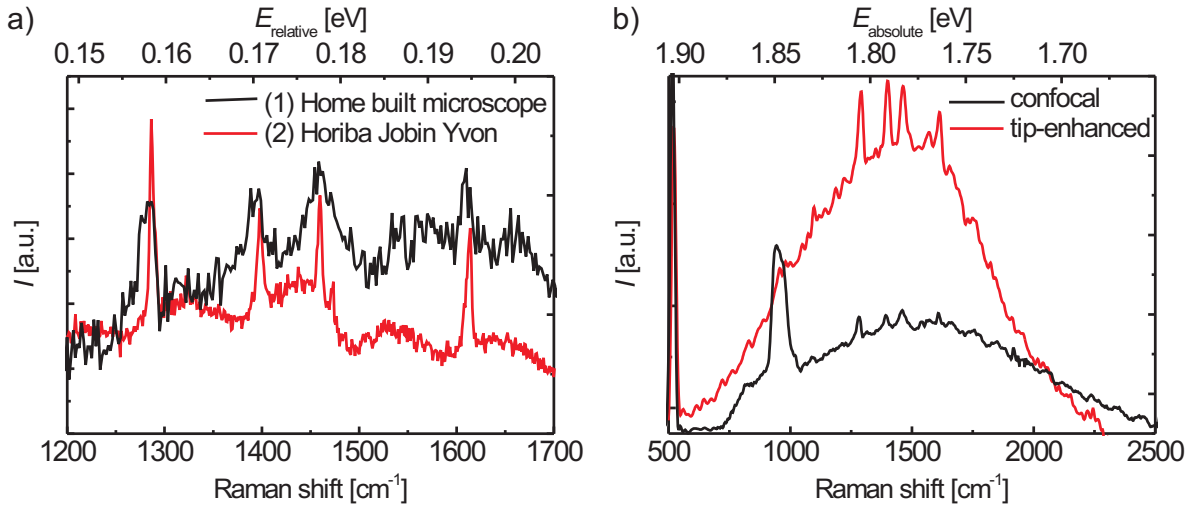


**Figure 5.51:** a) Confocal Raman spectra of a 30 nm thick DIP film on  $\text{Si}_{\text{Ntve}}$  measured with  $\lambda_{\text{ex}} = 633\text{ nm}$  for comparing measurements with 1) a homebuilt parabolic mirror microscope ( $g = 600\text{ mm}^{-1}$ ), 2) a Horiba Jobin Yvon microscope ( $g = 1800\text{ mm}^{-1}$ ). Except for some broadening due to different spectral resolutions, the spectra agree well. b) Tip-enhanced spectrum at a molecular boundary in comparison with the confocal spectrum, both showing DIP and Si Raman bands. In case of the tip-enhanced spectrum the PL background is significantly more pronounced and also the Raman bands are enhanced.

The fact that the near-field under the tip apex is polarized perpendicular to the sample surface favors an efficient coupling because the molecular transition dipoles are oriented along the long axis of the molecules. Mainly the out-of-plane component of the dielectric tensor has to be considered, which is  $\sim 10$  times larger than the in-plane component (see Sec. 5.4.2). Nevertheless, the excitation energy of the He-Ne laser lies with  $1.96\text{ eV}$  below the absorption maximum, where no efficient excitation is expected. Additional measurements performed by D. Zhang *et al.* can rule out two photon processes since a linear behavior between tip-enhanced PL intensity and incident laser power is observed [145]. Therefore, linear excitation must dominate, although the linear absorption is small in this energy range. Nevertheless, the geometric arrangement between light polarization and molecular orientation maximizes the pre-resonant Raman spectra, which depend on the angle  $\Theta$  between the electric field and the transition dipole as  $\cos^4\Theta$ .

The intensity increase at the molecular domain boundaries is essentially independent of

the step height observed in the topographic image. This indicates that the tip-enhanced signal predominantly originates from short tip-sample distances, which is in agreement with the observed small Si Raman bands compared to the confocal measurements. The observed lateral resolution can be understood from a simple model describing the intensity distribution around the tip apex, as described in Ref. [145]. Around the tip apex, the spatial dependence of the electric field induced by the plasmon excitation of the tip resembles a  $E \propto 1/r^2$  law with respect to the center of curvature [146], so that the enhancement of the field intensity has a dependence close to  $I = E^2 \propto 1/r^4$ . Placing the sample surface at a distance  $d$  below the tip apex, the intensity of the excitation field can be evaluated as a function of the lateral distance  $\rho$  from the tip axis, giving

$$I = E^2 \propto 1/[(r + d)^2 + \rho^2]^2 \quad (5.16)$$

so that the intensity decays to half its peak value at  $\rho = \sqrt{\sqrt{2} - 1}(r + d)$ . Tips with a typical tip radius  $r = 10$  nm and a tip-sample distance of 1.5 nm, result in  $\rho = 7.4$  nm, or a resolution of  $FWHM = 2\rho = 15$  nm, in excellent agreement with the sharpest structures observed ( $FWHM = 17$  nm) [145]. The strong intensity enhancement achieved directly below the tip is restricted to an area of about  $A = \pi\rho^2 = 170$  nm<sup>2</sup>, much smaller than the area of the confocal spot with a diameter of about 260 nm, which corresponds to  $A = 5.3 \times 10^4$  nm<sup>2</sup>. Nevertheless, the overall PL enhancement observed in Fig. 5.51 is  $\sim 2600$ , arising from a fraction of only  $3 \times 10^{-3}$  of the illuminated area, so that the enhancement in this central region needs to be of the order of  $8 \times 10^5$ .

Still, the question remains, why the domain boundaries show a more enhanced signal than the domains themselves. From the observed PL red-shift at the domain boundaries, it is inferred in Ref. [145] that this phenomenon results from an enhanced plasmon polariton coupling, which is in accordance to recent observations of guanine/ $\text{ClO}_4^-$  layers adsorbed on Au(111) crystals [147]. Furthermore, the non-radiative exciton decay at step edges may be reduced and the radiative recombination rate of a molecule at an edge could be enlarged with respect to emission from the bulk crystal. This could be induced by the enhanced near-field increasing the local photonic mode density significantly.

Considering the minimal lateral resolution of 17 nm achieved in the near-field imaging of the DIP film, the upper limit of the DIP exciton diffusion length in the lateral direction should be comparable to this value. Otherwise, if the locally near-field generated exciton could diffuse away from the tip probing region (about the dimension of the tip radius), sharp PL imaging could not be possible. Kurrle *et al.* [17] have reported an exciton diffusion length of 100 nm along the direction perpendicular to the substrate, which is expected to differ compared to the lateral direction due to the high structural order. Under the near-field excitation condition, the recombination rate is enhanced by a factor of about 900 and the radiative lifetime  $\tau_{\text{rad}}$  is reduced correspondingly. Therefore, the 100 nm diffusion length is expected to be greatly shortened according with  $L_{\text{diff}} = \sqrt{D\tau_{\text{rad}}}$ . In conclusion, it could be shown that DIP domain boundaries can be detected by tip-enhanced spectroscopic measurements with a lateral resolution of 17 – 40 nm, which

can be understood in terms of the highly focused electric field under the tip and in terms of exciton trapping at the boundaries. Furthermore, from the tip-enhanced spectra additional information about the tip-sample coupling can be deduced. These results open new perspectives for analyzing the local spectroscopic properties of organic thin films together with the local morphology at a spatial resolution far beyond the diffraction limit. This is highly relevant for device applications, since grain boundaries influence e. g. the electrical properties significantly [142].





## CHAPTER 6

# OUTLOOK

This chapter is devoted to discuss future perspectives arising from the results reported in this thesis.

While the out-of-plane component of the DIP post-growth spectrum could be theoretically described, open questions remain for the in-plane spectrum, which mainly concern the origin of the observed fourth mode but also the observed energy splitting of the first two modes. Although theoretical considerations and experimental low temperature measurements support that the fourth mode depends highly on the molecular order and is due to intermolecular coupling, the exact origin is still unclear. This issue can be addressed mainly by more complex theoretical calculations including more than the HOMO-LUMO transition.

The increase of the fourth mode during film growth on glass can still be interpreted as a transition from lower to higher order without exact knowledge of the origin of the fourth mode. Nevertheless, more structural information of DIP on glass would be helpful to support this idea. Since X-ray reflectivity suffers from scattering at the rough surface, near edge X-ray absorption fine structure spectroscopy (NEXAFS) could contribute to study the molecular tilt angle distribution in more detail at high as well as at low temperature.

In case of PEN films the growth at low temperatures would be interesting to study, which could allow to investigate the evolution of the bulk phase on Si substrates. Also measurements at high thicknesses ( $d > 20$  nm) could help to study the bulk phase.

Furthermore, measuring ellipsometry and DRS simultaneously, which would require a modification of the current setup, would allow to study the anisotropy and thus the structural order during growth. This would not only be helpful for DIP on glass, but also for other molecules such as PEN on various substrates. Also combining X-ray reflectivity with DRS measurements would be helpful to match structural and morphological information with optical properties. Nevertheless, this would require smooth films, such as DIP or PEN on Si<sub>Ntve</sub>, but rough films on glass, as they are observed at high temperatures for DIP and at room temperature for PEN, are difficult to investigate.

Since the DRS signal for DIP on Si<sub>Ntve</sub> is too weak and DIP on glass is quite rough,

it would be worth testing different substrates, such as indium tin oxide (ITO), mica or gold. Furthermore, ITO is of high relevance for solar cells or OLED's, where it serves as a transparent conductor, and also gold is used for metal contacts. Due to the changed chemical substrate properties different optical effects are expected during growth.

Once, the single optical film properties during and after growth are established, hetero-structures can be investigated, where a second film with different material is deposited on top of the first film. Hetero-structures are important for any kind of applications involving pn-junctions. Also the effect of nano-structured substrates would be interesting to explore. On the one hand, the effect of controlled 'roughness' or templating could be examined, on the other hand field-enhancement effects at the boundaries of metallic nano-structures, e. g. gold cones, could be investigated.

The optical methods for real-time measurements always average over a large sample area, but it would be good to also spatially resolve the optical signal. In case of homogeneous DIP films on  $\text{Si}_{\text{Ntve}}$ , the spatial resolution of 17 – 40 nm was demonstrated by tip-enhanced photoluminescence measurement making the grain boundaries visible. Even for 'homogeneous' samples tip-enhanced measurements reveal exciting results so that for nano-structured samples further interesting effects are expected. Since the experimental effort for those experiments is significant, confocal Raman spectroscopy could be tested first, investigating possible differences between e.g DIP on flat gold surfaces and on gold cones distributed over the surface.

## CHAPTER 7

# CONCLUSION

The aim of this work was to establish the anisotropic dielectric function of DIP films on SiO<sub>2</sub> and to study the optical properties during film growth. The experimental findings can be viewed as a basis for investigations of more complex systems like films grown on nano-structured substrates or multilayer systems that are of high relevance for technical applications. While this work focuses mainly on the optical properties of DIP films, also the optical response of PEN films during growth is studied for comparison.

First, the absorption spectrum of DIP in solution is investigated, which serves as the monomer reference. The spectra of DIP dissolved in acetone and in 1,2-dichlorobenzene coincide except for the energy position, which is due to different solvent shifts. The observed vibronic progression of the HOMO-LUMO transition allows the determination of the Huang-Rhys parameter  $S = 0.87$  experimentally, which is a measure of the electronic vibrational coupling. This result as well as the mode energy  $E = 0.17$  eV agrees well with constrained DFT calculations [40]. Due to Gaussian broadening arising from the fluctuating geometry of the surroundings of each dissolved chromophore, different internal vibrations, contributing to the vibronic subbands, cannot be distinguished. Therefore, the experimentally determined value corresponds to a sum over several internal modes. These modes are measured by Raman spectroscopy. Five modes in the energy range of  $E = 0.15 - 0.2$  eV are determined and compared to calculations based on the same constrained DFT calculations as applied to interpret the absorption spectra. The modes can be assigned to breathing modes of DIP which contribute to the coupling vibronic progression as calculations of their corresponding Huang-Rhys factors show.

The optical properties of DIP films on SiO<sub>2</sub> are anisotropic, which is due to the high structural order of the films, as reported in the literature and as reproduced by X-ray measurements. Since the films are polycrystalline, they exhibit uniaxial anisotropy with the optical axis oriented parallel to the surface normal. It is shown that a simple VASE measurement for DIP covering native oxide (Si<sub>Ntve</sub>) is not able to decorrelate the different directions. Instead, a DIP film on thermal oxide has to be included to the data analysis, utilizing interference enhancement. Also additional films grown on quartz glass can be used for decorrelation, although they exhibit some morphological issues. The type of

anisotropy, determined from multiple sample analysis, is consistent with structural studies on DIP thin films on Si substrates [11, 14], showing that the molecule is standing nearly upright. Since the HOMO-LUMO-transition is polarized along the long axis of the molecule, the tilt angle of the molecules relative to the surface normal can be determined to be  $\theta = (17 \pm 10)^\circ$  in agreement to the literature. Furthermore, from the area under the imaginary part of the dielectric tensor, a transition dipole of 6.6 Debye can be deduced.

Moreover, the thin film spectrum shows, similar to the monomer spectrum, a pronounced vibronic progression in both thin film components. Nevertheless the line shapes clearly differ between both components as well as between the monomer spectrum and the thin film spectra. These differences are due to intermolecular interactions. R. Scholz *et al.* could show that the out-of-plane component of the thin film can be theoretical described by an exciton model. The model is based on the experimental spectra determined from the solution and the thin film, as well as on structural film properties. It could be demonstrated that the experimental dielectric function is strongly influenced by the interference between Frenkel excitons and charge transfer excitons. While the Frenkel exciton model alone is not sufficient to describe the experimental data, the inclusion of mixed Frenkel-CT-states improves the model significantly. Based on electron and hole transfer parameters of  $t_e = -0.032$  eV and  $t_h = 0.066$  eV determined from DFT calculations for pairs of molecules, the difference between the excitation energy of CT and Frenkel states from the exciton model can be extracted as  $\Delta_0 = E_{00}^{\text{CT}} - E_{00}^{\text{F}} = 0.26 \pm 0.05$  eV. The in-plane component is less well understood, since it can be influenced more strongly by weak CT transitions related to higher transitions, requiring a more complex exciton model

For following DIP and PEN film growth in real-time on Si<sub>Ntve</sub> and on glass, ellipsometry as well as DRS measurements are employed and compared. Since the real-time measurements can only be performed at one angle of incidence, and the setup does not allow to measure ellipsometry and DRS spectra simultaneously, the optical anisotropy is difficult to determine during growth. Nevertheless, in contrast to ellipsometry, DRS is measured at normal incidence, which allows to investigate the in-plane component independently. Real-time ellipsometry data show for DIP on Si<sub>Ntve</sub> that no spectral changes occur below  $\sim 10$  nm, whereas small changes are visible for higher thicknesses. They are difficult to quantify because of the anisotropy and can be caused by roughness. Since ellipsometry measurements do not give unambiguous results in case of DIP on Si<sub>Ntve</sub>, the rest of the experimental findings are based on DRS measurements. On the contrary, the different orientation of the PEN transition dipole simplifies the ellipsometry analysis and allows to compare ellipsometry and DRS results. For extracting the dielectric function from the DRS data, a Matlab programme based on the well known matrix formalism is developed. It includes a Kramers-Kronig consistent Gaussian oscillator model and the effective medium approximation.

While the DRS-signal for DIP on Si<sub>Ntve</sub> is too small for analysis, measurements on quartz glass at  $T = 130$  °C reveal strong optical changes during film growth: A fourth mode at high energies evolves during growth and also some energy splitting becomes visible. In contrast, at low temperatures ( $T < -100$  °C) the intensity of the fourth mode is

strongly reduced. This indicates that it is highly related to the structural order of the film, which is smaller for low temperatures, as X-ray and AFM measurements show. These results in combination with the thickness dependence of the fourth mode indicate that the film exhibits some disorder in the beginning of growth at  $T = 130$  °C. It is induced by interfacial roughness of the glass substrate, whereas the highly ordered phase evolves above a certain thickness, where the influence of the substrate becomes less pronounced. In comparison, PEN films exhibit some energy red-shift during growth, similar to low temperature growth of DIP. Significant differences between growth on glass and on Si<sub>Ntve</sub> can be observed, which arise from morphological differences.

The real-time investigations show that the optical film properties depend highly on the film structure and on the microscopic film morphology, such as grain boundaries or other defects. Since ellipsometry and DRS measurements average over 1-4 mm<sup>2</sup> sample area, additional spatially resolved optical measurements are necessary for studying the microscopic optical properties in detail. Therefore, tip-enhanced near field optical microscopy based on a parabolic mirror microscope is performed in cooperation with D. Zhang on DIP films on Si<sub>Ntve</sub>, revealing fine optical details that are correlated to the local film morphology. It could be shown that the optical contrast is increased significantly at the molecular domain boundaries with a spatial resolution of 17 – 40 nm far beyond the diffraction limit. Additional spectroscopic information indicate that this is due to plasmon-polariton coupling and an increased radiative emission of PL photons. These results open new perspectives for analyzing spatially resolved spectroscopic properties of molecular films together with the local morphology.

## LIST OF ABBREVIATIONS

*Molecules:*

DIP	Diindenoperylene
PEN	Pentacene
PFP	Perfluoropentacene
PTCDA	Perylenetetracarboxylic dianhydrid

*Experimental techniques:*

OMBD	Organic molecular beam deposition
VASE	Variable angle spectroscopic ellipsometry
DRS	Differential reflectance spectroscopy
AFM	Atomic force microscopy
PL	Photoluminescence
TERS	Tip-enhanced Raman spectroscopy
NEXAFS	Near edge X-ray absorption fine structure spectroscopy

*Miscellaneous:*

Si <sub>Ntve</sub>	Si substrate covered with native oxide
Si <sub>ThOx</sub>	Si substrate covered with thermal oxide
APD	Avalanche photo diode
HOMO	Highest occupied molecular orbital
LUMO	Lowest unoccupied molecular orbital
RT	Room temperature
HT	High temperature
LT	Low temperature
CT	Charge transfer
ML	Monolayer
FT	Fourier transformation
AOI	Angle of incidence
TD-DFT	Time-dependent density functional theory
B3LYP	Mixed Hartree-Fock density functional approach according to Ref. [61,62]

# BIBLIOGRAPHY

- [1] M. Pope and C. E. Swenberg, Oxford University Press (1999), *Electronic processes in organic crystals and polymers*.
- [2] M. Schwoerer and H. C. Wolf, Wiley (2005), *Organische molekulare Festkörper*.
- [3] W. Brütting (ed.), Wiley (2005), *Physics of organic semiconductors*.
- [4] W. K. Tommie, P. F. Baude, C. Gerlach, D. E. Ender, D. Muyres, M. A. Haase, D. E. Vogel, and S. D. Theiss, Chem. Mater. **16**, 4413 (2004), *Recent progress in organic electronics: Materials, devices, and processes*.
- [5] J. Lewis, Materials Today **9**, 38 (2006), *Material challenge for flexible organic devices*.
- [6] S. R. Forrest, Nature **428**, 911 (2004), *The path to ubiquitous and low-cost organic electronic appliances on plastic*.
- [7] N. Karl, edited by R. Farchioni and G. Grosso, B. Springer (2001), *Charge carrier mobility in organic crystals*.
- [8] V. Coropceanu, J. Cornil, D. A. da Silva Filho, Y. Olivier, R. Silbey, and J.-L. Brédas, Chem. Rev. **107**, 926 (2007), *Charge transport in organic semiconductors*.
- [9] F. C. Spano, Annu. Rev. Phys. Chem. **57**, 217 (2006), *Excitons in conjugated oligomer aggregates, films, and crystals*.
- [10] I. Vragović and R. Scholz, Phys. Rev. B **68**, 155202 (2003), *Frenkel exciton model of optical absorption and photoluminescence in  $\alpha$ -PTCDA*.
- [11] A. C. Dürr, F. Schreiber, M. Münch, N. Karl, B. Krause, V. Kruppa, and H. Dosch, Appl. Phys. Lett. **81**, 2276 (2002), *High structural order in thin films of the organic semiconductor diindenoperylene*.

- [12] A. C. Dürr, N. Koch, M. Kelsch, A. Ruehm, J. Ghijsen, R. L. Johnson, J.-J. Pireaux, J. Schwartz, F. Schreiber, H. Dosch, and A. Kahn, *Phys. Rev. B* **68**, 115428 (2003), *Interplay between morphology, structure, and electronic properties at diindenoperylene-gold interfaces.*
- [13] A. C. Dürr, F. Schreiber, K. A. Ritley, V. Kruppa, J. Krug, H. Dosch, and B. Struth, *Phys. Rev. Lett.* **90**, 016104 (2003), *Rapid roughening in thin film growth of an organic semiconductor (diindenoperylene).*
- [14] S. Kowarik, A. Gerlach, S. Sellner, F. Schreiber, L. Cavalcanti, and O. Konovalov, *Phys. Rev. Lett.* **96**, 125504 (2006), *Real-time observation of structural and orientational transitions during growth of organic thin films.*
- [15] N. Karl, *Synthetic Metals* **133-134**, 649 (2003), *Charge carrier transport in organic semiconductors.*
- [16] A. K. Tripathi and J. Pflaum, *Appl. Phys. Lett.* **89**, 082103 (2006), *Correlation between ambipolar transport and structural phase transition in diindenoperylene single crystals.*
- [17] D. Kurrle and J. Pflaum, *Appl. Phys. Lett.* **92**, 133306 (2008), *Exciton diffusion length in the organic semiconductor diindenoperylene.*
- [18] M. A. Heinrich, J. Pflaum, A. K. Tripathi, W. Frey, M. L. Steigerwald, and T. Siegrist, *J. Phys. Chem. C* **111**, 18878 (2007), *Enantiotropic polymorphism in diindenoperylene.*
- [19] A. Hinderhofer, Master's thesis, Universität Tübingen, 2007, *Spektroskopische Untersuchungen an Pentacen und Perfluoropentacen.*
- [20] A. Hinderhofer, U. Heinemeyer, A. Gerlach, S. Kowarik, R. M. J. Jacobs, Y. Sakamoto, T. Suzuki, and F. Schreiber, *J. Chem. Phys.* **127**, 194705 (2007), *Optical properties of pentacene and perfluoropentacene thin films.*
- [21] X. N. Zhang, E. Barrena, D. de Oteyza, and H. Dosch, *Surf. Sci.* **601**, 2420 (2007), *Transition from layer-by-layer to rapid roughening in the growth of DIP on SiO<sub>2</sub>.*
- [22] V. M. Agranovich, R. D. Atanasov, and G. F. Bassani, *Chem. Phys. Lett.* **199**, 621 (1992), *Excitons in organic multiple quantum well structures.*
- [23] H. Proehl, R. Nitsche, T. Dienel, K. Leo, and T. Fritz, *Phys. Rev. B* **71**, 165207 (2005), *In situ differential reflectance spectroscopy of thin crystalline films of PTCDA on different substrates.*
- [24] M. Heilig, M. Domhan, and H. Port, *Journal of Luminescence* **110**, 290 (2004), *Optical properties and morphology of thin diindenoperylene films.*



- 
- [25] C. D. Dimitrakopoulos and D. J. Mascaro, IBM J. Res. & Dev. **45**, 11 (2001), *Organic thin-film transistors: A review of recent advances*.
- [26] C. J. Brabec, N. S. Sariciftci, and J. C. Hummelen, Adv. Funct. Mater. **11**, 15 (2001), *Plastic solar cells*.
- [27] A. Pochettino, Atti Acad. Lincei Rend. **15(1)**, 355 (1906).
- [28] A. Pochettino, Atti Acad. Lincei Rend. **15(2)**, 171 (1906).
- [29] Physik Journal, <http://www.pro-physik.de/Phy/pjtoc/26859/3>, 2008, schwerpunkt organische Elektronik.
- [30] C. C. Cedeño, J. Seekamp, A. Kam, T. Hoffmann, S. Zankovych, C. S. Torres, C. Menozzi, M. Cavallini, M. Murgia, G. Ruani, F. Biscarini, M. Behl, R. Zente, and J. Ahopelto, Microelectr. Eng. 61-62, 25 (2002): **61-62**, 25 (2002), *Nanoimprint lithography for organic electronics*.
- [31] J. B. Birks, Wiley-Interscience (1970), *Photophysics of aromatic molecules*.
- [32] K. Hannewald, V. M. Stojanović, J. M. T. Schellekens, and P. A. Bobbert, Phys. Rev. B **69**, 075211 (2004), *Theory of polaron bandwidth narrowing in organic molecular crystals*.
- [33] R. R. Lunt, N. C. Giebink, A. A. Belak, J. B. Benziger, and S. R. Forrest, J. Appl. Phys. **105**, 053711 (2009), *Exciton diffusion lengths of organic semiconductor thin films measured by spectrally resolved photoluminescence quenching*.
- [34] T. Smith, J. Electroanal. Chem. **150**, 277 (1983), *The effect of gross roughness on ellipsometry*.
- [35] H. Proehl, T. Dienel, R. Nitsche, and T. Fritz, Phys. Rev. Lett. **93**, 097403 (2004), *Formation of solid-state excitons in ultrathin crystalline films of PTCDA: From single molecules to molecular stacks*.
- [36] R. Ruiz, D. Choudhary, B. Nickel, T. Toccoli, K.-C. Chang, A. C. Mayer, P. Clancy, J. M. Blakely, R. L. Headrick, S. Iannotta, and G. G. Malliaras, Chem. Mater. **16**, 4497 (2004), *Pentacene thin film growth*.
- [37] M. Voigt, J. Pflaum, and M. Sokolowski, Phys. Stat. Sol. (a) **205**, 449 (2008), *Growth morphologies and charge carrier mobilities of pentacene organic field effect transistors with rf sputtered aluminium oxide gate insulators on ITO glass*.
- [38] R. Scholz, A. Kobitski, T. Kampen, M. Schreiber, D. Zahn, G. Jungnickel, M. Elstner, M. Sternberg, and T. Frauenheim, Phys. Rev. B **61**, 13 659 (2000), *Resonant Raman spectroscopy of 3,4,9,10-perylene-tetracarboxylic-dianhydride epitaxial films*.

- [39] R. Scholz, edited by G. Bassani, G. Liedl, and P. Wyder, Elsevier, New York (2005) *Organic semiconductors* in *Encyclopedia of Condensed Matter Physics*.
- [40] U. Heinemeyer, R. Scholz, L. Gisslén, M. I. Alonso, J. O. Ossó, M. Garriga, A. Hinderhofer, M. Kytka, S. Kowarik, A. Gerlach, and F. Schreiber, *Phys. Rev. B* **78**, 085210 (2008), *Exciton-phonon coupling in diindenoperylene thin films*.
- [41] G. Herzberg, edited by Krieger, Malabar (1950), *Molecular spectra and molecular structure, I. Spectra of diatomic molecules*.
- [42] J. Frenkel, *Phys. Rev.* **37**, 17 (1931), *On the transformation of light into heat in solids. I*.
- [43] N. S. Bayliss, *J. Chem. Phys.* **18**, 292 (1950), *The effect of the electrostatic polarization of the solvent on electronic absorption spectra in solution*.
- [44] A. S. Davydov, *Usp. Fiz. Nauk* **82**, 393 (1964), *The theory of molecular excitons*.
- [45] J. von Braun and G. Manz, Patent Num. 595 024: Verfahren zur Herstellung von Kondensationsprodukten des Fluoranthens, Deutsches Reichspatentamt, Berlin, 1934.
- [46] M. Münch, Ph.D. thesis, Stuttgart, 2001, *Strukturelle Beeinflussung der elektrischen Transporteigenschaften dünner organischer Schichten*, <http://elib.uni-stuttgart.de/opus/volltexte/2001/959/>.
- [47] E. Clar, L. J. Wiley (1972), *The aromatic sextet*.
- [48] I. C. Lewis and L. S. Singer, *Carbon*, Pergamon Press Ltd., Great Britain **5**, 373 (1967), *Further electron spin resonance studies of the pyrolysis of aromatic hydrocarbons*.
- [49] S. Kowarik, private communication.
- [50] S. Kowarik, Ph.D. thesis, Oxford University, 2006, *Real-time studies of thin films growth of organic semiconductors*.
- [51] A. Dürr, B. Nickel, V. Sharma, U. Täffner, and H. Dosch, *Thin Solid Films* 21393 (2005), *Observation of competing modes in the growth of diindenoperylene on SiO<sub>2</sub>*.
- [52] J. O. Ossó, Ph.D. thesis, Institut de Ciència de Materials de Barcelona, Max-Planck-Institut für Metallforschung, 2004, *Growth, Structure and optical properties of highly ordered organic thin film of phtalocyanine and diindenoperylene*.
- [53] D. G. de Oteyza, E. Barrena, M. Ruiz-Osés, I. naki Silanes, B. P. Doyle, J. E. Ortega, A. Arnau, H. Dosch, and Y. Wakayama, *J. Phys. Chem. C* **112**, 7168 (2008), *Crystallographic and electronic structure of self-assembled DIP monolayers on Au(111) substrates*.

- 
- [54] A. C. Dürr, F. Schreiber, M. Kelsch, H. D. Carstanjen, and H. Dosch, *Adv. Mater.* **14**, 961 (2002), *Morphology and thermal stability of metal contacts on crystalline organic thin films.*
- [55] S. Sellner, A. Gerlach, F. Schreiber, M. Kelsch, N. Kasper, H. Dosch, S. Meyer, J. Pflaum, M. Fischer, and B. Gompf, *Advanced Materials* **16**, 1750 (2004), *Strongly enhanced thermal stability of crystalline organic thin films induced by aluminum oxide capping layers.*
- [56] S. Sellner, A. Gerlach, F. Schreiber, M. Kelsch, M. Kelsch, H. Dosch, S. Meyer, J. Pflaum, M. Fischer, B. Gompf, and G. Ulbricht, *J. Mater. Res.* **21**, 455 (2006), *Mechanisms for the enhancement of the thermal stability of organic thin films by aluminum oxide capping layers.*
- [57] M. Scharnberg, J. Hu, J. Kanzow, K. Rätzke, R. Adelung, F. Faupel, C. Pannemann, U. Hilleringmann, S. Meyer, and J. Pflaum, *Appl. Phys. Lett.* **86**, 024104 (2005), *Radiotracer measurements as a sensitive tool for the detection of metal penetration in molecular-based organic electronics.*
- [58] M. Scharnberg, R. Adelung, and F. Faupel, *Phys. Stat. Sol. (a)* **205**, 578 (2008), *Influence of top layer geometries on the electronic properties of pentacene and diindenoperylene thin films.*
- [59] E. Barrena, D. G. de Oteyza, S. Sellner, H. Dosch, J. O. Ossó, and B. Struth, *Phys. Rev. Lett.* **97**, 076102 (2006), *In situ study of the growth of nanodots in organic heteroepitaxy.*
- [60] L. M. Ramaniah and M. Boero, *Phys. Rev. A* **74**, 042505 (2006), *Structural, electronic, and optical properties of the diindenoperylene molecule from firstprinciples density-functional theory.*
- [61] A. D. Becke, *Phys. Rev. A* **38**, 3098 (1988), *Density-functional exchange-energy approximation with correct asymptotic behavior.*
- [62] C. Lee, W. Yang, and R. G. Parr, *Phys. Rev. B* **37**, 785 (1988), *Development of the Colle-Salvetti correlation-energy formula into a functional of the electron density.*
- [63] S. Kowarik, A. Gerlach, W. Leitenberger, J. Hu, G. Witte, C. Wöll, U. Pietsch, and F. Schreiber, *Thin Solid Films* **515**, 5606 (2007), *Energy-dispersive X-ray reflectivity and GID for real-time growth studies of pentacene thin films.*
- [64] I. P. M. Bouchoms, W. A. Schoonveld, J. Vrijmoeth, and T. Klapwijk, *Synth. Met.* **104**, 175 (1999), *Morphology identification of the thin film phases of vacuum evaporated pentacene on SiO<sub>2</sub> substrates.*
- [65] A. C. Mayer, A. Kazimirov, and G. G. Malliaras, *Phys. Rev. Lett.* **97**, 105503 (2006), *Dynamics of bimodal growth in pentacene thin films.*

- [66] B. Stadlober, U. Haas, H. Maresch, and A. Haase, Phys. Rev. B **74**, 165302 (2006), *Growth model of pentacene on inorganic and organic dielectrics based on scaling and rate-equation theory.*
- [67] Y. Sakamoto, T. Suzuki, M. Kobayashi, Y. F. Yuan Gao, Y. Inoue, F. Sato, and S. Tokito, J. Am. Chem. Soc. **126**, 8138 (2004), *Perfluoropentacene: High-Performance p-n Junctions and Complementary Circuits with Pentacene.*
- [68] C. C. Mattheus, A. B. Dros, J. Baas, G. T. Oostergetel, A. Meetsma, J. L. de Boer, and T. T. Palstra, Synth. Met. **138**, 475 (2003), *Identification of polymorphs of pentacene.*
- [69] H. Yoshida, K. Inaba, and N. Sato, Appl. Phys. Lett. **90**, 181930 (2007), *X-ray diffraction reciprocal space mapping study of the thin film phase of pentacene.*
- [70] J. Puigdollers, A. O. C. Voz, I. Martin, M. Vetter, and R. Alcubilla, Thin Solid Films **427**, 367 (2003), *Pentacene thin-films obtained by thermal evaporation in high vacuum.*
- [71] C. Kim, K. Bang, I. An, C. J. Kang, Y. S. Kim, and D. Jeon, Curr. Appl. Phys. **6**, 925 (2005), *Morphology and ellipsometry study of pentacene films grown on native SiO<sub>2</sub> and glass substrates.*
- [72] D. Faltermeier, B. Gompf, M. Dressel, A. K. Tripathi, and J. Pflaum, Phys. Rev. B **74**, 125416 (2006), *Optical properties of pentacene thin-films and single crystals.*
- [73] J. A. Venables, C. U. Press (2000), *Introduction to surface and thin film processes.*
- [74] E. Hecht, O. V. M. Wien (2005), *Optik.*
- [75] J. Lekner, edited by M. Nijhoff (1987), *Theory of reflection of electromagnetic and particle waves.*
- [76] M. Born and E. Wolf, P. Press (1959), *Principles of optics.*
- [77] R. M. A. Azzam and N. M. Bashara, N. H. P. Company (1977), *Ellipsometry and polarized light.*
- [78] J. S. Toll, Phys. Rev. **104**, 1760 (1956), *Causality and the Dispersion Relation: Logical Foundations.*
- [79] J. A. Woollam Co., *WVASE32 Manual.*
- [80] D. E. Aspnes, Thin Solid Films **89**, 249 (1982), *Optical properties of thin films.*
- [81] *Operating and Maintenance Handbook Liquid Nitrogen Cooling, Vacuum Generators, 1997.*

- 
- [82] B. Johs, *Thin Solid Films* **234**, 395 (1993), *Regression calibration method for rotating element ellipsometers*.
- [83] J. D. E. McIntyre and D. E. Aspnes, *Surf. Sci.* **24**, 417 (1971), *Differential reflection spectroscopy of very thin surface films*.
- [84] N. S. Bayliss and E. G. McRae, *J. Phys. Chem.* **58**, 1002 (1954), *Solvent effects in organic spectra: dipole forces and the Franck-Condon principle*.
- [85] R. Scholz, I. Vragović, A. Y. Kobitski, G. Slavan, T. U. Kampen, M. Schreiber, and D. R. T. Zahn (2002), *Spectroscopic properties of a prototypic organic semiconductor: The case of PTCDA*.
- [86] C. V. Raman and K. S. Krishnan, *Nature* **121**, 501 (1928), *A new type of secondary radiation*.
- [87] D. A. Long, Wiley (2002), *The Raman effect: A unified treatment of the theory of Raman scattering by molecules*.
- [88] I. R. Lewis (ed.), M. Dekker (2001), *Handbook of Raman spectroscopy: from the research laboratory to the process line*.
- [89] S. Wartewig, Wiley-VCH (2003), *IR and Raman spectroscopy: fundamental processing*.
- [90] J. J. Laserna, John Wiley & Sons (1996), *Modern techniques in Raman spectroscopy*.
- [91] E. Abbe, *Arch. f. Mikroskop. Anat* **9**, 413 (1873), *Beiträge zur Theorie des Mikroskops und der Mikroskopischen Wahrnehmung*.
- [92] L. Novotny and S. J. Stranick, *Ann. Rev. Phys. Chem.* **57**, 303 (2006), *Near-field optical microscopy and spectroscopy with pointed probes*.
- [93] M. Sackrow, C. Stanciu, M. A. Lieb, and A. J. Meixner, *Chem. Phys. Chem.* **9**, 316 (2008), *Imaging nanometre-sized hot spots on smooth Au films with high-resolution tip-enhanced luminescence and Raman near-field optical microscopy*.
- [94] M. Sackrow, Ph.D. thesis, Universität Tübingen, 2008, *Confocal and near-field measurements with a parabolic mirror*.
- [95] K. Karrai and R. D. Grober, *Appl. Phys. Lett.* **66**, 1842 (1995), *Piezoelectric tip-sample distance control for near-field optical microscopes*.
- [96] M. A. Lieb and A. J. Meixner, *Optics Express* **8**, 458 (2001), *A high numerical aperture parabolic mirror as imaging device for confocal microscopy*.
- [97] J. Als-Nielsen and D. McMorrow, Wiley (2000), *Elements of modern X-ray physics*.

- [98] L. G. Parratt, Phys. Rev. **95**, 359 (1954), *Surface studies of solids by total reflection of X-rays*.
- [99] Parratt32, Version 1.5.2: [www.hmi.de/bensc/instrumentation/instrumente/v6/refl/parratt\\_en.htm](http://www.hmi.de/bensc/instrumentation/instrumente/v6/refl/parratt_en.htm).
- [100] <http://www.jpik.com/tutorial/>.
- [101] I. Horcas, R. Fernandez, J. M. Gomez-Rodriguez, J. Colchero, J. Gomez-Herrero, and A. M. Baro, Rev. Sci. Instrum. **78**, 013705 (2007), *WSXM: A software for scanning probe microscopy and a tool for nanotechnology*.
- [102] C. M. Herzinger, B. Johs, W. A. McGahan, J. A. Woollam, and W. Paulson, J. Appl. Phys. **83**, 3323 (1998), *Ellipsometric determination of optical constants for silicon and thermally grown silicon dioxide via a multi-sample, multi-wavelength, multi-angle investigation*.
- [103] R. A. Synowicki, Phys. Stat. Sol. (c) **5**, 1085 (2008), *Suppression of backside reflections from transparent substrates*.
- [104] Private communication with A. Hinderhofer.
- [105] D. J. D. Smet, J. Appl. Phys. **76**, 2571 (1994), *Ellipsometry of anisotropic substrates: Re-examination of a special case*.
- [106] E. Bortchagovsky, Thin Solid Films **307**, 192 (1997), *Ellipsometric method for investigation of the optical anisotropy of thin films: theory and calculations*.
- [107] M. Campoy-Quiles, P. G. Etchegoin, and D. D. C. Bradley, Phys. Rev. B **72**, 045209 (2005), *On the optical anisotropy of conjugated polymer thin films*.
- [108] W. A. McGahan, B. Johs, and J. Woollam, Thin Solid Films **234**, 443 (1993), *Techniques for ellipsometric measurement of the thickness and optical constants of thin absorbing films*.
- [109] O. Gordan, M. Friedrich, and D. Zahn, Thin Solid Films **456**, 551 (2004), *Determination of the anisotropic dielectric function for metal free phthalocyanine thin films*.
- [110] J.-P. Moy, Appl. Opt. **20**, 3821 (1981), *Immersion ellipsometry*.
- [111] C. M. Ramsdale and N. C. Greenham, Adv. Mater. **14**, 212 (2002), *Ellipsometric determination of anisotropic optical constants in electroluminescent conjugated polymers*.
- [112] H. Arwin, J. Mårtensson, and R. Jansson, Appl. Opt. **31**, 6707 (1992), *Line-shape analysis of ellipsometric spectra on thin organic films*.

- 
- [113] D. E. Aspnes, A. North-Holland (1976), *Spectroscopic ellipsometry of solids* in *Optical properties of solids: New developments*.
- [114] H. G. Tompkins, T. Tiwald, C. Bungay, and A. E. Hooper, J. Vac. Sci. Technol. A **24**, 1605 (2006), *Measuring the thickness of organic/ polymer/ biological films on glass substrates using spectroscopic ellipsometry*.
- [115] C. M. Herzinger, P. G. Snyder, B. Johs, and J. A. Woollam, J. Appl. Phys. **77**, 1715 (1995), *InP optical constants between 0.75 and 5.0 eV determined by variable-angle spectroscopic ellipsometry*.
- [116] R. Scholz, A. Y. Kobitski, D. R. T. Zahn, and M. Schreiber, Phys. Rev. B **72**, 245208 (2005), *Investigation of molecular dimers in  $\alpha$ -PTCDA by ab initio methods: Binding energies, gas-to-crystal shift, and self-trapped excitons*.
- [117] A. Y. Kobitski, R. Scholz, I. Vragović, H. P. Wagner, and D. R. T. Zahn, Phys. Rev. B **66**, 153204 (2002), *Low-temperature time-resolved photoluminescence characterization of 3,4,9,10-perylene tetracarboxylic dianhydride crystals*.
- [118] R. L. Fulton and M. Gouterman, J. Chem. Phys. **41**, 2280 (1964), *Vibronic coupling. II. spectra of dimers*.
- [119] J. S. Briggs and A. Herzenberg, J. Phys. B **3**, 1663 (1970), *Sum rules for the vibronic spectra of helical polymers*.
- [120] R. Scholz and M. Schreiber, Chem. Phys. **325**, 9 (2006), *Linear optical properties of perylene-based chromophores*.
- [121] P. M. Kazmaier and R. Hoffmann, J. Am. Chem. Soc. **116**, 9684 (1994), *A theoretical study of crystallochromy. Quantum interference effects in the spectra of perylene pigments*.
- [122] M. Hoffmann and Z. G. Soos, Phys. Rev. B **66**, 024305 (2002), *Optical absorption spectra of the Holstein molecular crystal for weak and intermediate electronic coupling*.
- [123] G. E. Jellison and F. A. Modine, J. Appl. Phys. **76**, 3758 (1994), *Optical functions of silicon at elevated temperatures*.
- [124] M. Kytka, A. Gerlach, F. Schreiber, and J. Kováč, Appl. Phys. Lett. **90**, 131911 (2007), *Real-time observation of oxidation and photo-oxidation of rubrene thin films by spectroscopic ellipsometry*.
- [125] F. D. Angelis, G. Das, and E. D. Fabrizio, Chem. Phys. Lett. **462**, 234 (2008), *Analysis of the interactions between pentacene film and air molecules by means of Raman spectroscopy*.

- [126] T. Itoh and N. Yamauchi, Appl. Surf. Sci. **253**, 6196 (2007), *Surface morphology characterization of pentacene thin film and its substrate with under-layers by power spectral density using fast Fourier transform algorithms.*
- [127] G. Yoshikawa, T. Miyadera, R. Onoki, K. Ueno, I. Nakai, S. Entani, S. Ikeda, D. Guo, M. Kiguchi, H. Kondoh, T. Ohta, and K. Saiki, Surf. Sci. **600**, 251 (2006), *In-situ measurement of molecular orientation of the pentacene ultrathin films grown on SiO<sub>2</sub> substrates.*
- [128] O. Ostroverkhova, S. Shcherbyna, D. G. Cooke, R. F. Egerton, R. R. Tykwinski, S. R. Parkin, and J. E. Anthony, J. Appl. Phys. **98**, 033701 (2005), *Optical and transient photoconductive properties of pentacene and functionalized pentacene thin films: Dependence on film morphology.*
- [129] K. O. Lee and T. T. Gan, Chem. Phys. Lett. **51**, 120 (1977), *Influence of substrate temperature on the optical properties of evaporated films of pentacene.*
- [130] M. Grobosch, R. Schuster, T. Pichler, M. Knupfer, and H. Berger, Phys. Rev. B **74**, 155202 (2006), *Analysis of the anisotropy of excitons in pentacene single crystals using reflectivity measurements and electron energy-loss spectroscopy.*
- [131] M. Brinkmann, G. Gadret, M. Muccini, C. Taliani, N. Masciocchi, and A. Sironi, J. Am. Chem. Soc. **122**, 5147 (2000), *Correlation between molecular packing and optical properties in different crystalline polymorphs and amorphous thin films of mer-Tris(8-hydroxyquinoline) aluminum(III).*
- [132] O. D. Gordan, C. Himcinschi, D. R. T. Zahn, C. Cobet, N. Esser, and W. Braun, Appl. Phys. Lett. **88**, 141913 (2006), *Reduced intermolecular interaction in organic ultrathin films.*
- [133] M. Dressel, B. Gompf, D. Faltermeier, A. Tripathi, J. Pflaum, and M. Schubert, Opt. Exp. **16**, 19770 (2008), *Kramers-Kronig-consistent optical functions of anisotropic crystals: generalized spectroscopic ellipsometry on pentacene.*
- [134] B. Conrad, W. Cullen, B. Riddick, and E. Williams, Surf. Sci. **603**, L27 (2009), *Pentacene islands grown on ultra-thin SiO<sub>2</sub>.*
- [135] I. Tonoco, J. Am. Chem. Soc. **82**, 4785 (1960), *Hypochromism in polynucleotides.*
- [136] R. K. Bullough, J. Chem. Phys. **43**, 1927 (1965), *Theory of hypochromism.*
- [137] W. Chegal, Y. J. Cho, H. J. Kim, H. M. Cho, Y. W. Lee, and S. H. Kim, Jap. J. Appl. Phys. **43**, 6475 (2004), *A new spectral imaging ellipsometer for measuring the thickness of patterned thin films.*



- 
- [138] M. Vaupel and M. Vinnichenko, Phys. Stat. Sol. (c) **5**, 1137 (2008), *Plasma flow induced local variation of dispersion constants of ITO-films observed with spectroscopic imaging ellipsometry*.
- [139] L. Gisslén and R. Scholz, *unpublished*.
- [140] D. A. Tenne, S. Park, T. U. Kampen, A. Das, R. Scholz, and D. R. T. Zahn, Phys. Rev. B **61**, 14 564 (2000), *Single crystals of the organic semiconductor perylene tetracarboxylic dianhydride studied by Raman spectroscopy*.
- [141] V. Presser, B.-E. Schuster, M. B. Casu, U. Heinemeyer, F. Schreiber, K. G. Nickel, and T. Chassé, J. Raman Spectrosc. accepted (2009), *Raman polarization studies of highly oriented organic thin films*.
- [142] J. Chen, C. K. Tee, M. Shtein, J. Anthony, and D. C. Martin, J. Appl. Phys. **103**, 114513 (2008), *Grain-boundary-limited charge transport in solution-processed 6,13 bis (tri-isopropylsilylethynyl) pentacene thin film transistors*.
- [143] L. Novotny and B. Hecht, C. U. Press (2006), *Principles of nano-optics*.
- [144] J. Steidtner. and B. Pettinger, Phys. Rev. Lett. **100**, 236101 (2008), *Tip-enhanced Raman spectroscopy and microscopy on single dye molecules with 15 nm resolution*.
- [145] D. Zhang, U. Heinemeyer, C. Stanciu, M. Sackrow, K. Braun, L. Henneman, X. Wang, R. Scholz, F. Schreiber, and A. J. Meixner, submitted, *Nanometer scale spectroscopic imaging of organic semiconductor film by plasmon-polariton coupling*.
- [146] A. Cvitkovic, N. Ocelic, and R. Hillenbrand, Optics Express **15**, 8550 (2007), *Analytical model for quantitative prediction of material contrasts in scattering-type near-field optical microscopy*.
- [147] B. Pettinger, K. F. Domke, D. Zhang, R. Schuster, and G. Ertl, Phys. Rev. B **76**, 113409 (2007), *Direct monitoring of plasmon resonances in a tip-surface gap of varying width*.



# LIST OF PUBLICATIONS

- U. Heinemeyer *et al.*, *Real-time spectral changes during growth of organic semiconductor films and thickness regimes*, in preparation.
- L. Gisslén *et al.*, *Resonant Raman spectra of diindenoperylene thin films*, in preparation.
- D. Zhang, U. Heinemeyer, C. Stanciu, M. Sackrow, K. Braun, L. E. Hennemann, X. Wang, R. Scholz, F. Schreiber and A. J. Meixner, *Nanometer scale spectroscopic imaging of organic semiconductor films by plasmon-polariton coupling*, submitted
- V. Presser, B.-E. Schuster, M. B. Casu, U. Heinemeyer, F. Schreiber, K. G. Nickel and T. Chassé, *J. Raman Spectrosc.*, accepted (2009), published online: ([www.interscience.wiley.com](http://www.interscience.wiley.com)) DOI 10.1002/jrs.2361, *Raman polarization studies of highly oriented organic thin films*.
- M. Kytka, L. Gisslén, A. Gerlach, U. Heinemeyer, J. Kováč, R. Scholz and F. Schreiber, *J. Chem. Phys.* **130**, 214507 (2009), *Optical spectra obtained from amorphous films of rubrene: Evidence for predominance of twisted isomer*.
- U. Heinemeyer, R. Scholz, L. Gisslén, M. I. Alonso, J. O. Ossó, M. Garriga, A. Hinderhofer, M. Kytka, S. Kowarik, A. Gerlach and F. Schreiber, *Phys. Rev. B* **78**, 085210 (2008), *Exciton-phonon coupling in diindenoperylene thin films*.
- U. Heinemeyer, A. Hinderhofer, M. I. Alonso, J. O. Ossó, M. Garriga, M. Kytka, A. Gerlach and F. Schreiber, *Phys. Stat. Sol. (a)* **205**, 927 (2008), *Uniaxial anisotropy of organic thin films determined by ellipsometry*.
- A. Hinderhofer, U. Heinemeyer, A. Gerlach, S. Kowarik, R. M. J. Jacobs, Y. Sakamoto, T. Suzuki and F. Schreiber, *J. Chem. Phys.* **127**, 194705 (2007), *Optical properties of pentacene and perfluoropentacene thin films*.
- U. Heinemeyer, M. C. Wengler and K. Buse, *Appl. Phys. Lett.* **89**, 112910 (2006), *Annihilation of the  $OH^-$  absorption due to domain inversion in MgO-doped lithium niobate crystals*.
- M. C. Wengler, U. Heinemeyer, E. Soergel and K. Buse, *J. Appl. Phys.* **98**, 064104 (2005), *Ultraviolet light-assisted domain inversion in magnesium-doped lithium niobate crystals*.



# DANKSAGUNG

Diese Arbeit wäre ohne Unterstützung anderer nicht möglich gewesen, weshalb ich mich an dieser Stelle bei allen bedanken möchte, die wesentlich zum Gelingen beigetragen haben.

Mein besonderer Dank gilt Prof. Dr. Frank Schreiber für das Ermöglichen dieser Arbeit und die gute Betreuung in den letzten Jahren, sowie für das mir entgegengebrachte Vertrauen.

Prof. Dr. Alfred Meixner danke ich für die fachliche Begutachtung dieser Arbeit und die gute Zusammenarbeit bei den Nahfeldmessungen in seiner Arbeitsgruppe.

Bedanken möchte ich mich vor allem auch bei Dr. Reinhard Scholz, der durch seine Rechnungen wesentlich zum Verständnis der statischen Spektren und der Ramanspektren beigetragen hat und auch bei vielen anderen Fragen jederzeit zur Seite stand. In diesem Zusammenhang möchte ich auch Linus Gisslén dankend erwähnen, der im Hintergrund einige der theoretischen Modellrechnungen durchgeführt hat.

Dr. Alexander Gerlach gilt mein Dank für die ständige Unterstützung im Labor und die vielzähligen Diskussionen, insbesondere für die Hilfe an der Vakuumkammer, die Dank seiner Vorarbeiten existierte und gute Dienste geleistet hat.

Alexander Hinderhofer danke ich für die aufschlussreichen Ellipsometrie-Diskussionen und die Untersuchung der statischen Spektren von Pentacen im Rahmen seiner Diplomarbeit, die einen wichtigen Grundstein für diese Arbeit gelegt haben. Katharina Broch möchte ich dafür danken, dass sie mich zum Schluss dieser Arbeit in jeder Hinsicht unterstützt und mir großes Verständnis zu Beginn ihrer Diplomarbeit entgegengebracht hat, was mir die schnelle Fertigstellung dieser Arbeit ermöglicht hat.

Allen weiteren Mitgliedern der Arbeitsgruppe Schreiber und dem Sekretariat gilt mein Dank für die fachliche und außerfachliche Unterstützung, sowie für die Zusammenarbeit in den letzten Jahren. Insbesondere Milan Kytka danke ich für viele Diskussionen rund um das Thema Ellipsometrie und zur Datenanalyse. Den Austauschstudenten Eric Oberla und Alexander Moore danke ich für die experimentelle Unterstützung bei DRS Messungen, die im Rahmen des RISE-Programmes stattgefunden haben.

Schließlich möchte ich mich bei Dr. Catrinel Stanciu und Dr. Dai Zhang für die gemeinsamen Experimente am Nahfeldmikroskop und für die vielen Diskussionen bedanken.

Für die ausführliche Einführung in AFM Messungen bedanke ich mich bei Frau Elke Nadler. Auch der Elektronikwerkstatt und der feinmechanischen Werkstatt gilt mein Dank für ihre Unterstützung, ebenso wie Prof. Dr. Jens Pflaum für das Aufreinigen der Moleküle und Dr. Robert Jacobs für aufschlussreiche Diskussionen.

Meinem Freund Sebastian danke ich für seine Geduld und seinen Beistand und dafür dass es ihn gibt. Mein größter Dank gilt meinen Eltern, die mich in jeder Hinsicht unterstützt haben, bis zum Ende. Danke für die gemeinsame Zeit.



# CURRICULUM VITAE

Ute Agnes Heinemeyer  
born on the 30th of April 1980 in Bonn

## EDUCATION

- 10/2005 - now      **Ph.D. studies**  
at the Eberhard-Karls university in Tübingen, institute  
of applied physics, supervised by Prof. Dr. Schreiber.  
Topic: *Optical properties of organic semiconductor thin  
films: Static spectra and real-time growth studies*
- 10/1999 - 08/2005      **Study of Physics**  
at the Friedrich-Wilhelms University in Bonn  
Minor: Philosophy  
Diploma thesis in the institute of applied physics, su-  
pervised by Prof. Dr. Buse. Topic: *Beeinflussung der  
ferroelektrischen Eigenschaften von Lithiumniobat mit  
UV-Licht*
- 09/1990 - 05/1999      **High school**  
at the Anno-Gymnasium in Siegburg

## STUDIES ABROAD

- 08/2002 - 05/2003      **Study of Physics**  
at the University of British Columbia in Vancouver,  
Canada  
Minor: Philosophy

